Single-top s channel cross-section measurement with the ALTAS detector

Caterina Monini

Université Joseph Fourier

THÈSE

Pour obtenir le grade de

DOCTEUR DE L'UNIVERSITÉ DE GRENOBLE

Spécialité : **Physique Subatomique et Astroparticules**

Arrêté ministériel : 7 Août 2006

Présentée par

Caterina Monini

Thèse dirigée par **Annick Lleres, Arnaud Lucotte**

préparée au sein **Laboratoire de Physique Subatomique et de Cosmologie de Grenoble (LPSC)**
et de **École Doctorale de Physique de Grenoble**

Mesure de la section efficace de production électrofaible de quark top en voie s, avec le détecteur ATLAS

Thèse soutenue publiquement le **12 Septembre 2014**,
devant le jury composé de :

Mr, Roberto Chierici
Dr. IPNL Lyon, Rapporteur
Mr, Denis Gelé
Dr. IPHC Strasbourg, Rapporteur
Mr, Christophe Furget
Prof. LPSC Grenoble, Examinateur
Mr, Laurent Vacavant
Dr. CPPM Marseille, Examinateur
Mrs, Annick Lleres
Dr. LPSC Grenoble, Directeur de thèse
Mr, Arnaud Lucotte
Dr. LPSC Grenoble, Directeur de thèse

Single-top s channel cross-section measurement with the ATLAS detector

Abstract

The work reported in this thesis is aimed at measuring with the ATLAS detector the only mechanism of top quark electroweak production which has not yet been observed at the Large Hadron Collider: the s-channel. Its interest relies in the confirmation of the Standard Model predictions but, as well, in the possibility of constraining several new physics scenarios when comparing the s-channel cross section with the one of the other single top production modes (the Wt and t-channel). After a general introduction upon top physics and the experimental setup employed for the detection and the reconstruction of the physics objects, we present two analyses realized with proton-proton collisions collected by the ATLAS detector at a center of mass energy of 7 and 8 TeV. Since the s-channel production is characterized by a very low purity and, at the same time, is not favoured at the LHC because it proceeds via quark-antiquark annihilation, a multivariate approach is applied in both cases to discriminate the signal. For the 7 TeV study, based on an integrated luminosity of 4.7 fb^{-1}, two boosted decision trees classifiers are optimized against the main sources of background; a cut realized on one of such discriminants implements a tight event selection, after which the second output distribution is used for a maximum likelihood fit to the data. This allows to set an upper limit on the s-channel cross section of 21.5 pb (14.3 pb expected), corresponding to a significance of 0.6 standard deviations (0.8 expected). The 8 TeV analysis, based on an integrated luminosity of 20.3 fb^{-1}, has a simpler strategy: only one boosted decision trees classifier is trained to isolate signal after a preliminary cut-based selection; its output distribution is then fitted to the data with the same approach than at 7 TeV, taking into account the systematic and statistical uncertainty via the generation of pseudoexperiments. The significance of the s-channel measurement being lower than 3 σ (1.3 standard deviation observed, 1.4 expected), only a 95% C.L. limit can be set on the cross section; the result is however improved and corresponds to 14.6 pb (7.9 pb expected).

Contents

Introduction

Since its discovery realized in 1995 at the TeVatron, the top quark persists in the focus of particle physics programmes as its singular features suggest that it may play a key role within the Standard Model. Such properties, as well as the cross section characterizing the several production mechanisms, can be measured precisely at the Large Hadron Collider, where abundant rates of top quarks are obtained thanks to the high collision energy and the large instantaneous luminosity. On the other hand, since many theoretical models predicting new physics involve the top quark, this context is also very fruitful for undertaking Beyond Standard Model searches in a comprehensive way. This thesis can hence be tought as a piece of this wide research puzzle, aimed at shading light on the top electroweak production; in particular, the work focuses on the lowest rate production mode taking place via proton-proton collisions: the s-channel. Its interest lies in the fact that such single top process is the less well known at the LHC, but its measurement would be crucial also in view of its high sensitivity to new physics scenarios.

Globally, this manuscript is structured into two main sections: the first aimed at illustrating the theoretical framework that allows to draw conclusions on the experimental results, and at detailing the CERN accelerator complex and the ATLAS detector; the second designed to report the two s-channel cross section analyses performed at a center of mass energy of 7 and 8 TeV.
In the first chapter will thus pass in review the main notions concerning top physics, mostly highlighting the differences between the production modes mediated by strong and electroweak interactions. A special emphasis will be conferred to the reasons encouraging the challenging single top analyses, from the extraction of some elements of the Cabibbo-Kobayashi-Maskava matrix, to the constraints that can be set on different BSM models. Then, the LHC and in particular all the components of the ATLAS detector will be described in Chapter 2, with the goal of understanding the basis of the reconstruction of the physics objects delineated in Chapter 3. Once defined the detection efficiency and the performance relative to the identification of such objects, we will begin to discuss the s-channel measurement. To avoid redundancy on the subjects which are common for the two performed analyses, the introductive Chapter 4 has been set up to define the signal and background phenomenology and the Monte Carlo simulations employed to model each channel, as well as the technical "tools": the data-driven techniques employed to estimate some background sources, the multivariate approach based on boosted decision trees, the systematic uncertainties and

the statistical framework. Afterwards, we will report in Chapter 5 the analysis of the proton-proton collisions data collected at 7 TeV and corresponding to an integrated luminosity of 4.7 fb^{-1}, which results in the determination of an upper limit on the s-channel cross section. Such measurement will be improved by the second analysis described in the sixth chapter of this manuscript, realized with a higher luminosity dataset (20.3 fb^{-1}) recorded at a center of mass energy of 8 TeV; in this case, more checks validating the results and the technical choices will be presented.

Chapter 1

Top quark physics

Among the elementary constituents of hadrons, the top quark exhibits unique properties which make it an excellent probe to investigate the Standard Model, and assess new physics sources. All the striking features are stemmed from its large mass of 173.2 $\pm$ 0.9 GeV [1] [1], five orders of magnitude greater than the one of the lightest quark. It is often speculated that a quark with almost the same mass than a Rhenium nucleus, might play a crucial role in the mechanism of electroweak symmetry breaking. In any case, the top quark turns out to provide decisive inputs to fits of global electroweak parameters that constrain the properties of the Higgs boson. Moreover, the experimental consequences of this peculiar mass are interesting in their own. The top quark decays before hadronizing in around $5 \cdot 10^{-25}$ s, in contrast with the lighter quarks that appear permanently confined in bound states. Instead of being depolarized by chromomagnetic interactions, therefore, its spin is directly transmitted to the decay products, conditioning their angular distributions. In addition, the final state of the decay process is almost exclusively characterized by the presence of a bottom quark and a W boson, as the mixing with the other two generations of quarks is negligible.

Discovered in 1995 by the CDF and DØ collaborations [3, 4], the top quark was extensively studied at the TeVatron collider. The kinematical properties of its production and decay mechanisms were investigated, together with the corresponding cross section; the mass was determined with an impressive precision of 0.5%, and the first W helicity analyses were realized. Despite the numerous results achieved with proton-antiproton collisions at a center of mass energy of 1.96 TeV, however, most of the measurements were limited by the poor statistics collected.
The high luminosity Large Hadron Collider is in comparison a top factory: the proton-proton collisions that took place in 2011 and 2012 at a center of mass energy of 7 and 8 TeV, respectively, generated more than eight millions of top quarks. With such a large statistics it was possible to use top physics as a way to confirm the Standard Model via precision measurements. At the same time, this quark so slighly affected by the complications arising from the strong interaction, represents a key element to

[1] The value reported here corresponds to the current world average. However the top quark mass has also been recently measured from the ATLAS and CMS collaborations, using 4.7 fb^{-1} of 7 TeV data in different $t\bar{t}$ decay channels: m_t=172.6 $\pm$ 0.4 (stat) $\pm$ 1.2 (syst) GeV. [2]

indirectly claim for new phenomena (via hypothetical deviation from the theoretical rates and features) or directly search for new particles.
After a brief introduction on the Standard Model, which successfully predicted the existence of this particle as weak-isospin partner of the bottom quark, we will present in this chapter a detailed description of the top phenomenology. We will focus on its production mechanisms, with a special attention to the implications due to the specific LHC setup; we will underline the differences between top quark pair generation via strong interaction and single top production via electroweak interaction, reviewing the latest experimental results. Finally, we will illustrate how the electroweak production of top quark can constrain models predicting new physics.

1.1 Theoretical framework

The Standard Model (SM) is a quantum field theory which sheds light on the subatomic physics by combining quantum mechanics and special relativity. Developed since the mid sixties, this theoretical framework describes in an elegant way the fundamental forces and the structure of matter, predicting with remarkable rigor numerous experimental outcomes. The great potential of this model relies on the role played by symmetries, which are mathematically implemented via group theory. Three Lie groups of transformations, whose parameters are continuous variables that can take infinite values, are introduced to describe the particle physics: the abelian (commutative) unitary group $U(1)$, the non-abelian special unitary group $SU(2)$ [2], whose Lie algebra is in isomorphism with the one of the SO(3) rotation group, and $SU(3)$. The continuous symmetries characterizing a given system are, on the other side, connected to physics via the Noether theorem, which essentially associate to them a conservation law. According to Yang-Mill theory [5], the (renormalizable) Lagrangian describing the elementary fermions and their interactions has to be invariant under a set of local gauge transformations that form a specific Lie group; this entails, inevitably, the existence of gauge bosons as mediator of the interactions themselves.
Glahow, Salam and Weinberg [6, 7, 8] proposed a description of the combined electromagnetic and weak interactions based on the $SU(2)_L \otimes U(1)_Y$ group; the associated fields, namely W_i^μ [3] and B^μ, interact with leptons and quarks via the weak isospin I and the hypercharge Y [4], respectively. Later on, an explanation of the quantum theory of strong interactions in terms of the group $SU(3)_C$ took gradually shape from the work of Gell-Mann, Ne'emanm, Zweigh and Fritzsh [9, 10, 11]. The derived gauge fields, G^μ, represent in this case directly the 8 gluons that couple to the color charge, which is a "prerogative" of quarks.
Tables 1.1 and 1.2 summarize schematically the properties of the elementary particles and the just mentioned gauge fields, in terms of Lie groups representation.

[2] SU(n) are Lie groups of $n \times n$ unitary matrices with determinant 1, whose dimension is n^2-1.

[3] By convention the latin indices $i,j,k \in (1,3)$, $a \in (1,8)$, while the greek indices μ, ν represent the components of a four-vector and thus $\in (0,4)$.

[4] The Gell-Mann Nishijima relation states $Q = I_3 + \frac{1}{2}Y$.

Fermions	Y	I	I_3	Q
$Q_L^i = \begin{pmatrix} u_L \\ d_L \end{pmatrix}, \begin{pmatrix} c_L \\ s_L \end{pmatrix}, \begin{pmatrix} t_L \\ b_L \end{pmatrix}$	1/3	1/2	$\begin{pmatrix} +1/2 \\ -1/2 \end{pmatrix}$	$\begin{pmatrix} +2/3 \\ -1/3 \end{pmatrix}$
$u_R^i = u_R, c_R, t_R$	4/3	0	0	2/3
$d_R^i = d_R, s_R, b_R$	-2/3	0	0	-1/3
$L_L^i = \begin{pmatrix} \nu_{eL} \\ e_L \end{pmatrix}, \begin{pmatrix} \nu_{\mu L} \\ \mu_L \end{pmatrix}, \begin{pmatrix} \nu_{\tau L} \\ \tau_L \end{pmatrix}$	-1	1/2	$\begin{pmatrix} +1/2 \\ -1/2 \end{pmatrix}$	$\begin{pmatrix} 0 \\ -1 \end{pmatrix}$
$e_R^i = e_R, \mu_R, \tau_R$	-2	0	0	-1

Table 1.1: The Standard Model fermions and their quantum numbers: hypercharge, weak isospin and its third component, electric charge in multiples of $e = 1.6 \times 10^{-19}$ C. The subscription L denotes the left handed $SU(2)$ isospin doublets, while R represents the right handed $SU(2)$ isospin singlets.

Bosons	Fields	Y	I	I_3	Q
g	G_μ	0	0	0	0
$W^\pm$	$\begin{pmatrix} W^+ \\ W^- \end{pmatrix} = \begin{pmatrix} \frac{W_\mu^1 + W_\mu^2}{\sqrt{2}} \\ \frac{W_\mu^1 - W_\mu^2}{\sqrt{2}} \end{pmatrix}$,	0	1	$\begin{pmatrix} +1 \\ -1 \end{pmatrix}$	$\begin{pmatrix} +1 \\ -1 \end{pmatrix}$
Z^0	$Z_\mu = cos\theta_W W_\mu^3 - sin\theta_W B_\mu$	0	0	0	0
γ	$A_\mu = sin\theta_W W_\mu^3 + cos\theta_W B_\mu$	0	0	0	0
H	$\begin{pmatrix} \phi^+ \\ \phi^0 \end{pmatrix} = \begin{pmatrix} 0 \\ \nu/\sqrt{2} \end{pmatrix}$	0	0	$\begin{pmatrix} +1 \\ 0 \end{pmatrix}$	$\begin{pmatrix} +1/2 \\ -1/2 \end{pmatrix}$

Table 1.2: The Standard Model Higgs and gauge bosons expressed in terms of the gauge fields are presented with their quantum numbers: hypercharge, weak isospin and its third component, electric charge. Three kinds of vector bosons account for the strong (g), weak ($W^\pm$, Z_0), electromagnetic (γ) interactions, while the only scalar particle, the Higgs that will be introduced below, endows their masses.

Considering just the gauge fields contribution, the SM Lagrangian is expressed by:

$$\mathcal{L}_{Gauge} = -\frac{1}{4}B_{\mu\nu}B^{\mu\nu} - \frac{1}{4}W^i_{\mu\nu}W^{i\mu\nu} - \frac{1}{4}G^a_{\mu\nu}G^{a\mu\nu} \tag{1.1}$$

$$\text{where } B_{\mu\nu} = \partial_\mu B_\nu - \partial_\nu B_\mu \tag{1.2}$$

$$W^i_{\mu\nu} = \partial_\mu W^i_\nu - \partial_\nu W^i_\mu - g_2\epsilon^{ijk}W^j_\mu W^k_\nu, \tag{1.3}$$

$$G^a_{\mu\nu} = \partial_\mu G^a_\nu - \partial_\nu G^a_\mu - g_3 f^{abc}G^b_\mu G^c_\nu. \tag{1.4}$$

These fields can be exploited to construct a covariant derivative (D_μ) replacing the standard derivative (∂_μ) with the aim of expressing a Lagrangian invariant under local gauge $SU(3)_C \otimes SU(2)_L \otimes U(1)_Y$ transformations also for fermions:

$$D_\mu = \partial_\mu + ig_1\frac{Y}{2}B_\mu + ig_2\tau^j W^j_\mu + ig_3\lambda^a G^a_\mu \tag{1.5}$$

$$\mathcal{L}_{Fermions} = \sum_{i=1}^{3} \bar{Q^i_L}i\gamma^\mu D_\mu Q^i_L + \bar{u^i_R}i\gamma^\mu D_\mu u^i_R + \bar{d^i_R}i\gamma^\mu D_\mu d^i_R + \bar{L^i_L}i\gamma^\mu D_\mu L^i_L + \bar{e^i_R}i\gamma^\mu D_\mu e^i_R \tag{1.6}$$

In the previous equations g_2, g_3 are the coupling constants, ϵ^{ijk}, f^{abc} the structure constants, τ^j, λ^a the generators for the $SU(2)$ and $SU(3)$ spaces, respectively. Even though the Lagrangians described by 1.1 and 1.6 are derived in a neat way, their consistency with experiment becomes a major problem given that no mass term is present. Brout, Englert [12] and Higgs [13] proposed a solution based on the concept of spontaneous symmetry breaking, due to the action of a complex scalar field filling the universe:

$$\Phi = \begin{pmatrix}\phi^+\\ \phi^0\end{pmatrix} = \frac{1}{\sqrt{2}}\begin{pmatrix}\phi_1 + i\phi_2\\ \phi_3 + i\phi_4\end{pmatrix};$$

Φ is a doublet in the $SU(2)$ space, carries non-zero $U(1)$ hypercharge, but is a $SU(3)$ singlet. Describing its dynamics with the simplest Lagrangian:

$$\mathcal{L}_{Higgs} = (D^\mu\Phi)^\dagger(D_\mu\Phi) - \mu^2\Phi^\dagger\Phi - \lambda(\Phi^\dagger\Phi)^2, \tag{1.7}$$

and requiring the potential depicted in Fig.1.1 with $\lambda > 0$ and $\mu^2 < 0$, Φ acquires a non-zero vacuum expectation value by virtue of its self interactions. The existence of a degenerate family of vacuum states and the consequent arbitrary choice of

$$< \Phi >_0 = \left\langle \begin{pmatrix}\phi^+\\ \phi^0\end{pmatrix} \right\rangle_0 = \frac{1}{\sqrt{2}}\begin{pmatrix}0\\ \nu\end{pmatrix},$$

implies the spontaneous breaking of the initial symmetry of the system. By performing a perturbation around the minimum, coupling terms of the Higgs field with the gauge bosons appear, and are interpreted as the seeked mass terms. Moreover, an additional massive scalar particle, the Higgs boson H, naturally supervenes; the discovery of the latter, finally achieved in 2012 at the LHC [14, 15], marked one more striking success for the SM.

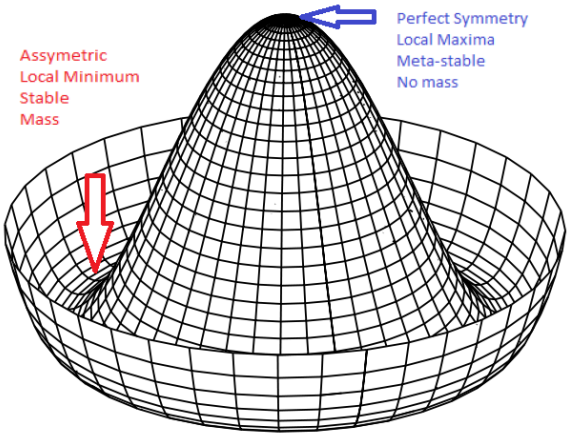

Figure 1.1: Representation of the Higgs potential in the plane (Re(Φ), Im(Φ)).

An $SU(2)$-invariant interaction between the Higgs field and the fermion Dirac fields, furthermore, can be introduced *ad hoc* to account for leptons and quarks masses:

$$\mathcal{L}_{Yukawa} = \sum_{i=1}^{3}\sum_{j=1}^{3} \Gamma_u^{ij}\bar{Q}_L^i i\tau^2\Phi^* u_R^j + \Gamma_d^{ij}\bar{Q}_L^i\Phi d_R^j + \Gamma_e^{ij}\bar{L}_L^i\Phi e_R^j + h.c., \tag{1.8}$$

where the coefficients Γ_u,Γ_d, Γ_e represent the 3x3 Yukawa complex matrices in the space of the three fermions generations.
In conclusion, the dynamics of the Standard Model of particle physics is entirely enclosed in the following Lagrangian:

$$\mathcal{L}_{SM} = \mathcal{L}_{Gauge} + \mathcal{L}_{Fermions} + \mathcal{L}_{Higgs} + \mathcal{L}_{Yukawa}. \tag{1.9}$$

The Yukawa matrices, entering in Eq. 1.8 to describe the Higgs couplings to the fermion fields, naturally introduce another subject which is of great interest for top physics: the flavor changing weak decays. Via a proper bi-unitary transformation (ie: $\Gamma_u \rightarrow U_u^{L\dagger}\Gamma_u U_u^R$), such matrices can be diagonalized in order to obtain the physical masses of the particles as eigenstates. The choice of a new basis to express the fermion fields has no effect on the leptons, since the neutrino mass is assumed to be null in the SM formulation, but institutes in the quark sector a new unitary matrix which takes the name of Cabibbo, Kobayashi and Maskawa, who formulate the theory:

$$V_{CKM} \equiv U_u^{L\dagger}U_d^L = \begin{pmatrix} V_{ud} & V_{us} & V_{ub} \\ V_{cd} & V_{cs} & V_{cb} \\ V_{td} & V_{ts} & V_{tb} \end{pmatrix}. \tag{1.10}$$

The CKM matrix can therefore be visualized as a rotation linking the eigenstates of the electroweak interaction with the mass eigenstates ($Q'_L = V_{CKM}Q_L$). If a generic

complex $N \times N$ matrix is characterized by $2N^2$ parameters, here the unitary condition

$$\sum_{k=1}^{3} V_{ik} V_{jk*} = \delta_{ij} \tag{1.11}$$

reduces this number to three Euler angles and one non trivial phase. The latter will enter in the wavefunction as $\exp[i(\omega t + \delta)]$, which is clearly not invariant under time reversal; for the CPT theorem this implies that the SM admits CP-violating reactions among quarks, but it is not the purpose of this thesis to detail more this topic.
The standard CKM matrix representation, thus, is made in terms of sines and cosines of the mixing angles ($c_{ij} = cos\theta_{ij}, s_{ij} = sin\theta_{ij}$) and the complex phase δ:

$$V_{CKM=} \begin{pmatrix} c_{12}c_{13} & s_{12}c_{13} & s_{13}e^{-i\delta} \\ -s_{12}c_{23} - c_{12}s_{23}s_{13}e^{i\delta} & c_{12}c_{23} - s_{12}s_{23}s_{13}e^{i\delta} & s_{23}c_{13} \\ s_{12}s_{23} - c_{12}c_{23}s_{13}e^{i\delta} & -c_{12}s_{23} - s_{12}c_{23}s_{13}e^{i\delta} & c_{23}c_{13} \end{pmatrix}. \tag{1.12}$$

Since it is known experimentally that $s_{13} << s_{23} << s_{12} << 1$, it is convenient to express this hierarchy in terms of the alternative Wolfenstein parametrization, written in the form of an expansion in $\lambda = sin\theta_{12}$. Defining

$$s_{12} = \lambda = \frac{|V_{us}|}{\sqrt{|V_{ud}|^2 + |V_{us}|^2}}, \quad s_{23} = A\lambda^2 = \lambda |\frac{V_{cb}}{V_{us}}|, \tag{1.13}$$

$$s_{13}e^{i\delta} = A\lambda^3(\rho + i\eta) = \frac{A\lambda^3(\bar{\rho} + i\bar{\eta})\sqrt{1 - A^2\lambda^4}}{\sqrt{1 - \lambda^2}[1 - A^2\lambda^4(\bar{\rho} + i\bar{\eta})]} = V_{ub}^*, \tag{1.14}$$

the matrix becomes:

$$V_{CKM=} \begin{pmatrix} 1 - \lambda^2/2 & \lambda & A\lambda^3(\rho - i\eta) \\ -\lambda & 1 - \lambda^2/2 & A\lambda^2 \\ A\lambda^3(1 - \rho - i\eta) & -A\lambda^2 & 1 \end{pmatrix} + \mathcal{O}(\lambda^4). \tag{1.15}$$

The new variables can then be exploited, together with the first condition in Eq. 1.11, to draw a unitary triangle in the $(\bar{\rho}, \bar{\eta})$ plane. Its sides, renormalized to the values $V_{ud}V_{ub}^*/V_{cd}V_{cb}^*$, 1, $V_{td}V_{tb}^*/V_{cd}V_{cb}^*$, and its internal angles, are an explicit visualization of some fundamental parameters of the SM, so that their precise determination is crucial. One of the goals of flavor physics is to overconstrain the CKM unitary triangle experimentally, as Fig. 1.2 depicts. The individual measurements of different processes involving quark mixing are reported with distinct color bands which should converge on the angle labeled α, and are used to perform a global fit with the CKMFitter tool. Such a fit, which relies as well on the SM constraints, gives as a result the most precise measurement of the nine elements of the CKM matrix (Eq. 1.16).
We will illustrate in Section 1.2.3 how the single top quark production contributes to asses in an alternative model-independent way the CKM vertices V_{td}, V_{ts} and V_{tb}. The usual determination of the two first parameters relies mainly on B-$\bar{B}$ oscillations mediated by box diagrams with top quarks, while the latter is currently extracted

by means of the ratio $R = \mathcal{B}(t \to Wb)/\mathcal{B}(t \to Wq)$ with the hypotheses of three fermions generations and unitarity of the CKM matrix.

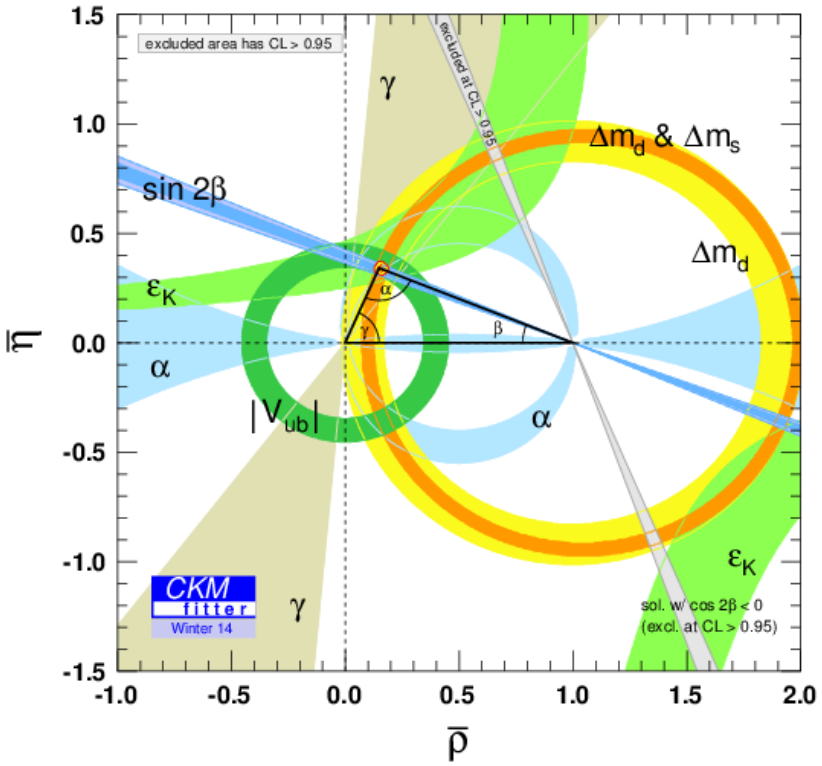

Figure 1.2: Contraints in the $\bar{\rho}$, $\bar{\eta}$ plane are shown as the result of multiple experimental measurements of the CKM matrix elements; the shaded areas correspond to a confidence level of 95% [16] [17].

$$V_{CKM} = \begin{pmatrix} 0.97427 \pm 0.00015 & 0.22534 \pm 0.00065 & 0.00351^{+0.00015}_{-0.00014} \\ 0.22520 \pm 0.00065 & 0.97344 \pm 0.00016 & 0.0412^{+0.0011}_{-0.0005} \\ 0.00867^{+0.00029}_{-0.00031} & 0.0404^{+0.0011}_{-0.0005} & 0.999146^{0.000021}_{0.000046} \end{pmatrix} \tag{1.16}$$

In conclusion, several measurements are progressively validating and molding the theoretical formalism that describes the quark electroweak decays. Such a formalism is actually an extension of the Glashow-Iliopoulus-Maiani mechanism, developed with the intent of explaining the absence of Strangness Changing Neutral Currents (SCNC) spotted experimentally in the Seventies. Firstly, the existence of the charm quark was proposed since it provides the observed SCNC cancellation, then, the third doublet (t,b) was integrated in a 3×3 matrix describing the electroweak interaction among quarks.

1.2 Top quark production at hadron colliders

The LHC is currently the most powerful experimental setup for generating top quarks via hard scattering processes [18]; such processes can be described by perturbative quantum chromodynamics (QCD) when expressed in terms of the interaction between the constituents of the colliding protons: valence quarks, sea quarks produced by the vacuum polarization, and gluons, which take over a fraction x of the total longitudinal momenta. By introducing a factorisation scale μ_F, the collision between hadrons can be represented in terms of a convolution between two distinct contributions; the short distance interaction between the participating partons of type i and j, $\hat{\sigma}^{ij}$, which can be calculated in the perturbative regime, and the long distance factors that specify the probability density of observing those partons with a certain x_i/x_j in the incoming hadrons. Such approach, displayed as an example in Fig 1.3, is formalized by the factorization theorem:

$$\sigma(pp/p\bar{p} \to X) = \sum_{i,j=g,q,\bar{q}} \int dx_i dx_j \underbrace{f_i(x_i, \mu_F^2) f_j(x_j, \mu_F^2)}_{\text{long-distance part}} \times \underbrace{\hat{\sigma}^{ij}(x_i, x_j)}_{\text{short-distance part}} . \quad (1.17)$$

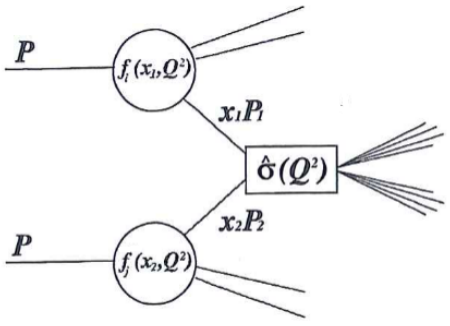

Figure 1.3: Parton model description of a hard scattering process (pp collision) using the factorization theorem.

The terms $f_i(x_i, \mu_F^2)$ are called parton distribution functions (PDFs); they can not be calculated a priori by perturbative QCD and are constrained in global fits on a large number of cross section data from experiments performed at SLAC, FNAL, CERN and at the electron-proton HERA collider at DESY. This extensive analysis resulted in the developement of many parametrizations for the description of the parton density functions at Leading Order (LO), Next-to-Leading-Order (NLO) and Next-to-Next-to-Leading-Order (NNLO): CTEQ [19], GJR [20], NNPDF [21], HERAPDF [22] and MSTW [23]. Such PDF sets differ essentially in the dataset used to constrain the fit, the value of the strong coupling α_S and of the quark masses, the way in which higher order corrections are implemented and the way the systematic uncertainties are treated. Figure 1.4 shows a specific PDF set at NLO, the MSTW 20080: the gluon distribution functions in the proton are peaked at low x values, while valence quark functions are enhanced at high x values.

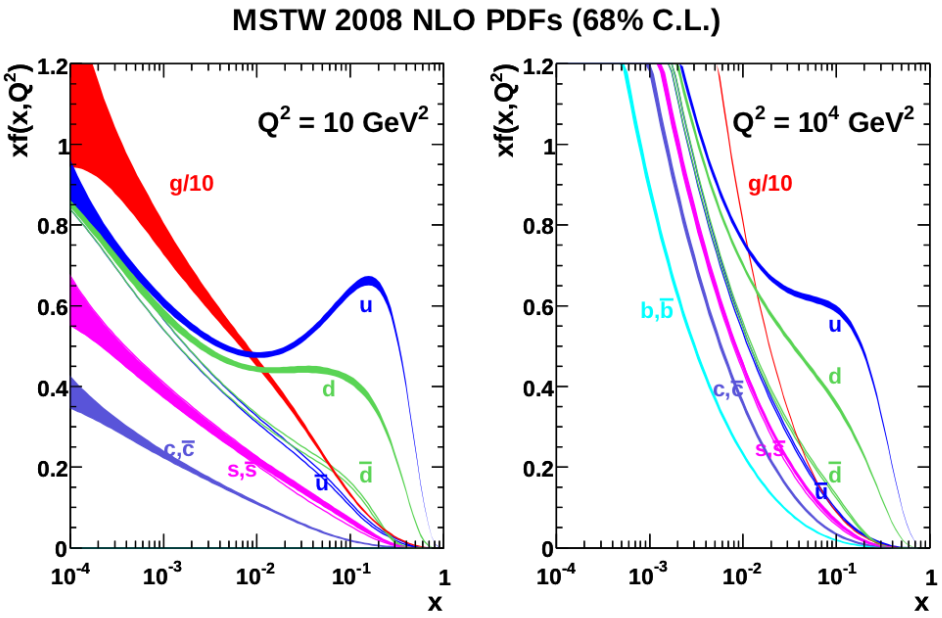

Figure 1.4: MSTW 2008 PDFs at Next-to-Leading-Order at scales of $Q^2 = 10\ GeV^2$ and $Q^2 = 10^4\ GeV^2$ at the LHC. The associated 1σ (68% C.L.) uncertainty bands are also represented.

1.2.1 Strong interaction production

A proton-proton LHC collision, illustrated with a factorization approach by the scheme in Fig 1.3, can generate a top quark pair via gluon-gluon fusion or quark-antiquark annihilation, as represented in Fig 1.5.

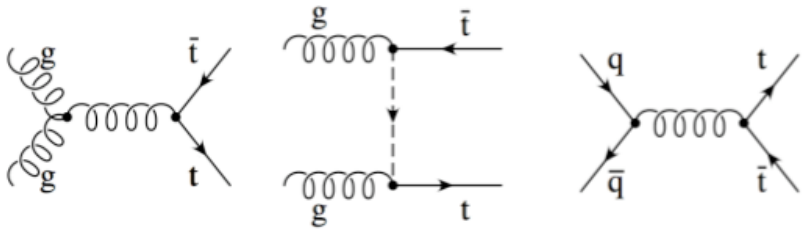

Figure 1.5: Feynman diagrams depicting the top pair production via strong interaction at hadron colliders. Only the lowest order processes based on gluon gluon fusion (on the left) and quark-antiquark annihilation (on the right) are shown.

Equation 1.17 can be used to deduce some properties of this production mechanism mediated by the strong interaction. First of all, to enable such process, the energy shared by the partons has to correspond, at least, to the mass of the top quark pair at rest; that means $\hat{s} \geq 4m_t^2$, and therefore:

$$x_i x_j = \frac{\hat{s}}{s} \geq \frac{4m_t^2}{s}. \tag{1.18}$$

By considering the plot in Fig.1.4, it seems apparent that the parton density functions fall off steeply at increasing values of the longitudinal momentum fraction; this implies that the partons would typically have an energy available close to the $t\bar{t}$ production threshold. With a further degree of approximation, we can also state that the interacting partons would share roughly the same x, and derive consequently the simple equation:

$$< x > \sim \sqrt{x_i x_j} \sim \frac{2m_t}{\sqrt{s}}. \tag{1.19}$$

Eq. 1.19 affirms that the higher is the center of mass energy, the smaller is the average fraction of longitudinal momentum taken by each parton; by computing the latter for several LHC and TeVatron configurations one obtains the table below:

	TeVatron		LHC	
	1.80 TeV	1.96 TeV	7TeV	8TeV
$< x >$	0.19	0.18	0.05	0.04
$q\bar{q} \rightarrow t\bar{t}$	90%		15%	13%
$gg \rightarrow t\bar{t}$	10%		85%	87%

Since the up and down valence quark PDFs are much larger than the ones of gluons and sea quarks at high x values, the generation of top quark pairs proceeds almost exclusively by quark-antiquark annihilation at the TeVatron, and gluon-gluon fusion at the LHC. The $t\bar{t}$ production cross section has been computed at NNLO in QCD, including resummation of NNLL soft gluon terms for the TeVatron and the LHC at different center of mass energies [24]:

Table 1.3: Top pair production predictions

	TeVatron @ 1.96 TeV	LHC @ 7 TeV	LHC @ 8 TeV
$\sigma_{t\bar{t}}$	$7.08^{+0.0+0.36}_{-0.24-0.24}$ pb	177^{+10}_{-11} pb	253^{+13}_{-15} pb

The calculation is performed considering a top mass of 173 GeV and taking into account the scale variation $\frac{m_t}{2} < \mu < 2m_t$ (first uncertainty in the cross section at TeVatron), as well as the PDF at 90 % C.L. (second uncertainty in the cross section at TeVatron). The energy scale is the same for the factorization and the renormalization ($\mu = \mu_F = \mu_R$), the latter being introduced in order to avoid divergences in the cross section calculation based on the evaluation of the first orders of a perturbative expansion. The first measurement of the top pair production cross section has been released in 1995 by the CDF [3] and the DØ [4] collaborations, and since then many analyses performed at the TeVatron and at the LHC achieved higher sensitivity. The latest public measurements released by the ATLAS and CMS collaborations are summarized in Fig. 1.6 as a function of the collision energy. All the reported values are consistent with each other and coherent with the theory predictions.

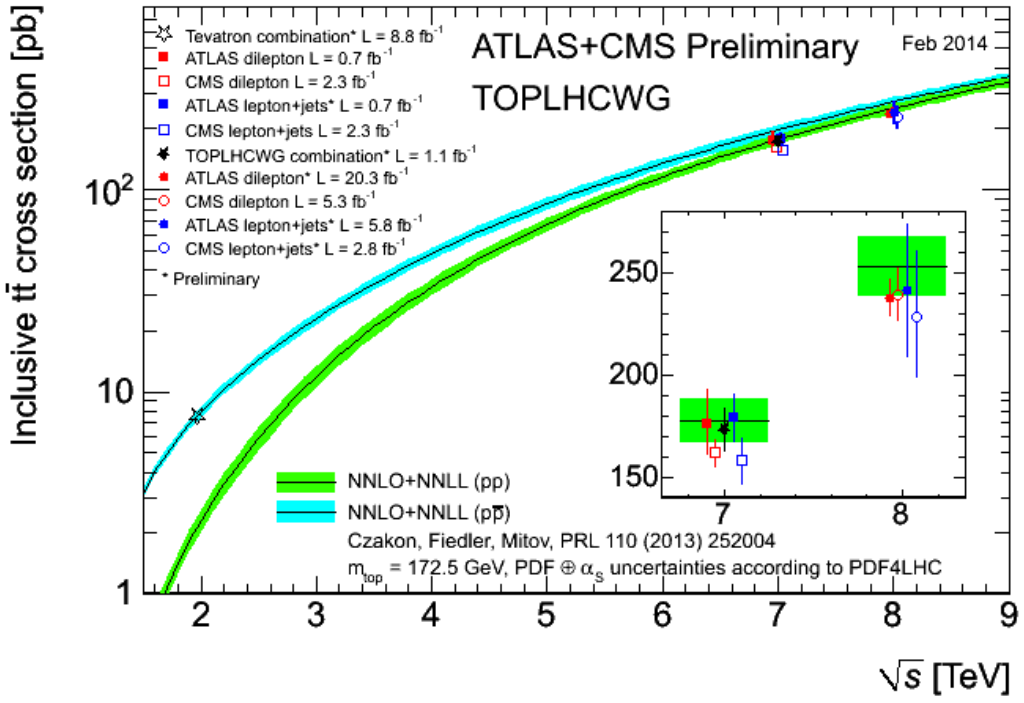

Figure 1.6: $t\bar{t}$ cross section measured via pp collisions at the LHC, as a function of the center of mass energy. TeVatron results for $p\bar{p}$ collisions are also reported, together with a comparison with NNLO+NNLL theoretical descriptions [25] for both colliders.

1.2.2 Electroweak interaction production

Proton-proton collisions taking place at the LHC allow also the production of top quarks via charged-current electroweak interaction. The three different production mechanisms are illustrated through the corresponding LO Feynman diagrams in Fig 1.7: the t-channel exchange of a virtual W-boson (a), the associated production of an on-shell W-boson and a top quark (b), the s-channel production involving the decay of a virtual W-boson (c).

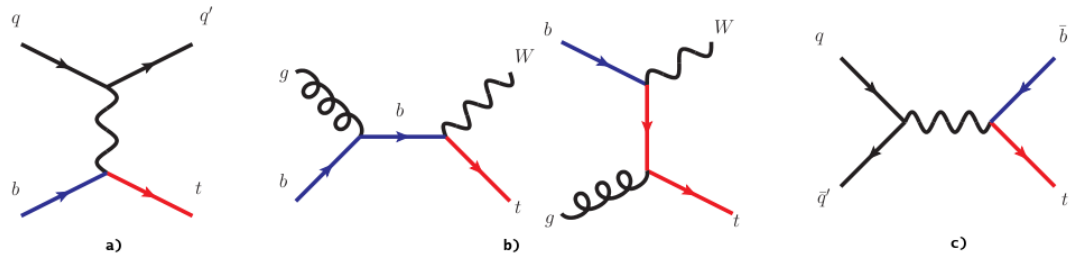

Figure 1.7: Feynman diagrams at leading order of single top quark production processes: (a) t-channel, (b) Wt channel and (c) s-channel.

As for the top quark production via strong interaction, approximate NNLO cross sections [26, 27, 28] are reported in Table 1.4, using the same conventions on the top mass and the uncertainty. The values below correspond to the inclusive production of single top quarks and antiquarks, which is clearly symmetrical at the TeVatron, and asymmetrical at the LHC.

Table 1.4: Predictions for single top production

	TeVatron @ 1.96 TeV	LHC @ 7 TeV	LHC @ 8 TeV
σ_t	$2 \times (1.04^{+0.00}_{-0.02} \pm 0.06)$ pb	$64.57^{+2.63}_{-1.74}$ pb	$87.76^{+3.44}_{-1.91}$ pb
σ_{Wt}	—	$15.74^{+1.17}_{-1.21}$ pb	$22.37^{+1.52}_{-1.52}$ pb
σ_s	$2 \times (0.523^{+0.001+0.030}_{-0.005-0.028})$ pb	$4.63^{+0.20}_{-0.18}$ pb	$5.61^{+0.21}_{-0.21}$ pb

The single top channels labels recall explicitly the Mandelstam formalism, which permits to formulate some simple predictions and generalizations by introducing three kinematic invariants to describe a generic $2 \to 2$ scattering process (Fig. 1.8):

$$\begin{aligned} s &= (p_1 + p_2)^2 = (p_3 + p_4)^2 \\ t &= (p_1 - p_3)^2 = (p_2 - p_4)^2 \\ u &= (p_1 - p_4)^2 = (p_2 - p_3)^2. \end{aligned} \tag{1.20}$$

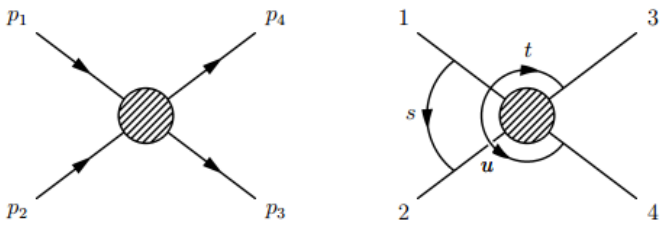

Figure 1.8: Visualization of the Mandelstam variables for a two particle scattering.

The **t-channel**-like reactions, for which the characteristic variable is the four momentum transfer squared, proceed via the exchange of a space-like mediator between the two initial particles; they are therefore very sensitive to anomalous couplings or non-standard currents that may modify the W-t-b vertex.
Focusing on the single top quark production via this partonic interaction scheme, we have to list multiple contributions to the t-channel cross section [26]: $ub \to dt$ (65.7%), $\bar{d}b \to \bar{u}t$ (21.4%), $cb \to st$ (2.7%), $ub \to st$ (3.6%), $cb \to dt$ (0.15%), $us \to dt$ (0.7%), where the three last processes are Cabibbo suppressed. The calculation of the Feynman scattering amplitude for each LO diagram shows that the t-channel cross section depends considerably on the collider energy ($\sqrt{s}$) [29]:

$$|\bar{\mathcal{M}}|^2 = \frac{g^4}{4}|V_{tb}|^2|V_{12}|^2\frac{1}{(k^2 - M_W^2)}s^2\left(1 - \frac{m_t^2}{s}\right), \tag{1.21}$$

where k indicates the four momentum and V_{12} the CKM matrix element that couples the other interacting quarks. This formula, with the previous table, reveals that this production mechanism will indeed benefit of the LHC run II, during which the collisions will take place at $\sqrt{s} = 13$ and 14 TeV.
Inclusive electroweak production of top quarks in the t-channel (and s-channel) has been observed for the first time in 2009 by the CDF [30] and DØ [31] collaborations at the TeVatron; both analyses employed multivariate techniques combined together and provided a measurement of $\sigma(p\bar{p} \to tb + X, tbq + X)$ with 5σ significance. Later on, ATLAS and CMS collaborations took advantage of the larger t-channel cross section expected at the LHC at a center of mass energy of 7 and 8 TeV, and realized more precise observations. The cross sections measurements are reported in Table 1.5.

The **Wt associate production** proceeds mainly via the $gb \to tW$ process (98%) since the contributions from the other initial states gd and gs are suppressed by the corresponding CKM matrix elements (V_{td}, V_{ts}). The fact that two different Feynman diagrams, of the s-channel and u-channel type, participate in the description of the process, makes more difficult to predict the impact that new physics would have on its cross section and kinematics. The calculation of the scattering amplitude $\mathcal{M} = \mathcal{M}_s + \mathcal{M}_u$ is therefore much more complex than 1.21, and not so explicit regarding the dependence on the collider center of mass energy:

$$\mathcal{M}_s = \frac{g_s g}{2\sqrt{2}} V_{tb} \bar{u}(p_t)\gamma^\mu \epsilon^*_\mu(p_W)(1-\gamma^5)\frac{\not{q}}{s}\gamma^\nu e_\nu(p_g)u(p_b) \tag{1.22}$$

$$\mathcal{M}_u = \frac{g_s g}{2\sqrt{2}} V_{tb} \bar{u}(p_t)\gamma^\mu \epsilon^*_\mu(p_W)(1-\gamma^5)\frac{\not{q} + m_t}{u - m_t^2}\gamma^\nu e_\nu(p_g)u(p_b), \tag{1.23}$$

where γ^μ are the Dirac matrices, $\gamma^5 = i\gamma_0\gamma_1\gamma_2\gamma_3$, $\not{q} = \gamma^\mu q_\mu$, ϵ and e represent the W-boson and the gluon polarization vectors. It can be shown with further calculations that the Wt channel cross section increases with $\sqrt{s}$ even more steeply than the t-channel. This fact, as well as the presence of a gluon in the initial state, explains the importance relying on this production mechanism at the LHC. The Wt channel cross section, which has not been measured at the TeVatron, has finally been determined with 4.2 and 6.1 standard deviations significance by the ATLAS and CMS collaborations, respectively (Table 1.5).

Table 1.5: Measured single top cross sections.

	TeVatron @ 1.96 TeV	
	CDF	DØ
σ_{t+s}	$2.3^{+0.6}_{-0.5}$ pb [30]	3.94 ± 0.88 pb [31]
	LHC @ 7 TeV	
	ATLAS	CMS
σ_t	84 ± 4 (stat)$^{+20}_{-19}$ (syst) pb [32]	83.6 ± 29.8(stat+syst)± 3.3(lumi) pb [33]
σ_{Wt}	16.8 ± 2.9(stat)± 4.9(syst) pb [34]	$15.6 \pm 0.4^{+1.0}_{-1.2}$ pb [35]
	LHC @ 8 TeV	
	ATLAS	CMS
σ_t	95 ± 2 (stat)± 18(syst) pb [36]	80.1 ± 5.7(stat)± 11(syst)± 4(lumi) pb [37]
σ_{Wt}	27.2 ± 2(stat)± 5.4(syst) pb [38]	23.4 ± 5.4 pb [39]

The **s-channel**-like processes, whose characteristic Mandelstam variable is the total center of mass energy squared, proceed via annihilation of the two incident partons into an intermediate time-like mediator, which then decays into a pair of particles; such processes are therefore particularly sensitive to resonances or stable unknown particles that may replace the standard mediator.
The single top s-channel production, which takes place almost exclusively via $u\bar{d} \to \bar{b}t$ (97.4 %), followed by $c\bar{s} \to \bar{b}t$ (1.1 %) and other Cabibbo suppressed pro-

cesses, is described by the following LO Feynman scattering amplitude:

$$|\bar{\mathcal{M}}|^2 = \frac{g^4}{4}|V_{tb}|^2|V_{12}|^2\frac{1}{(k^2 - M_W^2)}t^2\left(1 - \frac{m_t^2}{t}\right), \tag{1.24}$$

which can be retrieved from 1.21 by applying the crossing symmetry [5]. Equation 1.24 underlines that the single top s-channel cross section depends slightly on the collider center of mass energy, and consequentely that its measurement at increasing $\sqrt{s}$ at the LHC is not favoured; the production of the main sources of background, whose yield is much more important already at 7 TeV, will indeed increase more steeply reducing further the signal purity. Moreover, the presence of an antiquark in the initial state suggests that this partonic interaction is promoted in proton-antiproton collisions, and suppressed in proton-proton collisions, in which case the antiquark can only belong to the sea quarks. For these reasons, the history of experimental results on the s-channel single top production is marked by an overwhelming success of the TeVatron. After the first observation together with the t-channel, the CDF and DØ collaborations released in February 2014 [40] a combined measurement corresponding to 6.3 standard deviations significance: $\sigma_s = 1.29^{+0.26}_{-0.24}$ pb, in agreement with the SM expectation (Fig. 1.9).
This recent work relies on the application of several multivariate techniques, as well as on an accurate "sampling" of the final state; this last is characterized by a bottom quark, that hadronizes producing a b-jet, and the products of the top quark fragmentation, that consist almost exclusively in a W-boson and an other b-jet. In order to increase the signal acceptance, two different event topologies have been selected (an E_T^{miss}+jets sample integrates the standard lepton+jets sample) and separated into independent analysis channels based on the number of reconstructed jets and the quality of their b-tagging.

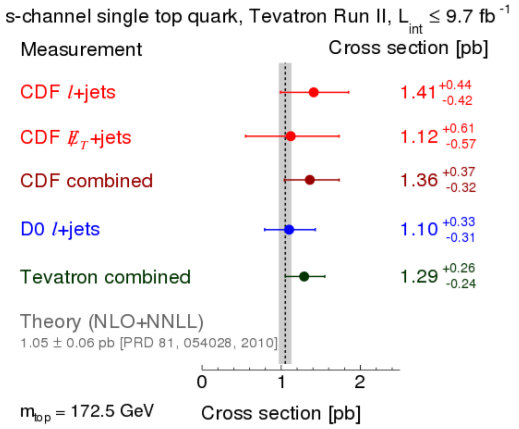

Figure 1.9: Measured s-channel cross section from each of the TeVatron analyses and various combinations, compared with the NLO+NNLL prediction.

[5]The crossing simmetries apply to the amplitudes of processes described by similar Feynman diagrams, but with different identifications of the external legs as incoming or outgoing.

This thesis reports the ATLAS effort on the s-channel single top production, started few years before the TeVatron's latest publications. Even if conscious that performing this delicate analysis in a "hostile context" like the LHC constitutes a real challenge, we bestow a great importance to the s-channel measurement. This production mechanism is in fact the most sensitive to the presence of a heavy resonance coupled to the top quark, and its knowledge may help to constrain many theoretical models, when expressed as a function of the measured cross section of the other single top channels. This point will be further detailed in the next section.

1.2.3 Interest of the single top measurements

We insisted in Section 1.1 on the importance of assessing experimentally the Cabibbo-Kobayashi-Maskawa matrix, which describes the flavour changing weak interactions among quarks. Single top measurements are especially valuable for the extraction of V_{tb}, since both the production and decay mechanisms are described in terms of a W-t-b vertex:

$$|V_{tb}|^2 = \frac{\sigma^{exp}_{single\ top}}{\sigma^{th}_{single\ top}}. \tag{1.25}$$

In the last years several publications profitted from this privileged approach which allowed a direct access to the V_{tb} matrix element, on the basis of the assumptions of $V_{tb} >> V_{td}, V_{ts}$ and left-handed weak coupling. No hypothesis on the number of fermions generations nor of unitarity of the CKM matrix are needed, as opposed to methods investigating the top quark branching ratios in top pair decays:

$$R = \frac{\mathcal{B}t \to Wb}{\mathcal{B}t \to Wq} = \frac{|V_{tb}|^2}{\sum_{q=1}^{3} |V_{tq}|^2} = |V_{tb}|^2. \tag{1.26}$$

More recentely, the measurement of $R = 0.90 \pm 0.04$ performed by the $D\emptyset$ collaboration [41] with a precision of 4.4%, triggered a new V_{tb} extraction method that takes into account the non negligible d- and s-quark contributions. The new technique described in [42] still focuses on single top production, but is model-independent in the sense that it is not based on any hierarchy of flavour texture, and can be applied to scenarios predicting 4 generations of fermions, as well as vector-like heavy quarks. It provides a general determination of $|V_{td}|, |V_{ts}|$ and $|V_{tb}|$ based on the expression of the measured event yields in terms of the integrated luminosity, the reconstruction efficiencies, the total single top production cross sections, the CKM elements and the measured branching ratio R. The constraints on the CKM matrix elements can then be deduced with five approaches which rely on different hypotheses:
- 'the R=1 method', for which $V_{tb} >> V_{td}, V_{ts}$;
- 'the 3SM method', that assumes 3 families but the measured R value, and appears to be the most stringent;
- 'the 4SM method', which relies on the hypothesis of four families, with $|V_{td}|^2 + |V_{ts}|^2 + |V_{tb}|^2 \leq 1$;
- 'the 4SM method', with the further 4×4 unitarity constraint;

- 'the free CKM method', that allows to quantify the non-SM top quark coupling without any hypothesis.
The first numerical analysis has been performed using the CDF results for a final state with two jets, one of which identified as a b-jet [43], and the R value measured by $D\emptyset$. Fig. 1.10 shows the p-value[6] referring to a χ^2 test statistic as a function of $|V_{tb}|$ for several methods. By looking for the intersection of the curve with the lines p-value = 0.3173, or p-value =0.0455, one can read off the 1-σ or, respectively, 2-σ ranges for $|V_{tb}|$. Analogous constraints are set on $|V_{td}|$ and $|V_{ts}|$ (Figs. 1.11(a), 1.11(b)), for the same models except the one predicting R=1, since by definition those CKM elements are forced to be zero.

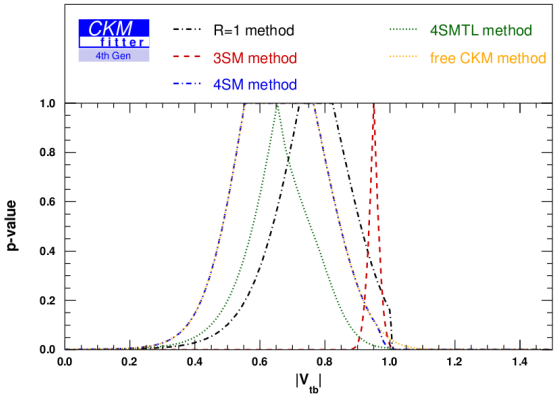

Figure 1.10: Constraints on $|V_{tb}|$ from the single top t-channel event yield $N_{1bjet}^{2jets} = 84.3 \pm 26.8$ measured by CDF; the p-values obtained with different methods are shown.

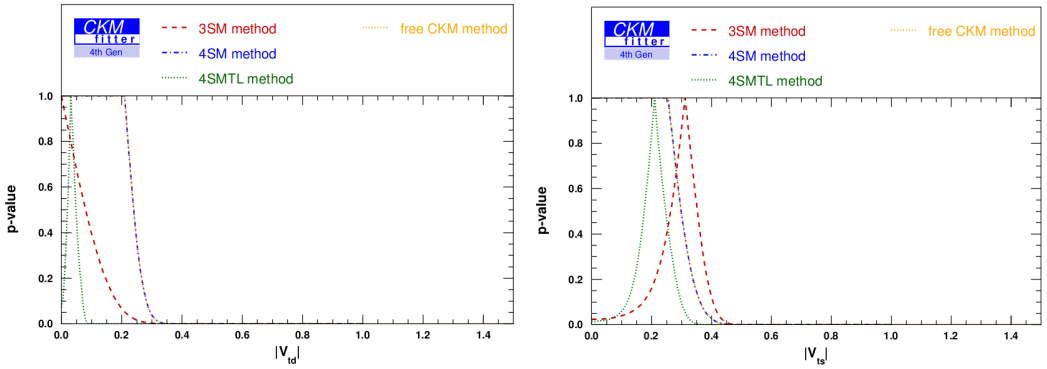

(a) (b)

Figure 1.11: (a) Constraints on $|V_{td}|$ and (b) $|V_{ts}|$ using the single top t-channel event yield $N_{1bjet}^{2jets} = 84.3 \pm 26.8$ for several scenarios.

[6]The p-value represents the probability under a given hypothesis of obtaining a test statistic result at least as extreme as the one that was actually observed. It will be further described in Section 4.6.2.

The ongoing studies on single top production are, at the same time, fundamental in order to shed some light on Beyond Standard Model (BSM) physics. As references [44], [45] underlined, the three channels result separately susceptible to different phenomena, so that the combination of their production rates provides a simultaneous indirect discrimination of several theoretical models. We will provide, in the following, a simple characterization of the main scenarios predicting new particles and couplings that may affect the top quark electroweak production, without any pretension of being exhaustive.

Extra gauge bosons
By postulating the existence of a gauge group larger than $SU(3)_C \times SU(2)_L \times U(1)_Y$, but which reduces to the latter at low energies, one can naturally introduce extra gauge bosons according to the mechanism presented in Section 1.1. The top-flavor model [46], for example, is based on the electroweak symmetry group $SU(2)_h \otimes SU(2)_l \otimes U(1)_Y$, where the third generation of fermions can experience a strong flavor interaction instead of the weak interaction advocated by the SM. This implies the presence of three heavy gauge bosons (W'^+, W'^-, Z'_0) that couple strongly with t, b, τ, ν_τ. Left-right symmetric models [47], on the other hand, introduce an additional $SU(2)_R$ under which right-handed fermions transform as doublets, and left-handed fermions as singlets (reversing the status described by the SM for $SU(2)_L$). The right-handed W' boson arising from such theories can in principle undergo leptonic or hadronic decays; however, the latter are particularly important since a W' boson which couples only to right-handed fermions can not decay to leptons when the right-handed neutrinos are heavier than m(W'). Another way of providing these additional gauge bosons is via extradimension theories, which authorize the SM fields to propagate, at least partially, in the supplementary dimensions and predict the consequent generation of Kaluza-Klein excitation towers [48]. The latters represent the excited states of the gauge bosons (i.e. W'^+, W'^-, Z'_0), which can couple to the SM fermions. We can now focus on the effect that a W' boson could eventually have on the electroweak production of top quark, keeping in mind what alluded at in the previous section: the s-channel rate results in general very sensitive to heavy particles that could be added to the standard W-boson contribution; the t-channel cross section, on the contrary, is subjected to a negligible effect, as the contribution of the non-standard mediator is suppressed by a factor proportional to its inverse mass in virtue of the space-like momentum. Concretely, single top s-channel production would be affected by the presence of this W' boson mainly in two ways: the diagrams of W'-exchange could interfere constructively or destructively with the SM ones, and the new particle could be eventually produced on shell and spotted as a peak around m(W') in the $(t, \bar{b})$ invariant mass. The t-channel process would not show particular effects, and Wt production neither, despite the fact that it may allow for the exotic reaction $bg \rightarrow W't$.

Extra scalar bosons

Scalar bosons are usually associated with the mechanism of spontaneous symmetry breaking, described in multiple ways by different theories, and are expected to have a strong coupling with the top quark because of the role they play in generating fermion masses. If the Standard Model implements only a neutral Higgs boson, its minimal supersymmetric extension (MSSM) predicts two neutral CP-even bosons (h^0, H^0), a neutral CP-odd boson (A^0) and two charged bosons ($H^{\pm}$). While the first three may appear like their SM Higgs partner, the latters would provide a unique signature of new physics. Charged Higgs lighter than the top quark would be predominantly produced as $t \rightarrow H^+b$ at the LHC, and could eventually be spotted in any of the single top channels with an excess in final states with τ [49]. Fig. 1.12(a) depicts, as an example, the LO Feynman diagram for such a process in the t-channel. Charged Higgs heavier than the top quark could instead decay as $H^+ \rightarrow t\bar{b}$ having hence an impact on the s-channel single top production by contributing to its propagator [49]. In reference [50] it is mentioned that although the high $tan\beta$ values relevant for this specific case are not favoured by the LHC searches for neutral MSSM Higgs bosons, an indirect measurement of the process illustrated in Fig 1.12(b) would be important to confirm those results or bring them into question.

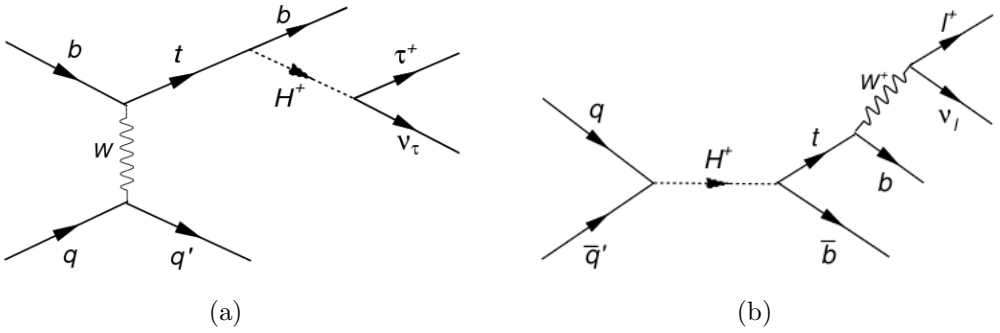

Figure 1.12: (a) t-channel single top Feynman diagram, where the top quark's decay involves a charged Higgs boson and a bottom quark. (b) s-channel single top Feynman diagram, in which a charged Higgs boson replaces the standard time-like W boson.

In other models that predict a dynamical breaking of the electroweak symmetry, like top-condensate and top-color assisted technicolor, scalar particles exist instead as bound states of top and bottom quarks; in analogy with the strong interaction bound states (π, ρ, ...) they are called top-pions. Such top-pions could enhance s-channel single top rate being produced as resonant states as illustrated in Fig. 1.13; in this case the strong $\pi^+ - c - \bar{b}$ coupling comes from the mixing between right-handed t- and c-quarks, which is not constrained by the CKM matrix. The techni-pions do not have, thus, a significant interference with the corresponding SM amplitudes, since the latter arise dominantly from left-handed light quarks. On the other hand, t and Wt channel cross sections would not be strongly affected by these new scalar bosons for the reasons already clarified in the previous paragraphs.

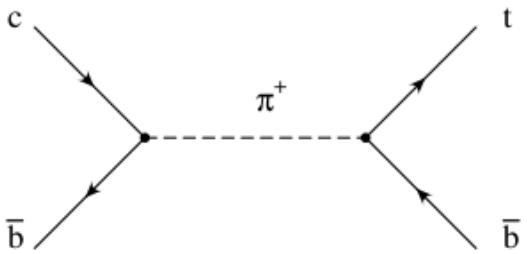

Figure 1.13: Top-pion production contributing to s-channel single top production is represented through a LO Feynman diagram.

Extra couplings
Flavour Changing Neutral Currents (FCNC), forbidden at LO by the Glashow-Iliopoulos-Maiani mechanism [51], are predicted at detectable rates by several extensions of the Standard Model, i.e. the above mentioned top-color assisted technicolor and the MSSM. These processes could strongly affect the single top production and decay via the new vertices Ztc, γtc, gtc.
The scenario illustrated in Fig. 1.14 gives an example of how a single top quark could be produced in terms of a FCNC Z-t-c interaction. The t-channel would have an increased rate, since the probability of finding a charm quark rather than a bottom in the incoming hadrons is higher (although the probable weakness of this extra coupling). Wt and s-channel would also receive some additional contributions from FCNC, but in terms of exotic production mechanisms characterized by different final states.

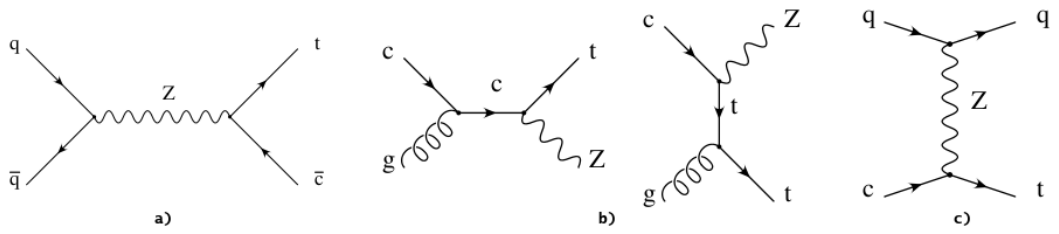

Figure 1.14: Feynman diagrams showing how a FCNC Z-t-c interaction contributes to the s-channel (a), exotic Wt channel (b), exotic t-channel (c) single top production modes.

It should be mentioned, finally, that Flavour Changing Neutral Currents would open also further top decay channels into light partons, slightly increasing all the SM single top rates.

Fourth generation of quarks
A simple extension of the SM predicts an additional chiral family of fermions which would change many observables directly, and indirectly via loop processes. Despite the fact that the recently measured branching ratios for the Higgs boson exclude, or strongly constrain, many of such models, it is still meaningful to study how top quark electroweak production could be affected by the presence of a further quark generation, conventionally named (t', b') [45, 52].
The effect of the mixing of the fourth and the third generations through a generalized CKM matrix could allow V_{tb} to deviate considerably from unity. In this case, the coupling between the top and bottom quarks and the W-boson would be modified regardless of the momentum flowing through the vertex; in other terms, all single top channels would exibhit cross sections which should be the same fraction of the ones predicted by the SM. In addition to mixing effects, the new $\bar{b'}$ quark could be directly produced through reactions such as $q\bar{q'} \rightarrow t\bar{b'}$; an eventual decay into the SM bottom quark could in principle increase t and s-channel single top rates.

Figure 1.15 summarizes the main concepts enunciated in this Section by comparing the single top t-channel and s-channel cross sections measured in 2013 by DØ [53], with the predictions from several Beyond Standard Model theories.
The *empty circle* in the plot represents the cross sections computed in the top-flavour framework, considering a W' boson of mass$m(\mathrm{W}')c^2 = 1$ TeV. This theory introduces a new angle ϕ to describe the mixing between heavy and light $SU(2)$ gauge couplings:

$$g_l = \frac{e}{sin\theta_W cos\phi} \quad ; \quad g_h = \frac{e}{sin\theta_W sin\phi} \quad ; \quad g_1 = \frac{e}{cos\theta_W}, \tag{1.27}$$

which in this particular case is such that $sin^2\phi = 0.05$.
The *triangle* symbolizes the predictions made in terms of couplings with techni-pions of mass $m(\pi)c^2 = 250$ GeV, and assuming a mixing between the right handed top and charm quarks of 20%.
The *square* presents instead the two single top production mechanisms via FCNC couplings of a gluon/top-quark/up-quark. Omitting the scale uncertainties, i.e. from varying the renormalization and factorization scales, the cross section for single top production can be written as:

$$\sigma_{qg\rightarrow t} = \sum_{q=u,c} (\frac{k_{qgt}}{\Lambda})^2 (b_{qL}|f_q^L|^2 + (b_{qR}|f_q^R|^2), \tag{1.28}$$

where b_{qL}, b_{qR} are simple constants scaling the left- and right-handed couplings, and Λ is the new physics scale, which has a dimension of energy and is related to the mass cut off scale above which the effective theory breaks down [7]. The value chosen for the calculation is $\frac{k_{ugt}}{\Lambda}$=0.036, given that the first search realized in 2007 by DØ provided

[7]Anomalous FCNC couplings can be described with an effective operator formalism [54] that considers the SM as the low energy limit of a more general theory valid at very high energies: $\mathcal{L}^{eff} = L^{SM} + \frac{1}{\Lambda}\mathcal{L}^5 + \frac{1}{\Lambda^2}\mathcal{L}^6 + o(\frac{1}{\Lambda^3})$.

an upper limit of 0.037 at 95% C.L.
Finally, the *rhombus* in the plot accounts for a four-generations-of-quarks model, where the the CKM 4×4 matrix is unitary, $|V_{ts}|$=0.2 and $|V_{tb}|$=0.8; these choice corresponds to the maximum possible value predicted in [52] for the V_{ts} element.

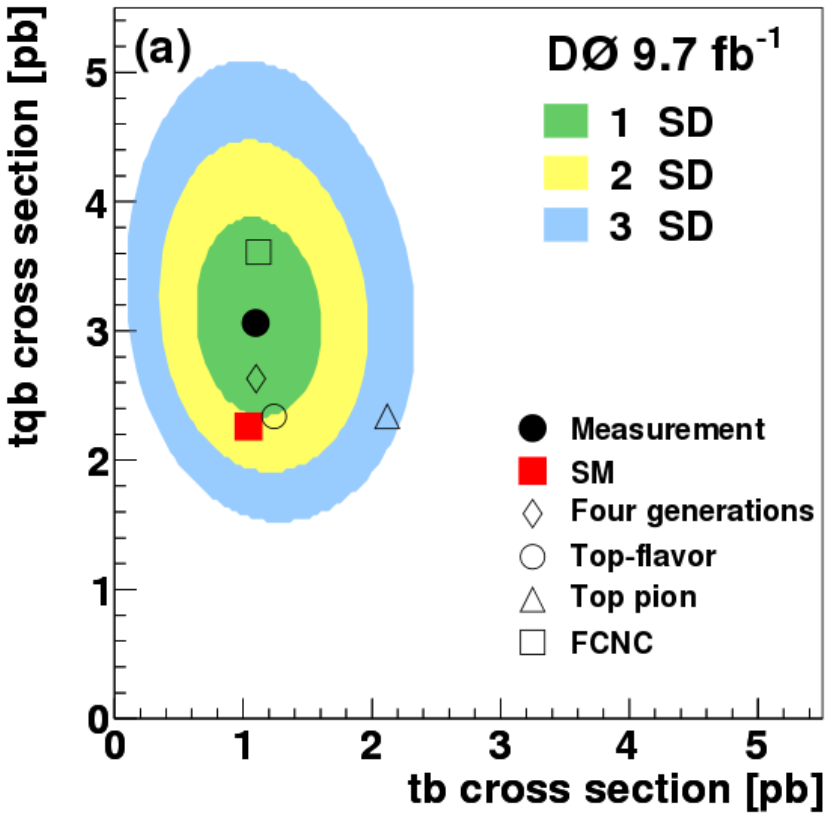

Figure 1.15: Simultaneous constraints of the single top t-channel and s-channel cross sections measured by the DØ collaboration. A comparison is realized with several predictions assuming BSM physics.

The DØ measurement (black circle) is shown together with the contours of equal probabilities for 1, 2 and 3 standard deviations in the two dimensional posterior for the combined multivariate discriminants; within the observed uncertainty the experimental value is in agreement with the SM prediction (red square) but, at the same time, with several BSM models.
Analogous plots may be produced with the LHC data that will be collected in the next years with a center of mass energy of 13 and 14 TeV. Due to the higher sensitivity, interesting information may be deduced by expressing the t-channel cross section as a function of the Wt one, knowing that the latter is in general less sensitive to new physics scenarios. If the combination of several multivariate techniques would allow to improve significantly the precision of the s-channel production rate measurement, also the equivalent of the plot in Fig 1.15 could provide useful constraints.

Chapter 2

Experimental setup

In order to better detail the context in which the single top s-channel cross section measurement has been realized, we will introduce here the CERN accelerator complex and the ATLAS apparatus.

2.1 The Large Hadron Collider

The 10 December 2008 the Large Hadron Collider was started up at the CERN facility near Geneva, with the goal of assessing a deeper knowledge of particle physics owing to proton-proton and heavy-ion collisions that would take place at a design center of mass energy of 14 TeV. The most powerful synchrotron in the world represents, nevertheless, just the last element of the accelerating chain, which is a succession of machines that boost particles to increasingly higher energies as shown in Figure 2.1.

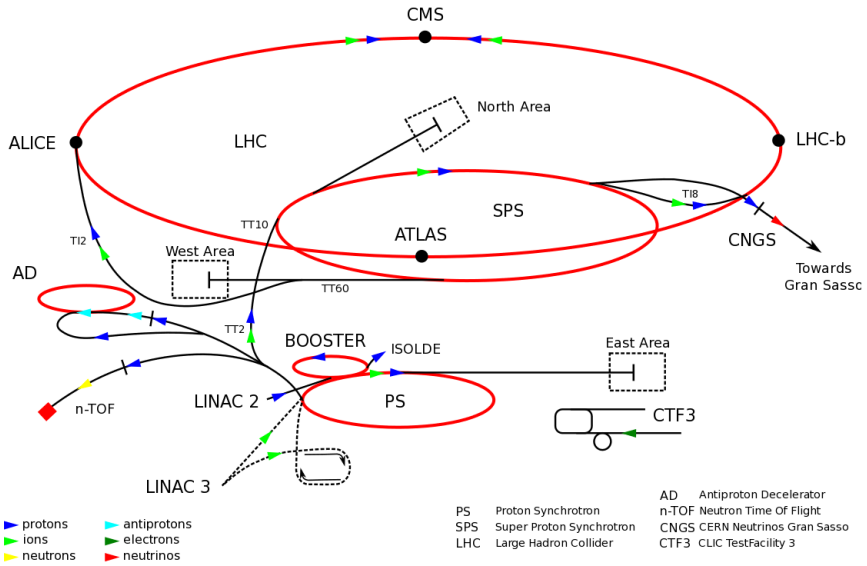

Figure 2.1: The accelerator complex at CERN.

Protons are initially produced in a duoplasmatron source, where electrons emitted from a cathode filament hit gaseous hydrogen atoms, and are then injected in the linear accelerator Linac2 to reach a preliminary energy of 50 MeV. On the other side, lead ions are formed in an Electron Cyclotron Resonance (ECR) [55] and later accelerated in Linac3 and in the Low Energy Ion Ring (LEIR). At this stage, both in the case of protons and heavy ions beams, the particles enter in the Proton Synchrotron Booster (PSB), where their energy increases up to 1.4 GeV, and in the Proton Synchrotron (PS), where they reach 26 GeV. Afterwards the beams are extracted to fill the Large Hadron Collider (LHC) via two specially assembled transfer lines.
The LHC [56] is built using the infrastructure of the Large Electron Positron collider, and consists thus in a 27-kilometer ring. Two counter-rotating beams are circulated in the evacuated beam pipes to avoid collisions with gas molecules; each one is submitted to a series of electromagnetic fields, and led to collide with the other at the insertion regions, where the experimental detectors are located. To accelerate the particles around the ring, 16 radio frequency (RF) cavities housed in 4 cylindrical refrigerators are used. The RF modules are molded to a specific size and shape, so that electromagnetic waves initially set up by a power generator become resonant and build up inside the cavity. The protons and lead-ions passing through feel the overall force and direction of the resulting electromagnetic field, and are therefore pushed forwards along the accelerator. More precisely, since the field in a RF cavity oscillates at a given frequency, particles can be accelerated or decelerated depending on their arrival time. In this way the beam is sorted into discrete packets called bunches. The bunch bending is ensured by 1232 superconducting niobium-titanium dipoles (Fig. 2.2), that generate a magnetic field of 8.4 T. This value, which constrains a circular orbit for a 7 TeV beam, can only be achieved through an external cooling; that is why a distribution system of liquid helium chills the magnets to a tempera-

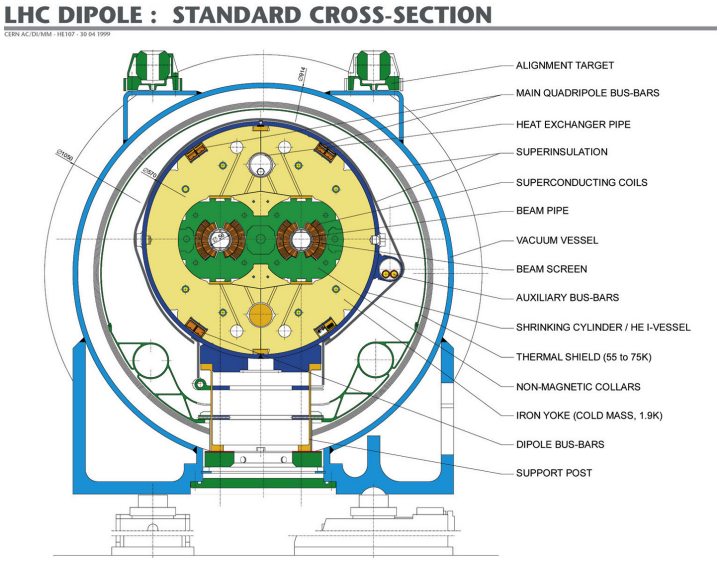

Figure 2.2: LHC dipole cross section.

ture of 1.9 K. The focusing of the bunches to a small size is mainly provided by 392

quadrupoles (Fig. 2.3), made up by four magnetic poles arranged symmetrically to squeeze the beams either vertically or horizontally; their shape will also be corrected by approximately 3700 additional multipole magnets.

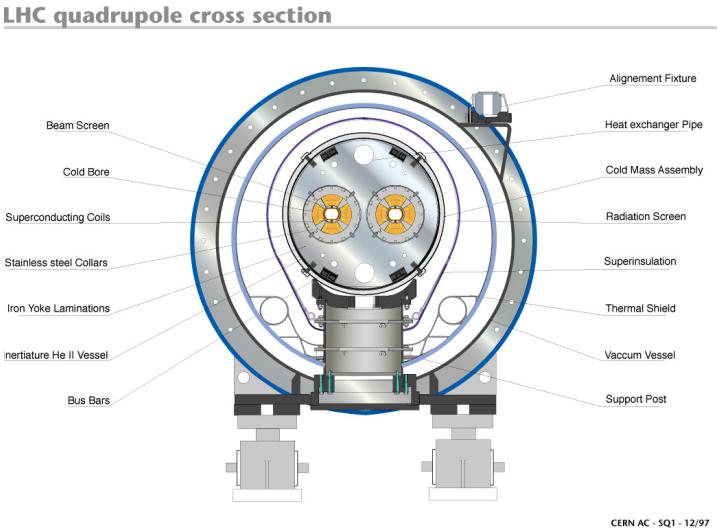

Figure 2.3: LHC quadrupole cross section.

Finally, the most complex insertion magnets are the 8 inner triplets that will further "compress" the bunches and bring them to smash in the four interaction points (IP). This system maximizes the number of collisions produced in the center of the LHC detectors:

- ATLAS [57] and CMS, [58] two general-purpose particles detectors conceived to explore a wide range of physics, including the search and description of the Higgs boson, supersymmetric particles, extra dimensions, dark matter candidates...
- ALICE [59], designed to investigate on the physics of strongly interacting matter at extreme energy densities,
- LHCb [60], aimed at studying matter-antimatter asymmetry through the bias of B hadrons,
- TOTEM [61], built for the measurement of the total elastic and diffractive cross-section,
- LHCf [62], devised to detect particles emitted in the forward direction in order to calibrate the cosmic rays background,
- MoEDAL [63], looking for the magnetic monopole and the highly ionizing Stable Massive Particles (SMPs) predicted by theories beyond the Standard Model.

The number of events taking place per second at the LHC IPs is given by

$$N_{evt} = \sigma L, \tag{2.1}$$

where σ is the cross section of the process under investigation, and L represents the machine luminosity. This last can be expressed as a function of the beam parameters:

$$L = \frac{n_b n_1 n_2 f_{rev}}{2\pi \epsilon_n \beta^*}, \tag{2.2}$$

where $n_{1/2}$ represents the number of particles per bunch, n_b the number of bunches per beam, f_{rev} the revolution frequency. The factor $\epsilon_n \beta^*$ characterizes the beam size, being composed by the normalized transverse beam emittance and the beta function which describes the beam optics; it can as well be expressed as $\Sigma_x \Sigma_y$, the product of the horizontal and vertical convolved beam widths.
When the detector will operate at the designed peak luminosity, with an energy per proton beam at 7 TeV, the parameters described above will reach the values collected in Table 2.1.

Table 2.1: LHC design parameters for proton beams at ATLAS and CMS IPs

L: peak luminosity	$10^{34} cm^{-2} s^{-1}$
$n_{1/2}$: number of particles per bunch	$1.15 * 10^{11}$
n_b: number of bunches per beam	2808
f_{rev}: revolution frequency	11245 Hz
ϵ_n: normalized transverse beam emittance	3.75μm rad
β^*: beta function	0.55 m

The peak instantaneous luminosity delivered to ATLAS per day during the proton-proton collisions of 2010, 2011 and 2012 is shown in Figure 2.4. If we integrate this observable over time we obtain the integrated luminosity, usually measured in femtobarn^{-1} or picobarn^{-1}, which is used to express the size of the collected datasets. Figure 2.5 represents, in green, the cumulative luminosity *delivered* to ATLAS for pp collisions (with stable beams) at 7 and 8 TeV centre of mass energies in 2011 and 2012; the cumulative luminosity *recorded* by ATLAS for the same period is instead depicted in yellow. For data to be recorded, the beams must be stable, the tracking detector must have completed the high voltage ramping and turned on the preamplifiers for the pixel system.

2.2 Luminosity measurement

The measurement of the delivered luminosity, considered a key component for the ATLAS physics programme [64], relies on the expression of this observable in terms of the average number of inelastic interactions per bunch crossing (μ) and the corresponding cross section (σ):

$$L = \frac{\mu f_{rev} n_b}{\sigma_{inelastic}} \times \frac{\epsilon}{\epsilon} = \frac{\mu_{vis} f_{rev} n_b}{\sigma_{vis}}, \tag{2.3}$$

where the detection efficiency has been introduced explicitly in order to extrapolate the experimentally observable quantities. As mentioned above, n_b and f_{rev} are known parameters for the LHC, while μ_{vis} is measured independently in ATLAS via a variety of dedicated subdetectors with several algorithms: the Minimum Bias Trigger Scintillators (MBTS), segmented counters that provide a trigger on minimum collision activity during a bunch crossing; the Beam Condition Monitors (BCM), four diamond sensors designed to check background levels and issue beam-abort requests, when beam losses could damage the ID; LUCID, a Cherenkov detector conceived to make statistically precise luminosity measurements separately for each bunch crossing within LHC fill pattern with no deadtime. The luminosity calibration relies thus on the determination of the visible cross section, which can be extracted by means of a comparison with Eq. 2.2; the number of protons per bunch ($n_{1/2}$) is measured at the LHC, while the horizontal and vertical convolved beam widths (Σ_x and Σ_y) are directly determined in a van der Meer (vdM) scan, in which the beams are separated in steps of a known distance. At the peak of the scan curve, corresponding to the configuration with the closest beams, one can finally obtain:

$$\sigma_{vis} = \mu_{vis}^{MAX} \frac{2\pi \Sigma_x \Sigma_y}{n_1 n_2}. \tag{2.4}$$

For each algorithm the visible cross section is hence determined as a function of the peak visible interaction rate divided by the bunch populations (an example is provided in Fig. 2.6) and the product of the convolved beam widths.
This procedure introduces several systematic uncertainties which are properly propagated to the luminosity measurement. Some are connected to the beams: their centering in the non-scanning plane at the beginning of a van der Meer scan, the random deviations from their nominal positions, and the emittance growth that would manifest as a slight increase of the measured value of Σ from one scan to the next; others depend more on the vdM technique, like the assumption that the particles densities in each bunch can be factorized into independent horizontal and vertical contribution, the lenght scale of each scan step, the choice of the fit model shown in Fig. 2.6 and the background subtraction; finally, the uncertainties related to the estimates of the beam parameters, and of the average number of visible interactions, which are realized via several detectors and algorithm. Globally, $\Delta L/L$ is found to be 1.8% for the 2011 dataset and 2.8% for 2012.

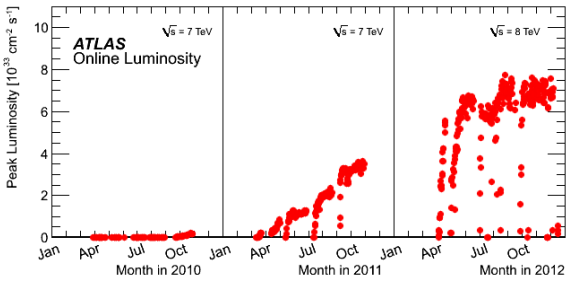

Figure 2.4: Peak Luminosity versus time in 2010, 2011 and 2012.

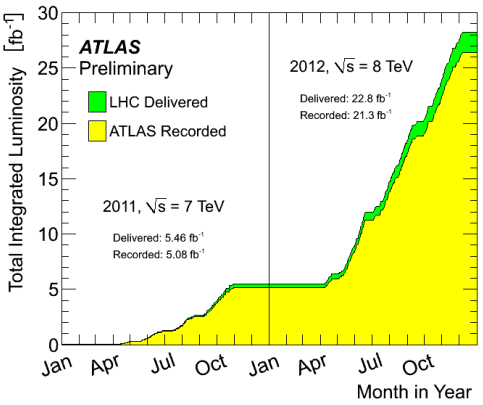

Figure 2.5: Total integrated luminosity versus time in 2011 and 2012.

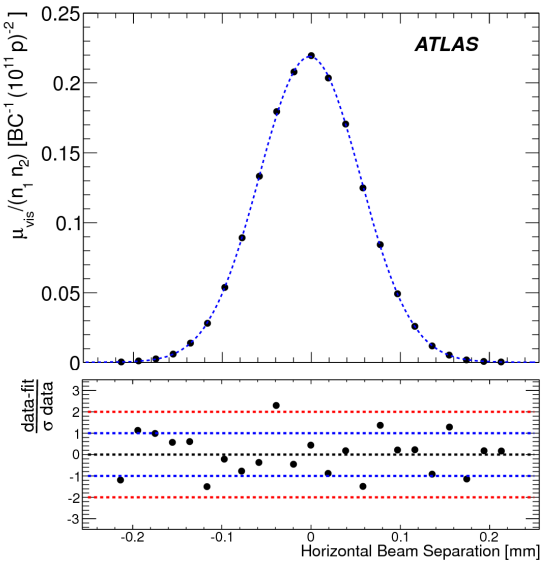

Figure 2.6: Visible interaction rate versus nominal beam separation for a van der Meer scan. The residual deviation of the data from the fit, normalized at each point to the statistical uncertainty (σ data), is shown in the bottom panel.

2.3 The ATLAS detector

ATLAS, acronym of **A** **T**oroidal **L**HC **A**pparatu**S**, is a multi-purpose detector optimized simultaneously for a large range of known and hypothetical physical processes; its cutting-edge technology grants in fact multiple tests of the Standard Model (SM) as well as several searches for phenomena that are typically expression of the Beyond Standard Model Physics (BSM).
The detector [65],[66], located about 100 meters underground in between the two SPS injection points, is a cylinder with a total length of 42 meters and a radius of 11 meters. As Figure 2.7 shows, it is actually comprised of many components nested inside one another and built symmetrically in the backward and forward directions. The inner most layer hosts the tracking detectors, aimed at measuring the momentum of charged particles and determining the vertex position. Beyond are situated the calorimeters, on which the computation of the energy loss by both charged and neutral particles is based. Finally, the muon spectrometer surrounds the barrel and the end-caps allowing the identification of those highly penetrating leptons. An essential element of the ATLAS detector is the magnet system that generates a stable, precise and predictable magnetic field for any sub-detector. This is realized through an electromagnetic solenoid enveloping the inner tracker, and several toroids magnets covering the muon spectrometer.

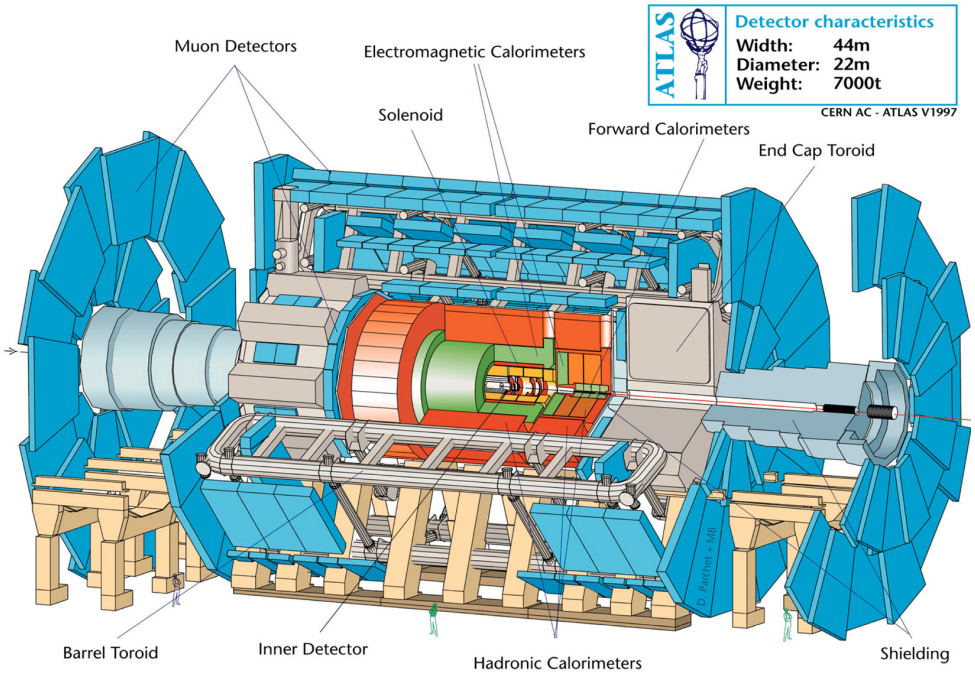

Figure 2.7: Cut-away view of the ATLAS detector.

Before detailing every detector component and the function each one fulfills, it is important to list some conventions that will be used in the following to provide position information.

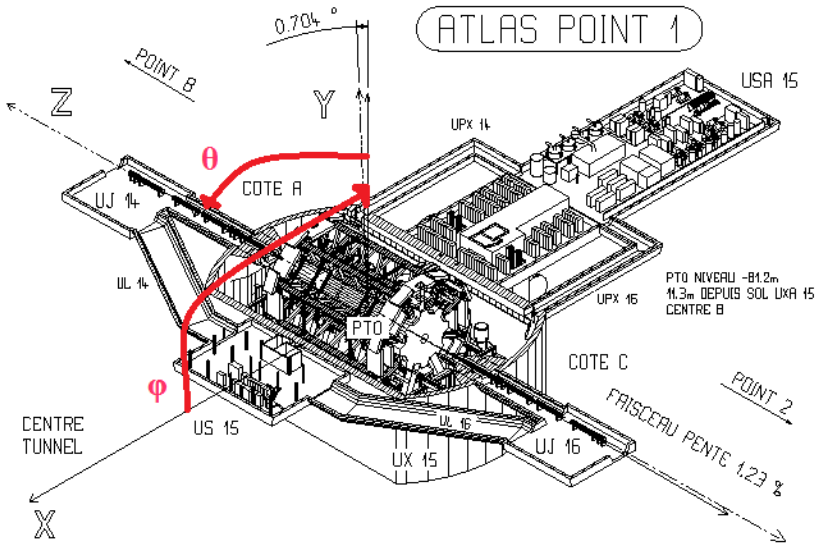

Figure 2.8: ATLAS coordinate system.

Figure 2.8 depicts the center of interaction as the origin of a cartesian and spherical coordinate system. The x-axis points towards the center of the LHC tunnel, the z-axis along the tunnel, the y-axis is slightly tilted with respect to vertical because of the small inclination of the collider itself.
The azimuthal angle in the plane (x,y), ϕ, is defined by the relation

$$tan\phi = \frac{p_y}{p_x},$$

where $p_{x,y}$ have to be intended as the momentum projection along the axes for the particle under analysis. The polar angle, θ, defined by the equation

$$tan\theta = \frac{p_T}{p_z},$$

is instead the angle between the beam axis and the transverse momentum vector.
The particles four-vectors, however, are in general expressed as a function of the azimuthal angle and the pseudorapidity, η, which is the the relativistic limit ($E \sim |\vec{p}|$) of the rapidity, y:

$$\begin{aligned} y &= \tfrac{1}{2} ln \tfrac{E+p_z}{E-p_z} \\ \eta &= \lim_{|\vec{p}|\to E} y = \tfrac{1}{2} ln \tfrac{1+cos\theta}{1-cos\theta} = ln[cot\tfrac{\theta}{2}] = -ln[tan\tfrac{\theta}{2}]. \end{aligned} \tag{2.5}$$

In the azimuthal-pseudorapidity angle space the distance ΔR is expressed as:

$$\Delta R = \sqrt{\Delta\eta^2 + \Delta\phi^2} \tag{2.6}$$

2.3.1 The magnet system

In a particle physics experiment the bending of the charged tracks and the subsequent momentum measurement rely on the specific magnet system, that is indeed a very crucial feature; for ATLAS, the presence of large toroids surrounding the detector has even determined its acronym. The configuration of the magnet system [67] is actually not only composed by toroids: as Fig. 2.9 shows, a central solenoid provides a constant magnetic field inside the inner detector and, outwardly, several toroids serve the muon spectrometer. The two kinds of magnets are both built with NbTi/Cu superconductors stabilized with Al, operated at a temperature of 4.5 K.

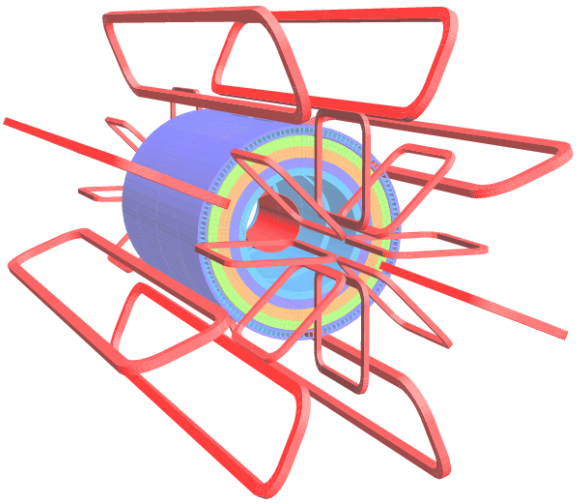

Figure 2.9: Geometry of magnet windings and tile calorimeter steel. The eight barrel toroid coils, with the end-cap coils interleaved are visible. The solenoid winding lies inside the calorimeter volume. The tile calorimeter is modelled by four layers with different magnetic properties, plus an outside return yoke.

The central solenoid envelops the cavity in which the tracker is housed, and shares the cryostat with the liquid argon calorimeter to reduce the material build up. With a length of 5.3 m and a radius of 1.2 m, it is designed to provide a magnetic field of 2 T parallel to the beam-axis, and of 2.6 T at the surface of the superconductor. Its radial thickness of 45 mm (corresponding to 0.66 radiation lengths X_0 [1]) is the minimum possible to grant good reliability, as well as not degraded energy measurements.

Three superconducting toroids are embedded in the outermost sub-detector, each one consisting of double-pancake coils assembled radially and symmetrically around the beam axis. One is located in the barrel, where the coils have an axial length of 25.3 m, extend radially from 9.4 m to 20.1 m, and generate a variable magnetic field with a the peak of 3.9 T in the pseudorapidity range $0 < \eta < 1.3$. Two more toroids are situated in the end-caps and are constituted by coils with an axial length of 5 m, an

[1] X_0 represents the average distance over which the electron energy is reduced by a factor $1/e$ due to Bremsstrahlung only.

inner radius of 1.65 m and an outer one of 10.7 m; there, the magnetic field reaches at most 4.1 T in the pseudorapidity range $1.6 < \eta < 2.7$.
This particular configuration is aimed at the creation of a magnetic field which is perpendicular with respect to the direction of the muons emerging from the interaction point; this implies the maximization of the trajectory deflection and thus a more precise momentum determination.

2.3.2 The inner detector

The inner detector [68] (ID) is a composite tracking system devised to identify and reconstruct the trajectory of the particles. Occupying a cylinder of 6.20 m in length and 1.05 m in radius just around the beam pipe, it is the component situated closest to the interaction point and is built therefore to be highly radiation tolerant. The ID provides a measurement of the primary vertex, coinciding with the interaction point, and the secondary vertices originated by the decay of long-lived particles. At the same time, it realizes several precision measurements of the tracks that are then exploited to calculate the direction of flight, the momentum and the sign of the charge through pattern recognition algorithms.

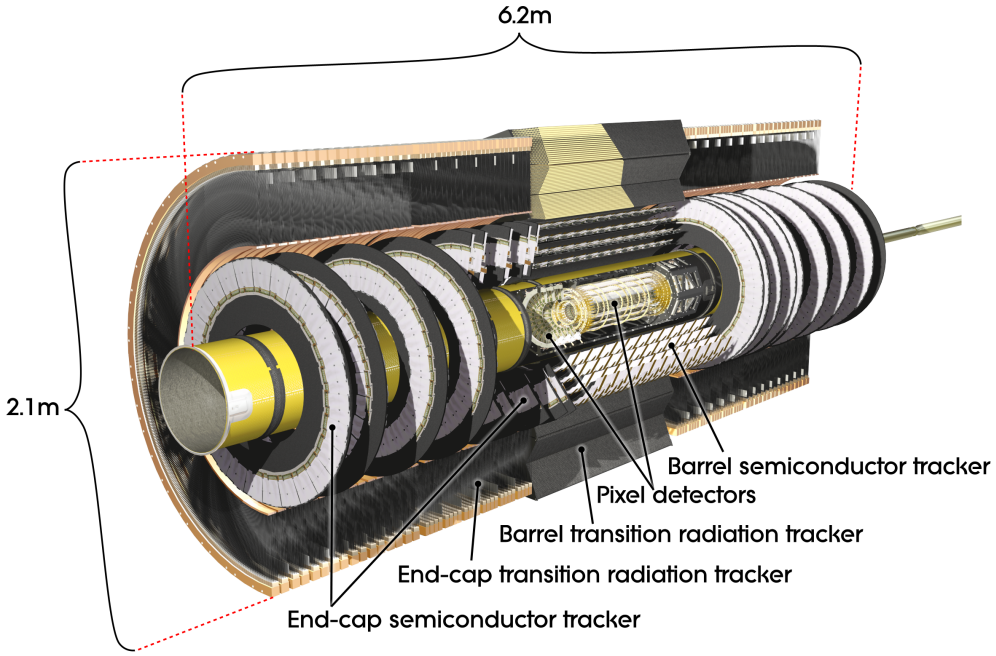

Figure 2.10: Cut-away view of the ATLAS Inner Detector.

Those tasks are actually achieved by several dedicated sub-detectors whose layout is outlined in Figs. 2.10 and 2.11: in the barrel region the high resolution pixel detector (Pixel), the silicon microstrip detector (SCT) as well as the transition radiation tracker (TRT) are arranged in concentric cylinders around the z-axis; in the end-caps, on the contrary, all the detectors are mounted on disks perpendicular to the beam direction. Each component will be fully presented in the following paragraphs.

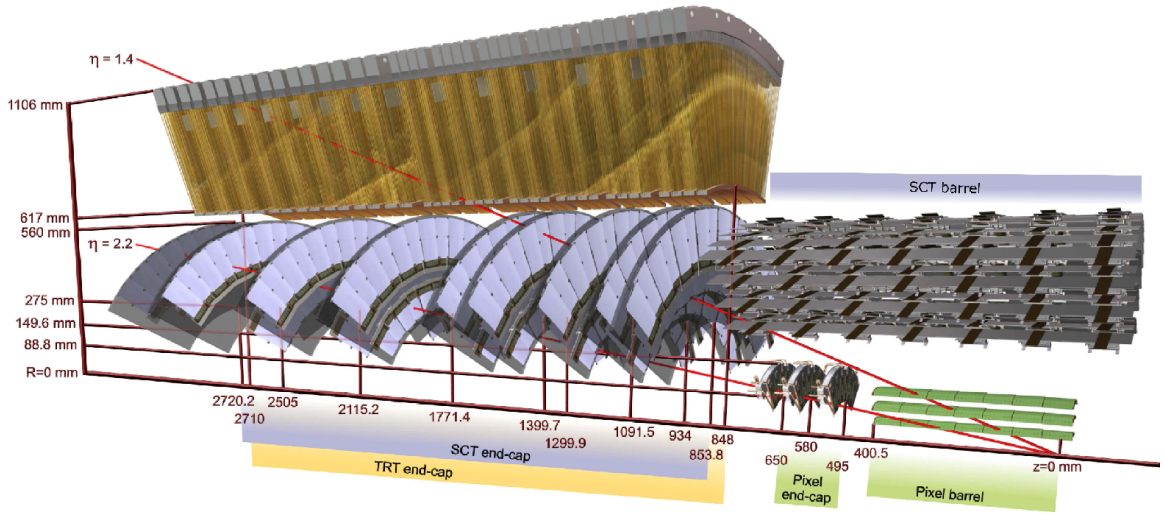

Figure 2.11: Drawing of the ATLAS Inner Detector traversed by two 10 GeV tracks with η=1.4 and 2.2. The transition radiation tracker is not shown in the barrel.

Pixel detector

The pixel detector [69], the ATLAS innermost element, provides up to three precision measurements of the charged tracks situated in a pseudorapidity region of $|\eta| < 2.5$. It is constituted of three concentric cylinders enclosing the beam pipe at average radii $R_0 = 50.5$ mm, $R_1 = 88.5$ mm, and $R_2 = 122.5$ mm, and three disks mounted in the end-caps at a distance from the interaction point of $z_0 = 49.5$ cm, $z_1 = 58.0$ cm, $z_2 = 65.0$ cm.

The basic unit of this detector is the module, a rectangular oxygenated n-on-n silicon sensor subdivided into 47,268 pixels. When an incident particle traverses this semiconductor medium releasing part of its initial energy, electrons-holes pairs are generated and drift towards the electrodes among which a bias voltage is applied. Essentially, to provide a high granularity position measurement these electrodes are segmented into 50×400 μm^2 pixels, each one able to transmit an own signal being directly bump-bonded to the electronics circuitry on the readout chips. Since the solenoid magnetic field makes the trajectory of the charged particles almost tangential, these elements are placed such that their longest dimension is parallel to the z-axis, while the shortest dimension is tangential; this configuration clearly optimizes the precision measurements of the Rϕ coordinate, resulting in a resolution of $\Delta(R\phi) \times \Delta z = 12 \times 66 \mu m^2$.

As previously mentioned, the sensors and the readout electronics have to comply with stringent radiation hardness requirements: they are built to withstand the dose expected after 10 years of ATLAS operation, corresponding almost to 300 kGy or 10^{15} $n_{eq} cm^{-2}$ [2].

[2]The fluence of particles is here expressed in terms of the damage created by a neutron with energy 1eV.

With its finely segmented layers situated close to the collision point, the pixel detector contributes significantly to the primary and secondary vertexes reconstruction; it determines the resolution on the impact parameter z_0, as well as on the lifetime of the B hadrons or τ leptons whose decay is displaced from the interaction point. Besides, it provides high quality tracking: it performs optimal space points measurements that will be used for fast triggering and full pattern recognition, and gives a first estimate of the momentum with a resolution of:

$$\frac{\sigma_{p_T}}{p_T} = 0.03\%\ p_T(GeV) + 1.2\%.$$

Semiconductor tracker

The semiconductor tracker [70], designed to provide eight precision measurements per track in the intermediate radial range, is composed by several sections: four barrel layers are located at 30.0 cm, 37.3 cm, 44.7 cm, 52.0 cm from the beam-axis, nine disks unevenly outstripped are situated on each end-cap.
Its basic building-block is the silicon p-on-n module (Figs. 2.12(a), 2.12(b)) arranged with 4 identical, single-sided sensors; one pair of sensors is daisy-chained to give 768 long strips of 126 mm length and with a pitch of 80 μm, and then glued back-to-back to the other pair, at a 40 mrad stereo angle to improve the resolution along the z-axis.

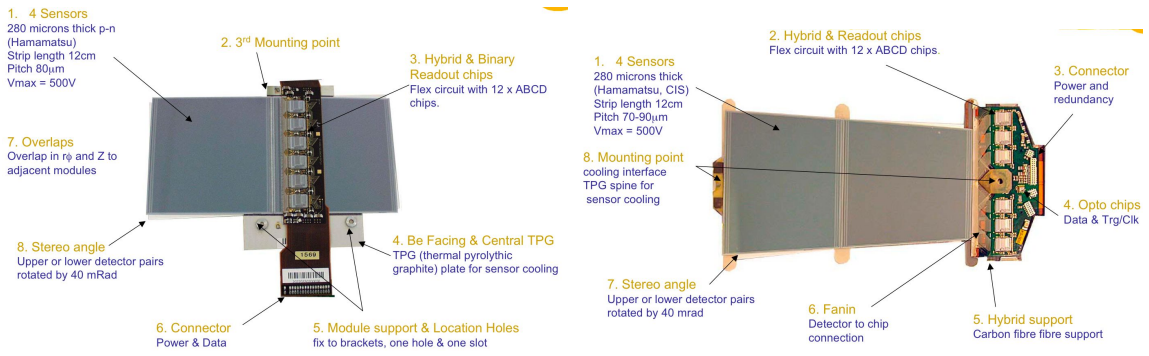

(a) (b)

Figure 2.12: (a) SCT barrel module and (b) SCT end-cap module.

Front-end readout chips are integrated on a multi-layer circuit and connected to the silicon strips by wire bonding. Both the silicon wafers and the electronics are devised to provide the required functionality even when exposed to high radiation doses.

With a similar functioning to the pixel detector, the SCT uses the hit information from each module side to construct a space-point; the effective design precision with which this is measured is $\Delta(R\phi) \times \Delta z = 17 \times 580 \mu m^2$, a slighly poorer resolution than the one cited in the previous paragraph.

Transition radiation tracker

The transition radiation detector [71],[72] (TRT) is a collection of drift tubes and radiators organized in three major modular components: the barrel, made up by three layers, and the wheels installed in each end-cap. On the whole, it occupies a cylindrical volume of inner radius of 56 cm and outer radius of 107 cm, covering the pseudorapidity range $|\eta| < 2$.
The basic tracking device on which TRT is set up is the 4 mm diameter straw, that acts as a proportional counter and whose functioning is sketched in Fig. 2.13. Its walls are kept at high voltage of negative polarity, serving as cathode; in its center the anode, a 30 μm diameter gold-plated tungsten wire, is kept at ground potential. The straw is filled with a gas mixture based on xenon (70%), CO_2 (27%) and O_2 (3%), that is ionized owing to the energy deposition of the particles emerging from the collision point. The applied electric field accelerates the ions-electrons pairs towards the electrodes, and generates some "avalanches" that have the effect of amplifying the collected signal. The information on the track position is hence gathered by the set of activated straws and, more precisely, for each one the distance of closest approach to the central wire is given by the measurement of the drift time. In the barrel the 144 cm long straws are located parallel to the beam axis, and contain anode wires that are electrically split and read out at both ends; in the end-caps, on the contrary, the 40 cm long straws are arranged radially, and read out just in their outer end.

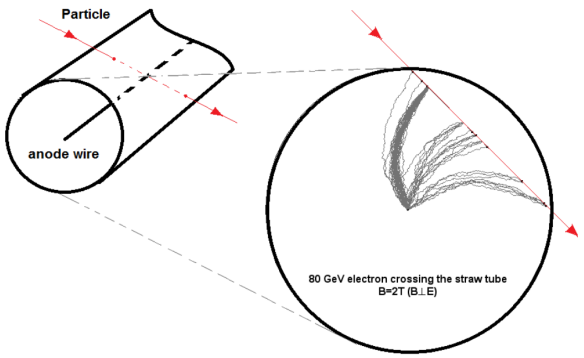

Figure 2.13: Reproduction of the effect produced by a 80 GeV electron traversing one straw of the ATLAS TRT. A graphic representation of the collection of electrons and ions towards the electrodes is also drawn.

The TRT provides the most reliable momentum measure, with a resolution of

$$\frac{\sigma_{p_T}}{p_T} = 0.05\%\ p_T(GeV) \oplus 1\%$$

for charged particles above 0.5 GeV.

Additionally, the detector implements electron-pion separation by integrating the transition radiation (TR) signature; this relies on the property of charged relativistic particles of emitting X-ray photons when they traverse a boundary characterized by different dielectric constants. Since the radiation intensity is inversely proportional to the Lorentz factor, the effect is stronger for electrons than for π mesons. As Figure 2.14 illustrates, the above mentioned drift tubes are interleaved with propylene foils and fibers, a pattern of different media that entails high TR probability. The soft X-rays produced in this way are then amply absorbed by the Xe atoms, depositing additional energy in the gas and leading to significantly higher redout signal. Typical TR energy deposition are distributed in the range of 8-10 keV for electrons, and are of the order of 2 keV for pions (Fig. 2.15).

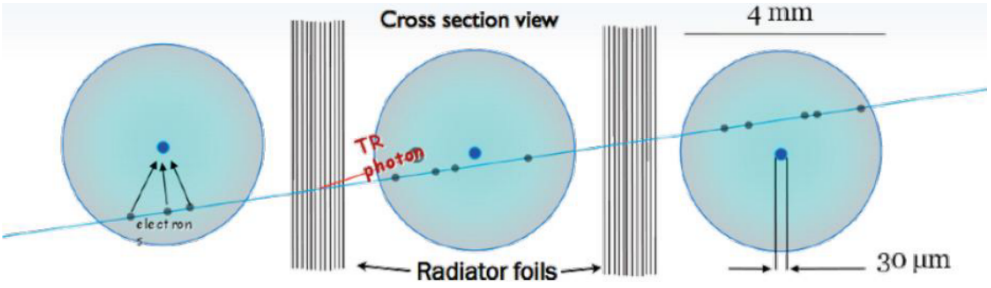

Figure 2.14: Schematic illustration of the trajectory of a relativistic charged particle traversing the ATLAS TRT. As a result of its interaction with the radiator foils, X-rays photons are produced with an angle $1/\gamma$ and enter in the adjacent proportional counter.

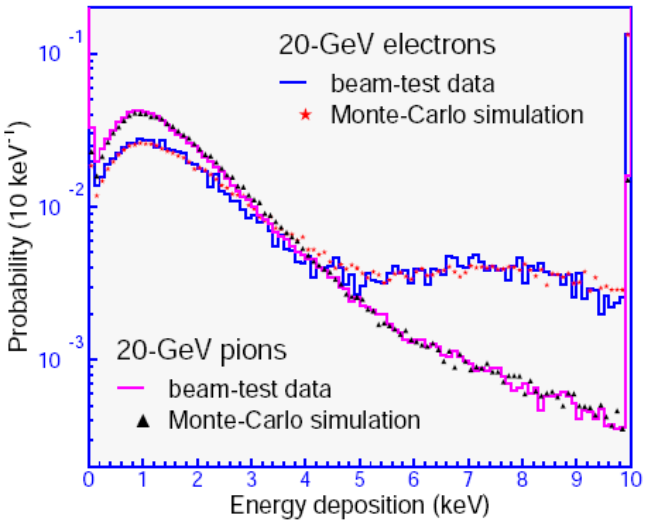

Figure 2.15: Differential energy spectra from data and simulation for a single straw with radiator. Beams of 20-GeV electrons and pions are considered.

2.3.3 The calorimetry

The main function of the calorimetry system is the energy measurement, realized in ATLAS via a sampling technique: layers of dense absorbers, that develop a "particle shower", are alternated with layers of active media, which produce an output signal proportional to the input energy. Different materials and geometries have been chosen in order to optimize the detection of distinct particles, and as a result we can distinguish several partitions (Fig. 2.16). The electromagnetic barrel and end-caps, situated in a pseudorapidity range of respectively $|\eta| < 1.457$ and $1.375 < |\eta| < 3.2$, are both lead-liquid argon calorimeters. They surround the inner detector, and provide electrons and photons identifcation and measurements with excellent position and energy resolution. The hadronic calorimeter, located in the outward region, is divided into two main components: the iron-scintillating fiber barrel covering $|\eta| < 1.7$, and the copper-liquid argon end-caps covering $1.5 < |\eta| < 3.2$. It is aimed at reconstructing the missing transverse energy (E_T^{miss}), as well as the energy deposited by narrow cones of particles produced by the hadronization of a quark or gluon (jets). Finally, the forward calorimeter that extends the detector coverage to $3.9 < |\eta| < 4.1$, is composed of three sections. The first one, made of copper-liquid argon, completes the electromagnetic calorimeter performance, the others, made of tungsten-liquid argon, are devised to perfect the hadronic calorimeter measurements.

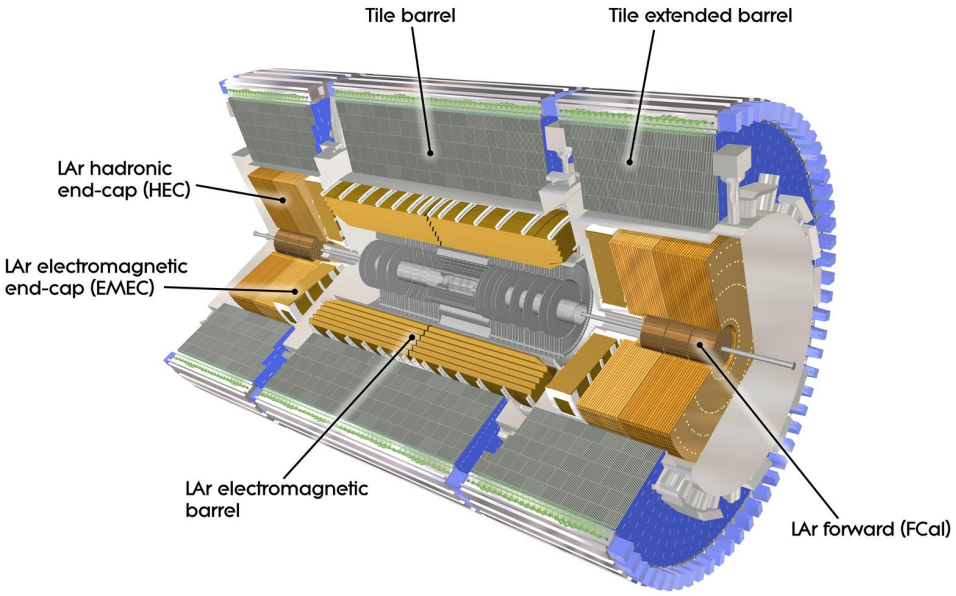

Figure 2.16: Overview of the ATLAS calorimeter.

All the component of the calorimetry system using liquid argon (LAr) as active media are embedded in cryostat vessels and kept at a temperature of 88 K.

The electromagnetic calorimeter

The electromagnetic calorimeter [73],[74] consists of thin lead plates with an accordion shape and a thickness varying as a function of the pseudorapidity, immersed in liquid argon (Fig. 2.17(a)). As previously mentioned, this configuration optimizes the production of electromagnetic showers evolving quickly in a limited space, and the following detection of the energy lost by ionization. For an electron traversing a dense medium like lead with the typical energy of a LHC collision [3] the Bremsstrahlung mechanism dominates. Due to the interaction with the nuclear electric fields, photons are emitted, and propagate in matter having good chance of converting in e^+e^- pairs. Those leptons can emit breaking radiation, inducing a chain effect that results in a cascade of electrons/positrons/photons that stops only once the lepton energy drops below the critical value. The particles belonging to the shower pass, then, through a layer of a different material, sensitive to ionization. Part of the deposited energy produces, here, electron-ion pairs, which are collected by applying a 2000V tension between the electrodes fixed on the absorber. The choice of the liquid argon technology relies on the response stability, the radiation tolerance and the linear behaviour as function of the deposited energy; the accordion geometry ensures, instead, azimuthal uniformity avoiding cracks.

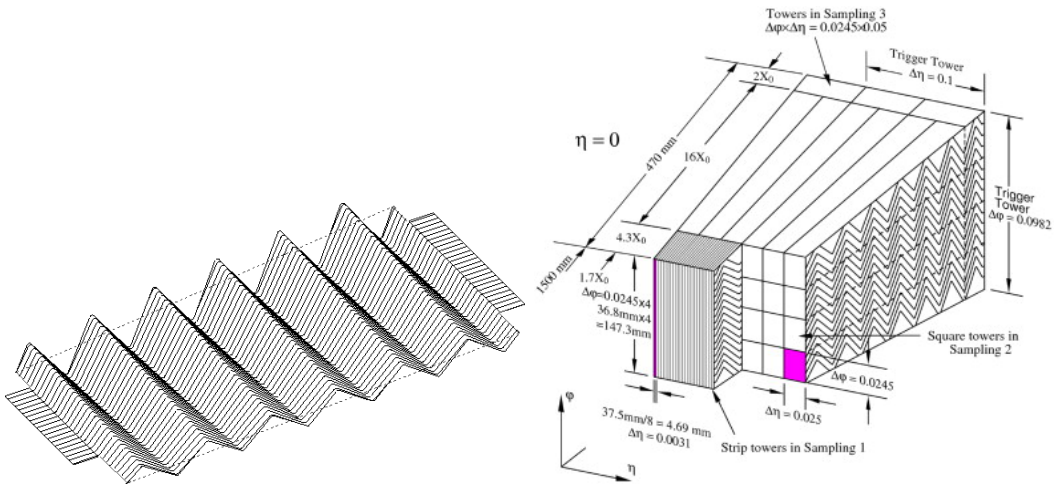

(a) (b)

Figure 2.17: (a) Accordion shape structure of the electromagnetic absorbers and electrodes. (b) Sketch of a barrel module showing the cell granularity in η and ϕ in the three samplings.

In order to determine the energy and position of electrons and photons with excellent resolution, the electrodes are laterally and longitudinally engraved to arrange fine cells. More precisely, three different samplings whose granularity is depicted in

[3]The energy loss of a light particle in matter is mainly due to collisions and radiation emission; for low incident energy the first phenomenon dominates, then for a specific value defined as critical energy (E_c) the two lead to the same effect, and finally for an incident energy greater than E_c, Bremmsstrahlung gives the most important contribution.

Fig. 2.17(b), are conceived according to different clustering of the readouts.
The front layer (sampling 1) is finely segmented along η, being constituted by strip towers of size $\Delta\eta \times \Delta\phi = 0.003 \times 0.100$, and has an active depth of almost 4.3 X_0. This geometry allows the separation between neutral pions decaying into two photons and jets involving individual photons.
The central layer (sampling 2), composed by squared towers of size $\Delta\eta \times \Delta\phi = 0.025 \times 0.025$, collects the main energy deposit within its 16 X_0 extent. Since it fully contains clusters with energy below 50 GeV, the noise can often be reduced by not adding the third sampling.
The back layer (sampling 3) is reached only by the highest energy particles, and is therefore devised to detect wide clusters with cells having double size in the η coordinate. These trigger towers, that extend across 2 X_0, are responsible for the separation of the electromagnetic and the hadronic showers.
To improve the precision in the energy reconstruction, a liquid argon thin layer is installed before the ones just detailed: the presampler. It measures the multiplicity of a cluster that develops because of the interactions with the inactive material which preceeds the calorimeter (inner detector, services and cryostat).

The overall energy resolution is parametrized by the following formula:

$$\frac{\sigma(E)}{E} = \frac{a}{\sqrt{E(GeV)}} \oplus \frac{b}{E(GeV)} \oplus c, \tag{2.7}$$

where the symbol $\oplus$ indicates that the terms are summed in quadrature. In equation 2.7, a is the "sampling term" which describes the statistical fluctuations of the electromagnetic shower and b is the "noise term" due to the electronics; their target values are respectively [75]: $a \sim 10\%$ GeV, $b \sim 170$ MeV (without pileup). Since the constant term which takes into account the non uniformity of the calorimeter and of its response, c, is the dominant one at high energy, it has been measured [76]. The table below reports the results obtained using 2010 $Z \rightarrow ee$ data for different

Sub-system	η-range	Effective constant term, c_{data}
EMB	$\lvert\eta\rvert < 1.37$	$1.2\% \pm 0.1\%$ (stat) $^{+\ 0.5\%}_{-\ 0.6\%}$ (syst)
EMEC-OW	$1.52 < \lvert\eta\rvert < 2.47$	$1.8\% \pm 0.4\%$ (stat) $\pm 0.4\%$ (syst)
EMEC-IW	$2.5 < \lvert\eta\rvert < 3.2$	$3.3\% \pm 0.2\%$ (stat) $\pm 1.1\%$ (syst)
FCal	$3.2 < \lvert\eta\rvert < 4.9$	$2.5\% \pm 0.4\%$ (stat) $^{+\ 1.0\%}_{-\ 1.5\%}$ (syst)

pseudorapidity regions.
The acronyms EMB stands for electromagnetic calorimeter barrel, EMEC-OW for the outer endcap wheel, EMEC-IW for the inner endcap wheel and FCal for the front calorimeter.

The hadronic calorimeter

As already outlined, the hadronic calorimeter [77],[78],[79], located behind the solenoid coil and the EM calorimeter, is composed by two partitions characterized by a different functioning. Their design is guided by the requirement of an excellent jet identification and reconstruction in the LHC environment.
The barrel, that occupies a cylinder of 11 m lenght, 2.28 m inner radius and 4.25 m outer radius, is subdivided into a central section ($|\eta| < 1$) and two extensions ($0.8 < |\eta| < 1.7$). It is essentially comprised of plastic scintillator tiles of 3 mm thickness embedded in steel absorbers, that develop hadronic showers. The particles transiting in the active media excite the atoms and molecules, that go back to their ground state by emitting a flash of light. The photons are at this stage collected by wavelength shifting fibers, and transmitted to two separate photomultiplier tubes; these devices convert the luminous signal to a current of photoelectrons which is proportional to the energy deposited at the beginning of the chain. The fiber grouping allows to define a three-dimensional cell structure in such a way as to form three radial samplings depth. For the first and the second layers the cells have a size equals to $\Delta\eta \times \Delta\phi = 0.1 \times 0.1$, for the outward one corresponding to $\Delta\eta \times \Delta\phi = 0.2 \times 0.1$.
The end cap hadronic calorimeter is structured in two wheels, containing flat copper absorbers placed orthogonally with respect to the beam axis. These plates have a thickness of 25 mm in the front wheel and 50 mm in the rear one, but in both components are interspersed with layers of liquid argon having a depth of 8.5 mm. The granularity of the readout cells, driven by the aim of reconstructing the decay $W \rightarrow jet + jet$ at high transverse momentum, is $\Delta\eta \times \Delta\phi = 0.1 \times 0.1$ for the region $|\eta| < 2.5$ and $\Delta\eta \times \Delta\phi = 0.2 \times 0.2$ beyond $|\eta| = 2.5$.

Similarly to what was discussed in the previous paragraph, the energy resolution can be expressed as:

$$\frac{\sigma(E)}{E} = \frac{52.9\%}{\sqrt{E(GeV)}} \oplus 5.7\%. \tag{2.8}$$

The forward calorimeter

Since the forward calorimeter [80] is conceived primarly for the detection of jets that would otherwise escape and degrade the resolution of the missing transverse energy, its location is the closest to the interaction point. The design is therefore harshly constrained by the hostile radiation environment, and results in an electrode structure with annular gaps filled with the active medium and oriented parallel to the beamline. Copper tubes acting as cathodes constitute the matrix shown in Fig. 2.18(a); each one contains an absorber rod (the anode) positioned concentrically and surrounded by a thin layer of liquid argon. The forward calorimeter is constituted by three modules lying one behind another inside a support tube that forms a structural part of the endcap cryostat: FCal1, FCal2, FCal3 (Fig. 2.18(b)).

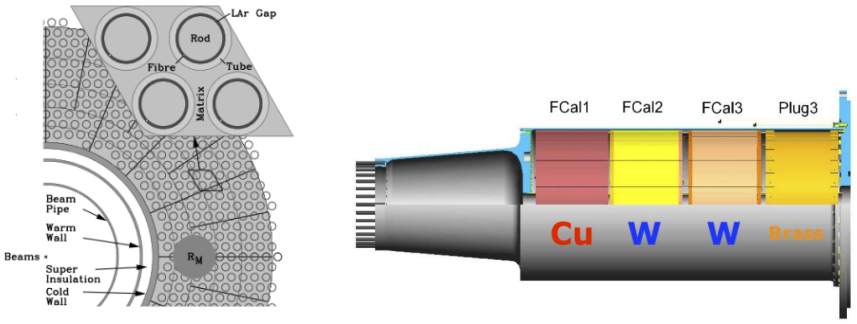

(a) (b)

Figure 2.18: (a) View of the forward calorimeter matrix illustrating a single electrodes group. R_M indicates the size of the Molière radius giving the scale of the transverse dimension of the particle shower. (b) Sketch of the FCal partitions.

They all share roughly the same architecture, but operate with rods of different materials and liquid argon gaps of different size, as the Table below underlines.

Section	Function	Rod material	LAr gap thickness
FCal1	Electromagnetic calorimetry	Copper	250 μm
FCal2	Hadronic calorimetry	Tungsten	375 μm
FCal3	Hadronic calorimetry	Tungsten	500 μm

2.3.4 The muon spectrometer

The outermost ATLAS subdetector [81], [82] is dedicated to the identification of the muons, very penetrating leptons that can emerge from all the calorimeter levels.
Its structure, whose layout is depicted in Figs. 2.19(a) and 2.19(b), shows a cylindrical symmetry around the beam axis. The barrel part is composed by three concentrical layers located at radii $R_0 \sim 5$ m , $R_1 \sim 7.5$ m, $R_2 \sim 10$ m and covering of $|\eta| < 1$, while the end-caps are constituted by four disks situated between 7 m and 23 m from the interaction point in the pseudorapidity range $1 < |\eta| < 2.7$. Four detector technologies and the toroidal magnet system complement each other to provide momentum resolution better than 3% for most tracks, and fast response for triggering.

Tracking chambers

Under the influence of the magnetic field, the particles trajectory is deflected and tends to be parallel to the beam pipe in the barrel, and radial in the end-caps; by interacting in several drift chambers, whose general functioning has been outlined in Section 2.3.2, muons generate multiple signals allowing a precise reconstruction of the z coordinate in the barrel and of the r coordinate in the end-caps.

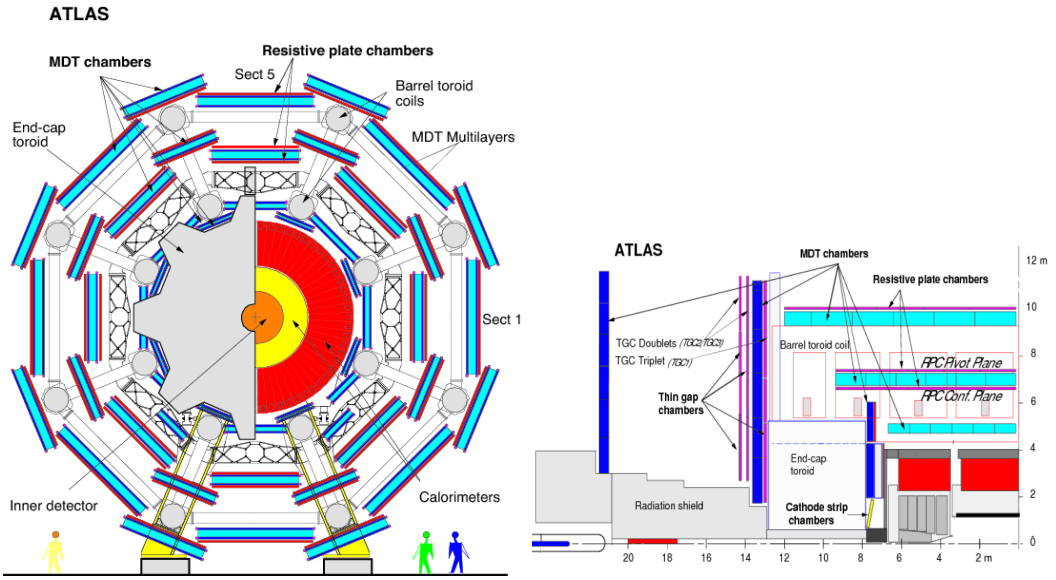

(a) (b)

Figure 2.19: (a) Schematic view of the muon spectrometer in the x-y (b) and z-y projections.

The pseudorapidity region $|\eta| < 2$ is equipped with rectangular chambers containing three to eight layers of monitored drift tubes (MDT) oriented along ϕ (Fig. 2.21(a)). The MDTs, filled with a pressurized gas mixture (Ar/CO_2), enclose a thin tungsten-rhenium anode wire held at a voltage of 3 kV; since the cathode walls are kept at ground potential, a radial electric field is generated in their interior. The design with multiple individual tubes provides mechanical robustness and very accurate measurements in the bending plane. Several hits per traversing track provide in fact a chamber resolution of about 35 μm in the z coordinate.

In the pseudorapidity range $2 < |\eta| < 2.7$, trapezoidal multilayer proportional counters are employed: the cathode strip chambers (CSC) sketched in Fig. 2.21(b). They consist of cathode planes separated by a gas filled ($Ar/CO_2/CF_4$) gap, and segmented into strips which are orthogonal with respect to the strips of the adjacent layers. Central anodes wires, oriented in the radial direction, are held at 1.8 kV. The r coordinate can thus be extracted, with a resolution of 40 μm, from the measurements realized in the planes with strips perpendicular to the anode wires; on the other side, the ϕ coordinate is determined with a resolution of 5 mm via the planes having strips parallel to the wires. This fine granularity and the fast response time are the features that led to the use of cathode strip chambers in this high particle flux region.

Trigger chambers

The muon spectrometer is also instrumented with a level 1 stand-alone trigger system, that applies a reduction rate of accepted events from 40 MHz to 75-100 kHz. Muons are required to come in time with bunch crossing and have a transverse momentum

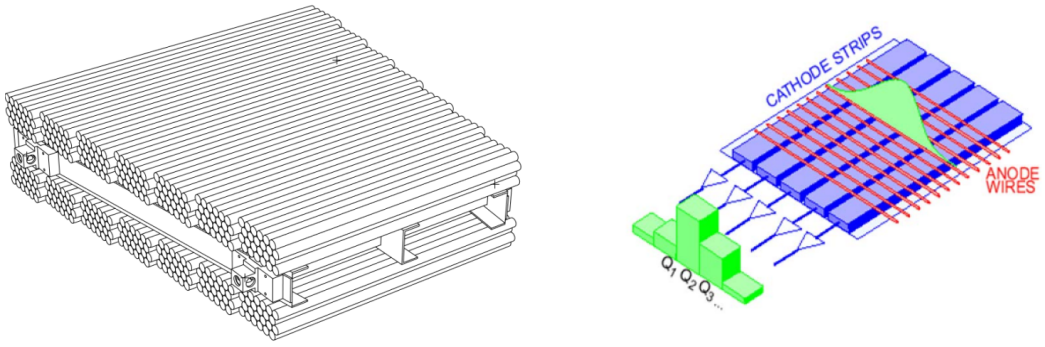

(a) (b)

Figure 2.20: (a) Module of monitored drift tubes. Particles from the interaction point traverse at least three such modules. (b) Schematic view of the setup of a cathode strip chamber and of its signal production.

greater than a certain threshold (typically few GeV/c). This signature is preferably revealed by detectors characterized by a very high time resolution and tiny latency time, even if at expense of the spatial resolution.

The resistive plate chambers (RPC) are installed as doublets on the central MDT station, where they are responsible for the low-p_T triggering, and as singlets at the third and outermost MDT layer. Each RPC is made of two parallel plastic laminate resistive plates of 2 mm thickness, among which the potential difference is almost 5 kV; these electrodes are separated by a 2 mm thick gap filled with a gas mixture ($C_2H_2F_4$). Here, the induced electric field is strong enough to accelerate freed electrons to an energy such that they are also capable of ionizing gas molecules in the gap, generating an "avalanche". The signal is read out from two orthogonal sets of strips that provide information for both the η and ϕ coordinates; it is still proportional to the eneregy released by the muon, but lacks of precision in the position meausurement (10 mm for both η and ϕ). The proportional amplification of the current guarantees, nevertheless, an excellent time resolution of 1.5 ns.

The thin gap chambers (TGC) are installed in the muon detector end-caps, where they constitute the trigger inner and middle stations. They resemble multiwire proportional chambers filled with a gas mixture (CO_2/C_5H_{12}), but with a distance between anode wires and graphite cathode planes which is smaller than the one between two anode wires. These wires, kept at 2.9 kV voltage, run parallel to the MDTs and provide the information on the bending coordinate for the trigger; additional read-out strips perpendicular to them measure the track position in the non-bending plane. The TGS are constructed in doublets and triplets, so that the trigger is based on requiring hit coincidences between the several layers. The provided time resolution is of 5 ns while the spatial resolution is 2-6 mm in r and 3-7 mm in ϕ.

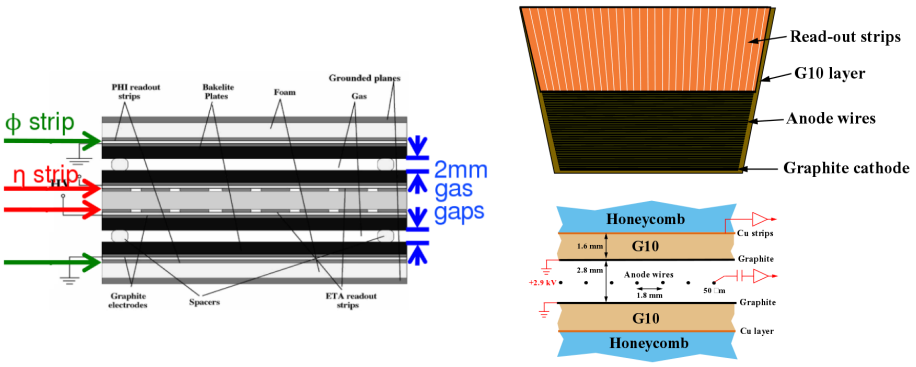

(a) (b)

Figure 2.21: (a) Schematic representation of a RPC providing muon trigger in the barrel region. (b) Sketch a TGC providing muon trigger in the end-caps.

2.3.5 The trigger system

At the design istantaneous luminosity the ATLAS detector will be exposed to an average of 25 proton-proton collisions every 25 ns, but physical limitations intervene in the recording rate and the storage capability compelling a selection of the data. Moreover, only a relatively small amount of events are really meaningful and interesting for the physics analyses. A trigger system is therefore set up with the goal of reaching a reasonable readout rate, preserving however a great variety of signatures that grant the exploration of the BSM and SM physics. The ATLAS trigger system [83] [84], [85], [86] consists of three levels performing a primary online event selection, and then refining and monitoring the decisions made during the previous step, as illustrated in Fig. 2.22.

The first rough skimming is realized by the **level-1 trigger** (L1), which is hardware based and implemented in custom-built electronics. Being designed to attain a rejection factor of 99.88%, L1 reduces the bunch crossing rate from 40 MHz to 75 kHz according to the decisions made by the central trigger processor (CTS). The latter treats coarse-granularity information from the muon spectrometer (via the RPC and TGC chambers), and from the calorimeters (via the trigger towers). The targeted objects are electron, photon, jet and muon tracks characterized by high p_T, as well as τ decaying into hadrons, or large missing and total transverse energy. With simple selection criteria of a rather inclusive nature, combinations of such objects are required in coincidence or veto. While the CTS treats the information with a maximum overal latency of 2.5 μs, the data are provisionally stored by the several sub-detectors pipeline memories. Afterwards, the selected events are transmitted to the readout drivers (RODs) and buffers (ROBs) where the second stage of the skimming begins. The level 1 trigger has the additional task of providing, for each electron/photon candidate, a region of interest (RoI) consisting in the η, ϕ coordinate plus some bits indicating which sets of thresholds have been passed.

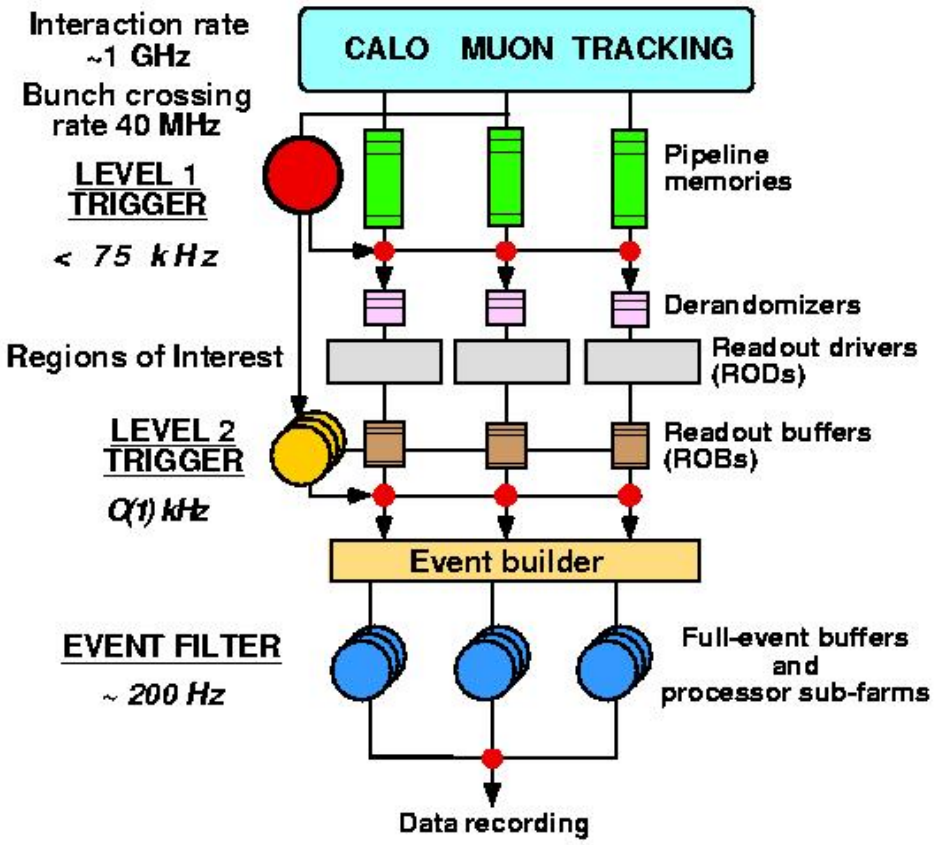

Figure 2.22: Overview of the ATLAS trigger system

The **level-2 trigger** (L2), which is part of the software based high level trigger (HLT) that runs on large computer clusters, reduces the output rate to around 3kHz in an average nominal processing time of 40 ms. It requests events buffered in the ROBs, and with the guide of the RoI map inspects further the zones in the (η,ϕ) plan that may contain interesting objects. This is realized by executing fast reconstruction algorithms based on detector information not available at L1, like tracking, and by considering the full granularity. If the event is accepted, the data fragments are collected by the event builder and assembled in a full event data structure.

The **event filter** (EF) comes then into play, reducing further the data to be written to permanent storage to reach a maximum rate of 200 Hz. It is the second component of the HLT, and employs offline physics and event reconstruction algorithms accessing the full event data. Within an average processing time of 4 s, the EF rejects events which do not conform to the physics requirements, which are at this stage higher thresholds in kinematics or more complicated variables. The fact that EF retrieves the complete event information allows, moreover, to perform a global calibration and to check the alignment; this is really a fundamental task for the physics quality control, as well as for the detector optimisation and performance.

Events passing the EF selection are organized in a hierarchical structure with the goal of grouping the ones that will share the same offline reprocessing, without wasting disk memory. A sequence of reconstruction or selection algorithms performed within the three trigger levels to pick out a specific signal, is collected into a trigger chain. Then, several closely related chains with different roles (primary, backup, supporting and monitoring) are grouped to define a trigger signature like "muons", "b-physics", "jets"... In general, all the events passing the primary chains are kept because these are for physics signals and should have the highest efficiencies possible. Backup chains have higher thresholds, and are used in case of an unexpected increase in luminosity or detector failure. Supporting chains are employed for maintaining or supporting a physics analysis (e.g. to extract backgrounds in a data-driven way or to extract the trigger efficiency). Monitoring chains, finally, are adopted to monitor the data quality (e.g. to check the performance of tracking by the inner detectors). The akin trigger signatures belonging to the same dataset are, then, arranged in streams with a maximal overlap of 10-15%. Only four of such streams are established in ATLAS, namely: electron/photon, muon, jet/τ/E_T^{miss} and minimum bias.

Chapter 3

Object reconstruction

We illustrated in the previous chapters the underlying theory of the single top production, as well as the experimental setup allowing its measurement. We will try, now, to establish a connection between the two topics by detailing how the physical objects characterizing the s-channel single top final state are reconstructed and identified by every component of the ATLAS detector. Separate sections will be thus dedicated to electrons, muons, transverse missing momentum and jets, for which the current performance and the detection efficiencies will be pointed out.

3.1 Electrons

An efficient detection of electrons and positrons is achieved in ATLAS via the precise tracking and transition radiation information in the inner detector, and owing to the fine segmentation of the electromagnetic calorimeter.

3.1.1 Trigger

Since at hadron colliders high p_T electron production is rare compared to that of jets, these particles are used for an accurate on-line event selection [87]. At the hardware-based first level trigger (L1), the reduced granularity of two adjacent calorimeter towers ($\Delta\eta \times \Delta\phi = 0.1 \times 0.1$) is employed to identify Regions of Interest where the deposited energy is above a certain threshold. At the second trigger level (L2), specific e/γ algorithms fulfilling stringent timing requirements are aimed at finding the cell with the largest E_T deposit. Finally, the event filter level (EF) exploits the offline reconstruction and identification algorithms that are detailed hereafter.

3.1.2 Reconstruction

The reconstruction of *central electrons* ($|\eta| < 2.5$) can be summarized in two main phases [88]: the detection and the characterization of the energy deposits in the electromagnetic calorimeter, and their association with the corresponding charged tracks. First of all, a sliding window algorithm is employed to scan the LAr calorimeter

with a granularity of 3×5 in η and ϕ (corresponding to middle layer cell units), in order to select narrow localized clusters with total transverse energy above 2.5 GeV. Then, the trajectories of the charged leptons which have been reconstructed in the inner detector are selected according to a loose matching with those seed clusters. The distance between the track impact point and the activated calorimeter cells is required to satisfy $\Delta\eta < 0.05$, $\Delta\phi < 0.1$ on the bending side and $\Delta\phi < 0.05$ on the other (this last asymmetric criterion accounting for Bresstrahlung losses). From 2012, a dedicated Gaussian Sum Filter (GSF) algorithm [89] is used to correct for radiation losses in the tracker, extrapolating more precisely the track position in the calorimeter. In the case where several tracks seem to correspond to the same electromagnetic cluster, a further selection is needed: the ones showing hits in the silicon microstrip detector are kept, and among them the track presenting the smallest distance from the cluster ($\Delta R = \sqrt{\Delta\eta^2 + \Delta\phi^2}$) is finally retained. After having realized this matching, the electron cluster is rebuilt using 3×7 longitudinal towers of cells in the barrel and 5×5 squares of cells in the end-caps. The energy measured in each cell is summed up, and then corrected to account for the leakages, as well as for the energy deposited before the calorimeter (i.e. in the inner tracker or the solenoid). Finally, the electron four-momentum is determined using information from both the final cluster and the best track matched to the original seed cluster.
The reconstruction of *forward electrons* ($2.5 < |\eta| < 4.9$), instead, relies only on the energy deposits released in the calorimeters. Topological clusters are created by neighbouring a variable number of cells in three dimensions, based on the significance of their energy content with respect to the expected noise. If the total transverse energy is greater than 5 GeV, and its hadronic component is small, an electron is reconstructed. The energy finally associated to this particle is determined as the sum of the contributions from every cell of the cluster, which should be corrected to account for the passive material traversed before reaching FCal. Electron's direction is instead evaluated from the barycenter of the cells belonging to the cluster.

3.1.3 Identification

The procedure enunciated in the last paragraph allows to reconstruct electrons which may actually be misidentified hadrons, or which are not produced in isolation (i.e arising from semi-leptonic heavy flavour decays or photon conversions). In order to improve the discrimination of isolated electrons produced in the decay of a Z or a W boson against such objects, which are considered as sources of backgrounds, a common cut-based selection was introduced [90]. This allowed to standardize the "quality" of the electrons used in the trigger and across analyses, by introducing three operating points corresponding to different background rejection values initially chosen using MC simulations, and later optimized several times during the data-taking. In 2011, when with the achieved instantaneous luminosity of 10^{33} cm^{-2} s^{-1} the background rejection afforded by the medium level was not enough to provide sustainable rates in the trigger, a new update was carried out; the recent isEM++ menu will be presented in the following just for central electrons, the ones selected in the s-channel cross section analyses.

The **loose++ identification** is built upon the list of observables described in Table 3.1 and schematically depicted in Figs. 3.1, 3.2. The "hadronic-leakage" parameters R_{had} and R_{had1} spot eventual jet activities associated to the electron cluster by measuring the ratio of energy deposited in the two calorimeters; the "shower-shape" variables R_η and $\omega_{\eta 2}$ estimate, instead, the extent of the shower in the middle layer of the EM calorimeter (which is considerably small for real electrons). Information coming from the first layer of the EM calorimeter, which has the finest granularity, grant the distinction of the close clusters: E_{ratio} is defined using the strips corresponding to the two highest energy maxima, ω_{stot} measures the shower width. Finally, some observables related to the track matching with the cluster ($\Delta\eta$) and the track quality are used: by requiring electron tracks to have pixel hits and a signifcant number of SCT hits, one can suppress the background from conversions with little losses in signal efficiency.

The **medium++ identification** relies on the application of tighter cuts on the variables listed for the loose selection, as well as on the addition of further constraints on the track quality (Fig. 3.3). The requirement of a given number of b-layer hits is particularly effective to reduce the contamination from the photon conversions occurring after the first pixel layer. Pions discrimination is instead mainly realized by demanding a big amount of high threshold TRT hits ($\propto f_{HL}$), which indicates the presence of transition radiation and is therefore characteristic of light charged particles, like electrons. Finally, events originating from heavy flavor decays are suppressed by compelling a low distance of closest approach to the primary vertex (d_0).

The **tight++ identification** is performed similarly to the medium++, tightening the operating point for each variable and improving further the conversion rejection and the track-cluster matching (Fig. 3.3). A significant fraction of electrons originated by photons interacting in the detector is removed by setting a veto on the tracks matching a conversion vertex (via the conversion bit). Different categories of background are also reduced owing to the ratio of the energy measured in the EM calorimeter to the momentum determined in the inner detector; E/p is close to one for real electrons, much lower for hadrons that interact almost only in the hadronic calorimeter, and greater than one for photons for which the impulse in the tracker can not be reconstructed properly. Also the difference in the azimuthal angle between the track and the cluster is required to be small at this level, although it is not a very powerful observable since strongly affected by Bremsstrahlung.

The isolation criterion is not included into the isEM++ menu since each individual analysis applies a dedicated requirement, together with further quality cuts.

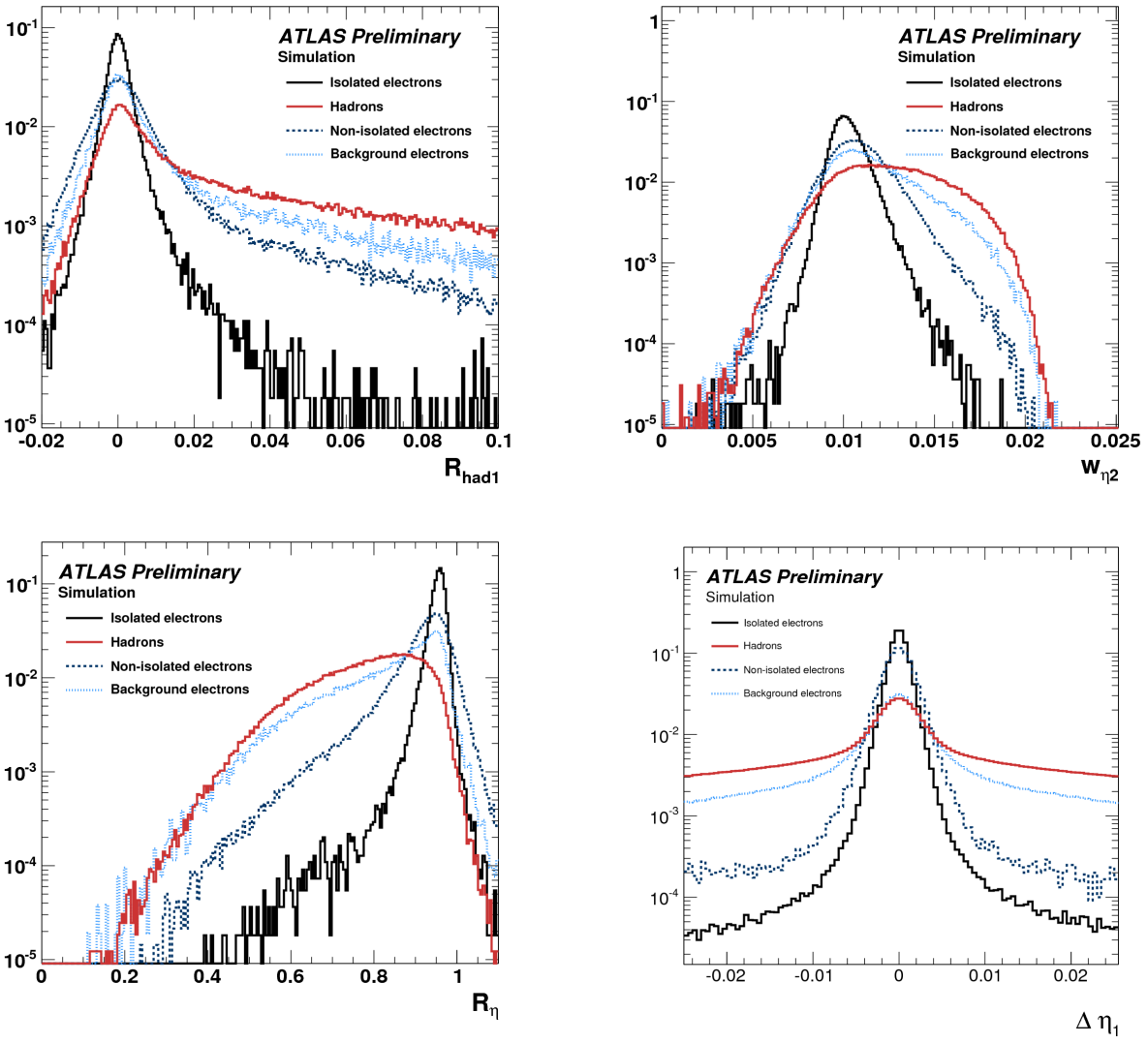

Figure 3.1: Electron identification variables [90]: hadronic leakage (R_{had1}), shower width in η ($\omega_{\eta 2}$) and ratio of energy in 3x7 over 7x7 cells (R_η) in the second sampling of the EM calorimeter, difference between the cluster and extrapolated track pseudorapidities ($\Delta\eta$). Several categories of reconstructed electrons are defined according to their matching with different simulated particles: true electrons arising from a Z or W boson (isolated e, in black), true electrons originating from b(c)-mesons (non-isolated e, in blue), true electrons coming from a Dalitz decay or a photon (background e, in light-blue), hadrons (in red).

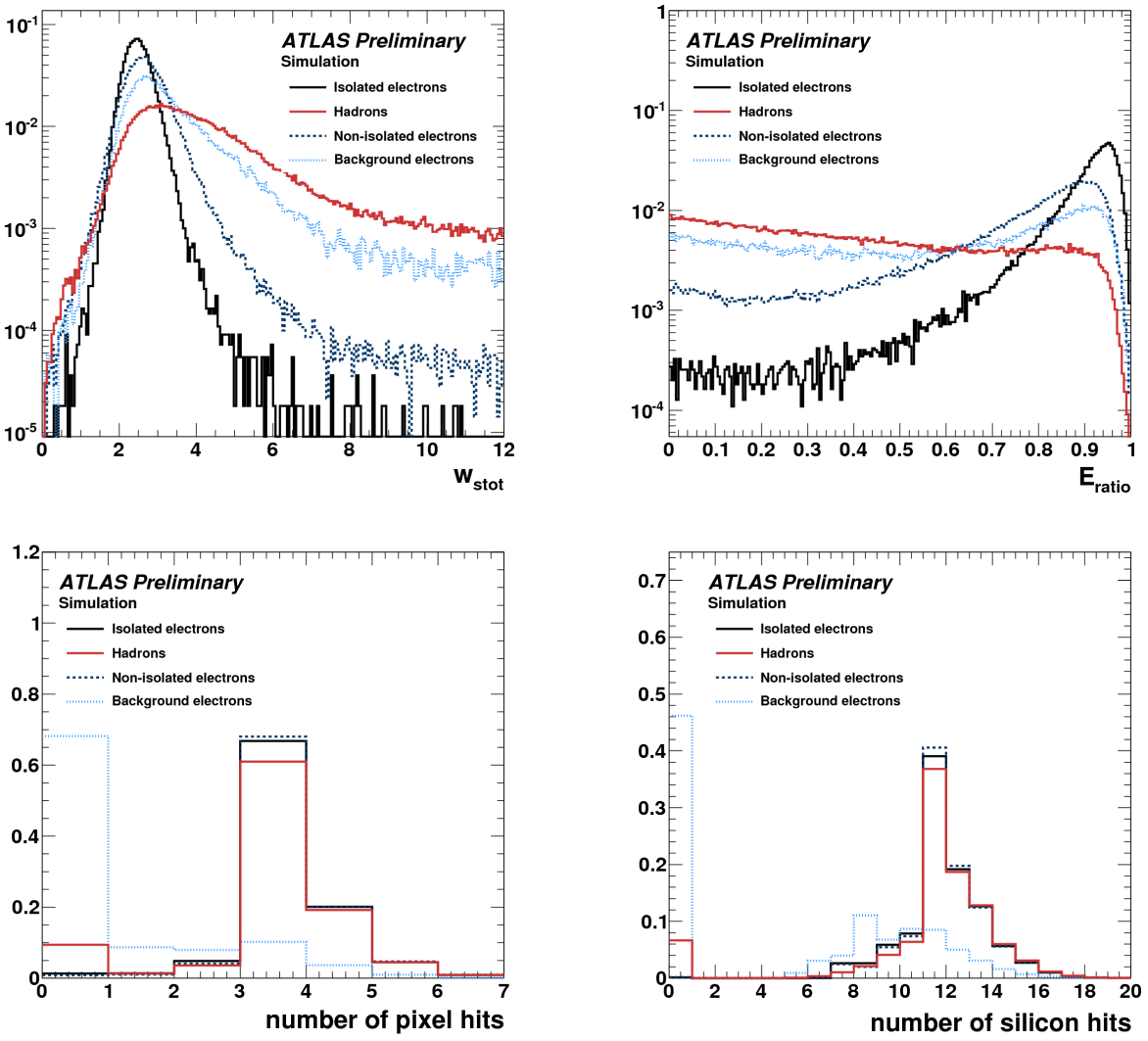

Figure 3.2: Electron identification variables [90]: shower width (ω_{stot}) and ratio of the energy difference associated with the largest and second largest energy deposit over the sum of these energies (E_{ratio}), both in the first EM calorimeter compartment; number of pixel and silicon hits. Several categories of reconstructed electrons are defined according to their matching with different simulated particles: true electrons arising from a Z or W boson (isolated e, in black), true electrons originating from b(c)-mesons (non-isolated e, in blue), true electrons coming from a Dalitz decay or a photon (background e, in light-blue), hadrons (in red).

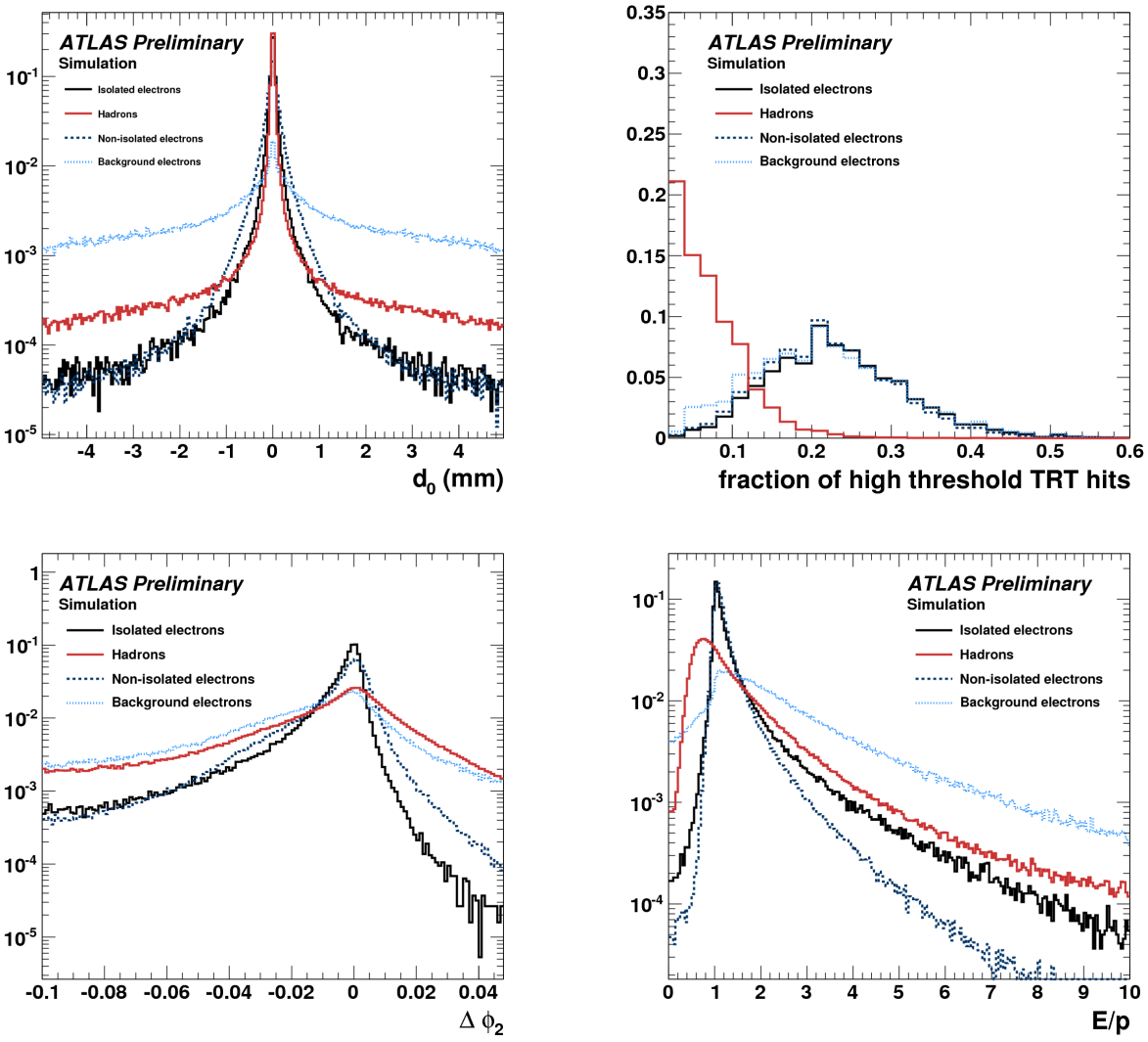

Figure 3.3: Variables used for the medium++ and tight++ electron identification [90]: transverse impact parameter (d_0), ratio of the number of high-threshold hits to the total number of TRT hits (f_{HT}), ratio of cluster energy to the track momentum (E/p) and difference in track and cluster azimutal angles ($\Delta\phi$). Several categories of reconstructed electrons are defined according to their matching with different simulated particles: true electrons arising from a Z or W boson (isolated e, in black), true electrons originating from b(c)-mesons (non-isolated e, in blue), true electrons coming from a Dalitz decay or a photon (background e, in light-blue), hadrons (in red).

Table 3.1: Definition of the variables used for the identification cuts of central ($|\eta| < 2.47$) electrons.

Type	Name	Description
Loose++ selection		
Hadronic leakage	R_{had1}	Ratio of E_T in the first layer of the hadronic calorimeter to E_T of the EM cluster (used over the range $\|\eta\| < 0.8$ and $\|\eta\| > 1.37$)
	R_{had}	Ratio of E_T in the hadronic calorimeter to E_T of the EM cluster (used over the range $0.8 < \|\eta\| < 1.37$)
Middle layer of EM calorimeter	R_η	Ratio of the energy in 3×7 cells over the energy in 7×7 cells centred at the electron cluster position
	$\omega_{\eta 2}$	Lateral shower width, $\sqrt{(\Sigma E_i \eta_i^2)/(\Sigma E_i) - ((\Sigma E_i \eta_i)/(\Sigma E_i))^2}$, where E_i is the energy and η_i the pseudorapidity of cell i and the sum is calculated within a window of 3×5 cells
Strip layer of EM calorimeter	ω_{stot}	Shower width, $\sqrt{(\Sigma E_i (i - i_{max})^2)(\Sigma E_i)}$, where i runs over all strips in a window of $\Delta\eta \times \Delta\phi \approx 0.0625 \times 0.2$, corresponding typically to 20 strips in η, and i_{max} is the index of the highest-energy strip
	E_{ratio}	Ratio of the energy difference between the largest and second largest energy deposits in the cluster over the sum of these energies
Track quality	n_{pixel}	Number of hits in the pixel detector
	n_{Si}	Number of total hits in the pixel and SCT detectors
Track cluster matching	$\Delta\eta$	Tighter $\Delta\eta$ requirements
Medium++ selection (includes loose)		
Same variables of the loose++ identification, at tighter operating points.		
Track quality	d_0	Tighter transverse impact parameter requirement
	n_{BL}	Number of total hits in the pixel B Layer (for the 2012 dataset, before the cut $\in$ the tight++ selection)
TRT	f_{LT}	Ratio of the number of low-threshold hits to the total number of hits in the TRT
EM calorimeter	$f3$	Ratio of energy deposit in 3rd sampling over all energy (for the 2012 dataset)
Tight selection (includes medium)		
Same variables of the medium++ identification, at tighter operating points.		
Track cluster matching	$\Delta\phi$	$\Delta\phi$ between the cluster position in the strip layer and the extrapolated track
	E/p	Ratio of the cluster energy to the track momentum
Conversion	*conv. bit*	Veto on electron candidates matched to reconstructed photon conversions

3.1.4 Energy scale

Even if the electron energy reconstructed in the electromagnetic calorimeter ($E^{measured}$) integrates a preliminary MC-based correction to account for the losses due to dead materials or cluster leakages, a slight miscalibration is still present:

$$E^{measured} = E^{true}(1 + \alpha_i). \tag{3.1}$$

The energy-scale correction factors α_i can be determined from real data enriched in $Z^0 \rightarrow e^+e^-$ or $J/\psi \rightarrow e^+e^-$ events by a fit minimizing the negative unbinned log-likelihood:

$$-ln(\mathcal{L}) = \sum_{i,j} \sum_{k=1}^{N_{jv}^{events}} -ln(\mathcal{L}_{ij}) \left(\frac{m_k}{1 + \frac{\alpha_i \alpha_j}{2}} \right), \tag{3.2}$$

and used later to correct the simulation. N_{jv}^{events} denotes the total number of decays, i and j the regions where the two electrons are detected, m_k their invariant mass, and the likelihood function L_{ij} the probability density function quantifying the compatibility of an event with the Z^0 (J/ψ) lineshape. The latest published results [88] disclose experimental energy-scale correction factors computed with 2010 collisions, which took place at $\sqrt{s} = 7$ TeV and corresponded to a luminosity of 40 pb^{-1}; as Fig. 3.4(a) demonstrates, α_i derived from Z^0 decays are within $\pm$ 2% in the barrel region and $\pm$ 5% in the the forward regions, oscillating a lot in correspondence to the transitions between different calorimeter systems. The variations within a determined system depend instead on the amount of material between the collision point and the calorimeter, on the high-voltage corrections, on the effects related to the electronic calibration and the lateral leakage. Once this in-situ energy calibration applied, the same α_i calculation is validated using J/ψ decays: for almost every pseudorapidity region the corrections are found to be close to zero, as reported in Fig 3.4(b). The plot provides also a representation of the total uncertainty related to this energy correction, which varies from 0.3% to 1.6 % for central electrons; it accounts for the statistical limitations due to the size of the event sample, the imperfect knowledge of the material traversed by the electrons, the presampler detector energy scale, the non-linearities in the electronic readouts, as well as the background contamination.

A complementary calibration method measures the ratio of the energy determined in the electromagnetic calorimeter, to the momentum extracted in the inner detector for the high statistic sample $W \rightarrow e\nu$. As Fig. 3.5(a) shows, E/p is close to unity, with a significant tail due to Bremsstrahlung occurring in the tracker; the unbinned distribution is fitted by a Crystal Ball function, and the correction factors are measured via the equation:

$$E/p_{data} = E/p_{MC}(1 + \alpha_{E/p}). \tag{3.3}$$

Fig. 3.5(b) illustrates that after the baseline calibration, the $\alpha_{E/p}$ factors are almost zero in every pseudorapidity region, the big fluctuations originating mainly from the fit procedure, the description of the material in front of the EMCal, the background contamination and the track momentum measurement.

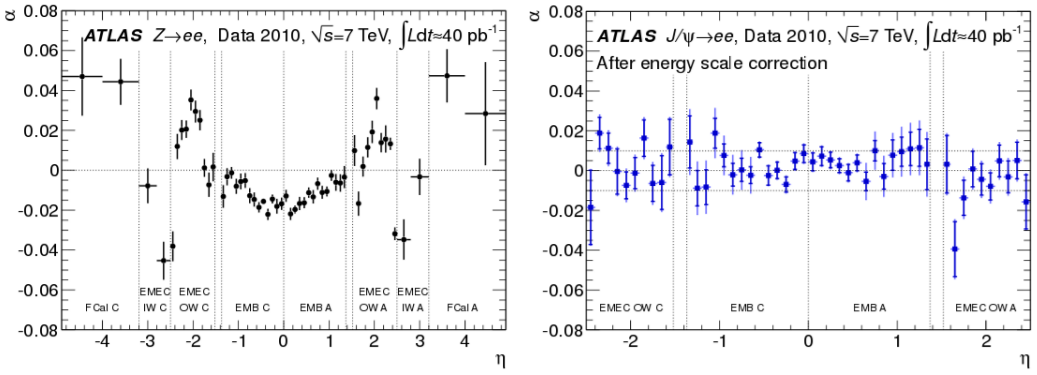

(a) (b)

Figure 3.4: (a) Energy scale factors as a function of the pseudorapidity of the electron cluster derived from the fit to $Z \to ee$ data; the uncertainties are statistical only. (b) Energy scale factors as a function of the pseudorapidity of the electron cluster derived from the fit to $J/\psi \to ee$ data, after the calibration obtained with (a); the inner error bars show statistical uncertainties, while the outer error bars include all systematic uncertainties [88].

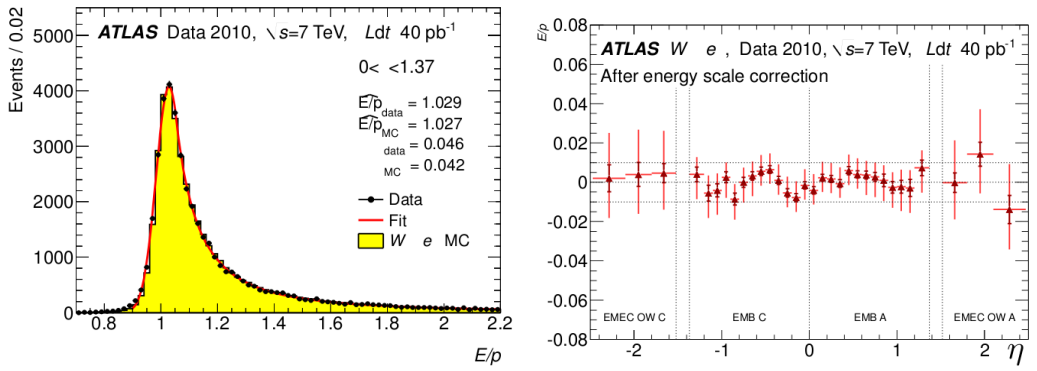

(a) (b)

Figure 3.5: (a) E/p distribution of electrons and positrons emitted via $W \to e\nu$ for $0 < \eta < 1.37$ in data (full circles) and simulation (filled histogram). The result of the fit with a Crystal Ball is shown with a full red line. (b) $\alpha_{E/p}$ scale factors as a function of the pseudorapidity of the electron cluster derived from the E/p fit, after the baseline calibration; the inner error bars show statistical uncertainties, while the outer error bars include all systematic uncertainties [88].

3.1.5 Energy resolution

The parametrization of the fractional electron energy resolution has already been provided in Section 2.3.3, as function of a stochastic term a, a noise term b and a constant term c:

$$\frac{\sigma(E)}{E} = \frac{a}{\sqrt{E(GeV)}} \oplus \frac{b}{E(GeV)} \oplus c^{1}. \tag{3.4}$$

The latest puplic results, that as mentioned before concern the 2010 data, provide only a measurement of the unique parameter which is non negligible at the energy scale of the analyses presented in this manuscript, c. The latter is determined from a comparison of the measured and predicted di-electron invariant mass resolution from $Z^0 \to e^+e^-$ decays, taking the values extracted from simulation for a and b. A Breit-Wigner convolved with a Crystal Ball function in the range 80-100 GeV for two central electrons (75-105 GeV for a central and a forward electron), is employed to fit the data distribution and extract:

$$c_{data} = \sqrt{2\left(\left(\frac{\sigma}{m_Z}\right)^2_{data} - \left(\frac{\sigma}{m_Z}\right)^2_{MC}\right) + c^2_{MC}}. \tag{3.5}$$

In Eq. 3.5 $c_{MC} \sim 0.5\%$ from simulation, m_Z denotes the boson mass and σ the gaussian component of the experimental resolution. The results obtained for the effective constant term c_{data} have been shown in Table. 2.3.3 for several components of the electromagnetic calorimeter; they are in general larger than predicted, taking nominal values from 1.2% to 2.5% . Such energy resolution parametrization is finally used to implement corrections (smearing) for the simulated events containing electrons.

3.1.6 Detection efficiency

The process of electron detection in ATLAS proceeds through the several phases enunciated above; when the online trigger selects events containing electrons, these particles are reconstructed and several variables tested in order to provide preliminary identification categories. At this stage, however, the number of electron events predicted by simulation does not match perfectly the experimental amount of candidates, despite the electromagnetic in-situ calibration; MC samples need to be corrected to reproduce the measured data efficiencies (usually as a function of the electron kinematic variables, such as η or E_T). For a single electron in the final state one can write the correction factor as the product of several ratios of data-to-MC efficiencies: the one related to the event preselection cuts, to the matching of an electromagnetic cluster with a reconstructed track in the fiducial region of the detector, the efficiency of the identification cuts relative to the reconstructed objects, and of the trigger with respect to all reconstructed and identified electron candidates. Such decomposition:

$$C = SF(\epsilon_{event}) \times SF(\epsilon_{reco}) \times SF(\epsilon_{ID}) \times SF(\epsilon_{trigger}) \times SF(\epsilon_{isolation}) \tag{3.6}$$

[1]The symbol $\oplus$ represents the quadratic sum.

allows to estimate each term independently via the tag-and-probe technique; this method relies on the selection of a clean and unbiased sample of "probe" electrons, using "tag" requirements on another object present in the event; concretely, one can, for example, analyze $Z^0 \to e^+e^-$ or $W \to e\nu$ decays, determining the fraction of loose electrons passing the same selection cuts than the tight electrons or neutrinos that allowed the detection. In this paragraph we will consider separately each term, apart from ϵ_{event} ; their nominal values are applied as scale factors, and the corresponding uncertainties propagated in the s-channel cross section measurements.

The reconstruction efficiency is measured via tag-and-probe methods using Zee, $J/\psi ee$, $We\nu$ samples; the results are reported in Figs. 3.6(a), 3.6(b) for the complete 2011 and 2012 datasets. The improvements spotted in 2012 depend on the optimised electron GSF track fitter, and on the technique aimed at favouring the primary electron track in case of cascades due to Bremsstrahlung. The total uncertainty associated to the reconstruction efficiency correction at 7 TeV varies from few percents in the lowest E_T bin, to 0.5% for transverse energies above 35 GeV; at 8 TeV, instead, it is between 0.5 % and 1.5 % for $E_T < 20$ GeV and below 0.5 for larger transverse energies.

The identification efficiencies obtained via tag-and-probe method applied to Zee samples are instead shown in Figs. 3.7(a), 3.7(b) for the 2011 and 2012 datasets. They refer to slightly different identification criteria, due to a re-optimization applied in 2012 with the goal of mitigating the impact of the harsher pile-up conditions. Furthermore, an additional operating point, the $Multilepton$, has been developed in the context of searches for multi-lepton final states, exploiting specific cuts on high/low Bremsstrahlung categories using GSF information. At 7 TeV, the total uncertainty corresponding to the identification efficiency scale factor ranges from 5-10% for $E_T < 20$ GeV, to few per mil for higher transverse energies; at 8 TeV it is around 5% for $E_T < 20$ GeV and 1-2% for E_T above that threshold.

Also the trigger efficiency is evaluated with a tag-and-probe method on Zee events, with respect to offline electrons passing the $medium++$ identification.
During the 2011 data-taking, several triggers were used due to changing pile-up conditions. From period A to J, the requirements for electrons firing L1 and High Level Trigger were, respectively, $E_T > 14$ GeV and $E_T > 16$ GeV; the corresponding signature name was EF_e20_medium. During period K, the transverse energy threshold was increased to 16 GeV at L1 and 22 GeV at HLT, producing EF_e22_medium electrons. For L and M periods, finally, the trigger was seeded by L1 items with η-dependent thresholds and a hadronic leakage requirement to define $EF\_e22vh\_medium1$ electrons.
For the 2012 dataset, on the other hand, two triggers were combined in a logical OR to improve the efficiency at high E_T : ($e24vhi\_medium1$ or $e60\_medium1$). The first one was based on a η dependent threshold on transverse energy, together with additional requirements on the longitudinal shower shape and hadronic leakage at L1; at HLT, a further E_t threshold of 24 GeV and the track isolation were compelled. The

second trigger provided a less stringent identification selection but required 60 GeV deposited in the calorimeter at HLT. The efficiencies corresponding to the trigger signatures used for the 7 TeV analysis are shown in Figs. 3.8(a), 3.8(b) as a function of the electron transverse energy and pseudorapidity; their total uncertainty varies from 5-10% to 1%. Similarly, the 8 TeV efficiencies are illustrated in Figs. 3.9(a), 3.9(b) for the combination with the logical OR of the two trigger signatures described above; the corresponding uncertainty ranges from about 5% to 1%.

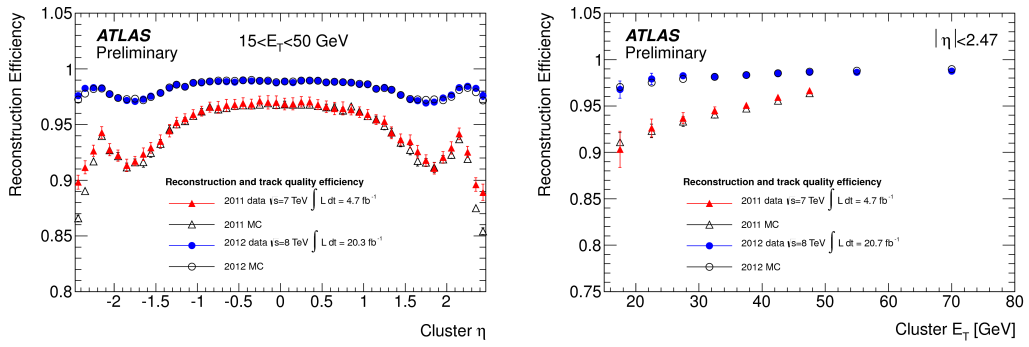

(a) (b)

Figure 3.6: (a) Efficiency of electron reconstruction and track quality is shown for the 2011 (red triangles) and 2012 (blue circles) datasets as a function of the cluster $|\eta$ (b) and E_T. Data are described by filled markers, while simulation by open markers; for both the statistical and systematic uncertainty is reported [91].

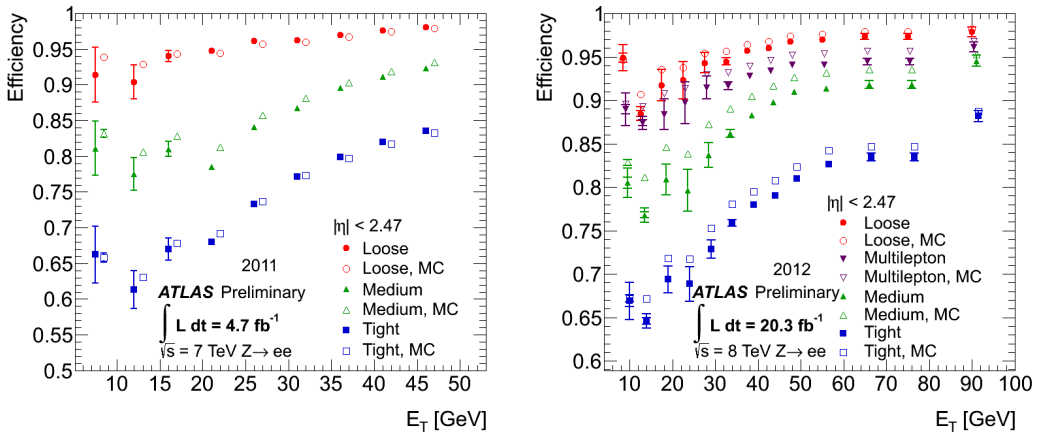

(a) (b)

Figure 3.7: (a) Identification efficiency of electrons from Zee decays for the 2011 Loose, Medium and Tight set of cuts and (b) for the 2012 Loose, Medium, Tight and Multilepton set of cuts as a function of the reconstructed energy for $|\eta|$ <2.47. In both plots, data are described by filled markers, simulation by open marks, and the error bars represent the statistical and systematic uncertainty [91].

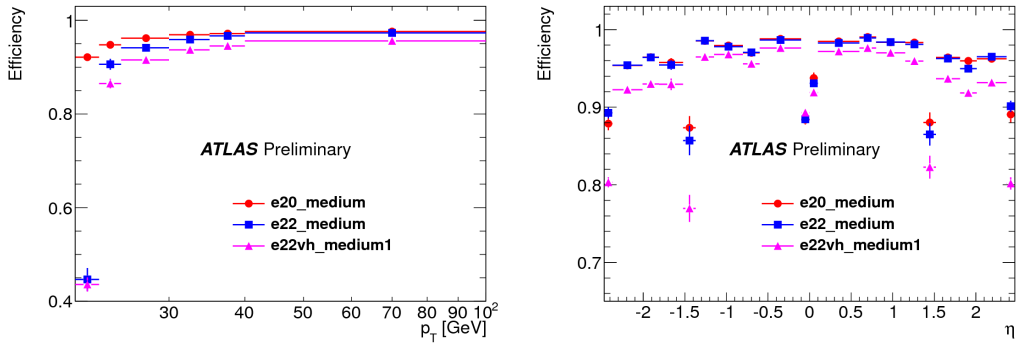

(a) (b)

Figure 3.8: (a) Efficiencies as a function of the offline *medium++* electron η for the $e20\_medium$, $e22\_medium$ and $e22vh\_medium1$ triggers and (b) as a function of the offline-reconstructed electron pseudorapidity. The vertical bars represent the total uncertainty [87].

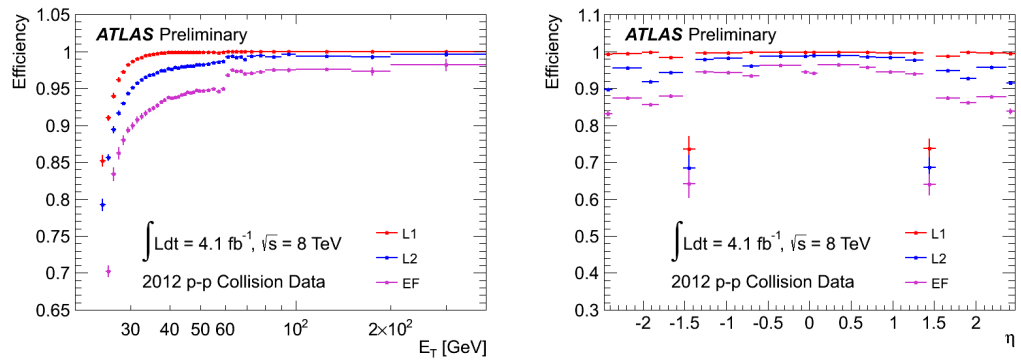

(a) (b)

Figure 3.9: (a) L1, L2 and EF trigger efficiencies for the single electron triggers used to select medium and high E_T electrons: $e24vhi\_medium1$ OR $e60\_medium1$ are shown as a function of the offline-reconstructed electron transverse energy (b) and pseudorapidity. The vertical bars represent the total systematic uncertainty [92].

3.2 Muons

Muons are highly penetrating particles precisely reconstructed and identified in ATLAS via the muon spectrometer (MS) and the inner detector (ID); additional information on the energy deposited in the calorimeter may contribute, to a lesser extent, to their detection.

3.2.1 Trigger

Since final state muons represent distinctive signatures for many physics studies performed with the collisions of high energy protons, their trigger selection is essential. At L1, the signals from fast-response muon trigger detectors are processed by custom built hardware; they carry the information on the estimated muon p_T, as well as the one on the detector position. Then, L2 trigger selects precisely the region in which the interesting features reside (RoI), and performs a fast track reconstruction with a simple algorithm. Finally, the EF makes use of the offline muon reconstruction software to refine the trigger decision to use the full detector information.

3.2.2 Reconstruction

Several reconstruction criteria have been pinpointed according to the available information from each sub-detector system; this led to the definition of four muon categories with different prerogatives [93] [94].

- *Standalone muons* (SA) are reconstructed only via the trail released in the muon spectrometer. By extrapolating the MS track back to the point of closest approach to the beam line, taking into account the multiple scattering and the energy loss in the calorimeters, the direction of flight and the impact parameter can be derived.

- *Segment-tagged muons* (SM) are identified when an inner detector track extrapolated to the muon spectrometer is associated with at least one MDT or CSC track segment. The parameters associated to such candidates are, however, only those estimated in the inner detector.

- *Combined muons* (CB) are obtained by combining two tracks, independentely reconstructed in MS and ID. The muons parameters are defined either from a statistical combination of the two tracks, or from a refit of the full track, depending on the reconstruction chain which will be described in the following.

- *Calorimeter-tagged muons* (CaloTag) are described by an ID track matching an energy deposit in the calorimeter as expected from a minimum ionizing particle. This class is characterized by the lowest muon purity, but recovers acceptance in the uninstrumented region of the MS.

The reconstruction of the first three muon types is performed with two independent and complementary strategies based on distinct algorithm sequences: Chain 1 and 2.

Chain 1 relies on a statistical combination of the standalone and inner detector muons track parameters, by means of their covariance matrices.
More specifically, the reconstruction procedure begins with the local search, in a muon chamber, for the straight line track segments in the bending plane; these segments, connecting multiple MDT hits, are required to point towards the center of ATLAS. The hit coordinate in the non-bending plane is measured by the trigger chambers (TGC, RPC) or, if not available, extracted from the MDT drift time. When the examination is accomplished in every muon station, if at least two track segments are found in the same region of interest, they are combined using three-dimensional tracking in the magnetic field. The resulting *standalone* track is then extrapolated to the interaction point and associated, with tight matching requirements, to a track reconstructed in the inner detector to provide a *combined* muon candidate.

Chain 2 performs instead a global refit of the muon track using the hits from both the ID and MS subdetectors.
In the muon spectrometer the track identification is not based on a spatial association of hits, but on a pattern recognition performing a Hough transform [95] over the full space. Straight line segments are reconstructed in each muon station and associated among them from the outer to the inner regions according to two main requirements: the segments shall share the same pattern, and the global reconstructed trajectory has to be compatible with a curved track. Once that the *standalone* MS track has been reconstructed and refit to account for the traversed material effects, it is *combined* with an ID track via a dedicated fit procedure. This technique recovers the missing, or wrongly associated, hits in the muon spectrometer, and grants a stronger rejection power against fake associations and decays in flight.

3.2.3 Identification

The sample of reconstructed muons is composed by a big amount events arising from b and c hadrons semileptonic decays, as well as light mesons (i.e π or K) decays in flight. In order to select isolated muons produced by Z or W bosons, therefore, an additional series of identification cuts is performed. We will detail here only the ones aimed at refining the purest reconstruction category (combined muons) employed for the s-channel cross section analyses [96]. These particles are required to be within the inner detector acceptance ($|\eta| < 2.5$), have a transverse momentum greater than 20 GeV and belong to the plateau of the single muon trigger efficiency (which will be introduced later). A procedure of overlap removal with jets is used ($\Delta R(\mu, j) < 0.4$), together with a more generic isolation requirement, which has a different definition in the 7 TeV and 8 TeV analyses. In 2011, the sum of the transverse energy in a cone of $\Delta R = 0.2$ around the muon was compelled to be smaller than 4 GeV, and the sum of the transverse momentum of ID tracks in a cone of $\Delta R = 0.3$ around the muon had to be lower than 2.5 GeV; then, in order to improve the pile-up robustness, a mini-

isolation criterion was introduced letting the radius of the cone vary as a function of the muon p_T. In addition to that, muon candidates are requested to pass a sequence of quality cuts concerning the inner detector track, which are summarized hereafter:
- B-layer hits ≥ 1 in active modules,
- sum of pixel hits and dead pixel sensors crossed by the track ≥ 1,
- sum of SCT hits and dead SCT sensors traversed ≥ 6,
- sum of missing pixel and SCT layers ≤ 1,
- if $\eta_{MS} < 1.9$, total number of TRT hits ≥ 5,
- if $n_{TRT}^{tot} > 5$, fraction of outlier [2]TRT hits $\leq$ than 90%.

3.2.4 Momentum scale and resolution

Since the momentum resolution and scale are crucial parameters for the muon detection, it is worthy to correct the simulation in order to reproduce correctly the collected data; this is usually realized via data-driven techniques which are based on the analysis of the di-muon decays of Z bosons, J/ψ or Υ resonances.
In order to reflect the real momentum resolution, which is dominated by the inner detector in the range of interest of the reported analyses, it is necessary to parametrize it as a function of two main factors: on one hand the intrinsic resolution of the detector sub-components together with any residual misalignement, on the other the effects of multiple scattering. The momentum scale miscalibration, instead, can be extracted by determining the average deviation of the di-muon invariant mass from the world-average $m(Z)c^2$, $m(J/\psi)c^2$, $m(\Upsilon)c^2$ measurements. By considering these distinct aspects, the simulated momentum reconstructed in the ID and MS can be corrected with the following equation which essentially encompasses a shift and a smearing:

$$p_T^{Cor,det} = p_T^{MC,det} \times s^{det}(\eta)(1 + \Delta a^{det}(\eta)G(0,1) + \Delta b^{det}(\eta)G(0,1)p_T^{MC,det}); \qquad (3.7)$$

the index *det* represents here the inner detector or the muon spectrometer [3] , $G(0,1)$ a normally distributed random variable with mean 0 and width 1, and s^{det}, Δa^{det}, Δb^{det} denote the the correction factors for momentum scale, "intrinsic resolution", "multiple scattering resolution", respectively. The correction parameters are determined in 16 different pseudorapidity regions of the detector via a MC template fit, in an iterative way to improve the stability of the results. The term describing the resolution correction due to multiple scattering is shown in Fig. 3.10(a) for the MS, while the one representing the spacial resolution appears in Fig. 3.10(b) for the ID.

[2] TRT outliers are measurements associated to the ID track that either appears in a drift tube not crossed by the track, or belongs to a set of TRT measurements that failed to form a smooth trajectory together with the Pixel and SCT measurements.

[3] The corrected p_T for the muon is actually obtained as the average of the ID and MS corrections, wheighted by the inverse square of their ID and MS momentum resolution:

$$p_T^{Cor} = p_T^{MC}\left(1 + \frac{\frac{\Delta^{MS}}{\sigma^{2MS}} + \frac{\Delta^{ID}}{\sigma^{2IS}}}{\frac{1}{\sigma^{2MS}} + \frac{1}{\sigma^{2IS}}}\right).$$

The main systematic uncertainty derives from the variation of the mass window for the particle decaying into the pair of muons. Since independent measurements constrain Δa^{ID} and Δb^{MS} to be small, these remaining terms are set to zero and not extracted from the fit. The momentum scale factors s^{ID} and s^{MS} are illustrated in Figs. 3.11(b), 3.11(a), with small systematic uncertainties of 0.1-0.2% introduced mostly to cover a possible momentum dependence on the correction. To conclude, Figs. 3.12(a) 3.12(b) give an overview of the global effect of the momentum resolution and scale corrections. The di-muon invariant mass of combined isolated muons with $p_T > 25$ GeV for simulated $Z^0 \to \mu^-\mu^+$ decays plus background events is compared to data; on the right, the application of the just described factors improves considerably the agreement over the full energy range. All the reported plots refer to the 2012 data-taking, for a corresponding integrated luminosity of 20.4 fb^{-1}; muons reconstructed with the Chain 1 algorithm are shown, but analogous results are found with the Chain 2 algorithm.

An alternative method based on the muon track fit uncertainty $\sigma_{q/p}$ has been employed to validate the previous correction factors estimates. Since MC simulation studies showed that the inverse of the reconstructed momentum $1/p_{rec}$ is gaussian distributed around the true inverse muon momentum $1/p_{gen}$ in good approximation, the systematic shift of p_{rec} with respect to p_{gen} and the underestimation of the resolution can be corrected via an $\alpha(\eta)$ and a $\beta(\eta)$ factor, respectively, in this way:

$$T(1/p_{rec}, 1/p_{gen}) = \frac{1}{\sqrt{2\pi}\beta(\eta)\sigma_{q/p}} exp\left[\frac{(1/p_{rec} - 1/\alpha(\eta)p_{gen})^2}{2(\beta(\eta)\sigma_{q/p})^2}\right]. \quad (3.8)$$

Due to the good momentum resolution, also the muon pair invariant mass $m_{\mu\mu}$ is gaussian distributed around its true value m_{gen}, with a resolution $\sigma_{\mu\mu}$ varying from event to event according to the configuration of the muons in $\eta - \phi - p_T$ space. This means that more precisely $m_{\mu\mu}$ is a superposition of Gaussian distributions with different variances:

$$T(m_{\mu\mu}, m_{gen}) = \int_0^\infty f(\sigma^2_{m_{\mu\mu}}) \frac{1}{\sqrt{2\pi}\beta(\eta)\sigma_{m_{\mu\mu}}} exp\left[\frac{(m_{\mu\mu} - \alpha(\eta)m_{gen})^2}{2(\beta(\eta)\sigma_{m_{\mu\mu}})^2}\right] d\sigma^2_{m_{\mu\mu}}. \quad (3.9)$$

A fit of the invariant mass spectrum in $Z^0 \to \mu^-\mu^+$ events with a convolution of the generated invariant mass and the di-muon resolution of eq. 3.8, allows to extract the $\alpha(\eta)$ and $\beta(\eta)$ parameters and the calibration of the response function. The mass and momentum scale factors agree at a level of 0.05%, while the mass and momentum resolution factors are compatible at a level of 3% ; these values are thus assigned as relative total uncertainty on the fit results for the two parameters.

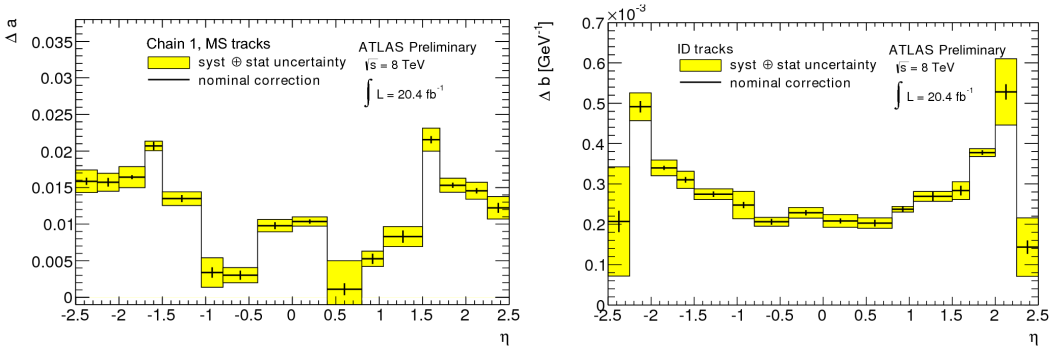

(a) (b)

Figure 3.10: (a) Δa resolution correction term for the MS (b) and Δb resolution correction term for the ID; both are derived from $Z^0 \rightarrow \mu^-\mu^+$ data for the Chain 1 reconstruction and should be applied in MC samples. The total (statistical and systematic) uncertainty is shown in yellow [93].

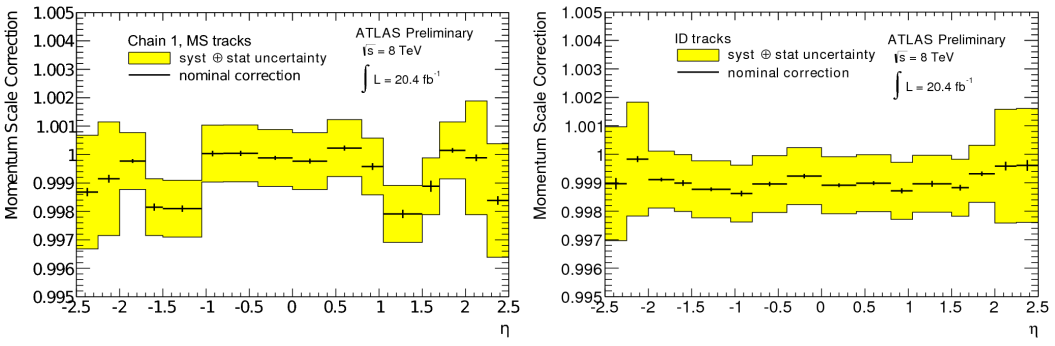

(a) (b)

Figure 3.11: (a) MS (b) and ID momentum scale correction; both are derived from $Z^0 \rightarrow \mu^-\mu^+$ data for the Chain 1 reconstruction and should be applied in MC samples. The total (statistical and systematic) uncertainty is shown in yellow [93].

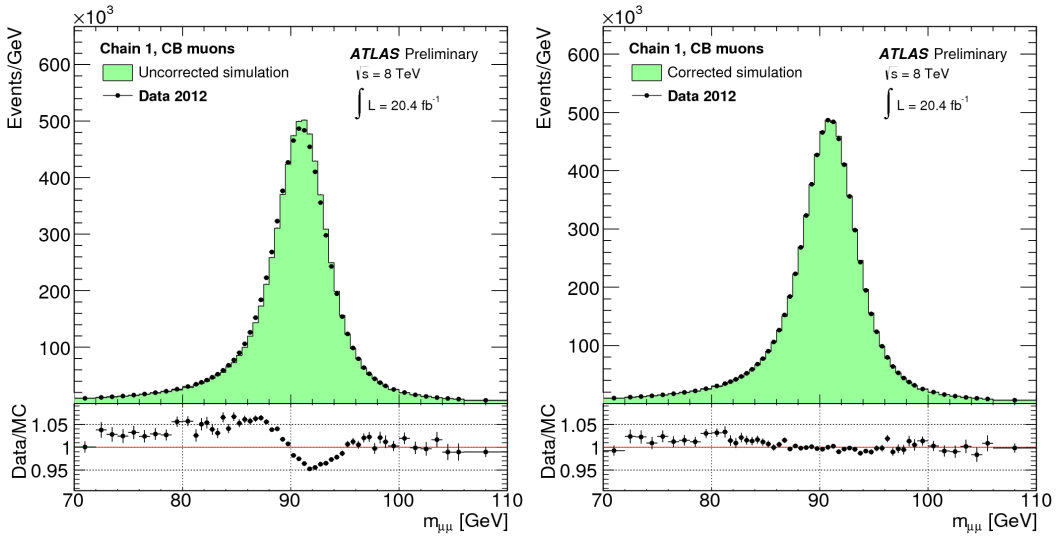

(a) (b)

Figure 3.12: (a) Di-muon invariant mass [93] for 2012 data (black points) and simulation (filled histograms) of $Z^0 \rightarrow \mu^-\mu^+$ plus background events without (b) and with the correction scale factors applied [93].

3.2.5 Detection efficiency

Similarly to what is explained in Section 3.1.6, simulated events containing isolated muons passing the reconstruction, identification and trigger selections should be somehow rescaled to match the number of observed events by data-to-MC efficiency ratios.

The reconstruction efficiency of the different muon types can be decomposed in the product of the reconstruction efficiency in the inner detector, the reconstruction efficiency in the muon spectrometer, and the matching efficiency between the two measurements that are performed independently [4]. The three contributions are measured via the tag-and-probe method previously introduced, on an enriched and purified sample of $Z^0 \rightarrow \mu^-\mu^+$ events; the two candidates are essentially required to have opposite sign, a transverse momentum greater than 20 GeV and an invariant mass within 10 GeV from the Z-boson pole (a more precise description of the selection cuts can be found in [97]). The "tag" object is a good quality combined muon which triggers the readout of the event, while the nature of the "probe" depends on the measurement realized: standalone or combined muons are used to evaluate the inner detector or calorimeter efficiencies, CaloTag muons [5] or ID tracks are employed to compute the muon spectrometer and the matching efficiencies.
Figs. 3.13(a), 3.13(b) represent the global reconstruction efficiency for a combined muon as a function of its pseudorapidity, computed with 2011 data corresponding to

[4] In the case of Chain 2, this last term includes also the refitting procedure.

[5] Since 2012 CaloTag muons replaced ID track probes, since this choice reduces the background by an order of magnitude without biasing the efficiency measurement.

collisions which took place at a center of mass energy of 7 TeV; the nominal value is typically above 95%, but it drops at $\eta \sim 0$, as in this region the MS is only partially furnished with muon chambers to provide space for services, and at $|\eta| \sim 1.2$, because the transition regions between barrel and end-caps are poorly equipped. Since for these pseudorapidity values no standalone momentum measurement is available, the CB muon efficiency is decreased. The effect is less evident for Chain 2 CB muons as the fit procedure includes the recovery of missing spectrometer hits, and thus allows to reconstruct those particles even from MS tracks without a momentum measurement (such as found in the transition regions). Further experimental results show that the spotted efficiency losses can be be fixed when considering combined muons together with standalone muons; $\epsilon(CB+ST)$ is thus constant over all the pseudorapidity range (except 0) and, as well, independent on the transverse momentum, as predicted. For Figs. 3.14(a), 3.14(b), which illustrate the reconstruction efficiency computed with 2012 data, almost the same considerations can be made. The systematic uncertainties, which are not depicted in the plots, arise from three main factors: the evaluation of the residual background contamination affecting the tag-and-probe sample (0.2%), the efficiency measurements at lower tansverse momenta (1% for $7 < p_T < 10$ GeV, 2% for $p_T < 7$ GeV) and at larger tansverse momenta (1 % $\times\ p_T$, for $p_T > 100$ GeV).

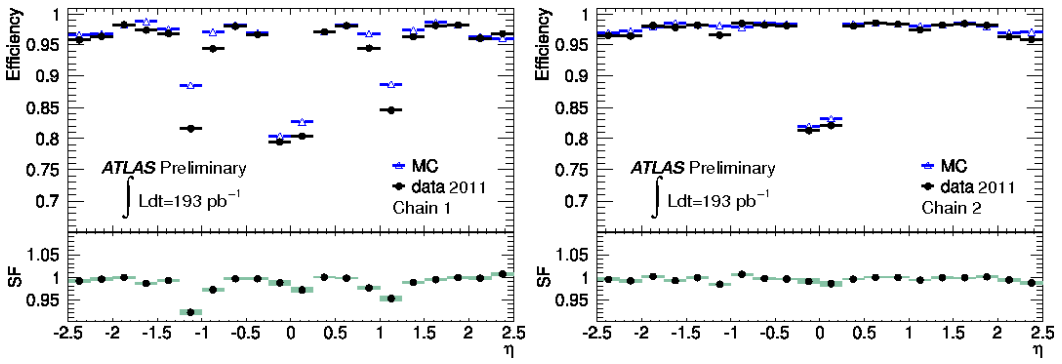

(a) (b)

Figure 3.13: (a) Reconstruction efficiency for Chain 1 (b) and Chain 2 combined muons as a function of η for simulation (open triangles) and data (black dots) collected in 2011 (the uncertainties are statistical only). The origin of the significant data/MC discrepancy in the regions corresponding to $|\eta| \sim 1.2$ and $|\eta| \sim 1.0$ is still under investigation. ID muons are used as "probes" [98].

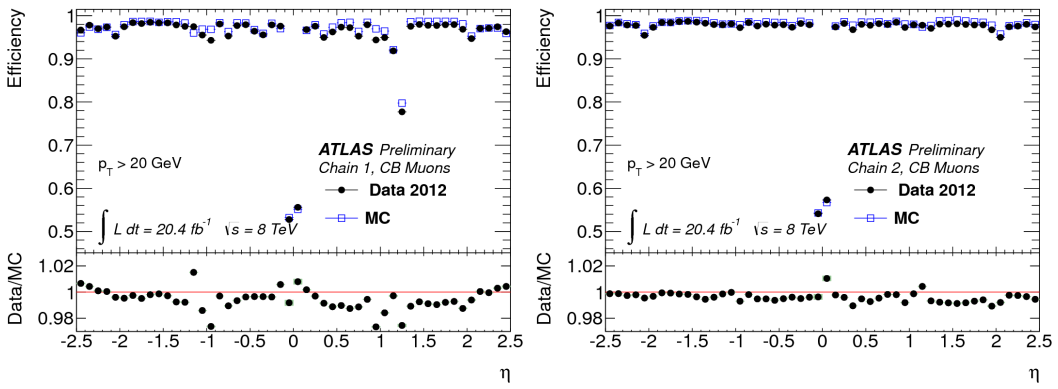

(a) (b)

Figure 3.14: (a) Reconstruction efficiency for Chain 1 (b) and Chain 2 combined muons as a function of η for simulations (open triangles) and data (black dots) collected in 2012. The origin of the large data/MC discrepancy in the regions corresponding to $|\eta| \sim 1.2$ and $|\eta| \sim 1.0$ is still under investigation. CaloTag muons are used as "probes" [93].

The tag-and-probe method with Z boson decays is also applied in order to determine the muon identification efficiency and provide the corresponding scale factors to rescale the MC simulation. These are found to be within 1% of unity for the 2011 dataset and 0.5% for the 2012 dataset, for which the new mini-isolation criterion has been integrated.

Finally, the trigger efficiency is evaluated following the same approach. For the 7 TeV s-channel cross section analysis, two trigger menus were considered for muons: below the luminosity of $1.0 \times 10^{33} cm^{-2} s^{-1}$, the $mu18$ signature was employed to select single muons with transverse momentum greater than 18 GeV, which fired two (three) coincidence trigger stations in the barrel (endcap); above this luminosity threshold, the $mu18\_medium$ signature was introduced to identify single muons with transverse momentum greater than 18 GeV, and coincidence of hits in the three stations in both barrel and end-caps regions. The trigger efficiency is reported in Figs. 3.15(a), 3.15(b) as a function of the muon pseudorapidity for the $mu18\_medium$ case; "outside-in" label identifies a trigger chain which starts from the muon spectrometer track and proceeds towards the inner detector track. For transverse momenta greater than 20 GeV, $\epsilon_{trigger}$ has a plateau around 70% in the barrel and around 90% in the endcaps, with a systematic uncertainty of typically 1% per bin estimated by varying the tag-and-probe selection cuts. Such efficiency includes the geometric acceptance of the L1 trigger chambers, so it accounts for the limited geometric coverage of the barrel due to the crack at around η=0.
For the 8 TeV s-channel cross section analysis, two trigger menus which differed from each other in the p_T threshold and the application of the isolation criterion in EF, were combined in a logical OR. The mu_24i_tight signature was based on a transverse momentum threshold of 22 GeV at L1 and of 24 GeV at EF, intended to give a plateau

for offline $p_T \geq$25 GeV; at the same time, the ratio of the p_T sum of the ID tracks in a cone of $\Delta R = 0.2$ to the muon p_T was required to be less than 0.12. The *mu_36_tight* signature was similar, but with a greater transverse momentum threshold of 36 GeV at EF. The trigger efficiency for the combined chains, shown in Figs. 3.16(a), 3.16(b), still presents a plateau around 70% in the barrel and around 86% in the endcaps. The difference between the values obtained in the two pseudoraoidity regions is justified by a different geometric acceptance of the L1 trigger chambers, as for the 7 TeV case.

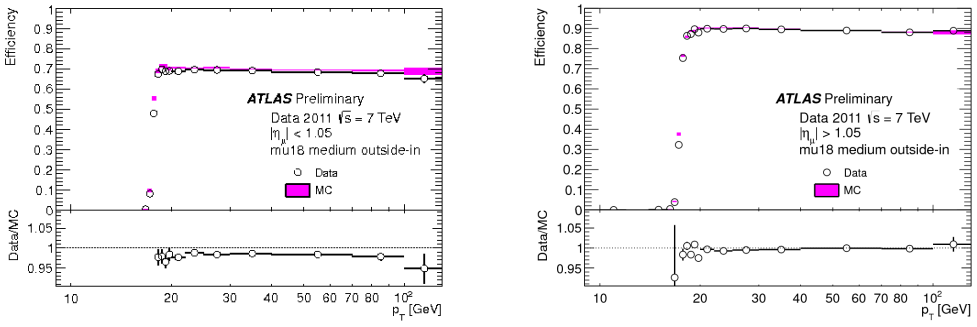

(a) (b)

Figure 3.15: (a) Efficiency of the 2011 *mu*18*_medium* single muon trigger, with respect to the offline reconstructed muons in the barrel region ($|\eta| < 1.05$). (b) and in the endcap regions ($|\eta| > 1.05$). Open circles represent data, while filled box MC events; the vertical error bars and the vertical size of the boxes show the statistical errors [99].

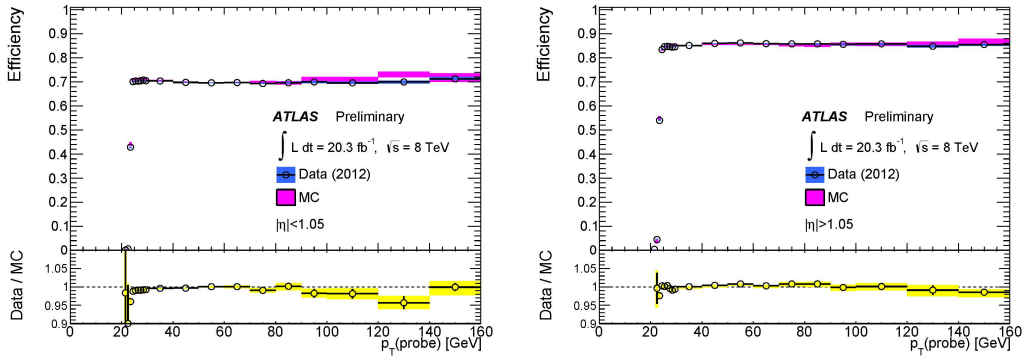

(a) (b)

Figure 3.16: (a) Efficiency of the 2012 single muon triggers *mu*24*i_tight* and *mu*36*_tight* convolved in a logical OR with respect to the offline reconstructed muons in the barrel region ($|\eta| < 1.05$) (b) and in the endcap regions ($|\eta| > 1.05$). Blue boxes represent data, pink boxes MC events; their vertical dimension stands for both statistical and systematic uncertainties [99].

3.3 Jets

Due to the confinement, the experimental signatures of quarks and gluons are assortments of color-singlet hadrons which tend to travel collinearly, forming a conic "spray" of particles called jets. Since the s-channel single top final state is characterized by the presence of two b-quarks, the analysis performance relies on the ATLAS proper jets reconstruction and precise modeling of their energy response.

3.3.1 Reconstruction

The mechanism of jet reconstruction can be essentially decomposed in two stages [100]: topoclusters [101] are built from topologically connected calorimeter cells containing a significant signal above noise, and later are grouped by a finding algorithm into jets.
When the energy deposited in a calorimeter cell is above four times the standard deviation of the energy distribution measured in random events, the clusterization seed is found; the neighboring cells presenting a signal over noise ratio greater than two are gradually merged in the three dimensions. In this new collection, the local maximum energy deposit will be set as a new seed, giving rise to the formation of another cluster, in an iterative way. For the 2011 dataset, the calibration was performed at electromagnetic (EM) scale, which correctly measures the energy deposited by particles produced in electromagnetic showers in the calorimeter. In 2012, instead, the local cluster weighting (LCW) method was used with the goal of improving the resolution, reducing fluctuations. LCW firstly arranges clusters as hadronic or electromagnetic, depending on the longitudinal shower depth and energy density, and then applies energy corrections derived according to this classification for single charged and neutral pion MC simulations. The effects of calorimeter non-compensation, of noise thresholds causing signal losses, and of energy lost in the non instrumented regions are taken into account.
In order to define jets that may be selected in the s-channel analysis from the topological clusters, the *anti-k_t* algorithm [102] is employed; jets are pinpointed when the distance between two topoclusters i and j is minimal:

$$d_{i,j} = min(k_{ti}^{-2}, k_{tj}^{-2}) \frac{\Delta_{ij}^2}{R^2}. \tag{3.10}$$

In Eq. 3.10, $\Delta_{ij} = \sqrt{(\eta_i - \eta_j)^2 + (\phi_i - \phi_j)^2}$, k_t is the transverse momentum and R the radius of the topocluster (set to 0.4). Such jets have conical shapes centered around the higher k_t cells, and an energy corresponding to the sum of the one collected in all the cells that identify the shower.

3.3.2 Identification

As previously described for leptons, jets reconstruction is followed by an identification procedure aimed at rejecting background candidates not originating from hard processes [103]. The latters can be produced in "beam-gas events", where one proton collided with the residual gas within the beam pipe, or "beam-halo events", i.e. caused by interactions in the tertiary collimators in the beam-line far away from the ATLAS detector; at the same time, cosmic ray muons overlapping in-time with collision events, as well as the calorimeter noise, may mimic particle showers. Several variables are analyzed in order to perform sequences of cuts and determine two quality selections; we will detail the most important in the following.
Sporadic noise bursts in the hadronic endcap calorimeter and coherent electronic noise in the electromagnetic calorimeter can lead to energy deposits not due to real particles, which may be reconstructed as fake jets. These phenomena, however, typically cause a characteristic pulse that can be used to distinguish them from ionization signals; the quadratic difference between the measured and the expected electronic response (Q^{LAr}_{cells}) is indeed a very discriminating variable. From this cell level observable, several jet level quantities can be derived: the average jet quality ($\langle Q \rangle$), defined as the energy squared weighted average of the pulse quality of the calorimeter cells in the jet, and normalized such that $0 < \langle Q \rangle < 1$; the fraction of the energy in LAr calorimeter cells with poor signal shape quality (f_Q^{LAr}) and the fraction of the energy in HEC calorimeter cells with poor signal shape quality (f_Q^{HEC}).
Cosmic rays or beam-induced backgrounds are caused by particles which do not come from the proton-proton collision at the center of the detector; they can be, therefore, spotted by energy deposits alligned in a different direction with respect to that of the main shower developement. The electromagnetic energy fraction (f_{EM}), the maximum energy fraction in any calorimeter layer (f_{max}) and the fraction of charged particles within the jet (f_{ch}) are used to suppress the fake jet contribution. Finally, to discriminate jet candidates which are not synchronous with the beam collision, the jet time (t_{jet}) is considered; this is computed from the time of the calorimeter cell energy deposits (recorded by the trigger) weighted by the square of the cell energies.

3.3.3 Energy scale

The energy of the jets reconstructed from topoclusters at the EM or LCW scale needs to be calibrated to the hadronic scale, and somehow connected to the energy of the parton which initiated the shower [104]. The procedure consists of four steps:

- The first correction is applied in order to account for the energy offset caused by pile-up interactions, comprising additional proton collisions in a recorded event (in-time pile-up) and past and future collisions influencing the energy deposited in the current bunch crossing (out-of-time pile-up). Scale factors are determined from MC simulations by studying how the difference between the true and the reconstructed jet p_T depend on the number of primary vertices, and on the expected average number of interactions per bunch crossing; such corrections are expressed in bins of jet pseudorapidity and transverse momentum.

- The position of the jet is then adjusted such that the cone formed by the topological clusters points towards the primary vertex of the interaction, instead of the geometrical center of ATLAS. By comparing the kinematics of reconstructed jets with the one of simulated "truth jets", a slight correction is applied to the pseudorapidity and the transverse momentum.

- In a similar way, the energy of the jet formed from topoclusters at EM or LCW scale is compared with the one of an isolated "truth jet" from a inclusive jet MC sample including pile-up events. The calibration is expressed as the inverse of the response $\mathcal{R} = E_{jet}^{EM/LCW}/E_{jet}^{truth}$ for various jet energies as a function of the pseudorapidity. Figure 3.17 gives an exemple for jets at the EM scale as a function of the jet pseudorapidity, and for various energies.

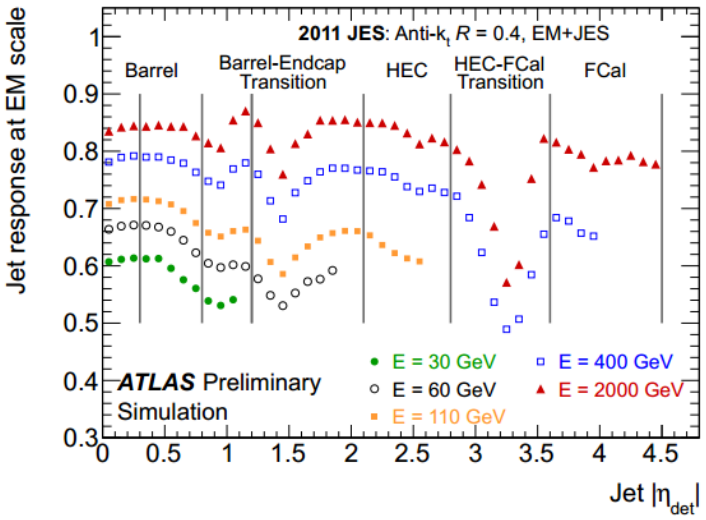

Figure 3.17: Average energy of jets formed from topo-clusters calibrated at EM scale with respect to the truth jet energy ($E_{jet}^{EM}/E_{jet}^{truth}$) as a function of η_{jet} (also indicated are the different calorimeter regions). The inverse of the response shown in each bin is equal to the average jet energy scale correction. This result is based on PYTHIA inclusive jet samples [104].

- Finally, a residual adjustement is applied to jets reconstructed in data via in situ techniques that exploit the p_T balance between the jet and a reference object; the ratio $\langle p_T^{jet}/p_T^{ref}\rangle_{data}/\langle p_T^{jet}/p_T^{ref}\rangle_{MC}$ is obtained from a combination of γ+jet, Z+jet and multijet final states and gives an estimate of the bias affecting the jet energy scale.

The most recent public result showing the total fractional JES uncertainty is plotted in Figs. 3.18(a), 3.18(b) for two pseudorapidity regions of interest for the analyses reported in this manuscript. The values, extracted from the 2010 dataset and MC simulations at $\sqrt{s} = 7$ TeV, range between 7% and 3% depending on the jet transverse momenum and pseudorapidity. Several separate contributions are presented:

- the calibration method (black cross in the plot), since non-closure effects can be spotted for example for kinematic observables of a calibrated jet which are not restored to that of the corresponding truth jet;
- the inaccurate calorimeter response to low p_T particles and neutral hadrons (blue open square);
- the inadequate detector simulation due to the limited knowledge of the exact geometry, mainly for what it concerns the presence of additional dead material (blue filled square), and of the modelling of the particles interactions;
- the discrepancies between the MC and the observed calorimeter cell noise thresholds, that can lead to biases in the jet reconstruction and calibration (red filled inverted triangle);
- the particular choice of the modelling of the hard subprocess and soft processes (red filled triangle) and of the parameters related to the jet fragmentation (black filled circle);
- the data driven in-situ intercalibration (green open circle);
- the modelling of the multiple proton proton collisions (pile up).

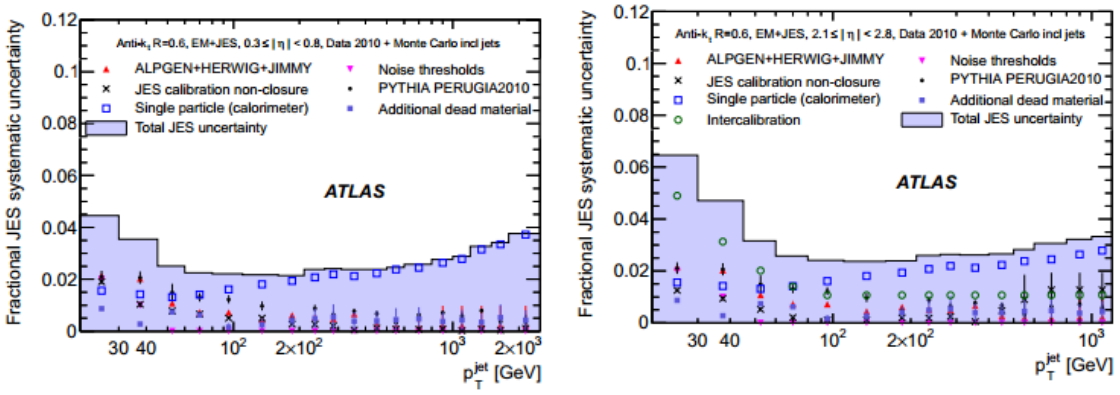

(a) (b)

Figure 3.18: (a) Fractional jet energy scale systematic uncertainty as a function of jets p_T in the pseudorapidity region $0.3 < |\eta| < 0.8$ in the barrel and (b) $2.1 < |\eta| < 2.8$ in the calorimeter endcaps. The total uncertainty is shown as the solid light shadow area, but the single uncertainties are also present [105].

3.3.4 Energy resolution

The jet energy resolution is currently determined in ATLAS via the dijet balance (2011 dataset) and the bisector techniques (2011 and 2012 datasets) [106].
The first one relies on the study of the asymmetry between the transverse momentum of two jets:

$$A(p_T^1, p_T^2) = \frac{p_T^1 - p_T^2}{p_T^1 + p_T^2}. \tag{3.11}$$

If the two jets are the unique highly energetic particles, for the conservation of the momentum in the transverse plane: $\overrightarrow{p_T^1} = -\overrightarrow{p_T^2}$; and if, moreover, they are measured in the same pseudorapidity region, it follows that $\sigma(p_T^1) = \sigma(p_T^1) = \sigma_{p_T}$. The resolution of the asymmetry previously introduced can therefore be expressed as a function of the fractional energy resolution:

$$\sigma_A = 2 \times \frac{\sqrt{\sigma^2(p_T^1) + \sigma^2(p_T^2)}}{\langle p_T^1 + p_T^2 \rangle} \sim \frac{\sigma_{p_T}}{\sqrt{2} p_T} \tag{3.12}$$

The simulated $A(p_T^1, p_T^2)$ distribution is segmented in pseudorapidity bins and modeled with a Gaussian centered in zero and with a width σ_A, that is determined by means of a fit to the data; this parameter used to characterize the asymmetry distribution allows, then, to determine the jet p_T resolution (Eq. 3.12). σ_A is actually recomputed to account for the effects due to the presence of additional soft jets in the sample, for a series of cut-off threshold values of their transverse momenta $p_{T,3}$. A soft radiation correction factor is obtained as $K_{soft}(p_T) = \left(\frac{\sigma_{p_T}}{p_T}\right)_{p_{T,3} \longrightarrow 0} / \left(\frac{\sigma_{p_T}}{p_T}\right)_{p_{T,3}<10 \text{ GeV}}$.
The bisector method, instead, is based on the definition of an imbalance vector $\vec{P}_T$, defined as the vector sum of the two leading jets transverse momenta in a di-jet event. This vector is projected along an orthogonal coordinate system in the transverse plane, (ϕ, η), where η is chosen in the direction that bisects $\Delta\phi_{12} = \phi_1 - \phi_2$ (the angle formed by $\vec{p}_T^1$ and $\vec{p}_T^2$) as depicted in Fig. 3.19. Even if for a perfectly balanced di-jet event, $\vec{P}_T = 0$, many sources give rise to fluctuations and thus to a non-zero variance of its ϕ and η components, which are denoted σ_ϕ and σ_η respectively. At particle level, $\vec{P}_T^{part}$ receives contributions from ISR mostly, which should be isotropic in the (ϕ, η) plane, leading to similar fluctuations in both components. It can be shown that:

$$\frac{\sigma(P_T)}{\langle P_T \rangle} = \frac{\sqrt{\sigma_\phi^{2\ calo} - \sigma_\eta^{2\ calo}}}{\sqrt{2}\,\langle P_T \rangle\,|\cos\Delta\phi_{12}|}. \tag{3.13}$$

The resolution is thus expressed in terms of calorimeter observables only, and soft radiation effects are minimized by subtracting in quadrature σ_η from σ_ϕ at calorimeter level. As Fig. 3.20 demonstrates, the simulation describes well the jet energy resolution measured in data, even if small differences are seen in the low p_T range. This plots refers to a measurement realized in 2011 using the EM+JES calibration in anti-k_T R=0.4 cluster jets, but similar results (not yet public) are obtained for 2012 data, using the LCW+JES calibration. The recommended procedure both for the

2011 and 2012 datasets is, hence, not to apply any smearing for the nominal samples, but just as a systematic uncertainty to cover the disagreement, which is below 10%.

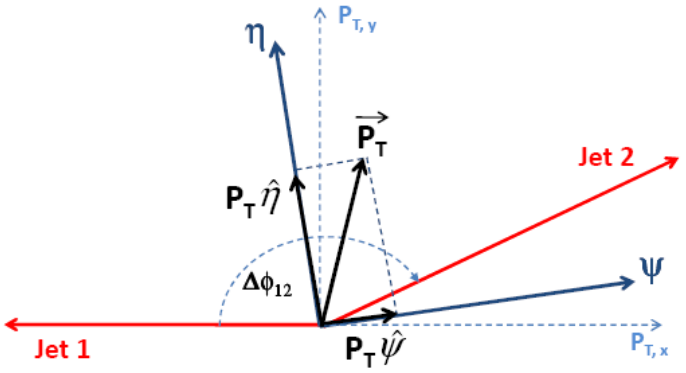

Figure 3.19: The η-axis corresponds to the azimuthal angular bisector of the dijet system in the transverse plane, it is orthogonal to the ϕ-axis.

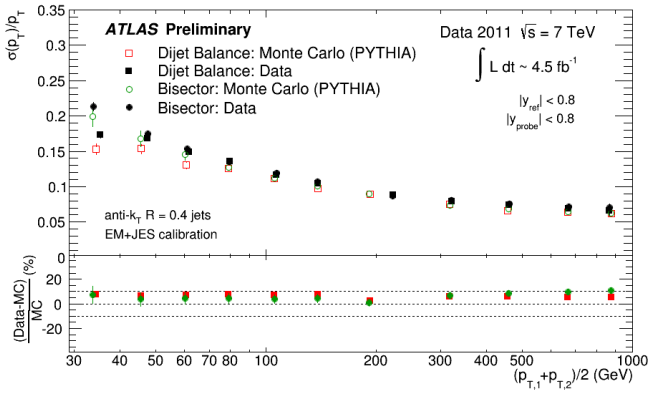

Figure 3.20: Fractional jet energy resolution as a function of the average jet transverse momenta measured with the di-jet balance (squares) and bisector (circles) in-situ techniques using the EM+JES calibration in anti-k_T R=0.4 cluster jets. The bottom plot shows the relative difference between data results (black) and Monte Carlo simulation for each method. The dotted lines indicate a relative difference of 10%. Only statistical errors are shown [107].

3.3.5 Pile-up suppression

Since the particles associated with jets extend across a wide area of the detector, the overlap with particles originating from pile-up events is quite frequent, resulting in a degraded reconstruction of the kinematics. As we mentioned in the previous section, a preliminary procedure has been implemented in ATLAS to correct the jet energy scale with the aim of subtracting the effect of additional pp collisions; it is nevertheless necessary to reject further spurious calorimeter jets arising from local fluctuations in pile-up activity, as well as real jets originating from single pile-up interactions [108]. Information from the tracks associated with jets is exploited to obtain a measure of the fraction of the energy associated with a particular primary vertex (PV): the jet vertex fraction (JVF)[6]. Once the hard-scatter vertex with the highest $\sum p_T^2$ of constituent tracks is identified as the PV, the JVF variable can be used to select jets having a high likelihood of originating from that vertex, as Fig. 3.21 schematically depicts. Different thresholds are applied on this quantity in the two s-channel cross section analyses, following the recommendations from the top group; the working point achieving the best rejection factor for "multiple interactions" jets while maintaining an efficient selection of hard scatter jets is $|JVF| > 0.75$ at 7 TeV, and $|JVF| > 0.5$ at 8 TeV, where only jets with $p_T < 50$ GeV and $\eta < 2.4$ [7] have been considered.

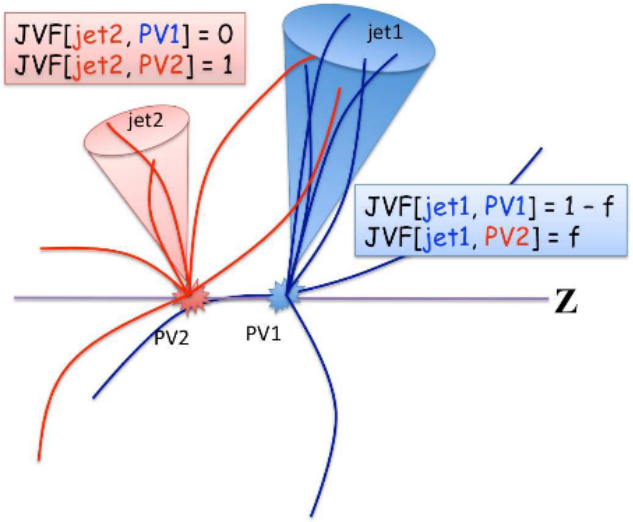

Figure 3.21: Schematic representation of the JVF principle.

[6]JVF is calculated as the ratio of the sum of transverse momentum of matched tracks that originate from a chosen PV to the sum of transverse momentum of all matched tracks in the jet, independently of their origin.

[7]The 8 TeV requirements depend on the fact that pile-up jets are expected to be soft, and that for such pseudorapidity region good tracking information is available.

3.3.6 B-tagging

We will stress in Section 4.1 that the identification of jets arising from the hadronization of bottom-quarks is essential for the analysis of the s-channel single top production. This paragraph is thus intended to outline the typical features of such b-jets, and the experimental techniques employed to discriminate them from the jets originating from light or c-quarks.
B-hadrons are characterized by a long lifetime of almost 1.5 ps that leads to a significant flight path L of several millimeters; their weak decay, thus, is significantly displaced with respect to the primary interaction, and identifies the so-called secondary vertex (SV), as Fig. 3.22 illustrates. b-jets are identified via the transverse (d_0) and longitudinal (z_0) impact parameters, defined respectively as the transverse (r, η) projection and z coordinate of a track at the point of closest approach to the primary vertex; depending on the jet pseudorapidity and transverse momentum, the inner detector spacial resolution may allow also to directly measure SV. Moreover, in the 40% of the cases, the heavy B-hadrons decay into an electron or a muon which are characterized by a high transverse momentum with respect to the direction of the bottom quark; this implies that usually b-jets are wider than light jets and have higher invariant masses.

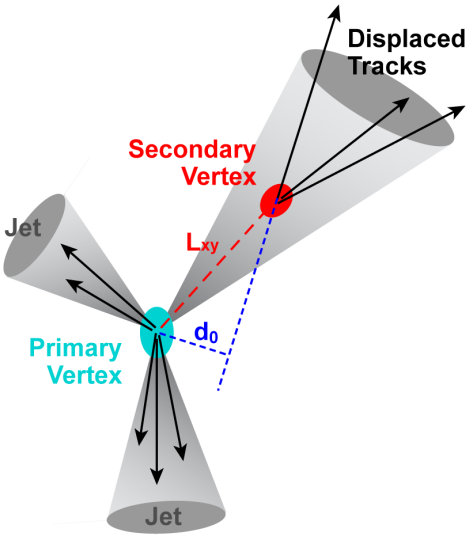

Figure 3.22: Illustration (not to scale) of a displaced vertex coming from a b-jet with high impact parameter tracks.

All these properties are exploited by specific b-tagging algorithms based on a likelihood ratio to compare the measured value of a discriminating variable X_i to reference MC distributions obtained for light- ($u(X_i)$)[8] and b-jets ($b(X_i)$). Such approach results in the determination of a weight associated to the jet, assuming that the N_T

[8] $u(X_i) = f(X_i|H_l)$ has to be intended as the likelihood function for the non-b hypothesis and $b(X_i) = f(X_i|H_b)$ the likelihood function for the b hypothesis. These concepts will be developed further in Section 4.6.

tracks constituting the jet are independent:

$$w_{jet} = \sum_{i=1}^{N_T} ln \frac{b(X_i)}{u(X_i)}; \tag{3.14}$$

the higher is w_{jet}, the larger is the probability that the jet actually originates from a bottom-quark. Several working points of the b-tagging algorithms are defined by different cut values applied on the jet weight; each one corresponds to a different b-tagging efficiency and probability of falsely tagging a jet which arises from light or c-quarks. This last is usually expressed in terms of light- and c-rejection rates, that correspond to the inverse of the light- and c-efficiencies. The b-jets identification is realized in this analysis by means of the MV1 tagger, the output of a neural network classifier trained with three high performance b-tagging algorithms as input [109, 110]: IP3D, JetFitter+IP3D, and SV1.
The IP3D tagger uses the transverse and longitudinal impact parameter significance of each track within the jet; for tracks originating from b- and c-hadron decays, the point of closest approach lies usually upstream with respect to the jet direction, while for prompt tracks from the primary vertex its position is random.
The JetFitter employs a Kalman filter to find the position of b and c vertices on a common line which includes the primary vertex. The discrimination between b, c, and light jets is then realized with a likelihood based on the masses, momentum, flight-length significance, and track multiplicities of vertices as inputs.
The IP3D and JetFitter tagger results are combined into a neural network with additional variables describing the topology of the decay chain; the output discriminant variable (called JetFitterCombNN) is used to make tagging decisions.
Finally, the SV1 tagger exploits the secondary vertex properties, like the invariant mass of all the tracks associated to it, the distance between the jet axis and the line joining the PV to the SV, the ratio of the sum of the energies of all the tracks in the vertex to the sum of the energies of all the tracks in the jet. These observables are combined using the likelihood ratio formalism described previously.
Figs. 3.23(a) and 3.23(b) show the light- and c-rejections rates as a function of the b-tagging efficiency for different b-tagging algorithms. MV1 has been employed in the 7 and 8 TeV s-channel analyses because it is the one yielding better performance in the discrimination of b-jets from light-jets; W+light jets production constitutes in fact an important source of background. A higher c-jet rejection rate is achieved by JetFitterCombNNc, which is indeed a combination of I3PD and JetFitter optimized to reject c-jets, but this feature is not essential for the analyses reported in this manuscript. Each b-tagging algorithm needs to be calibrated with data for a series of operating points. The measured b-tagging efficiency (ϵ_b^{data}) can either be determined using dijet events with soft-muon tag (with the p_T^{rel} or $System8$ methods), either using top quark pair events; ϵ_b^{data} is afterwards employed to provide p_T- and η-dependent scale factors that need to be applied to all the simulation samples as an event weight:

$$k_{\epsilon_b}^{data/MC} = \frac{\epsilon_b^{data}}{\epsilon_b^{MC}}.$$

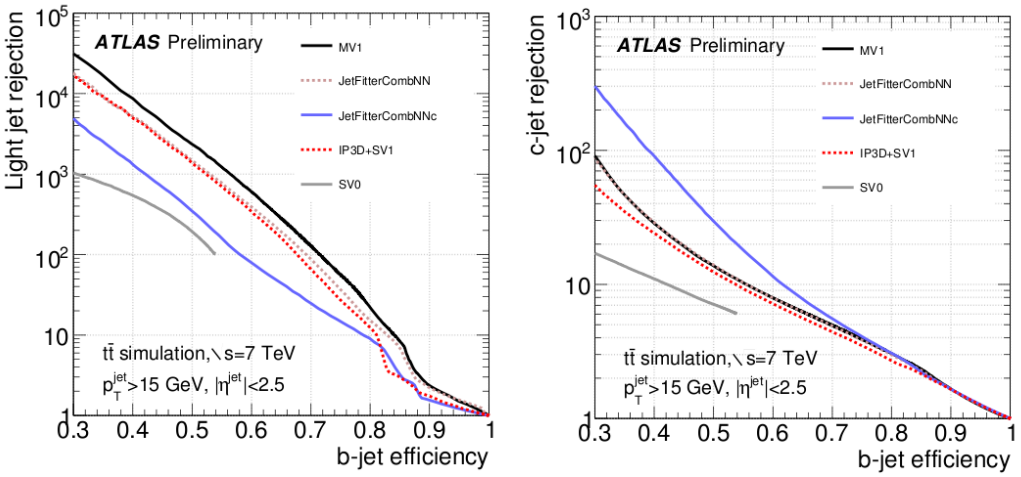

(a) (b)

Figure 3.23: (a) Light- and (b) c-rejection as a function of the b-tagging efficiency.

3.4 Transverse missing momentum

The E_T^{miss}, defined as the event momentum imbalance in the plane perpendicular to the beam axis, is a fundamental observable to spot the presence of neutrinos, which can not be detected within ATLAS. Since its measurement relies on the contributions from all the physical objects present in the event, the missing transverse momentum results very sensitive to misreconstruction, misidentification, as well as to additional proton-proton collisions. Its analysis deserves, thus, a particular caution.

3.4.1 Reconstruction

The missing transverse momentum vector, whose module is expressed by $E_T^{miss} = \sqrt{(E_x^{miss})^2 + (E_y^{miss})^2}$ and orientation in terms of the azimuthal coordinate as $\phi^{miss} = arctan(E_y^{miss}, E_x^{miss})$, is determined with the information retrieved from the calorimeters and the muon spectrometer. The energy deposits in the calorimeter are associated with a reconstructed and identified high-p_T parent object in a specific order: electrons, photons, hadronically-decaying τ-leptons, jets and finally muons. Cells belonging to a topocluster, but not associated with any such objects, are also taken into account in the calculation ($E_T^{miss,CellOut}$), as well as the ones corresponding to low momentum jets ($E_T^{miss,SoftJets}$). All these distinct contributions can be expressed as [111], [112]:

$$E_{x,y}^{miss} = E_{x,y}^{miss,e} + E_{x,y}^{miss,\gamma} + E_{x,y}^{miss,\tau} + E_{x,y}^{miss,jets} + E_{x,y}^{miss,SoftJets} + E_{x,y}^{miss,\mu} + E_{x,y}^{miss,CellsOut}. \quad (3.15)$$

In Eq 3.15, the standard ATLAS electron calibration has been used, photons are calibrated at the electromagnetic scale, while τ-jets with the LCW method, subtracting an energy offset to reduce pile-up effects and applying the τ energy scale. The jets, calibrated with the LCW+JES scheme, contribute to the $E_{x,y}^{miss,jets}$ term if their transverse momentum is greater than 20 GeV, otherwise to $E_{x,y}^{miss,SoftJets}$.
Finally, the muon term is computed by summing the momenta of muon tracks reconstructed within the pseudrapidity region $|\eta| < 2.7$. Due to the high vulnerability mentioned above, the E_T^{miss} response needs to be checked in several ways: in $Z \rightarrow ll$ events, considering its projection along the transverse direction of the Z boson for different p_T values; analyzing the reconstructed mass in $W \rightarrow l\nu$ and $W \rightarrow \tau\tau$, decays; examining the linearity of MC events in different channels. We will introduce, in the following, two among the several techniques employed to estimate the absolute energy scale and resolution of the transverse missing momentum.

3.4.2 Energy scale

The E_T^{miss} linearity, defined as the mean value of $(E_T^{miss,reco} - E_T^{miss,true})/E_T^{miss,true}$, is expected to be zero if the reconstructed missing transverse momentum has the correct scale. In order to extract the corresponding correction, this observable is thus investigated for simulated events containing genuine E_T^{miss} due the presence of a neutrino, like $W \rightarrow e\nu$, $W \rightarrow \mu\nu$. Fig. 3.24 reports the linearity computed for both channels at 7 TeV, as a function of the true missing transverse momentum; the bias at low $E_T^{miss,true}$ is up to 15% but, as expected, it decreases quickly for higher values and reaches 5% (3%) for $W \rightarrow e\nu$ ($W \rightarrow \mu\nu$) when $E_T^{miss,true} > 40$ GeV. Figs. 3.25(a), 3.25(b) show the same quantity for the 8 TeV dataset; several techniques, not implemented in the s-channel analysis, have been checked in order to reduce the impact of pile-up events, which are known to deteriorate in particular the jet and soft term of the reconstructed missing transverse momentum. The label STVF describes a method based on the rescaling of the $E_{x,y}^{miss,SoftTerm} = E_{x,y}^{miss,SoftJets} + E_{x,y}^{miss,CellsOut}$ by the fraction of momenta of tracks associated to the hard scattering vertex; other data-driven methods are based on the idea that the jet area embodies the jets' susceptibility to contamination from diffuse noise, allowing to detect the contribution of pile-up events and neutral or forward particles, for which the track information is not available. The plots illustrate that the bias is within 5% for large $E_T^{miss,true}$ values, and depends slightly on the pile-up suppression techniques (a deterioration is spotted for $STVF$ events, for which it reaches the 7%).

3.4.3 Energy resolution

The resolution is estimated with a data-driven technique based on the analysis of the width of the combined $(E_x^{miss} - E_x^{miss,true})$ and $(E_y^{miss} - E_y^{miss,true})$ distributions in $Z \rightarrow ll$ events; since in this case no genuine E_T^{miss} is present, the true values are supposed to be null. For each event, both E_x^{miss} and E_y^{miss} are plotted in bins of $\sum E_T$, which is the total energy deposited in the calorimeters summed to the muon transverse momenta; the distributions are fitted with a gaussian over a range

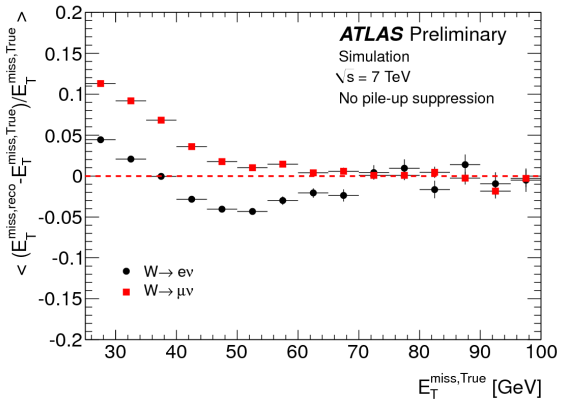

Figure 3.24: E^{miss} linearity in $W \rightarrow e\nu$ (in red) and $W \rightarrow \mu\nu$ (in black) MC events as a function of the true missing transverse momentum, with $\sqrt{s} = 7$ TeV [111].

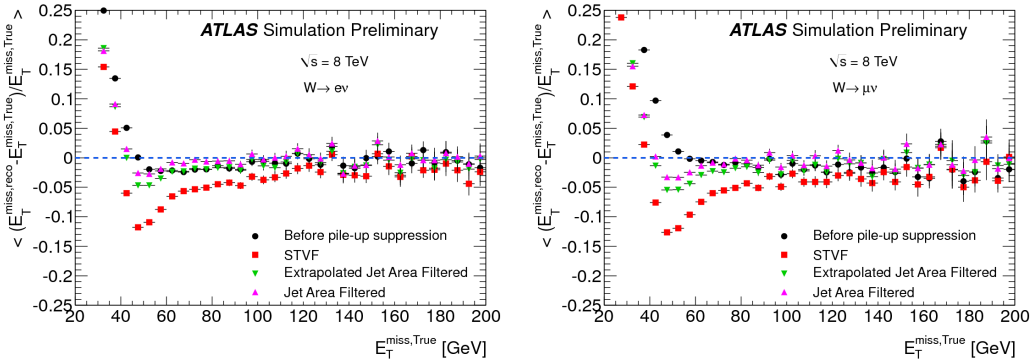

(a) (b)

Figure 3.25: (a) E_T^{miss} linearity in $W \rightarrow e\nu$ and (b) $W \rightarrow \mu\nu$ MC events as a function of the true missing transverse momentum, with $\sqrt{s} = 8$ TeV. Several techniques aimed at suppressing pile-up events are tested [112].

spanning twice the expected resolution obtained in previous studies. Afterwards, the Gaussian width (σ) plotted as a function of $\sum E_T$, is fitted with the approximation $\sigma = k\sqrt{\sum E_T}$: deviations from this simple law are expected in the low $\sum E_T$ region due to the calorimeters noise and in the high $\sum E_T$ region, where the constant term in the jet energy resolution dominates. Fig. 3.26(a) shows the $E^{miss}_{x/y}$ resolution from the 2011 dataset for $Z \rightarrow ll$ events, in a pretty good agreement with the fit obtained with the function introduced above; this allows to use the parameter k as an estimator of the resolution, and compare it in various physics channels in data and in simulation. The same kind of plot is presented in 3.26(b) for the 2012 dataset, where a striking improvement is apparent due to the several techniques employed to suppress pile-up events.

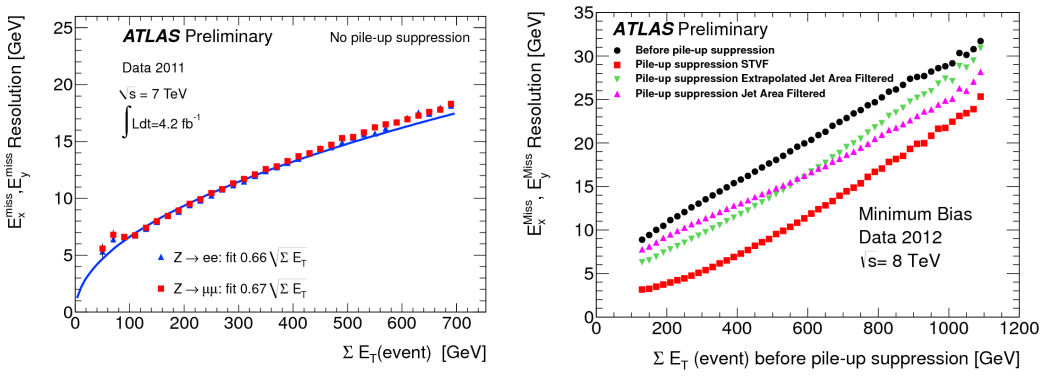

(a) (b)

Figure 3.26: (a) E^{miss}_x and E^{miss}_y resolution as a function of the total transverse energy of the event in data at $\sqrt{s} = 7$ TeV [111] (b) and $\sqrt{s} = 8$ TeV [112]. The resolution before pile-up suppression has been compared with the one obtained after the application of three distinct techniques.

Chapter 4

Strategy of the single top s-channel analysis

In this thesis two datasets, corresponding to collisions taking place at a center of mass energy of 7 and 8 TeV, have been examined; therefore, two analysis strategies have been carried out to optimize the s-channel cross section extraction. This chapter is intended to outline the common phenomenology and the tools that have been employed in both cases. First of all, we will present the main features of the single top s-channel production mode, and compare them with the properties of other physical processes sharing a similar final state. This will naturally introduce the issues of background modeling and rejection, which are topics of central importance. Secondly, we will provide a general description of the multivariate technique adopted to increase the signal discrimination: the implementation of Boosted Decision Trees (BDT) provided by the ROOT Toolkit for Multivariate Data Analysis (TMVA) [113]. Before illustrating the statistical framework chosen to interpret the results, we will outline the Monte Carlo samples employed to model the signal and background processes, and the main sources of statistical and systematic uncertainties affecting the cross-section measurements.

4.1 Event topology for signal and background

We already discussed in Section 1.2.2 the phenomenology of single top production mediated by space-like W bosons, so we will consider here just the **single top s-channel** signature. The Standard Model predicts that the top-quark decays via the weak interaction into a real W boson and a bottom quark; strange or down-quark production is in fact strongly suppressed, as the negligible CKM elements V_{ts} and V_{tb} demonstrate. The s-channel final state is hence composed by two b-jets, which as already outlined result from the hadronization of the two bottom quarks, and the W boson decay products that may be leptonic or hadronic: $e\,\nu_e$, or $\mu\,\nu_\mu$, or $\tau\,\nu_\tau$, or jets. Even if the theoretical frame is well known at LO, some caution is needed for the experimental detection of such process. At the LHC, it is in fact crucial to limit the event selection to a clean signature in order to reduce the overwhelming

multijet background. This leads to bypass the analysis of the hadronic or tauonic W decays even if the corresponding branching ratios are, respectively, 47% and 11%. τ leptons, indeed, decay before reaching the inner detector usually producing one or three mesons, often accompained by neutral pions, that would be unlikely distinguishable from the main backgrounds. Less frequently, they decay into electrons or muons which are instead selected in the conventional way ($\mathrm{W} \rightarrow \tau\nu_\tau \rightarrow e\nu_e\nu_\tau/\mu\nu_\mu\nu_\tau$). The s-channel cross section measurement will therefore be performed by requiring two central b-jets, one isolated electron or muon and large missing transverse momentum to account for the undetected neutrino; all the tracks corresponding to those particles have to be characterized by high transverse momenta for a preliminary background rejection. Since other sources of background may lead to a similar signature, we will discribe in the following their main features.

The **single top t-channel** production proceeds via W-gluon fusion and results in a final state composed by a light quark, a bottom quark and a top quark. The light quark often recoils softly against the top, and ends up in the forward pseudorapidity region of the detector; the bottom quark is also usually emitted collinearly to the beam direction, and since it originates from gluon splitting, it is characterized by a soft transverse momentum. At the detector level the signature consists, thus, in one forward light jet, one forward soft b-jet, together with the products of the top quark decay. t-channel events may fulfill the signal selection when the W boson decays leptonically, the light jet escapes from the required pseudorapidity acceptance, and the spectator b-jet passes the established p_T and η thresholds. The **single top Wt-channel** represents another mechanism leading to the electroweak production of a top quark in association with an on-shell W boson. Since the top quark decay entails the presence of a second W boson, a large multiplicity of final states is achievable: full hadronic ($W + t \rightarrow q\bar{q}q\bar{q}b$) with a branching ratio of 44%, semileptonic ($W + t \rightarrow q\bar{q}l\nu_l b$) with a branching ratio of 45%, and dileptonic ($W + t \rightarrow l^-\nu_l l^+\bar{\nu}_l b$) with a branching ratio of 9%. The semileptonic final state is the one that could better fake the s-channel signature, once that one jet escapes the acceptance selection and the other results b-tagged. These two single top production mechanisms, whose predicted rates are described in Table 1.4, constitute therefore a source of background which is barely discernable from the signal.

Top quark pairs events, mainly produced via gluon fusion but also through quark-antiquark annihilation, represent a high rate background which may mimic the s-channel. Again, multiple final states corresponding to different branching ratios can be obtained, as Fig. 4.1 illustrates. In the dileptonic decay mode (Fig. 4.2(a)), two central b-jets and two charged leptons are emitted with high transverse momentum. If one of the leptons escapes unidentified from the detector acceptance or its p_T does not pass the estabilished threshold, the $t\bar{t}$ production mimics exactly the signal signature in terms of particle content. The two neutrinos will, in fact, generate a large missing transverse momentum that is compatible with single top production. The semi-leptonic final state (Fig. 4.2(b)), on the other hand, can contribute to the selected samples if only two of the produced jets are identified.

The contribution from this background source is particularly significant because the cross section for top quark production mediated by the strong interaction (top pairs) is more than 2 times greater than the production of top quark mediated by the weak interaction (all the three single top channels), as table 1.3 summarizes.

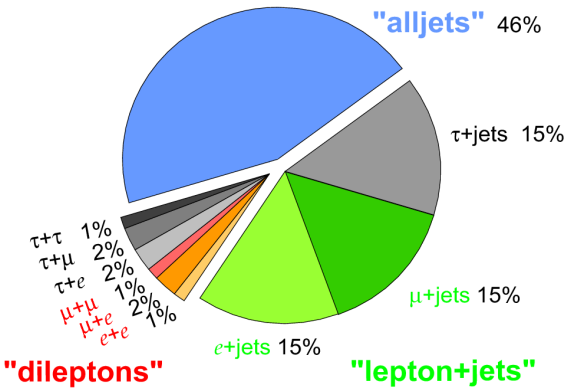

Figure 4.1: Pie chart for the top pairs branching ratios.

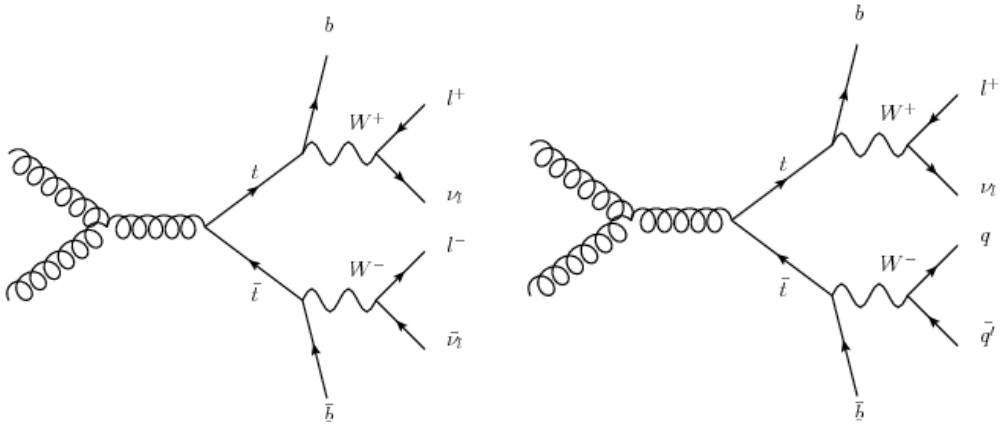

(a) (b)

Figure 4.2: (a) Tree level Feynman diagrams for the dileptonic and (b) the semileptonic top pairs decay.

W bosons can be also directly produced in proton-proton collisions in association with jets. In order to simplify the analysis of these events, we will group, in the following, different jet multiplicities and flavour compositions: the **W+heavy flavour jets** sample represents a W boson emitted with 2 b-jets or 2 c-jets or 1 c-jet, together with further light jets [1]; the **W+light flavour jets** sample comprehends, instead, a W boson produced just with several light jets. Depending on the decay mode of the vector boson and on the possible jets misidentification as b-jets, W+jets events may fake the signal. In general, even if the final state tracks are characterized by high transverse momentum, the W-b invariant mass is peaked at lower values than for the events containing real top quarks. However, this is often not sufficient to reduce significanly the W+jets background contribution, whose total production cross section illustrated in Figs. 4.3 and 4.4 is several order of magnitude greater than the signal one. More details on the production rate of each W+jets flavour sample will be provided separately for pp collisions at a center of mass energy of 7 TeV (Chapter 5) and 8 TeV (Chapter 6).

The production of a Z boson in association with jets represents a sizebly smaller background, whose main contribution depends on the emission of a pair of opposite charge leptons (with a branching ratio of almost 9%). When the vector bosons decays into ee and $\mu\mu$ final states, **Z+jets** events can fulfill the selection requirements if one of the leptons escapes unidentified and if only two jets are detected and b-tagged; in this case, the absence of transverse missing energy allows a distinction from the the s-channel signature. When a τ is produced, instead, several scenarios may lead to a final state faking the signal one, according to the decay of this lepton; furthermore, large missing transverse energy would be always detected. **Diboson** events can also generate a "signal-like" signature if one of the particles undergoes a leptonic decay and the other a hadronic decay. WW/WZ/ZZ final states may consist of a charged lepton, transverse missing momentum and jets, but they are in general easily discerned from the s-channel production. For Z+jets and diboson backgrounds, thus, only a reduced fraction of the total production cross section depicted in Figs. 4.3 and 4.4 arises from the phase space selected in the s-channel analyses.

At the LHC, pp collisions produce with the largest probability **multijet** events which should hardly pass the selection criteria. Nonetheless, several causes can induce a jet mis-identification in terms of an electron or a muon, giving rise to a "fake lepton": b-jets or long lived mesons like $\pi^{\pm}$ or $K^{\pm}$ can decay producing genuine leptons that appear to be isolated. Also π^0 showers, as well as conversion or direct photons, can be reconstructed as electrons. These circumstances may lead to a semileptonic final state analogous to the signal one. Since the multijet production cross section is several order of magnitude above the signal one (as Fig. 4.5 shows for $\sqrt{s}$=7 TeV), and the mis-reconstruction mechanisms above described are detector-dependent, methods based on data are the most appropriate to constrain this background source.

[1] Specific procedures are applied to remove the overlap between samples with different jet multiplicities and flavour composition.

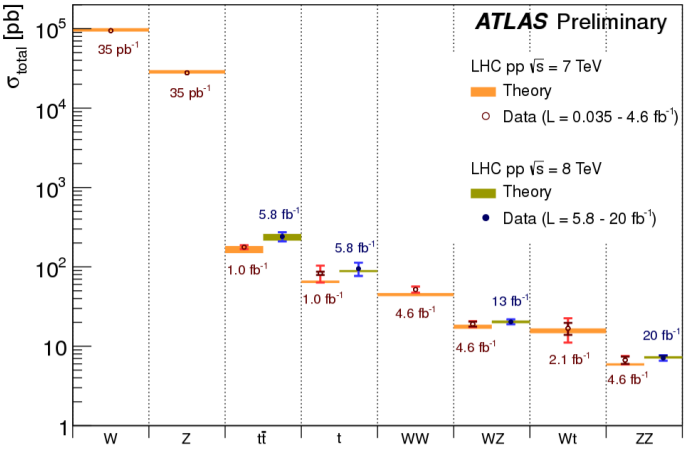

Figure 4.3: Summary [114] of several Standard Model total production cross section measurements accomplished by the ATLAS collaboration at a center of mass energy of 7 and 8 TeV. The plot shows a comparison with the corresponding theoretical expectations calculated at NLO or higher order.

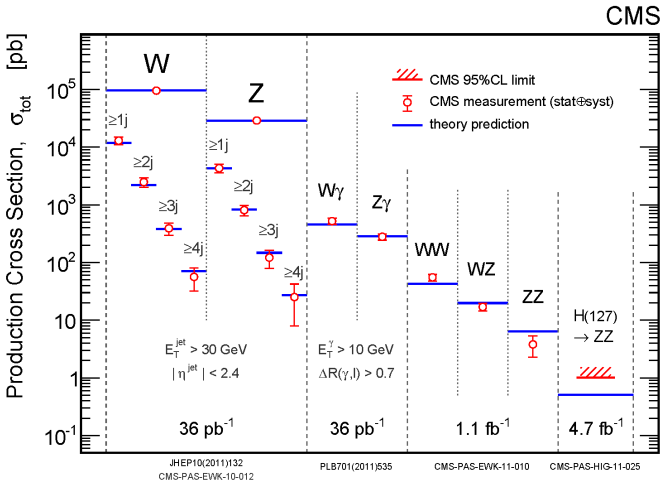

Figure 4.4: Analogous review on the electroweak production cross sections realized by the CMS collaboration. W+jets and Z+jets measurements are presented also per jet multiplicity.

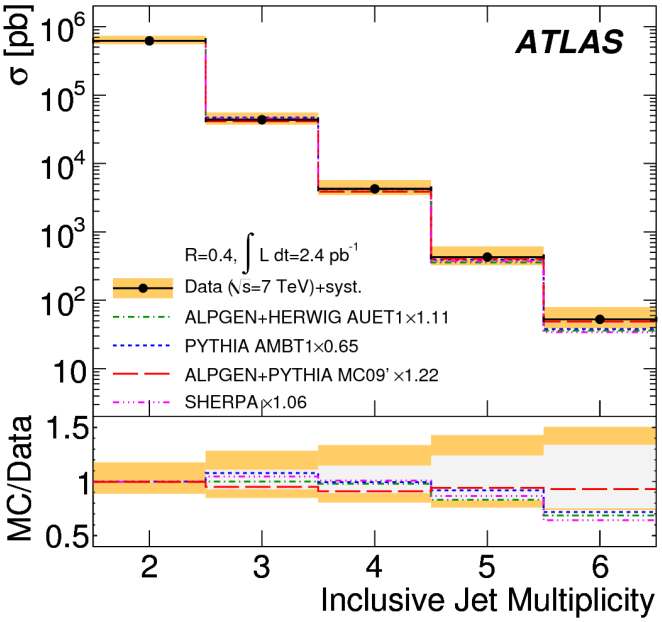

Figure 4.5: Theoretical and observed inclusive multijet cross section as a function of the jet multiplicity [115]. The darker shaded band corresponds to the systematic uncertainty excluding the contribution from the luminosity.

4.2 Data driven background estimates

The great majority of the background contributions presented in the previous section is normalized to the theoretical prediction and modeled through Monte Carlo templates. In some particular cases, however, a data-driven estimate is needed, as well as an alternative way to model the shape of the observable distributions [116], [117], [118], [119].

4.2.1 Multijet

Multijet is undoubtely the most difficult background to predict theoretically as the detector interactions leading to fake signatures are arduous to simulate accurately. Multijet modelling and normalization is therefore currently derived from data via two different techniques.

The jet-electron model

A suitable way to analyze events stemming from multijet processes that pass the s-channel selection, consists in creating a template of fake leptons from the jet-electron model, and perform a binned likelihood fit to the data. As the name suggests, this technique is usually applied for the electron+jets channel.

To model the *shape*, this procedure relies on the selection of events with exactly one jet sharing similar kinematics with a signal electron, from a dijet MC sample. This "jet-electron" should have the same p_T threshold and η acceptance as a signal electron, 80-95% of its energy deposited in the electromagnetic calorimeter, and at least 4 tracks to reduce the contribution from converted photons; a randomly drawn positive or negative charge is finally assigned to it. Jet-electron events are picked out if they contain exactly one jet fulfilling all the mentioned criteria, no additional lepton candidate, and if they pass all the s-channel selection cuts that will be detailed in Chapter 5, except the E_T^{miss} requirement. The missing transverse momentum is corrected to bring back the jet contribution to the electromagnetic energy scale.
On the other side, the multijet *normalization* is estimated through a binned likelihood fit on the measured transverse W boson mass distribution. This is performed in a sideband ($m_T(W) < 30$ GeV) where no signal events can be found [2] and then extrapolated to the signal region, as the sketch in Fig. 4.6 reports. The choice of this variable among others relies on the best modelling obtained after the application of the fit results. As real electrons with pseudorapidity falling in the electromagnetic crack region cannot be faked by the jet-electron model, the multijet normalization estimates are derived separately for events with a central jet-electron ($|\eta| < 1.5$) and for events with a forward jet-electron ($|\eta| > 1.5$).
A global *systematic uncertainty* of 50% on the extracted multijets rates has been evaluated from pile-up studies, cross checks using less sensitive variables for the binned likelihood fit and comparisons with an alternative multijet background estimations (matrix method), described in the next section.

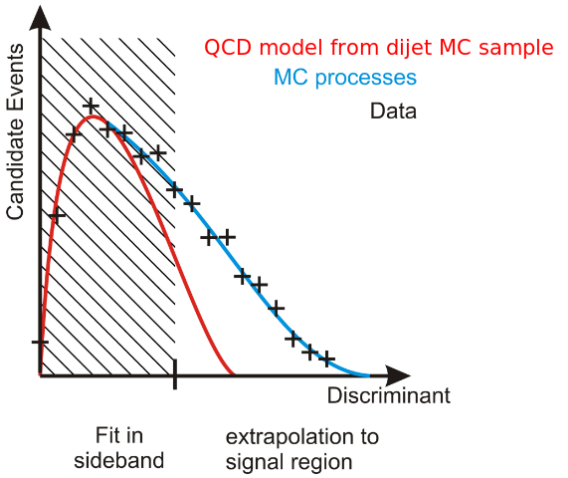

Figure 4.6: Sketch representing the determination of the rate of multijet background via the jet-electron model. A binned likelihood fit is performed using the shapes from fake lepton model and the shapes of the real W events from MC simulation. Both shapes are fitted to data in a sideband of a discriminating distribution: $m_T(W)$.

[2] by definition of the preselection cuts.

The matrix method

The matrix method provides an estimate of the multijet background which relies on the selection of two categories of events which differ on the lepton identification criteria; a tight sample is defined by the final requirements applied in the analysis, while a larger loose sample is obtained by releasing the lepton isolation enunciated in Sections 3.2.3 and 5.2. The number of events belonging to each sample can be expressed as a linear combination of the number of events containing a real and a fake lepton:

$$N^{loose} = N^{loose}_{real} + N^{loose}_{fake} \tag{4.1}$$

$$N^{tight} = \epsilon_{real} N^{loose}_{real} + \epsilon_{fake} N^{loose}_{fake}, \tag{4.2}$$

where ϵ_{real} (ϵ_{fake}) represents the probability to identify a real (fake) lepton as an isolated tight lepton. This system can be solved for N^{tight}_{fake}, which specifies the number of events passing the signal selection arising from mis-identified jets.

$$N^{tight}_{fake} = \frac{\epsilon_{fake}}{\epsilon_{real} - \epsilon_{fake}} (N^{loose} \epsilon_{real} - N^{tight}). \tag{4.3}$$

- The real efficiency, $\epsilon_{real} = N^{tight}_{real}/N^{loose}_{real}$, is derived from data, selecting the physics processes producing isolated prompt leptons (i.e. Z/W bosons decays) [3]. In the 7 TeV analysis the tag-and-probe [4] method is applied for muons, and ϵ_{real} is found to be $\sim 96\% \pm 2\%$ for almost all jet bins and in the pretag and tag samples (where the uncertainty is statistical only). In the 8 TeV analysis, instead, real efficiencies are determined for electron/muon samples via a combination of tag-and-probe and High $E_T^{miss}/m_T(W)$ methods [5]. The results are shown in Fig. 4.7 as a function of the pseudorapidity for electrons passing the two triggers used, respectively EF-e24vhi-medium1 and EF-e60-medium1, and for muons. The tag-and-probe estimate, which is derived independently of the b-tagging, tends to align better with the non b-tag alternative estimate for electrons, while is systematically lower for muons (studies are ongoing to better understand this effect). Both measurements can be used for the analyses and their difference allows to formulate the systematic uncertainty.

- The fake efficiency is measured within a multijet-enriched region which is defined specifically for the 7 TeV muon channel, as well as for the 8 TeV electron and muon channels. In the first case, this control sample is obtained by applying the cuts: $E_T^{miss} < 20$ GeV and $E_T^{miss} + m_T(W) < 60$ GeV. Only non-prompt muons characterized by high significance of the transverse impact parameter

[3] Prompt leptons originate directly from the primary vertex or the decay of short lived states.

[4] Tag-and-probe is a technique based on the selection of a tight lepton (tag) and a loose one (probe), both produced from the decay of a well known resonance. Essentially the efficiency corresponds to the fraction of loose probe candidates passing the tight cuts.

[5] These alternative methods rely on the definition of a control region ($E_T^{miss} > 150$ GeV or $m_T(W) > 100$ GeV) characterized by a negligible amount of fake leptons. Here the efficiency can simply be computed as the fraction of loose and tight single lepton events.

relative to the primary vertex, d_0^{sig}, are considered for computing ϵ_{fake}. The multijet background, in fact, is expected to be dominated by heavy flavour jets, and the leptons coming from heavy flavour decay usually have large d_0^{sig}. This ansatz can be demonstrated by counting the tight and loose leptons with d_0^{sig} larger than a given threshold x, with a pseudo-dataset that combines the MC prompt (real) lepton sample and the MC multijet (fake) sample. This sort of tight-to-loose efficiency function defined as:

$$\epsilon(x) = \frac{\sum_{d_0^{sig}>x} N^{tight}}{\sum_{d_0^{sig}>x} N^{loose}}$$

is shown in Fig. 4.8(a) for the full and the multijet MC templates after a d_0^{sig} threshold sampling. The fact that the two curves approach each other asymptotically means that the leptons with large d_0^{sig} are non-prompt and mainly from the multijet events. Moreover, by assuming that the contributions from prompt and non-prompt leptons can be respectively approximated by a Gaussian and a linear function, an euristical parametrisation of the efficiency function can be introduced: $\epsilon(x) = ae^{-bx^2} + cx + d$. The fake efficiency corresponds to the constant d in the equation. Fig. 4.8(b), representing $\epsilon(x)$ reconstructed from the real data, shows a curve behaving similarly and suggests that the parametrisation assumption is still valid for measuring ϵ_{fake} from real data. This is thus realized, for each jet bin separately, and in slices of lepton pseudorapidity; the fake efficiency is found to be around 1.2 % within 0.1 to 0.4 % for the pretag and the tag samples (where the uncertainties are statistical only).
The fake efficiency is determined in a simpler way in the 8 TeV analysis; it corresponds to the ratio of tight to loose misidentified leptons selected in a control region (CR) which should be very pure and well described by simulation. For the muon case, the best CR is defined by $|d_0^{sig}| > 5$, while for electrons the cuts $m_T(W) < 20$ GeV and $E_T^{miss} + m_T(W) < 60$ GeV are preferred. Here, once that the small amount of real leptons taken from MC is subtracted, ϵ_{fake} can be measured; the obtained values are depicted in Fig. 4.9 as s function of the pseudorapidity. The associated uncertainty is estimated by comparing the results obtained with different control regions and parametrizations (for the electron channel), and includes as well an error of 10% on the rejection of real leptons.

The matrix method allows also to retrieve the multijet background *shape*, by reweighting the loose data sample (previously defined) according to:

$$w_{tight} = \epsilon_{fake} \frac{\epsilon_{real} - 1}{\epsilon_{real} - \epsilon_{fake}}. \tag{4.4}$$

Comparisons with other estimation methods (e.g. jet electron model or matrix method using the low W transverse mass region as control region) show that a global *systematic uncertainty* of 50% needs to be assigned to the fake leptons rate.

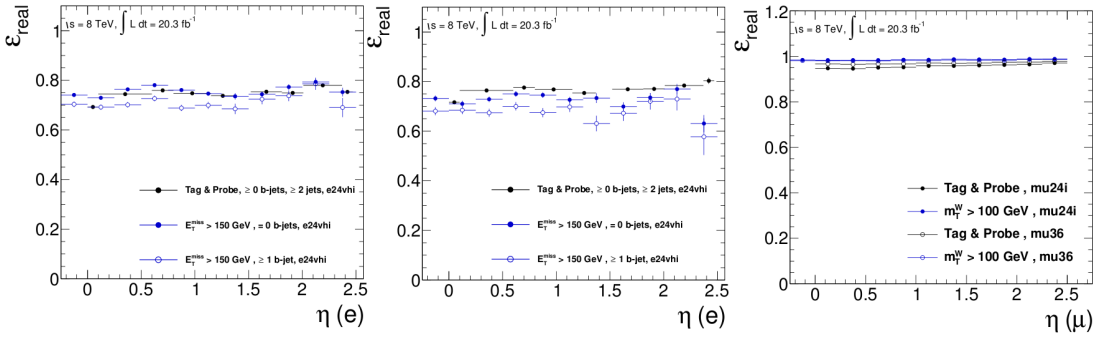

Figure 4.7: Comparison of ϵ_{real} as measured in data with the tag-and-probe (black points) and high $E_T^{miss}/m_T(W)$ (blue points) as a function of the lepton η. Electrons fulfilling the EF-e24vhi-medium1 trigger (on the left), the EF-e60-medium1 trigger (in the middle), and muons (on the right) [119]. In general, in the matrix method implementation ϵ_{real} factors are taken as η -dependent; they are however parametrized as a function of additional variables (i.e. the transverse momentum of the leading jet, distance between the lepton and the closest jet...) when they show a significant dependence.

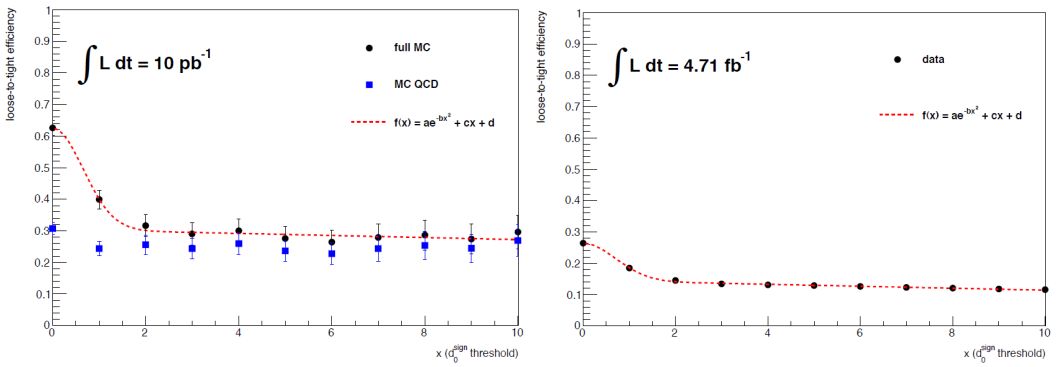

(a) (b)

Figure 4.8: (a) The loose-to-tight efficiency measured on the the full MC sample (filled circles), the multijet MC sample (filled squares) and (b) the real data (filled circles) [117]. The (pseudo-)data measurements are parametrized by $f(x) = ae^{-bx^2} + cx + d$ using a χ^2 fit. The fitted results are shown by the dashed lines.

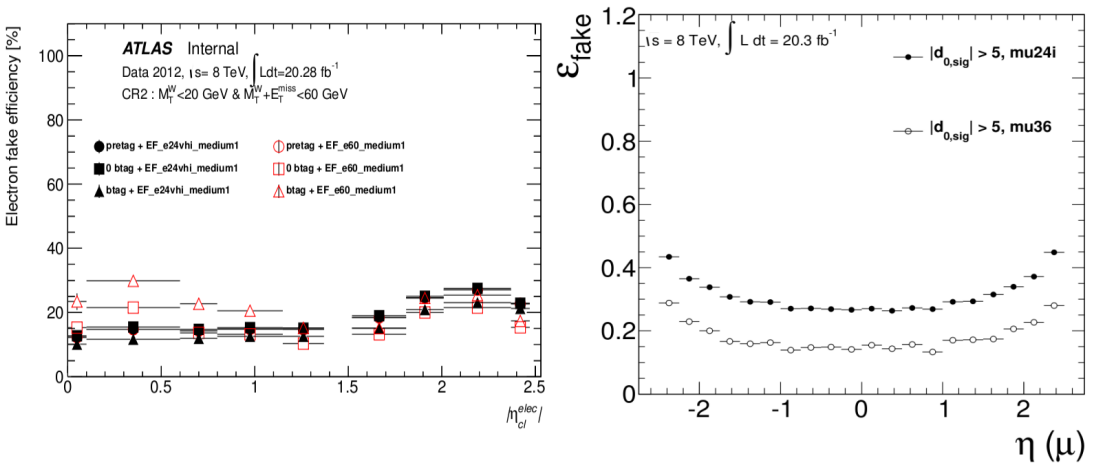

Figure 4.9: ϵ_{fake} as a function of the electron (left) and muon (right) pseudorapidity [117]. As mentioned for ϵ_{real} , these factors may be additionally parametrized as a function of other variables for which they show significant dependence. For the electron sample several b-tagging requirements are investigated for the two trigger criteria in order to mitigate the effect of the different sources of fake electrons and their contribution to the control region.

4.2.2 W+jets

The distributions and acceptances for the W+jets background are taken from the Monte Carlo templates, while the theoretical cross sections are corrected through data driven scale factors that can be derived with two alternative procedures.

The tag counting method

The W+jets overall normalization, together with the heavy flavour composition, can be determined via a tag and counting method coupled to a χ^2 minimization. This estimation is realized considering two event categories that differ this time on the b-tagging requirement. The pretag/tag samples have to be intended, respectively, as a generic loose/tight b-tagging selection; the meaning that they will adopt in each analysis will be explicitly specified in the corresponding chapter.
The *overall normalization* is extracted for each jet bin from the pretag sample, assuming that the W+jets background contributes to smooth out entirly the disagreement between data and simulation yields:

$$Norm = \frac{N^{data}_{W+jets}}{N^{MC}_{W+jets}} = \frac{N^{data} - N^{MC}_{top} - N^{MC}_{ew} - N^{MC}_{multijet}}{N^{MC}_{W+jets}}; \tag{4.5}$$

N_{top} represents the expected contributions for the $t\bar{t}$ and single top events, N_{ew} the expected contributions for Z+jets and diboson events, and $N_{multijet}$ the expected contribution for multijet events.

The *flavour composition* is afterwards evaluated by including the tag sample, and expressed in terms of the data-driven correction factors K_{bb}, K_{cc}, K_c, K_{light}. For each jet bin, the relations between the pretag and tag W+jets yields in the simulated and data samples are:

$$\begin{cases} N^{tag,MC} = N^{pretag,MC}(F_{bb}^{MC}P_{bb} + F_{cc}^{MC}P_{cc} + F_{c}^{MC}P_{c} + F_{light}^{MC}P_{light}) \\ N^{tag,data} = N^{pretag,data}(F_{bb}^{data}P_{bb} + F_{cc}^{data}P_{cc} + F_{c}^{data}P_{c} + F_{light}^{data}P_{light}) \end{cases} \tag{4.6}$$

where the factors $P_{bb,cc,c,light}$ are the b-tagging probabilities for each W+jets flavour type, and the $F_{bb,cc,c,light}$ represent the flavour fractions in the pretag sample (the unknown to be measured from data).
By integrating the normalization condition and the sum rule which relates the flavour fractions:

$$F_{bb}^{MC/data}(1 + k_{ccbb}) + F_{c}^{MC/data} + F_{light}^{MC/data} = 1,^{6} \tag{4.7}$$

the flavour scale factors

$$K_{bb,cc,c,light} = \frac{F_{bb,cc,c,light}^{data}}{F_{bb,cc,c,light}^{MC}}$$

are extracted with a χ^2 minimization procedure. The two free parameters are K_{bb} and K_c (K_{cc} being assumed equal to K_{bb} and K_{light} computed from the sum rule), and the minimization is performed on the differences between the observed and expected W+jets event yields in the 1 and 2 jet bins, where the systematic uncertainties are reduced. K-factors can be, however, easily derived for other jet multiplicities (i) following:

$$K_{bb,cc,c,light}^{i} = \frac{K_{bb,cc,c,light}^{1\&2}}{F_{bb}^{MC,i}K_{bb}^{1\&2} + k_{ccbb}F_{bb}^{MC,i}K_{bb}^{1\&2} + F_{c}^{MC,i}K_{c}^{1\&2} + F_{light}^{MC,i}K_{light}^{1\&2}}. \tag{4.8}$$

The *uncertainty* on the overall normalization and the flavour correction could in principle be estimated through the generation of pseudo-experiments testing the impact of each statistical and systematic source; these will be extensively described in Section 4.5.

The likelihood fit

The *normalization* of the W+jets can be alternatively extracted from the likelihood fit to the data of the classifier distribution which will be introduced in the next section. The fitting procedure aimed at measuring the single top s-channel cross section, in fact, outputs the factors that should rescale all the Standard Model processes, the backgrounds cross sections being considered as nuisance parameters. In this case, an overall normalization can be extracted without considering the flavour composition corrections.

[6] We have introduced in 4.7 the assumption that $Fcc = k_{ccbb}F_{bb}$, where k_{ccbb} is the ratio between $c\bar{c}$ and $b\bar{b}$ fractions taken from MC simulation.

4.3 Boosted decision trees

In the following chapters we will show that the determination of the single top s-channel cross section is a great challenge due to the low signal purity, and to the considerable similarity of the signal and background distributions. It is therefore of extreme importance to obtain an optimal event discrimination, which is a well-defined problem with a unique solution [120], [121]. Given the probability that an event described by the variables $\mathbf{x}$ is of the signal class S:

$$p(S|\mathbf{x}) = \frac{p(\mathbf{x}|S)p(S)}{p(\mathbf{x}|S)p(S) + p(\mathbf{x}|B)p(B)}, \tag{4.9}$$

the signal can be extracted with the smallest possible uncertainty by reweighting the events with $p(S|\mathbf{x})$. In practice, an achievable solution consists in building a function which approximates the conditional class probability, using equal numbers of signal and background events $p(S) = p(B)$:

$$D(\mathbf{x}) = \frac{p(\mathbf{x}|S)}{p(\mathbf{x}|S) + p(\mathbf{x}|B)}. \tag{4.10}$$

This can be realized by machine learning techniques that understand how to determine the discriminant $D(\mathbf{x})$ from the analysis of a subset of events (a training dataset); such information is then employed for the classification in two output classes of a second subset of events. The Boosted Decision Trees method (BDT) is based on this principle; initially developed in the context of pattern recognition and data mining, it has later been employed in several fields: medical diagnostic, social science, insurance... and just recently [122] in high energy physics.

4.3.1 Growing a Decision Tree

A Decision Tree (DT) extends a simple cut-based analysis into a multivariate technique, by avoiding the rejection of the events failing a particular criterion [123]. Within the training sample, a sequential selection is implemented by cutting on the variable that accords, at each step, the best signal-background separation. This procedure results in a subdivision of the phase space into orthogonal zones that are finally identified as signal-like or background-like. Therefore events are never lost, but only associated according to their features to those regions.
Mathematically, DTs are binary trees (even if in principle they can deal with multiple output classes) constituted by nodes that split recursively into two daughters, until the achievement of a stopping criterion. Fig. 4.10(a) provides a sketch of a simplified decision tree: the events are initially classified through a root node, representing here a cut on the H_T [7] distribution, which usually contributes a lot in the discrimination of single top processes; then, they follow different selection chains depending on the fulfilling of the requirements specified in the other internal nodes. The totality of

[7] H_T is the scalar sum of the transverse momentum of the selected jets, lepton and neutrino.

the analyzed events ends up into final leaves identified with a discrete value of signal purity $\frac{S}{B+S}$.

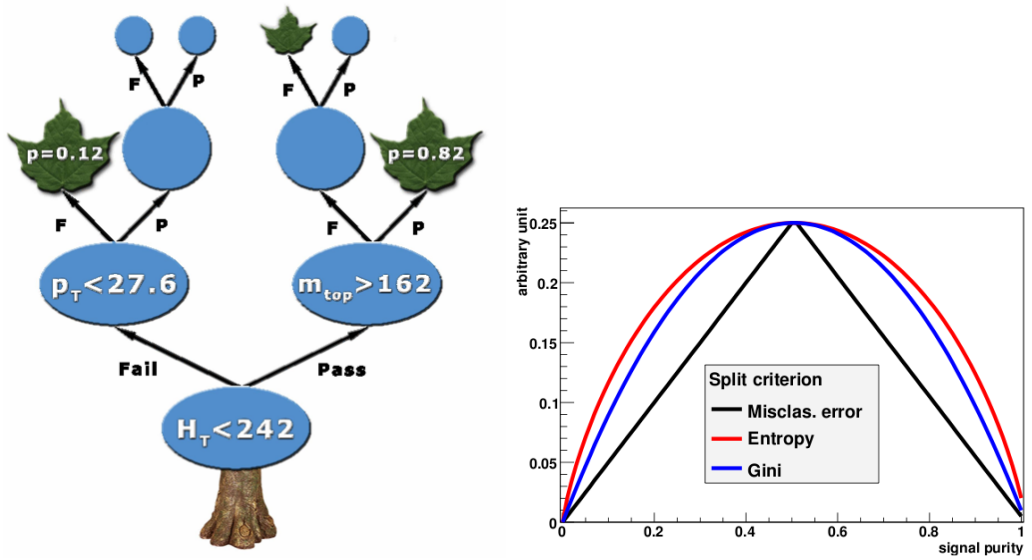

(a) (b)

Figure 4.10: (a) Graphical depiction of a decision tree. Blue ellipses are internal nodes, with their associated splitting criterion, while green leaves are terminal nodes characterized by a purity p. (b) Popular impurity functions implemented in the TMVA package as function of signal purity.

An important DT optimization to be realized in the training phase concerns the choice of the splitting criterion, which constitutes the algorithm core. This latter is based on the maximization of a figure of merit representing the decrease of impurity i for the split S of a node t into the daughters t_f and t_p:

$$\Delta_i(S,t) = i(t) - p_p i(t_p) - p_f i(t_f), \tag{4.11}$$

where p_p is the fraction of events that passed the split and are collected into the node t_p, and p_f the fraction of events that failed the split and are collected into the node t_f. The TMVA package [113] proposes many impurity functions that describe to what extent the node is a mixture of signal and background; all share, however, the same basic features which are illustrated in Fig. 4.10(b):
- they are maximal for an equal signal/background contribution, and minimal for nodes characterized by a perfect separation beween the two samples
- they are symmetric in signal and background purities ($p_S = \frac{S}{B+S}$, $p_B = \frac{B}{B+S}$)
- they are strictly concave in order to reward purer nodes.
For both the performed analyses the Gini index of diversity has been chosen:

$$Gini = 1 - \sum_{i=S,B} p_i^2 = 2p_S(1-p_S) = \frac{2SB}{(S+B)^2}. \tag{4.12}$$

Once that the splitting criterion has been defined by inserting the impurity function 4.12 in 4.11, all the input variables are scanned over their range to find the best cut value. This procedure is realized via a discrete sampling, the granularity of bins being defined by the user through the parameter $nCuts$.
Concerning the variable selection, decision trees do not put many constraints; they can deal simultaneously with continuous or discrete input distributions, without any theoretical limitation on the total number since they are not affected by the "curse of dimensionality" which forbids the use of too many variables in most multivariate techniques [113]. No issues are found with variables duplication or strong correlation, but the classification procedure can be compromised because of mismodelling. All the input distributions, therefore, have to be well described since any discrepancy between the data and the simulation will provide an artificial separation that the DT could use, misleading the analyser.
These classifiers give proof of being human readable, owing to trace which criteria an event satisfies to reach a particular leaf, powerful and resistant to most features associated to variables. They show, nevertheless, a considerable unstability depending on an excessive optimization for the training sample, which may cause a lack of generality and a distorted physical interpretation. The effect is strengthen by the recursive splitting which reduces gradually the sample size, increasing the statistical uncertainties that affect the final classification. On the whole, decision trees suffer therefore of an hyper-specialization, so that a tiny change in the training sample may lead to drastically different tree structure; this phenomenon, named "overtraining", can be detected through a comparison of the performance results obtained with two different datasets: the training and the test samples. There are also some solutions to counteract this effect: one approach relies on the use of stopping conditions, the other on pruning. For the current analyses we require that the decision trees have a maximum number of layers, denoted $MaxDepth$, and that each terminal leaf contains at least a minimum number of events, namely $MinNodeSize$. Otherwise we could have built very large classifiers and cut on the irrelevant branches and subtrees exploiting a dedicated algorithm.

4.3.2 Boosting

Despite the shrewdness of growing a classifier avoiding overtraining and defining "densely populated" phase-space regions, a single decision tree can not perform a statistically significant classification. Boosted algorithms are thus implemented to build a forest of trees that can maximize the generalisation potential, and overwhelm the shortcoming of the discrete output. Essentially, the events that were misclassified during the training of the first classifier are associated to a higher weight and analyzed again by another decision tree; the procedure is iterated until the number of trees reaches the limit $NTrees$ set by the user, and achieves in the combination of all the DTs to a more stable classifier. The output of the latter is a weighted average expressed by a continuous distribution.

From a statistical point of view, the final BDT classifier is an expansion in the base functions $f(\mathbf{x}, a_m)$, that are the "weak learners" representing the M trees contributions:

$$F(\mathbf{x}; P) = \sum_{m=0}^{M} \beta_m f(\mathbf{x}, a_m),\ P \in \{\beta_m, a_m\}_0^M; \tag{4.13}$$

α_m is the boost weight for the tree m derived from the misclassification rate of the previous tree (m-1), and β_m controls the learning rate of the boosting algorithm. Using a training sample $\{\mathbf{x_i}, y_i\}$ of known (y-$\mathbf{x}$) values, the parameters P can be adjusted such that the deviation between the model response $F(\mathbf{x})$ and the true value y is minimised; the deviation is measured by the so-called loss-function $L(F, y)$. The most popular boosting method, AdaBoost, employs an exponential loss which lacks robustness in presence of outliers or mislabelled data point [113]. The two undertaken analyses are therefore based on an alternative boosting algorithm, the GradientBoost [124] which relies on a binomial log-likelihood loss:

$$L(F, y) = ln(1 + e^{-2F(\mathbf{x})}y). \tag{4.14}$$

The numerical minimisation is accomplished via the steepest-descent approach, for which the parameters for the next boost step (weights) are such that one moves along the steepest gradient of the loss function.

4.3.3 BDT application

For the extraction of the single top s-channel cross section, no variable providing a powerful signal discrimination has been found. The boosted decision trees approach has therefore allowed to develop, from several kinematic and topological distributions, a continuous output characterized by a strong separation power. This of course does not contain more information than the initial degrees of freedom, but its fit leads to better performance than the fit of whatever variable.
Different choices have been taken for the training samples used to model the signal and the main background contributions in the 7 and 8 TeV analyses, so the dataset will be introduced in the corresponding chapter, together with the parameters optimization. A common procedure concerns instead the selection of the input variables, which is essentially based on two criteria: good modelling, and considerable separation power S. The latter is evaluated owing to the parametric function

$$\begin{cases} x = F_s(\epsilon) \\ y = F_b(\epsilon) \end{cases} \tag{4.15}$$

where $F_s(\epsilon)$ and $F_b(\epsilon)$ represent the cumulative functions for a given variable for the signal and backgrounds events, respectively. S is defined by the area between the curve described by 4.15 and the bisector $F_s(\epsilon) = F_b(\epsilon)$, as Fig. 4.11 illustrates for the p_T(l)+ E_T^{miss} distribution. Different separation power thresholds have been considered to define several input variable sets; the one minimizing the expected total (statistic and systematic) uncertainty on the s-channel cross section has been employed.

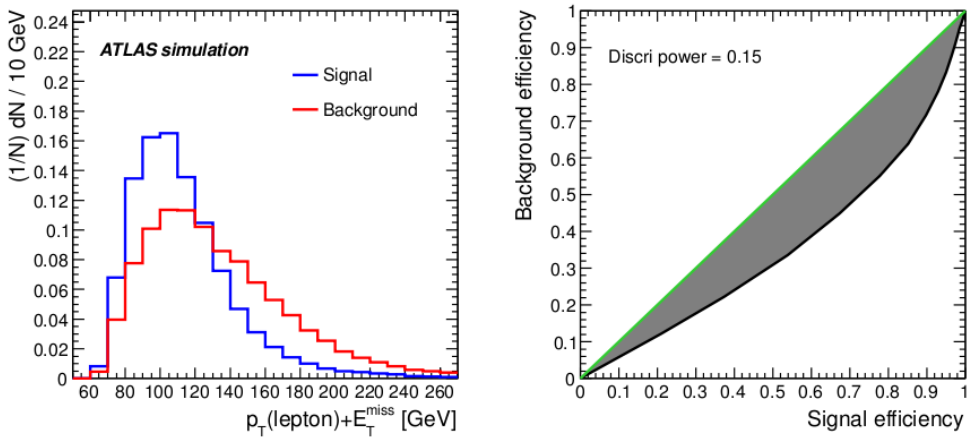

Figure 4.11: p_T(lepton)+ E_T^{miss} distribution normalized to unity for the signal (blue histogram) and background (red histogram). On the right, the corresponding efficiency curve is depicted in black, together with the diagonal line which instead is in green; the discriminant power is given by the surface area bounded by the two curves.

4.4 Monte Carlo simulations

The role of Monte Carlo simulations is crucial to validate and fully understand the observed data in every analysis phase, from the object reconstruction to the estimate of the signal to background fraction, its optimization, and finally the statistical interpretation of the results. For each physics process, events are generated according to different parton density functions; hard scattering processes described to some fixed order in pertubative chromodynamics are handed over to a parton shower, which dresses incoming and outcoming partons with additional radiation; then, the interaction scale falls triggering the non perturbative hadronization process. Color-singlets hadrons are finally produced, and unstable particles are decayed. The events generated in this manner are later passed to a Geant4-based simulation software [125], capable of modeling the particles interactions within ATLAS. Finally, the digitization process converts the detector information in electronic signals, similarly to what happens for real collision data; in this phase, the effect of multiple proton-proton collisions at a variable rate is included in order to reproduce the distribution of the average number of interactions per bunch crossing ($\langle\mu\rangle$) observed in data.
Let us consider, now, how each of the physics processes described in Section 4.1 is modeled for the 7 and 8 TeV s-channel analyses. In both setups, all the processes involving real top quarks are produced assuming $m_t = 172.5$ GeV, and normalized to the theoretical approximate NNLO cross sections (reported in Tables 1.3 and 1.4).

- **s-channel**, **Wt** and **top pair** productions are simulated with the next-to-leading order POWHEG generator [126] using CT10 as PDFs [127]; the parton shower, hadronization and underlying event are realized by PYTHIA (version 6.4.25) [128] tuned to the Perugia 2011 quark parameterization [129] . The Wt NLO cross section calculation is performed with the diagram removal scheme.

- **t-channel** single top events are modelled in different ways for the two s-channel analyses; at 7 TeV we use the AcerMC multi-leg leading order generator (version 3.8) [130, 131] coupled to the modified LO MRSTLO** set of PDFs [132]. For the two considered partonic processes (q+$g \rightarrow q'$+t+b and q+$b \rightarrow q'$+t), the parton shower, hadronization and underlying event are performed by Pythia with the same parameterization than above. For the 8 TeV analysis, instead, events are produced with Powheg generator using the CT10 PDFs set and Pythia tuned to the Perugia 2011 quark parameterization, similarly to what is done for the signal.

- **W+jets** and **Z+jets** productions are simulated using the leading order Alpgen generator (version 2.14) [133] coupled with the CTEQ6L1 [134] set of PDFs; the parton showering is realized with Herwig (version 6.5.20) [135] in connection with Jimmy for the underlying model [136] at 7 TeV, and with Pythia tuned to the Perugia 2011 parameters at 8 TeV. These background contributions consist actually of several sub-processes with different number of partons in the final state (up to five), which are generated separately. The "MLM" matching scheme [133] is applied to reduce the double-counting problems that may arise, as an example, with W/Z+n partons events populating the same phase space than events with $(n-1)$ partons but with hard radiation from the shower. W+jets production, moreover, is splitted in different samples according to the jet flavours ($Wb\bar{b}$, $Wc\bar{c}$, Wc and Wlight), which may spot analogous overlap issues. These are overcome by combining and re-classifying all the W+jets events according to the variable HFOR [137], obtained by matching the jets in the event with the quarks in truth level after parton showering minimizing $\Delta R = \sqrt{(\Delta\phi)^2 + (\Delta\eta)^2}$. Finally, the Z+jets sample is normalized to the NNLO calculation [138], and the W+jets sample via the data-driven techniques explained in Section 4.2.2.

- The **diboson** processes WW, WZ, ZZ are generated using the showering and hadronization generator Herwig with the ATLAS Auet2 tune [139] based on the Cteq6l1 PDFs set, and afterwards scaled according to the NLO calculations [140].

- Finally, the **multijet** background for the 7 TeV electron+jets channel is modeled using a Pythia dijet sample with a jet filter to enrich in electron-like jets of transverse energy E_T >17 GeV and pseudorapidity $|\eta|$ <2.7. For the 7 TeV muon+jets channel and the 8 TeV analysis, instead, the multijet contribution is directly estimated from data by using an enriched control region (Section 4.2.1).

In order to assay the systematic uncertainties related to the particle generator and to the parton showering, we analyze different Monte Carlo samples with respect to the baseline configuration. At 7 TeV, for the top quark pair and the single top s-channel contributions, a comparison between the event samples produced by the nominal Powheg+Pythia and the alternative MC@NLO (version 4.01) [141] generator with the CT10 set of PDFs coupled to Herwig allows to estimate the global impact of the

theoretical modelling, For the Wt and t-channel single top productions, instead, only the effect of parton showering is tested by investigating the AcerMC+Pythia and AcerMC+Herwig samples. For the 8 TeV analysis, all the processes involving the production of real top quarks simulated with Powheg+Pythia for the nominal configuration, are compared with the MC@NLO+Herwig model (aMC@NLO+Herwig for the t-channel). Moreover, the analysis of the Wt events modeled with Powheg+Pythia using the diagram substraction scheme (DS) permits to estimate the uncertainty associated to the NLO calculation scheme.

Initial and final state radiation effects are studied thanks to a $t\bar{t}$ sample generated with more and less parton shower activity [142], with AcerMC interfaced with Pythia (Auet2b tune with Cteq6l1 PDFs). At 7 TeV the same kind of study is performed also for the signal sample, while at 8 TeV s-channel Powheg templates with the renormalization and factorization scales increased or descreased by a factor two have been preferred; the hard generator is coupled to Pythia with the P2012, P2012radHi or P2012radLo tunes and Cteq6l1 PDFs.

Two additional samples are introduced to determine the uncertainty on the W+jets shape. For the 7 TeV analysis, the alternative events are generated with Alpgen+Herwig with different choices of the matching scale and of the functional form of the factorisation scale. For the 8 TeV analysis, instead, we employ the leading order Sherpa [143] generator with the CT10 PDFs.

4.5 Systematic uncertainties

The s-channel cross section measurements realized with a center of mass energy of 7 and 8 TeV entail of course an intrinsic uncertainty. This one depends on the statistical flucuations in the recorded dataset and simulation templates, as well as on the systematic imprecisions related to the detector response and the theoretical models used to interpret the results. The systematic uncertainties can be indeed ideally classified into two categories: the ones involving the mismodelling introduced in the objet reconstruction, together with the miscalibration of several observables, and the ones concerning the normalization, the parton density functions uncertainties, the hadronization and showering biases...in few words, the modeling. This section is thus conceived to detail every uncertainty source that will affect the two analyses.

4.5.1 Modelling uncertainties

Theoretical normalization

The event yields associated to the top pair, single top, Z+jets and diboson processes are evaluated using the selection acceptances and the theoretical cross sections calculations. The uncertainty of the latters depends on the specific choice of the energy scales for the renormalization and factorization, that is propagated into the coupling constants and the parton density functions. For the processes involving

real top quarks, moreover, a supplementary uncertainty includes the effect of varying the top mass pole of ± 1 GeV. According to the theoretical predictions provided in [24, 144, 26, 27, 28] , different relative uncertainties have been respectively assigned to the $t\bar{t}$, t-channel, Wt, s-channel [8] productions in the 7 TeV (8 TeV) analysis: ±10% (±6%), ±5% (±4%), ±8% (±7%), ±4% (±4%). For the diboson production a 5 % relative uncertainty has been estimated [140], while for the Z+jets process, different contributions are added in quadrature: a theoretical uncertainty of ±5% is considered for the Z inclusive production, a factor of ±24% is credited to each jet acccording to the Berends scaling [145, 146], and an additional ±50% uncertainty is included to account for the heavy flavour composition. For background processes that are merged in the statistical analysis, the normalization uncertainty corresponds to the average, weighted according to the relative event yields.

Multijet normalization
The multijet background is normalized through the data-driven techniques described in Section 4.2.1, for which the assigned systematic uncertainty is ±50%.

***W*+jets normalization**
The uncertainty on the W+jets normalization could be in principle either extrapolated from control samples via the tag counting method, or directly from the signal events via a likelihood fit to the data. However, we prefer to apply the same W+jets "constraint" in the two analyses, even if the nominal estimate is realized in different ways. According to [145, 146], a theoretical uncertainty of ±10% is evaluated for the W+light jets normalization, while for the W+heavy flavour a sum in quadrature of several contributions, similarly to what explained for Z+jets, yields different factors for each jet-bin. The inclusive theory (±4%), the Berends scaling (±24% per additional jet) and the heavy flavour (±50%) uncertainties give a global uncertainty of ±56% for the 1-jet bin, ±60% for the 2-jets bin and ±65% for the 3-jets bin.

Initial and final state radiation (ISR/FSR)
In every process that contains coloured or charged objects in the initial or final state, the radiation of gluons or photons may give large corrections to the overall topology of events: the particles momentum can undergo strong variations, as well as the jet-multiplicity. As an example among many other, we can consider a 2-jets event that migrates into the 3-jets bin due to the presence of a radiated gluon. The impact of the ISR/FSR in the final measurement is determined via specific event samples generated with different renormalization scale, QCD cutoff energy and maximum transferred momentum to the emitted gluons; this alternative tuning reproduces events characterized by greater or smaller probability of emitting radiation. According to the collaboration prescriptions, we include the specific samples introduced in Section 4.4 for the signal (only in the 7 TeV analysis) and the main background source containing real top events, $t\bar{t}$; we symmetrize the difference in acceptance and extract the shape

[8] The theoretical uncertainty on the signal is employed in the computation of the significance and cross section limit, as it will be detailed in Section 4.6.

variation with respect to the nominal samples.

Monte Carlo generator and parton shower modelling
By simulating the production of events with a specific Monte Carlo generator, we accept as unique its renormalization scheme and its way of dealing with the real or virtual emissions. To assess the error introduced by this choice, we can perform the analysis with event samples generated according to distinct models. Also the approximation schemes introduced to calculate the emission of gluons from accelerated coloured partons and other gluons involve a systematic uncertainty, which can be evaluated via the comparison of event samples produced with different parton shower descriptions. We symmetrize thus the differences in acceptance between the nominal MC samples and the ones described in Section 4.4 for testing the theoretical modelling, and take them as rate systematic uncertainty; the corresponding variations in the distributions shapes are also considered.

Parton distribution functions
A further systematic uncertainty is related to the parton distribution functions which, as previoulsy discussed in Section 1.2, describe the way in which the proton's momentum is shared between gluons, valence quarks and different flavours of sea quarks. First of all one should investigate the variation of the parameters entering in the PDF, that is the momentum fraction x_i and the scale of interaction Q^2; then, the final measurement should be carried out with different sets of PDFs to determine the influence of the choice of the reference set. A sort of combination between these "intra-PDF" and "inter-PDF" uncertainties, quantifying the current puzzlement about the parton densities, can be realized following the PDF4LHC [147] working group recommendations. The events are thus reweighted according to the PDF eigenvectors which specify the uncertainty on each of the parameters used, and the envelope of variations used to estimate the error is calculated considering the CT10, MSTW2008 and NNPDF23 PDF sets.

Signal generator scale
The uncertainty on the s-channel generator scale is evaluated by comparing the POWHEG+PYTHIA samples with varied renormalization and factorization scales to the nominal one. The smallest and largest differences in acceptance are taken as systematic uncertainties, for which also the shape variation is taken into account.

W+jets shape modelling
The uncertainty on the modelling of the W+jets background is estimated by comparing the shapes provided by the baseline ALPGEN+PYTHIA sample with the ones obtained with the alternative samples introduced in the previous section for the 7 and 8 TeV analyses. The differences are symmetrized and taken as up and down systematic uncertainties.

4.5.2 Experimental uncertainties

Luminosity
The impact of the uncertainty related to the luminosity on the signal and background acceptances is straightforward to predict, as the event rate of each process is proportional to the integrated luminosity; this uncertainty will thus affect in the same way all the samples for which the normalization is not data-driven. Technically, the associated error described in Section 2.2, is found to be 1.8 % for the 2011 dataset (7 TeV analysis), and 2.8 % for the 2012 dataset (8 TeV analysis); the latter value corresponds to a *preliminary* calibration of the luminosity scale derived from beam-separation scans performed in November 2012.

Lepton energy/momentum scale
We illustrated in Chapter 3 that the procedure of energy (momentum) calibration for electrons (muons) proceeds via rescaling the measured values; the correction factors take into account the radiation losses as well as the misreconstruction effects. These factors are shifted in both directions by 1σ uncertainty to check how they bias the object and event selections. The energy (momentum) is recalculated, and the analysis performed again for these varied samples.

Lepton energy/momentum resolution
Another systematic uncertainty pertains to the resolution of the electron energy and muon momentum, and is evaluated by a $\pm 1\sigma$ smearing of those observable in the simulated samples. If for the electrons the energy is simply "degraded" by convoluting the nominal value with a gaussian function:

$$E_{corrected} = E_{measured}[1 + G(0, 1\sigma_{resolution})],$$

for the muons the procedure is slightly more complex, as Eq. 3.7 shows. The contributions from the inner detector and muon spectrometer being decorrelated, the uncertainty on the transverse momentum resolution is expressed by two distinct variations ($\pm 1\sigma_{ID}$ and $\pm 1\sigma_{MS}$). Once that the energy/momentum distributions of the simulated leptons have been re-smeared according to this uncertainty, the event rate and the distribution shapes are checked newly.

Lepton efficiency
Scale factors are applied to the Monte Carlo lepton trigger, reconstruction and identification efficiencies in order to reproduce the ones measured in the data. To assess the impact of the uncertainties associated to these scale factors, the predicted event-yields are re-computed once that they have been shifted up and down by 1σ variation.

Jet reconstruction efficiency
The jet reconstruction efficiency is derived by matching calorimeter based jets with charged tracks reconstructed in the ID via a tag-and-probe method. The small difference observed between simulation and data is applied to the MC samples by dropping

jets according to the efficiency curve. The resulting difference in acceptance with respect to the nominal samples is symmetrized and quoted as a systematic uncertainty.

Jet energy scale
The jet energy is calibrated after the reconstruction at the EM or LCW scales, as explained in Section 3.3.3. Some imprecisions affecting the calorimeters response, as well as the simulation of the detector and the physics processes, however, may lead to a different correction. At the same time, it should be clear that many approximations are introduced in the calibration method: an *average* scale factor is determined for *central* jets, and is then estimated for the non central ones. A global uncertainty on the jet energy scale should therefore be included, and its effect evaluated for our analyses. Specific simulation samples are in fact generated with the energy of the reconstructed jets shifted by $\pm 1\sigma$ variation, and the event selection is performed again to assess the overall effect.

Jet energy resolution
The jet energy resolution measured in 2011 and 2012 data via the dijet balance and the bisector techniques showed a general agreement with the MC simulation. The recommended procedure is hence not to apply any smearing for the nominal measurement, but to use smearing within 1σ to express the systematic uncertainty. A MC template produced according to this prescription is analyzed to check the influence of this systematic on the acceptances and the distribution shapes of each process.

Jet vertex fraction efficiency
The uncertainty associated to the efficiency of the cut on the jet vertex fraction, applied in order to reduce the pile-up contamination as explained in Section 3.3.5, is estimated via $\pm 1\sigma$ variations applied on the associated scale factors.

Jet b-tagging
Scale factors derived from measurements of the b-tagger performance in data are applied to MC events containing b, c and light jets, in order to correct the simulation. This leads, hence, to three uncorrelated sources of systematic uncertainties: b-tagging, c-tagging and mis-tagging efficiencies. The effects of these three contributions are evaluated by shifting by $\pm 1\sigma$ the scale factors applied to each simulated jet, and repeating the analysis.

Missing transverse momentum
The uncertainty introduced in the measurement of the transverse missing momentum, which represents the opposite of the sum of all the detected p_T in the event as outlined by Equation 3.15, has been estimated in different ways in the two s-channel analyses. In both approaches, however, only the contributions of the calorimeter cells not associated to any reconstructed object (CellsOut) and of the jets with transverse momentum in the range 7-20 GeV (SoftJets) have been taken into account. The variations (described above) which affect the reconstructed lepton and jets are in fact automatically propagated to the E_T^{miss} computation.

For the 7 TeV analysis, the global energy scale and resolution uncertainty influencing the CellsOut and SoftJet terms has been assessed via a unique $\pm 1\sigma$ variation before re-doing the selection of the simulation samples; the error connected to pile-up interactions has been also taken into account via a separate $\pm 1\sigma$ variation. For the 8 TeV analysis, instead, the effects of the energy scale and resolution are estimated independently by varying simultaneously the SoftJets and CellOut terms by $\pm 1\sigma$.

4.6 Statistical analysis

In order to assess the single top s-channel contribution in the selected data sample, a binned maximum likelihood fit is performed to the BDT output distribution. The impact of the statistical and systematic uncertainties discussed in Section 4.5 is integrated via a frequentist approach, which is based on the generation of pseudo-experiments with systematically varied samples of simulated events. This statistical inference will not only provide a global uncertainty related to the measurement, but also a way to determine the signal significance and to set an upper limit on the production cross section.

4.6.1 Cross section measurement

The likelihood function is given by the convolution of the Poisson distributions in the individual bins of the histogram, and the gaussian constraints for each background source:

$$L(\beta^s;\beta_j^b) = \prod_{k=1}^{Nbins} \frac{e^{-\mu_k}\mu_k^{n_k}}{n_k!} \cdot \prod_{j=1}^{Nbackgrounds} G(\beta_j^b;1.0,\Delta_j) \tag{4.16}$$

with

$$\mu_k = \mu_k^s + \sum_{j=1}^{B} \mu_{jk}^b, \quad \mu_k^s = \beta^s \cdot \widetilde{\nu^s} \cdot \alpha_k^s, \quad \mu_{jk}^b = \beta_j^b \cdot \widetilde{\nu_j} \cdot \alpha_{jk}. \tag{4.17}$$

The s-channel normalization factor β^s, together with the factors corresponding to each background source (the nuisance parameters β_j^b) are determined by minimizing the negative logarithm of the likelihood function: $-logL(\beta^s,\beta_j^b)$.
In each bin k, n_k represents the number of observed events, while μ_k the corresponding expectation value defined as the sum of the contributions for signal (μ_k^s) and for background (μ_{jk}^b). For a process j, the expectation value in each bin k is given by the product of the predicted number of events in the selected sample ($\tilde{\nu}^s$ for signal or $\tilde{\nu}_j^b$ for background), the scale factor (β^s or β_j^b), and the fraction of events falling in this bin (α_k^s or α_{jk}^b). The set of α_{jk} constitutes the normalized template histogram obeying the condition $\sum_{k=1}^{Nbins}\alpha_{jk}=1$. The mean value of the gaussian constraints is set to one and the width Δj to the relative uncertainty with which the cross sections are predicted (listed in Sec 4.5). A different procedure is suitable for the multijet sample, whose contribution is already determined from data, and for which the classifier distribution is not sensitive; in this case we squeeze the width of the

gaussian that parametrizes its a-priori knowledge, and we consider the corresponding uncertainty only in the generation of the pseudoexeriments.
Once that the method employed to extract the "nominal" cross section has been clarified, one should consider that the statistical and systematic uncertainties cause variations in the signal acceptance, the background rates and the shape of the distribution to be fitted. It is only by performing the cross section measurement from the entire set of pseudoexperiments, that one obtains an estimator of the probability density of *all possible outcomes* of the measurement; the standard deviation of this estimator distribution is itself an estimator of the corresponding uncertainty.
When performing random drawings with respect to the expected signal and background normalizations, the standard deviation of the BDT response fit gives the expected uncertainty; when, instead, the measured cross sections are introduced in the pseudoexperiments by rescaling all the event yields, the standard deviation estimates the observed uncertainty of the measurement.
For each pseudo experiment and each process labelled by index j, this frequentist procedure can be summarized in the four following steps:

- The backgroud expectation values ($\widetilde{\nu_j}$) are varied within their cross section uncertainties throwing a random number β_j^{gen} according to a log-normal distribution with mean one and width Δj. Using a log-normal distribution as prior has the advantage of avoiding unphysical negative values by construction.

- The acceptance uncertainties $\epsilon_{i,j-}$ and $\epsilon_{i,j+}$ are included by varying the expectation values $\widetilde{\nu^s}$ and $\widetilde{\nu_j}$ accordingly for all the systematic uncertainties S. This is realized by throwing a gaussian distributed random number δ_i for each systematic source, using a mean of zero and a width of one. The expectation values used for the generation of the pseudoexperiment are given by:

$$\nu_j^{gen} = \widetilde{\nu_j} \cdot \beta_j^{gen} \cdot \left\{ 1 + \sum_{i=1}^{S} |\delta_i| \cdot (H(\delta_i) \cdot \epsilon_{i,j+} + H(-\delta_i) \cdot \epsilon_{i,j-}) \right\}, \tag{4.18}$$

  where H denotes the Heaviside function; this equation implies that in order to keep ν_j^{gen} positive, some δ_i are rejected.

- The number of events for individual background and signal processes n_j is determined from Poisson distribution with mean ν_j^{gen}.

- Finally, the classifier is obtained by drawing n_j times the template distribution of each process j. The shape uncertainties are included by generating systematically altered distributions by varying bin-by-bin (labelled by index k) the nominal distribution in a similar way than for the expectation values; the same systematic nuisance parameters (δ_i) are in fact employed:

$$\alpha_{jk}^{gen} = \alpha_{jk} + \sum_{i=1}^{S} |\delta_i| \cdot \left\{ (\alpha_{jki}^{+} - \alpha_{jk}) \cdot H(\delta_i) + \cdot (\alpha_{jki}^{-} - \alpha_{jk}) \cdot H(-\delta_i) \right\} \tag{4.19}$$

The pseudo-experiments generated as described above allow to estimate the statistical errors coming from the data; they are indeed included via the Poissonian drawings of the numbers of events n_j around the varied expectation values $\widetilde{\nu_j}$ (rate statistical variations) and via the drawings of the resulting numbers of events according to the varied template distributions (shape statistical variations). Statistical uncertainties due to the size of the MC samples are instead added by throwing for each process a bin-per-bin random number according to a Gaussian distribution of mean one and of width equal to the statistical error associated to the bin (the root square of the quadratic sum of the event weights).

For a given ensemble of pseudoexperiments, a complete distribution of the fitted parameter β^s is produced. The corresponding positive and negative uncertainties, which are expressed with respect to the expected SM value ($\beta^s = 1$), are computed as follows. In order to absorb the possible asymmetry of the curve, a factor called bias defined as the difference between the mean value and 1 ($\Delta =< \beta > -1$) is added in quadrature to the standard deviation, according to its sign:

$$\text{if } \Delta > 0 \begin{cases} \text{Negative unc.} = \sigma \\ \text{Positive unc.} = \sqrt{\sigma^2 + \Delta^2} \end{cases} \quad \text{if } \Delta < 0 \begin{cases} \text{Negative unc.} = \sqrt{\sigma^2 + \Delta^2} \\ \text{Positive unc.} = \sigma. \end{cases}$$

In addition to the global uncertainty related to the cross section measurement, it is worthy to check the individual contributions arising from the several sources described in Section 4.5. A breakdown list containing such information can be drawn once that dedicated pseudoexperiments have been generated separately for each kind of statistical error and systematic uncertainty (in the latter case by giving as input only the corresponding varied rates and shapes, and by drawing only the associated parameters).

4.6.2 Significance

In order to assess the sensitivity of the analysis method, i.e. determining the probability of the observed signal being just a background fluctuation, an hypothesis test is performed. Two ensembles of pseudoexperiments are carried out, one involving only contributions from background processes, the other integrating also the signal events, according to the Standard Model predictions. Each ensemble is used to compute, for each pseudoexperiment, the following test statistic which corresponds to a log-likelihood ratio:

$$Q = -2ln\frac{L(\beta^s = 1)}{L(\beta^s = 0)}. \tag{4.20}$$

The likelihood function is the one described by Eq. 4.16, which implements the background-only hypothesis ($\beta^s = 0$) or the signal+background hypothesis ($\beta^s = 1$). The *expected Q-value* (Q_1) is defined as the median value of the Q distribution obtained from the signal+background ensemble of pseudoexperiments ($f(Q|s+b)$); it is employed in the determination of the *p-value*, which quantifies instead the probability

that the background-only hypothesis describes accurately our results:

$$p_b = P(Q \leq Q_1|b) = \frac{\int_{-\infty}^{Q_1} f(Q|b)dQ}{\int_{-\infty}^{+\infty} f(Q|b)dQ}, \tag{4.21}$$

where $f(Q|b)$ represents the Q distribution obtained from the background-only pseudo-experiments. The expected significance is then derived by converting this p-value into units of standard deviation of a normal distribution:

$$\text{significance} = \sqrt(2) * Erf^{-1}(2p_b - 1), \tag{4.22}$$

$$\text{where } \; Erf(z) = \frac{2}{\sqrt{\pi}} \int_0^z e^{-t^2} dt.$$

The observed significance can be assessed following an analogous procedure: one should first of all extract the *observed Q-value* by evaluating the test statistic from the fit to the data, and then obtain the corresponding *observed p-value*.

4.6.3 Upper limit

Since the significance computed as described above will not reach 3σ for the two s-channel analyses, and the uncertainty associated to the cross section measurements will be still considerable in both cases, the results will be expressed in terms of an upper limit [148, 149]. Among several procedures to draw frequentist upper limits, the CL_s method has been chosen; it is in fact the most conservative, leads to the same results of a Bayesian limit on the mean value of a poissonian or gaussian distribution, and it would eventually allow for comparisons with other experiments.
It can be determined once that another *p-value* associated to the signal+background hypothesis is computed, similarly to what has been discussed for 4.21:

$$p_{s+b} = P(Q \geq Q_0|s+b) = \frac{\int_{Q_0}^{\infty} f(Q|s+b)dQ}{\int_{-\infty}^{+\infty} f(Q|s+b)dQ}. \tag{4.23}$$

Q_0 represents the *expected Q-value*, defined this time as the median of the Q distribution obtained from the background-only ensemble of pseudoexperiments $f(Q|b)$. p_{s+b} has thus to be interpreted as the probability of finding a Q-value greater or equal to Q_0, under the assumption of the signal+background hypothesis.
The signal model is regarded as excluded at a confidence level of $1 - \alpha = 95\%$ if:

$$CL_s \equiv \frac{p_{s+b}}{1 - p_b} < \alpha, \tag{4.24}$$

where p_b is defined in Eq. 4.21. This actually means that the Standard Model s-channel cross section is rescaled up to reach the CL_s exclusion value of 95 % confidence level. The corresponding observed limit can simply be determined by replacing the Q_0 value with the one obtained by computing the test statistic from real data.

Chapter 5

s-channel cross section analysis at 7 TeV

Having introduced the characteristic phenomenology of the s-channel single top production, and cited the main difficulties arising in the signal discrimination, we will now present the global procedure undertaken to extract the cross section. We will focus, in this chapter, on the analysis performed with the full dataset collected by the ATLAS detector at a center of mass energy of 7 TeV. Starting with an introduction on the data and simulation samples, we will detail the event preselection aimed at a primary skimming to reduce the background contamination. Then, the multivariate approach motivated in Section 4.3 will be explained; it is essentially based on the development of two Boosted Decision Trees (BDT) classifiers, each one trained with the goal of discerning the signal kinematical and topological features from the ones of an important source of background. The two discriminant output distributions are employed in a sequential way: after having performed a cut on one of them to reduce the W+jets contamination, the other is fitted to extract the signal contribution. The statistical analysis will allow to set a limit on the production cross section, investigate the corresponding statistical and systematic uncertainties, together with the significance.

5.1 Dataset

5.1.1 Data sample

The analysis uses the full proton-proton collision data collected in 2011 at a center of mass energy of 7 TeV. Events are selected with unprescaled single electron and muon triggers, then filtered using a Good Runs List (GRL) [1] which requires the stability of the LHC beams and the good quality of the ATLAS sub-components and triggers. The resulting total luminosity of the data sample is 4.66 fb^{-1}.

[1] Data are continuously monitored online and offline to give a full status of the detector and data taking environment; for each luminosity block, which is a basic time unit of data taking, flags are assigned for every subsystem and checked by the center trigger processor (CTP).

5.1.2 Monte Carlo samples

The Monte Carlo simultations employed for each of the physics processes that fulfill our event selection have been already described in Section 4.4; we will hence report only two schematic tables summarizing the set of samples which model the top electroweak and strong production (Table 5.1), and the other background sources (Table 5.2). For the estimation of some of the systematic effects, Monte Carlo samples with huge statistics are required and the fast simulation package ATLFAST2 [150] is used instead of the full GEANT4 detector modeling.

Process	σ [pb]	Generator	N_{events}
t-channel ($\ell\nu$)	20.9	AcerMC+Pythia	9 000 000
s-channel ($\ell\nu$)	1.5	Powheg+Pythia	900 000
Wt (all decays)	15.7	Powheg+Pythia	950 000
$t\bar{t}$ (no fully hadronic)	90.6	Powheg+Pythia	10 000 000
$t\bar{t}$ (no fully hadronic)	90.6	MC@NLO+Jimmy	15 000 000
t-channel ($e\nu$)	7.0	AcerMC+Herwig	200 000
t-channel ($\mu\nu$)	7.0	AcerMC+Herwig	200 000
t-channel ($\tau\nu$)	7.0	AcerMC+Herwig	200 000
Wt (all decays)	15.7	AcerMC+Herwig	300 000
Wt (all decays)	15.7	AcerMC+Pythia	300 000
s-channel More/Less PS ($e\nu$)	0.5	AcerMC+Pythia	200 000
s-channel More/Less PS ($\mu\nu$)	0.5	AcerMC+Pythia	200 000
s-channel More/Less PS ($\tau\nu$)	0.5	AcerMC+Pythia	200 000
$t\bar{t}$ More/Less PS (no fully hadronic)	90.6	AcerMC+Pythia	10 000 000

Table 5.1: Monte Carlo samples used to simulate baseline top and top pair productions, and to estimate the systematic uncertainy related to their theory modelling. The associated cross sections (which include the W decay branching ratio of 0.108 per lepton flavour) are also shown.

Process	σ [pb]	Generator	N_{events}
$Z \to \ell\ell$ + 0 parton	2506.8	ALPGEN+JIMMY	24 000 000
$Z \to \ell\ell$ + 1 partons	504.1	ALPGEN+JIMMY	6 000 000
$Z \to \ell\ell$ + 2 partons	151.5	ALPGEN+JIMMY	2 200 000
$Z \to \ell\ell$ + 3 partons	42.0	ALPGEN+JIMMY	900 000
$Z \to \ell\ell$ + 4 partons	10.5	ALPGEN+JIMMY	235 000
$Z \to \ell\ell$ + 5 partons	3.0	ALPGEN+JIMMY	75 000
$W \to \ell\nu$ + 0 parton	25 992.5	ALPGEN+JIMMY	10 500 000
$W \to \ell\nu$ + 1 partons	4 699.2	ALPGEN+JIMMY	7 500 000
$W \to \ell\nu$ + 2 partons	1 360.8	ALPGEN+JIMMY	11 250 000
$W \to \ell\nu$ + 3 partons	366.8	ALPGEN+JIMMY	3 000 000
$W \to \ell\nu$ + 4 partons	92.4	ALPGEN+JIMMY	750 000
$W \to \ell\nu$ + 5 partons	25.2	ALPGEN+JIMMY	210 000
$W \to \ell\nu + b\bar{b}$ + 0 parton	56.8	ALPGEN+JIMMY	475 000
$W \to \ell\nu + b\bar{b}$ + 1 partons	42.9	ALPGEN+JIMMY	205 000
$W \to \ell\nu + b\bar{b}$ + 2 partons	20.8	ALPGEN+JIMMY	175 000
$W \to \ell\nu + b\bar{b}$ + 3 partons	9.1	ALPGEN+JIMMY	70 000
$W \to \ell\nu + c\bar{c}$ + 0 parton	153.0	ALPGEN+JIMMY	1 275 000
$W \to \ell\nu + c\bar{c}$ + 1 partons	125.6	ALPGEN+JIMMY	1 050 000
$W \to \ell\nu + c\bar{c}$ + 2 partons	62.5	ALPGEN+JIMMY	525 000
$W \to \ell\nu + c\bar{c}$ + 3 partons	20.4	ALPGEN+JIMMY	170 000
$W \to \ell\nu + c$ + 0 parton	979.5	ALPGEN+JIMMY	6 500 000
$W \to \ell\nu + c$ + 1 partons	311.6	ALPGEN+JIMMY	2 070 000
$W \to \ell\nu + c$ + 2 partons	77.2	ALPGEN+JIMMY	520 900
$W \to \ell\nu + c$ + 3 partons	17.3	ALPGEN+JIMMY	115 000
$W \to \ell\nu + c$ + 4 partons	4.3	ALPGEN+JIMMY	30 000
WW (all decays)	17.0	HERWIG	2 400 000
WZ (all decays)	5.5	HERWIG	1 000 000
ZZ (all decays)	1.3	HERWIG	250 000

Table 5.2: Monte Carlo samples used for simulation of W+jets, Z+jets and diboson productions, with the associated cross sections.

5.2 Selection of lepton+jets events

This section is dedicated to describe the "refinement" of the physics objects reconstructed within the ATLAS detector, as well as the preliminary cuts applied to select lepton+jets events, leading to the definition of signal and control regions.

5.2.1 Object definition

The main features of the physics objects which are of interest for the s-channel cross section analysis have been introduced in Chapter 3; only additional requirements, therefore, will be presented in the following.
Electron candidates that pass the tight++ identification criteria are selected if the pseudorapidity of the corresponding cluster is $|\eta_{cl}| < 2.47$ (excluding the calorimeter barrel-endcap transition region: $1.37 < |\eta_{cl}| < 1.52$), and if $p_T > 25$ GeV. Isolation criteria require, in addition, minimum calorimeter activity and only few tracks in an $\eta - \phi$ cone around the electron; the first condition is gauged using the Etcone20 variable, defining the total energy of the cells in a cone of radius $\Delta R = 0.2$ around the candidate, corrected for pile-up events depending on the number of vertices; the second one with Ptcone30, the scalar sum of the transverse momenta of all the tracks within a cone of $\Delta R = 0.3$ around the electron, not including the p_T of the latter. Electrons are selected with Etcone20 and Ptcone30 at 90% isolation efficiency; moreover, to suppress the further contamination from non-prompt leptons, electrons are removed when a jet is detected within ΔR = 0.2 from the electron direction.
Muon candidates, identified by matching the muon spectrometer hits with the inner detector tracks (combined μ), are required to fulfill the tight requirements listed in Section 3.2.3, where isolation is also included, $p_T > 25$ GeV and $|\eta| < 2.5$. The jet-overlap removal described above is also applied for muons.
Jets are reconstructed from calorimeter clusters using the anti-k_T algorithm with a radius parameter of 0.4, correcting the detector response by p_T- and η-dependent factors to provide an average energy scale calibration. In order to reject the possible background contamination and the in-time pileup, we apply the event cleaning cuts detailed in Section 3.3.2, and the jet vertex fraction cut described in Section 3.3.5 ($|JVF| > 0.75$); furthermore, jet candidates have to fulfill $p_T > 30$ GeV. Since the single top s-channel signature is identified by the presence of a pair of bottom quarks, we employ the MV1 algorithm introduced in Section 3.3.6 to select b-jets. In order to detect the secondary vertices with enough resolution, jets are required to be central, within the inner detector pseudorapidity acceptance of $|\eta| < 2.5$. The operating point of the MV1 tagger chosen for this analysis corresponds to 85% b-tagging efficiency and a light (charm) quark rejection factor of 9 (2) measured, respectively, in $t\bar{t}$ and inclusive-jets simulated samples; the choice of such a loose criterion is subject to the necessity of obtaining a consistent MC modeling of the preselected data while maintaining low loss in signal acceptance. The 70% working point, which optimizes the signal discrimination, introduces in fact b-tagging scale factors that are sensitively smaller than unity in the jet momentum range of interest for the analysis, and cause non negligible discrepancies between the observed and the simulated distributions; a

comparison with the 85% working point scale factors is reported in Figs. 5.1 and 5.2. It should be noted that such consideration derives only from the analysis of the nominal samples and is not based on the evaluation of the different b-tagging uncertainty introduced by the two operating points.

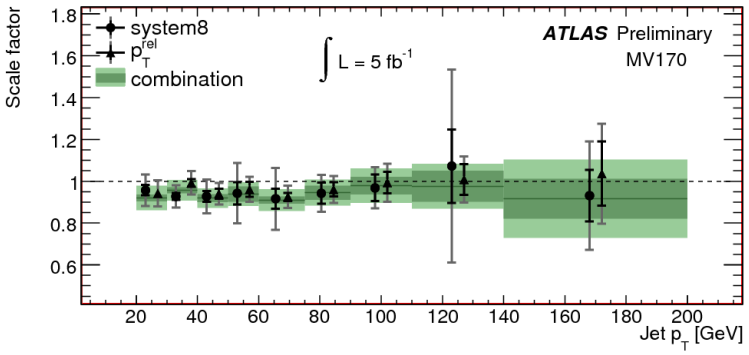

Figure 5.1: The data-to-simulation scale factor for the MV1 tagging algorithm at 70% effciency, obtained by combining the p_T^{rel} and system8 results. The dark green band represents the statistical uncertainty of the combined scale factor while the light green band shows the total uncertainty.

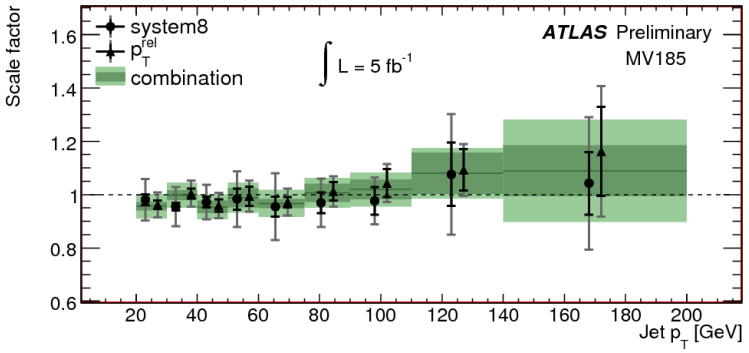

Figure 5.2: The data-to-simulation scale factor for the MV1 tagging algorithm at 85% effciency, obtained by combining the p_T^{rel} and system8 results. The dark green band represents the statistical uncertainty of the combined scale factor while the light green band shows the total uncertainty.

The **missing transverse momentum**, which measures the momentum imbalance due to escaping neutrino in the transverse plane with respect to the proton beams, is reconstructed according to Eq. 3.15. The longitudinal component is instead determined by using the W-boson pole-mass constraint ($m(W) = 80.42$ GeV) which leads to the following quadratic equation:

$$p_z^2(\nu) - 2 \cdot \frac{\mu \cdot p_z(\ell)}{E^2(\ell) - p_z^2(\ell)} \cdot p_z(\nu) + \frac{E(\ell)^2 \cdot E_T^{miss\,2} - \mu^2}{E^2(\ell) - p_z^2(\ell)} = 0 \tag{5.1}$$

$$\mu = \alpha + E_T^{miss}\beta \;\;,\;\; \alpha = \frac{m(W)^2 - m(\ell)^2}{2} \;\;,\; \beta = p_x(\ell)\cos\phi^{miss} + p_y(\ell)\sin\phi^{miss}; \tag{5.2}$$

$p_i(\ell)$ are the momentum components of the charged lepton, $E(\ell)$ its energy, $p_z(\nu)$ the longitudinal momentum component of the neutrino and ϕ^{miss} the azimuthal angle associated to the missing transverse energy. When the solutions of Eq. 5.1 are both real, the one with the smallest absolute value is chosen since it provides the best resolution for the neutrino longitudinal momentum. Due to the non-perfect resolution and calibration of the missing transverse energy measurement and also to additional contributions (extra neutrinos from B-hadrons and τ decays, extra p_T contributions due to ISR/FSR ...), however, the transverse mass of the W can be larger than its pole-mass making the determinant negative; in that case, the imaginary solution is replaced by the $p_z(\nu)$ value obtained for $\Delta = 0$. The neutrino and the lepton four-momenta are then combined to reconstruct the W-boson which, also, is associated to the leading and subleading b-jet to build up two top candidates called in the following $Top\_j1\nu l$ and $Top\_j2\nu l$, respectively.

5.2.2 Event preselection

Before applying specific criteria to select s-channel final states, generic event quality requirements are employed to remove mis-reconstructed and non-collision background events; besides the jet cleaning previously mentioned, events must contain at least one good primary vertex candidate, reconstructed from at least five tracks, and not be affected by EMCal noise bursts.
The signal signature is afterwards reproduced by requiring exactly one isolated lepton (electron or muon) with p_T >25 GeV, missing transverse momentum fulfilling the condition $E_T^{miss} > 30$ GeV, and the presence of one, two or three jets. A rejection cut exploiting the kinematic properties of the multijet events, which are characterized by a low W boson transverse mass, is also employed to reduce the number of fake leptons:

$$\mathrm{m_T(W)} = \sqrt{2\mathrm{p_{T,\ell}E_T^{miss}}\left(1 - \cos\Delta\phi\left(\mathrm{p_{T,\ell}, E_T^{miss}}\right)\right)} > 30\ GeV. \tag{5.3}$$

Several samples, which differ in the number of selected jets and b-jets, are employed to discriminate signal and properly control the main sources of background in the statistical fit; they are presented in detail in the following.

- The **signal-enriched sample** is constituted by the events passing the above-mentioned preselection and which are characterized by the signature of exactly two jets (*2 jets bin*).

  - The 2-tag sample ($2J2B$) collects the ones with both jets achieving the b-tagging requirement. It represents our signal region, that will be skimmed further on via a cut on one of the boosted decision trees output distributions. The expected s-channel purity corresponds to the 1.4%, to be compared with the W+jets and $t\bar{t}$ contaminations, which are respectively of 47% and 33%.
  - The 1-exclusive-tag sample ($2J1B_{exc}$), formed by the events with exactly one of the selected jets tagged as b-jet, is used for the procedure of W+jets normalization.
  - The 1-inclusive-tag sample ($2J1B_{inc}$) comprises the events with at least one of the selected jets tagged as b-jet. W+jets events belonging to this high statistics sample are employed in the training phase of the boosted decision trees. This choice is a consequence of the lack of statistics of the 2J2B W+jets sample, and has been validated in Appendix A.

- The **W+jets-enriched sample** is constituted by the events passing the above-mentioned preselection and which are identified by the signature of 1 jet only (*1 jet bin*).

  - The 1-tag sample ($1J1B$) is composed by the ones with one b-tag jet, and is essentially used to constrain this background in the statistical fit that will be performed to extract the signal cross section. The expected W+jets purity reaches the 90%, while the s-channel and $t\bar{t}$ contaminations are around 0.1% and 1.3% respectively.
  - The pretag sample ($1J0B$), containing events on which no b-tagging requirement is applied, is needed for the W+jets normalization in the 1 jet bin.

- The **$t\bar{t}$-enriched sample** is constituted by the events passing the above-mentioned preselection and identified by the signature of exactly 3 jets (*3 jets bin*).

  - The 2-exclusive-tag sample ($3J2B_{exc}$) is composed by the ones with exactly two b-tag jets, and similarly allows to constrain this background in the final statistical fit. In this control region the expected $t\bar{t}$ purity is 67%, the W+jets contamination still important (23%), and the s-channel contamination negligible (0.4%).
  - The 1-exclusive-tag sample ($3J1B_{exc}$), made by events with exactly one b-tag jet, is required for the W+jets normalization in the 3 jets bin.

5.2.3 Data-driven background estimates

Events stemming from **multijet** processes that pass the s-channel selection have been analyzed via different data-driven techniques (Sec. 4.2.1), depending on the final state characterized by the signature of two b-jets and one electron or muon. In the first case the jet-electron model has been employed: a dijet MC sample shapes this background and a maximum likelihood fit to the transverse W boson mass (in the sideband $m_T(W)$ <30 GeV) fixes its normalization. Since this method has been specifically set up for electrons, a different strategy is preferred to extract the fake leptons contribution to the muon channel. The matrix method relies on the analysis of two data samples, that differ on the application of the isolation criteria; a "loose" template, which has by definition more statistics, can be specifically reweighted to represent the multijet background.

W+jets background normalization, poorly predicted by simulation, is also determined from data via the tag counting method explained in Section 4.2.2 coupled to a χ^2 minimization procedure. The overall and the heavy-flavour scale factors are computed separately for each jet bin using a "pretag" and a "tag" set; the measured values, together with the considered datasets, are reported in Table 5.3. With a frequentist approach based on the generation of pseudoexperiments we estimate a total uncertainty of 10-30 % (increasing with the number of selected jet) on the overall normalization, of $\approx$ 100% on $K_{b\bar{b}}$, of $\approx$ 50 % on K_c and of 15-35% on K_{light}.

jet bins	"pretag" sample	"tag" sample	$Norm$	$K_{b\bar{b}}$	K_c	K_{light}
1 jet	$1J0B$	$1J1B$	1.0	1.4	1.0	1.0
2 jets	$2J1B_{exc}$	$2J2B$	1.0	1.3	1.0	0.9
3 jets	$3J1B_{exc}$	$3J2B_{exc}$	0.9	1.3	1.0	0.8

Table 5.3: Overall and flavour correction factors for W+jets obtained with the combined electron+muon sample for the 3 jet-bins.

W+jets estimate should be realized in dedicated control regions in order to be completely independent from the extraction of the signal contribution. Two factors, nonetheless, justify and legitimate the choice of using the 2J2B sample: on one hand, the fact that after the preselection described in Section 5.2.2, the expected s-channel purity is still as low as 1.4%; on the other hand, the necessity of modeling properly the 2 jets 2-tag sample, since K-factors obtained from the pretag and the 1-tag samples would not be representative of the flavour contributions typical of the signal-enriched region. The impact of the statistical and systematic uncertainties on the W+jets normalization estimated via the generation of pseudo-experiments has not been considered in the statistical fit to extract the s-channel cross section in order to avoid double counting of the sources of error. We associated to the W+jets normalization the conservative uncertainty defined in Section 4.5.

5.2.4 Event yields

Once described how the expected signal and background contributions are estimated, we present the predicted and observed event yields for the electron and muon channels in each jet bin used in the analysis; more precisely, since the "pretag" sample in each jet-bin is only used to determine the data-driven W+jets normalization, we focus on the "tag" datasets.
As previously introduced, W+jets production constitutes the dominant process for the 1J1B sample; due to the intrinsic properties of the b-tagger algorithm and the loose operating point chosen, the rate of events with a W boson produced in association with a light or charm-jet is still the highest one after the b-tagging requirement. Also in the 2J2B sample, W+jets represents the most important background source; the contribution from the different flavors shows almost the same tendency, although much more $Wb\bar{b}$ and $Wc\bar{c}$ events are selected since two tagged jets are required. Top pair production represents the second ranked background process, followed by the t-channel single top production.
Finally, the $3J2B_{exc}$ dataset is characterized by an overwhelming $t\bar{t}$ contribution, arising from semileptonic top decays in which one jet escapes the selection.
To have a quick visualization of the modeling and the relative contribution from each physics process, the distribution of the transverse W boson mass is reported for the three event samples; we show, in this way, a key observable for the analysis which allows to monitor the position of the peak. For completeness, the most important lepton and jets kinematic variables are collected in appendix B; overall, a good agreement between data and simulation is spotted in all the plots, as well as in the following tables summarizing the contributions of each physics process.

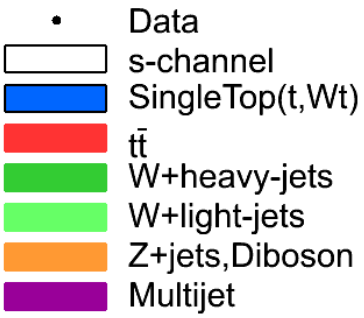

Figure 5.3: Legend showing the color code used in the following plots.

1 jet-1 tag sample

Table 5.4 lists the event yields obtained after the application of the preselection cuts and the b-tagging requirement in the 1 jet bin. The expectations are derived using theoretical cross sections with the exception of the multijet and W+jets samples, for which they are extracted with data driven techniques.

Channel	1J1B muon	1J1B electron
s channel	195 ± 2	150 ± 1
t channel	2618 ± 6	2119 ± 5
Wt channel	494 ± 6	433 ± 5
$t\bar{t}$	2363 ± 10	1997 ± 9
W+light jets	10153 ± 418	74371 ± 358
Wbb	59074 ± 57	4796 ± 50
Wcc	4728 ± 66	7622 ± 57
Wc	59074 ± 212	47227 ± 190
Z+jets	4727 ± 47	4260 ± 48
diboson	1225 ± 6	961 ± 5
Multijet	5068 ± 2534	7780 ± 3890
Total prediction	191191 ± 3944	151719 ± 3915
data	193092	150143
$S/\sqrt{(B)}$	0.46	0.39
S/B	0.11 %	0.10%

Table 5.4: Event yields for the electron and muon channels in the 1 jet 1-tag sample. The uncertainty parametrises the limited size of the MC samples and the error associated to the data-driven normalization for the multijet background.

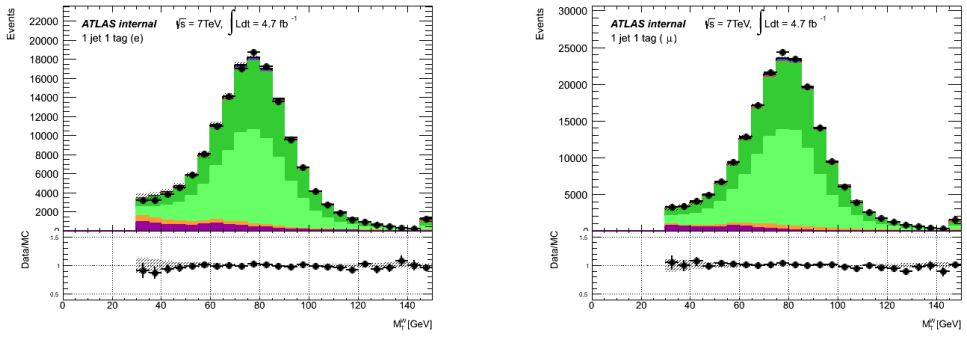

(a) (b)

Figure 5.4: (a) W boson transverse mass distribution in the 1 jet 1-tag sample for the electron+jets (b) and the muon+jets channels. The shadowed bands correspond to the total statistical uncertainty in the expected Monte Carlo distributions added to a 50% uncertainty on the multijet normalization.

2 jets-2 tag sample

Table 5.5 lists the event yields obtained after the application of the preselection cuts in the 2 jets bin, together with the b-tagging requirement for both jets. The conventions on the expectations and the corresponding uncertainties are the ones described in the previous paragraph.

Channel	2J2B muon	2J2B electron
s channel	166 ± 1	133 ± 1
t channel	715 ± 3	594 ± 3
Wt channel	275 ± 4	245 ± 4
$t\bar{t}$	3998 ± 13	3213 ± 12
W+light jets	2377 ± 63	1761 ± 51
Wbb	1174 ± 26	866 ± 22
Wcc	921 ± 22	671 ± 18
Wc	1784 ± 40	1496 ± 37
Z+jets	177 ± 6	237 ± 9
diboson	142 ± 2	118 ± 2
Multijet	281 ± 141	540 ± 270
Total prediction	11788 ± 165	9906 ± 283
data	12258	10088
$S/\sqrt{(B)}$	1.51	1.36
S/B	1.37 %	1.38%

Table 5.5: Event yields for the electron and muon channels in the 2 jets 2-tag sample. The uncertainty parametrises the limited size of the MC samples and the error associated to the data-driven normalization for the multijet background.

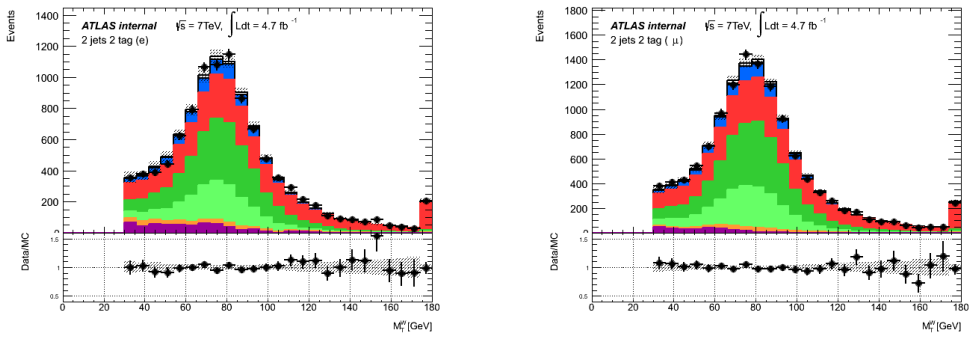

(a) (b)

Figure 5.5: (a) W boson transverse mass distribution in the 2 jets 2-tag sample for the electron+jets (b) and the muon+jets channels. The shadowed bands correspond to the total statistical uncertainty in the expected Monte Carlo distributions added to a 50% uncertainty on the multijet normalization.

3 jet-2 tag sample

Table 5.6 lists the event yields obtained after the application of the preselection cuts in the 3 jets bin, with the b-tagging requirement for two among the three jets.

Channel	$3J2B_{exc}$ **muon**	$3J2B_{exc}$ **electron**
s channel	55 ± 1	43 ± 1
t channel	597 ± 5	500 ± 5
Wt channel	411 ± 6	344 ± 5
$t\bar{t}$	7888 ± 19	6641 ± 17
W+light jets	1048 ± 39	807 ± 32
Wbb	590 ± 19	498 ± 18
Wcc	496 ± 17	394 ± 15
Wc	649 ± 25	548 ± 23
Z+jets	104 ± 4	224 ± 6
diboson	60 ± 1	52 ± 1
Multijet	160 ± 80	420 ± 210
Total prediction	11788 ± 103	10476 ± 219
data	12611	10696
$S/\sqrt{(B)}$	0.50	0.42
S/B	0.45 %	0.41%

Table 5.6: Event yields for the electron and muon channels in the 3 jets 2-tag sample. The uncertainty parametrises the limited size of the MC samples and the error associated to the data-driven normalization for the multijet background.

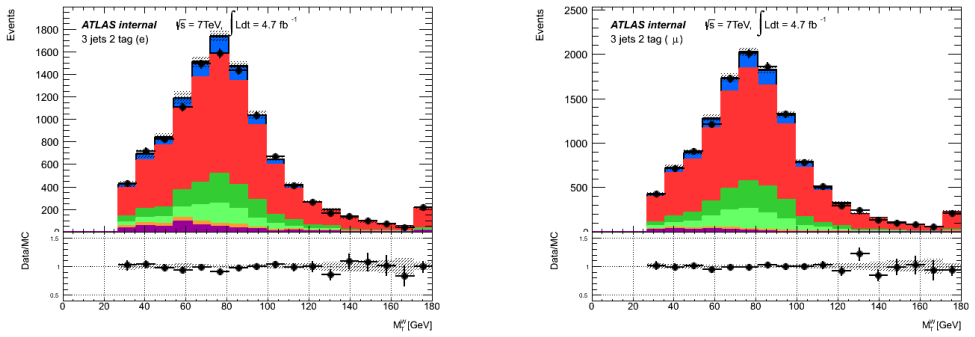

(a) (b)

Figure 5.6: (a) W boson transverse mass distribution in the 3 jets 2-tag sample for the electron+jets (b) and the muon+jets channels. The shadowed bands correspond to the total statistical uncertainty in the expected Monte Carlo distributions added to a 50% uncertainty on the multijet normalization.

5.3 Multivariate analysis

As previously mentioned, there are two main reasons for which the determination of the single top s-channel cross section is so challenging: firstly, even in the 2 jets 2-tag sample the signal-to-background ratio is still very low, reaching 1.4% for both electron and muon channels as highlighted in table 5.5; secondly, there is a considerable similarity in the signal and backgrounds distributions, as can be seen in the plots collected in Appendix B. To optimize the signal discrimination, therefore, we carry out a multivariate analysis based on boosted decision trees (Section 4.3). More precisely, since the s-channel single top production is mainly affected by two sources of background characterized by different kinematics, *two* classifiers are defined. The first one is aimed at optimizing the separation of W+jets events from top quark events; its output distribution is used afterwards to perform a cut defining a "signal region" where the W+jets contamination is strongly reduced. After this step, the main background contribution originates from top quark pair events, and we use hence a second classifier focused on separating $t\bar{t}$ from signal events.

5.3.1 BDT classifier against W+jets

The implementation of a BDT classifier designed to discriminate signal events from $Wb\bar{b}$, $Wc\bar{c}$, Wc and Wlight jets production is performed in the 2 jets 2-tag sample. In principle, 2J2B events should be randomly splitted to create the training and the test samples; however in order to avoid significant limitations due to statistical fluctuations, higher statistics samples are utilized. On one hand, W+jets events are modeled from the $2J1B_{inc}$ MC template both in the training and testing case, even if they are normalized to the expected 2J2B yields; on the other, s-channel events are produced by two different NLO generators, MC@NLO for training and POWHEG for testing. Both choices are legitimated in Appendix A, where the equivalence of the main normalized kinematical distributions of the samples in question has been proven. Finally, in order to reduce the statistical fluctuations, we combine the electron+jets and muon+jets final states, after having verified that the MC modelling adequately reproduces data in both cases.

The BDT input variables are chosen among the ones showing a good data/MC agreement and having a separation power S higher than 5% (the calculation has been detailed in Section 4.3.3). 28 variables belonging to several categories such as object/event kinematics and angular distributions, have been selected: they are sorted in Table 5.7 according to the corresponding separation power. All the validation plots are instead reported in Appendix C.

With the aim of improving the signal efficiency maintaining a good compatibility between training and test samples, that is avoiding overtraining, many configurations have been tuned. A setting making use of 600 decision trees with at maximum 4 nodes and a minimum of 40 events per final leaf has been chosen without pruning.

Variable	S	Definition
$\Delta\eta(l, j1)$	0.139	$\Delta\eta$ between the lepton and the leading jet
$p_T(j2)$	0.138	Second jet p_T
$Ht(j1, j2)$	0.136	Scalar sum of the p_T of the jets
$\Delta\eta(t2, j1)$	0.112	$\Delta\eta$ between the subleading jet and the top quark $Top\_j1\nu l$
$\Delta\eta(t1, j2)$	0.106	$\Delta\eta$ between the leading jet and the top quark $Top\_j2\nu l$
$\Delta R(l, j1)$	0.105	ΔR between the leading jet and the lepton
$\Delta\eta(j1, j2)$	0.104	$\Delta\eta$ between the leading and the second jet
$p_T(Top\_j1\nu l)$	0.103	p_T of the top quark reconstructed through the leading jet
H_T	0.098	Scalar sum of the p_T of the selected jets, lepton and neutrino
$p_T(Top\_j2\nu l)$	0.096	p_T of the top quark reconstructed through the second jet
$P_T(l, j1)$	0.096	p_T of the system composed by the lepton and the leading jet
$Whelicity\_j1\nu l$	0.095	W helicity[1] from the top quark (reconstructed via the leading jet) decay
$\Delta\Phi(t1, j2)$	0.091	$\Delta\Phi$ between the subleading jet and the top quark
$m(Top\_j1\nu l)$	0.088	Mass of the top quark reconstructed through the leading jet
$E_T(l)$	0.087	Transverse energy of the lepton
$Centrality$	0.083	Ratio of H_T to the sum of the objects energies
$\Delta\Phi(t2, j1)$	0.077	$\Delta\Phi$ between the leading jet and the top quark
$Sphericity$	0.073	Sphericity measures the summed $p_\perp^2$ with respect to the event axis
$E(j2)$	0.072	Second jet energy
$m(j1, j2)$	0.066	Mass of the system composed by the jets
$E_T(j1, j2)$	0.066	Transverse energy of the system composed by the jets
$cos\theta(Top\_j2\nu l)$	0.062	Top spin correlation[2] in helicity basis
$m(l, j2)$	0.062	Mass of the system composed by the lepton and the subleading jet
$Whelicity\_j2\nu l$	0.061	W helicity from the top quark (reconstructed through the second jet)
$m(l, j1)$	0.058	Mass of the system composed by the lepton and the leading jet
$m(Top\_j2\nu l)$	0.053	Mass of the top quark reconstructed with the second jet and the leptons
$Aplanarity$	0.051	Aplanarity measures the transverse momentum out of the event plane

Table 5.7: Input variables for the BDT_{W+jets}

[1] Cosine of the angle between the direction of the lepton in the W-boson reference frame, and the W-boson in the top quark reference frame.

[2] Cosine of the angle between the direction of the lepton in the top quark reference frame, and the top in the center of mass reference frame.

The cut values maximizing the increase of separation between parent and daughter nodes are selected by scanning over the variable range with a granularity of 20 bins. Finally, the classification performance is increased by boosting via the Gradient Boosting algorithm that, with respect to the most popular AdaBoost method, offers more robustness in presence of outliers owing to a binomial log-likelihood loss function. The parameter which controls the weight of the individual trees is called shrinkage, and is set to 0.5.

Table 5.8: Parameters of the BDT_{W+jets}

NTrees	600
MaxDepth	4
nEventsMin	40
PruneMethod	NoPruning
nCuts	20
BoostType	Gradient Boosting
Shrinkage	0.5

The signal and background BDT outputs for the training and test samples are shown in Fig. 5.7(a); the Kolmogorov-Smirnov test quantifying the compatibility between two distributions shows that the classifier is not affected by overtraining. Fig. 5.7(b) illustrates, on the other hand, the background rejection as a function of the signal efficiency obtained with the classifier. To stress further the gain that the application of this multivariate technique entails in the single top s-channel discrimination, we compare the separation power of the BDT output distribution (30%) with the one of the highest ranked variable (14%); it is therefore suitable to cut on such derived distribution, instead of a simpler set of direct variables.

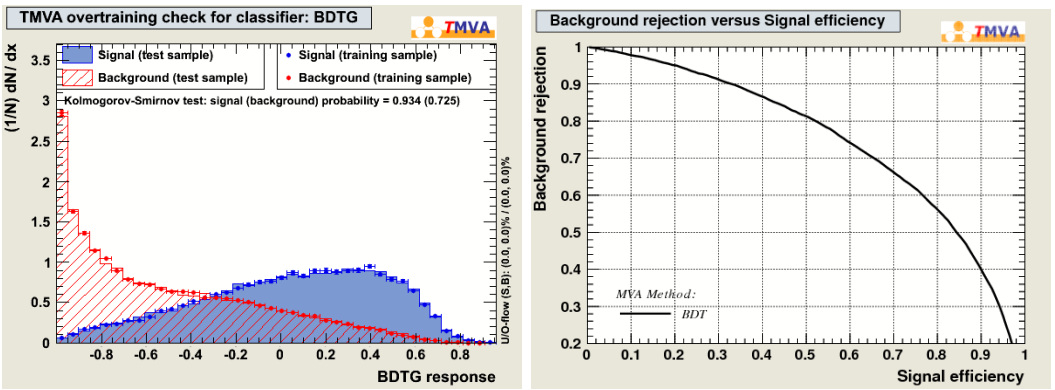

(a) (b)

Figure 5.7: (a) Classifier outputs for training and test samples for signal and W+jets. (b) Background rejection plotted as a function of the signal efficiency.

5.3.2 BDT classifier against top quark pairs

Following the same procedure as the one described in the previous paragraph, we optimize a classifier to reject $t\bar{t}$ events. Again, we investigate the possibility of using larger statistics sets to model the shapes. Similarly to what has been realized for the BDT_{W+jets}, the signal training and test samples are produced, respectively, with POWHEG and MC@NLO generators. This procedure can not be applied in the case of $t\bar{t}$ sample because of an important presence of negative weights in the events generated with MC@NLO, which are treated in a different way by the boosting algorithm; to avoid overtraining, thus, top quark pair production is modeled by the nominal POWHEG 2J2B sample.

A large set of distributions has been analyzed, and 20 well modeled variables (Table 5.9) characterized by a high separation power have been selected as BDT input. The corresponding validation plots are instead reported in Appendix C.

Variable	S	Definition
$p_T(l,\nu,j1,j2)$	0.215	p_T of the system composed by all the final particles (vectorial sum)
$\Delta\Phi(t1,j2)$	0.193	$\Delta\Phi$ between the top quark and the second jet
$\Delta\Phi(t2,j1)$	0.178	$\Delta\Phi$ between the top quark and the leading jet
$p_T(l)+E_T^{miss}$	0.159	Sum of the lepton p_T and of the transverse missing energy
E_T^{miss}	0.125	Transverse missing energy
$m(Top\_j2\nu l)$	0.089	Mass of the top quark reconstructed through the subleading jet
$\Delta\Phi(j1,j2)$	0.089	$\Delta\Phi$ between the 2 jets
$p_T(l)$	0.085	Lepton p_T
$m_T(W)$	0.084	Transverse mass of the W boson
$\eta(j1,j2)$	0.081	Pseudorapidity of the system constituted by the 2 jets
$H_T(j1,j2)$	0.081	Scalar sum of the jets p_T
$m(Top\_j1\nu l)$	0.075	Mass of the top quark reconstructed through the leading jet
$m(l,j2)$	0.073	Mass of the system composed by the second jet and the lepton
$m(l,\nu,j1,j2)$	0.069	Mass of the system composed by all the final particles
$\Delta R(j1,j2)$	0.063	ΔR between the two jets
$\eta(l,j1)$	0.063	Pseudorapidity of the system constituted by the leading jet and the lepton
$m(l,j1)$	0.061	Mass of the system composed by the leading jet and the lepton
$\Delta\Phi(j2,E_T^{miss})$	0.059	$\Delta\Phi$ between the second jet and the transverse missing energy
$\Delta\eta(t2,j1)$	0.051	$\Delta\eta$ between the top quark and the leading jet

Table 5.9: Input variables for the $BDT_{t\bar{t}}$

The best setting found for the classifier is summarized in Table 5.10. 300 decision trees with a maximum depth of 4 and at least 35 events in each final leaf are used without pruning. The cut values that optimize the separation between the parent and the daughter nodes are selected by scanning over the variable range with a granularity of 30 bins. A "forest of trees" is built via the Gradient Boosting algorithm, with a shrinkage parameter of 0.7.

Table 5.10: Parameters of the $BDT_{t\bar{t}}$

NTrees	300
MaxDepth	4
nEventsMin	35
PruneMethod	NoPruning
nCuts	30
BoostType	Gradient Boosting
Shrinkage	0.7

BDT outputs for signal and background are compared in Fig. 5.8(a), where the agreement between the training and test samples indicates that no overtraining is spotted. The background rejection as a function of the signal efficiency is also reported in Fig. 5.8(b). Finally, we check the separation power for the $BDT_{t\bar{t}}$ output distribution; this is found to be 32%, still greater than the one of the most discriminating variable: S=21% for $p_T(l, \nu, j1, j2)$.

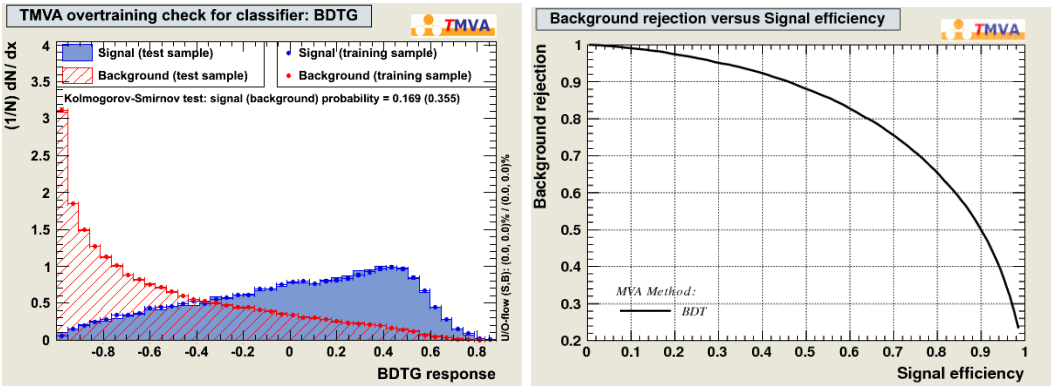

(a) (b)

Figure 5.8: (a) Classifier outputs for training and test samples for signal and W+jets. (b) Background rejection plotted as a function of the signal efficiency.

5.4 Fit procedure

The strategy of the current analysis is based on a simultaneous fit of three variables which will allow to extract the single top s-channel cross section and constrain, at the same time, the most significant backgrounds. As previously mentioned, the event selection has been carried out for three distinct samples: the 1 jet and 3 jets bins characterized respectively by a high W+jets and top quark pair purity, the 2 jets bin enriched in signal events. In the next paragraphs we will explain how a distribution can be selected for each of those samples, and be used for the fit with the intent of reducing the systematic uncertainties and avoiding statistical fluctuations that may lead to unreasonable contributions from some background sources.

5.4.1 Signal discrimination owing to BDT classifiers

For the 2 jets bin we followed a multivariate approach resulting in the two discriminant distributions presented in Figs. 5.9(b) and 5.9(a). After a check on the data/MC agreement, which is rather good considering the double b-tagging requirement, we can proceed by applying a threshold on the BDT_{W+jets} distribution. This practice defines a signal region where the remaining contamination of W+jets is minimal and implies, at the same time, that the impact of the large W+jets uncertainty on the cross-section determination will be strongly reduced.

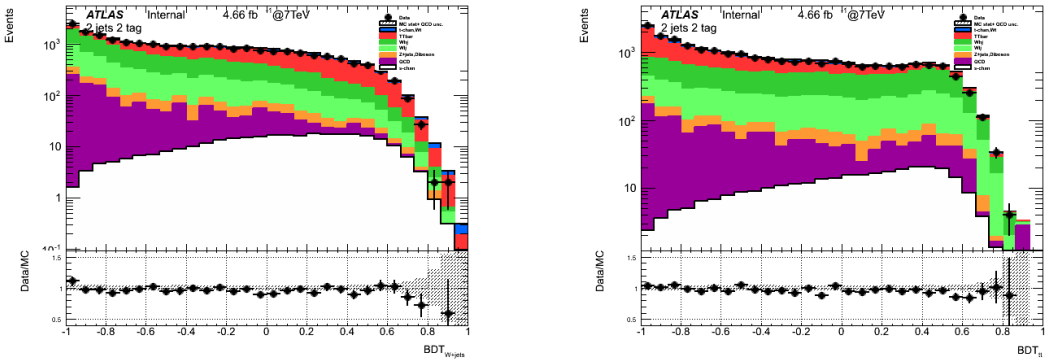

(a) (b)

Figure 5.9: (a) Output distributions of the classifiers trained against W+jets and against and (b) $t\bar{t}$ for the 2J2B sample. A logarithmic scale is used to better localize the signal, in white..

The threshold value has been defined to optimize the expected 95% C.L. limit [2] and total systematic uncertainty on the s-channel cross-section, as summarized in Table 5.11. The best configuration corresponds to the cut BDT_{W+jets} output greater than 0.4; hence, a $BDT_{t\bar{t}}$ classifier created with the set of events satisfying such criterion will be fitted. Figs. 5.10(a) and 5.10(b) depict the result of this choice, and add further information on the global uncertainty associated to the BDT distributions allowing a more precise control of the modelling. The shadowed bands represent in this case the statistical uncertainty depending on the size of the Monte Carlo samples, and all the systematic uncertainties affecting each channel except the ones related to the normalization. The latter are treated by the statistical tool in a particular way, being incorporated both in the gaussian constraints in the fit and in the generation of pseudoexperiments, so we preferred not to include them in the plots. In spite of the poor statistics, we can confirm that the expected $BDT_{t\bar{t}}$ distribution matches the observed one within the uncertainty interval.

[2] This is expressed in Table 5.11 in terms of the scale factor SF that multiplies the predicted cross section, meaning that $\sigma_{s-channel} \leq SF * \sigma^{SM}_{s-channel}$.

BDT_{W+jets} **cut**	**0.3**	**0.4**	**0.5**
s channel	94	68	42
t channel	189	127	74
Wt channel	58	37	19
$t\bar{t}$	1270	831	461
W+jets	623	409	220
diboson, Z+jets	40	28	16
Multijet	33	22	6
Total MC	2307	1541	838
Data	2215	1415	779
$S/\sqrt{B}$	2.0	3.1	1.5
S/B	4.2 %	4.6 %	5.3 %
Limit Exp. scale factor	3.74	3.14	3.72
Total uncertainty	261%	160%	210%

Table 5.11: Event yields for several thresholds on the BDT_{W+jets} distribution.

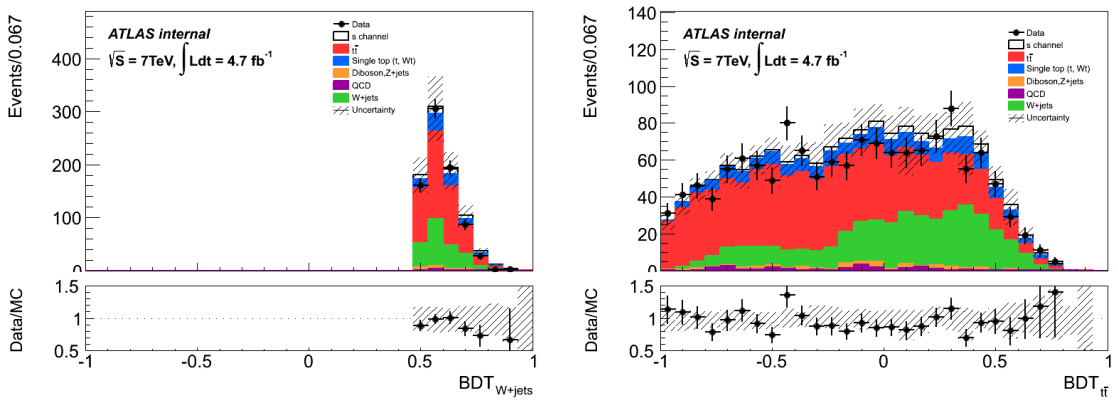

(a) (b)

Figure 5.10: (a) Output distributions of the classifiers trained against W+jets and (b) and against $t\bar{t}$ for the 2J2B signal region defined by the events fulfilling the requirement BDT_{W+jets} output>0.4. The shadowed band accounts for all the systematic and statistical uncertainties of each MC sample, except the ones related to the normalization.

5.4.2 W+jets constraint

For the 1 jet bin, the selection of a distribution to be fitted in order to constrain the W+jets events is not really crucial, since the signal discrimination is realized elsewhere. Therefore we choose arbitrarily the transverse mass of W-boson, which is reproduced in Fig. 5.11; in the plot, the shadowed bands reflect the statistical error and all the systematic uncertainties affecting each channel, except the ones related to the normalization.

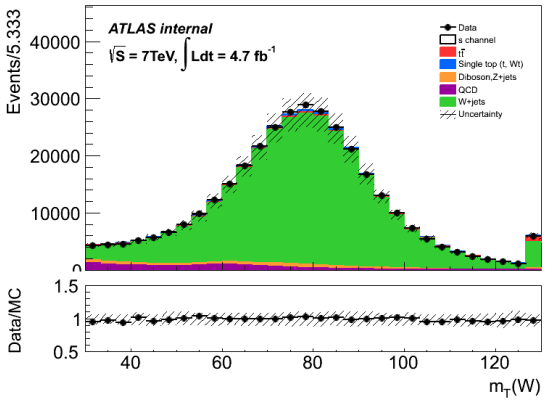

Figure 5.11: Transverse mass of W boson for the 1J1B sample. The shadowed band accounts for all the systematic and statistical uncertainties of the MC samples, except the ones related to the normalization.

5.4.3 Top quark pair constraint

For the 3 jets bin, analogous considerations can be made. We decided to adopt the distribution of the vectorial sum of the transverse momenta of all the final particles in order to constrain $t\bar{t}$ events in the fit. This variable, characterized by the highest separation power between top pair and single top productions, is modelled properly as Fig. 5.12 illustrates; in the plot, the shadowed bands reflect the statistical error and all the systematic uncertainties affecting each channel, except the ones related to the normalization.

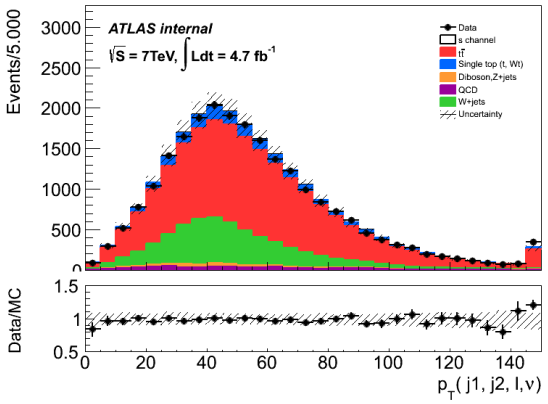

Figure 5.12: Transverse momentum of the system composed by all the final particles for the $3J2B_{exc}$ sample. The shadowed band accounts for all the systematic and statistical uncertainties the MC samples, except the ones related to the normalization.

5.5 Systematic and statistical uncertainties

The several sources of systematic uncertainty described in Section 4.5, as well as the effects due to the statistics of the collected data and simulated event samples, need to be propagated in the s-channel cross section measurement. Such uncertainties have an impact on the rate of the individual background and signal contributions and, in some cases, on the shape of the distributions to be fitted; this effect is properly taken into account in the generation of pseudoexperiments.

5.5.1 Rate uncertainties

The relative systematic and statistical uncertainties on the predicted event yields for the signal and background processes are listed in Table 5.12 for the 1 jet bin, in Table 5.13 for the 2 jets bin signal region, and finally in Table 5.14 for the 3-jets bin.
In order to reduce the statistical fluctuations in the fit, some production mechanisms have been merged; on one hand, the Wt and t-channel single top processes, on the other the Z+jets and diboson productions. The multijet background is not represented because the only uncertainty associated to it is the one on the data-driven normalization (50%).

5.5.2 Shape uncertainties

In order to determine the sources of uncertainty which have a significant impact on $BDT_{t\bar{t}}$, $m_T(W)$ and $p_T(l, \nu, j1, j2)$ shapes, a Kolmogorov-Smirnov test is performed by comparing, for each signal and background process and each systematic component, the Monte Carlo nominal distributions with the $\pm 1\sigma$ systematically varied distributions. Only shape differences leading to a Kolmogorov-Smirnov test value lower than 0.6 are considered as relevant sources of systematic shape uncertainties; the final list is reported in Table 5.15.
The uncertainties due to the statistics of the Monte Carlo samples are only integrated via the induced variations in shape, which are thus included for every physics process. The statistical uncertainties on the rates are implemented through Poissonian fluctuations on the expected event yelds.

Rate systematic [%]	s-channel	$t\bar{t}$	t-channel,Wt	W+jets	Z,diboson
E_T^{miss} energy scale & res	-1.76/-2.05	-1.19/-1.94	-1.83/-2.04	-1.46/-2.32	0.07/-0.35
E_T^{miss} pile-up	-1.66/-2.14	-1.85/-1.94	-1.76/-2.13	-1.09/-2.66	2.17/-4.41
Lepton trigger & reco	1.93/-1.93	1.95/-1.95	1.94/-1.94	1.93/-1.93	1.94/-1.94
Electron resolution	-1.11/-1.11	-1.11/-1.1	-1.09/-1.12	-1.09/-1.07	-1.11/-1.23
Electron scale	-0.87/-1.24	-1.08/-1.18	-0.91/-1.23	-0.75/-1.32	-1.02/-1.33
Muon ID resolution	-0.85/0.85	-0.83/-0.83	-0.84/-0.84	-0.84/-0.85	-0.78/-0.79
Muon MS resolution	-0.86/-0.87	-0.83/-0.84	-0.85/-0.85	-0.84/-0.84	-0.77/-0.76
Muon scale	-0.67/0	-0.77/0	-0.69/0	-0.55/0	-0.54/0
Jet reconstruction	-1.91/0	1.85/0	1.92/0	-1.93/0	-1.16/0
Jet resolution	-2.90/0	-1.67/0	-2.90/0	-0.64/0	3.00/0
Jet scale	-6.94/1.21	-16.8/9.26	-6.81/1.21	6.37/-6.14	8.65/-7.88
Jet vertex fraction	-0.75/-0.55	-0.32/-1.02	-0.76/-0.56	-0.78/-0.46	-0.77/-0.64
b-tagging	4.99/-5.87	4.51/5.66	4.82/-5.25	2.22/-2.40	1.90/-2.10
c-tagging	0.04/-0.04	0.74/-0.74	0.33/-0.33	0.43/-0.43	0.21/-0.21
mis-tagging	0.18/-0.18	0.57/-0.58	0.47/-0.48	6.17/-6.17	8.23/-8.23
W+jets shape	—	—	—	-4.27/0	—
Luminosity	1.18/-1.18	1.18/-1.18	1.18/-1.18	1.18/-1.18	1.18/-1.18
ISR/FSR	-0.37/0.37	-17.4/17.4	—	—	—
Theory modelling, s-ch.	-2.43/2.43	—	—	—	—
Theory modelling, $t\bar{t}$	—	-26.7/26.7	—	—	—
Parton showering, t-ch.	—	—	-3.37/3.37	—	—
Parton showering, W	—	—	-2.38/2.38	—	—
Normalization	—	11.0/-11.0	6.0/-6.0	56.0/-56.0	56.0/-56.0

Table 5.12: Relative variations (up/down) due to the various instrumental, theoretical and normalization uncertainties on the signal and background event yields in the 1 jet 1-tag sample, quoted in per cent. Muon scale, jet reconstruction and jet resolution are asymmetric uncertainties for which only the positive variation is reported.

Rate systematic [%]	s-channel	$t\bar{t}$	t-channel,Wt	W+jets	Z,diboson
E_T^{miss} energy scale & res	-0.84/-0.02	-0.09/ 0.15	-0.58/ 0.11	-6.76/-7.41	-3.74/4.16
E_T^{miss} pile-up	-1.03/ 1.90	0.62/ 0.83	-0.76/ 0.90	-0.04/-3.66	-0.30/-0.35
Lepton trigger & reco	1.95/-1.95	1.99/-1.99	1.98/-1.98	1.93/-1.93	2.24/-1.94
Electron resolution	0.00/-0.15	0.16/-0.04	-0.15/-0.18	0.95/-0.46	-1.10/ 0.24
Electron scale	0.00/ 0.03	-0.32/ 0.21	-0.19/-0.16	-1.69/-0.56	7.33/-8.04
Muon ID resolution	-0.09/0.03	0.76/ 0.02	-0.09/ 0.03	-0.04/-0.20	-0.00/-0.00
Muon MS resolution	0.00/-0.11	0.25/ 0.05	-0.04/ 0.06	0.44/-12.9	-0.00/-0.00
Muon scale	-0.14/0	0.15/0	0.02/0	-3.96/0	0/0
Jet reconstruction	0.09/ 0	1.33/0	1.20/0	1.32/0	1.24/0
Jet resolution	-1.56/0	-0.16/0	-0.53/0	4.34/0	6.97/0
Jet scale	2.09/-4.26	-6.56/3.52	0.17/-0.16	-12.0/ 0.13	-3.34/-6.43
Jet vertex fraction	0.49/-0.71	1.00/-1.01	0.64/-0.56	0.59/-0.79	0.86/-0.91
b-tagging	8.15/-18.3	7.64/-15.4	5.87/-12.4	15.9/-3.08	0.73/-0.44
c-tagging	0.06/-0.07	0.20/-0.20	0.33/-0.33	0.90/-0.86	0.65/-0.62
mis-tagging	0.23/-0.23	0.91/-0.91	4.21/-4.20	12.2/-11.5	16.5/-15.2
W+jets shape	—	—	—	-8.6/0	—
Luminosity	1.18/-1.18	1.18/-1.18	1.18/-1.18	1.18/-1.18	1.18/-1.18
ISR/FSR	-8.09/8.09	-1.41/1.41	—	—	—
Theory modelling, s-ch.		—	—	—	—
Theory modelling, $t\bar{t}$	—	-1.25/1.25	—	—	—
Parton showering, t-ch.	—	—	-8.01/8.01	—	—
Parton showering, W	—	—	-1.59/1.59	—	—
Normalization	—	11.0/-11.0	6.0/-6.0	60.0/-60.0	60.0/-60.0

Table 5.13: Relative variations (up/down), due to the various instrumental, theoretical and normalization uncertainties on the signal and background event yields in the 2 jets 2-tag signal region, quoted in per cent. Muon scale, jet reconstruction and jet resolution are asymmetric uncertainties for which only the positive variation is reported.

Rate systematic [%]	s-channel	$t\bar{t}$	t-channel,Wt	W+jets	Z,diboson
E_T^{miss} energy scale & res	-0.06/-0.08	0.05/-0.02	0.12/0.02	2.85/-0.17	0.21/-0.74
E_T^{miss} pile-up	0.05/-2.10	1.19/-0.05	0.24/-0.01	0.51/-0.30	0.15/-0.53
Lepton trigger & reco	1.96/-1.96	1.96/-1.96	1.96/-1.96	1.95/-1.95	2.13/-1.94
Electron resolution	-0.03/-0.17	0/0	-0.04/0.11	0/0	0.11/-0.59
Electron scale	0.25/-0.29	0.18/-1.18	0.25/-0.13	0.24/-0.24	-0.59/-0.80
Muon ID resolution	0/0	0/0	0/0.01	0.03/-0.01	-0.03/-0.02
Muon MS resolution	0/0	0/0	0.02/0.02	-0.02/0	0.06/0
Muon scale	0.11/0	0.13/0	0.16/0	0.26/0	0.10/0
Jet reconstruction	-0.04/-0	0.03/0	-0.05/0	-0.08/0	-0.14/0
Jet resolution	0.01/0	-0.83/0	-0.60/0	5.36/0	9.97/0
Jet scale	8.22/-6.24	-2.75/-0.05	5.84/-4.56	15.2/-8.15	19.9/-8.16
Jet vertex fraction	0.77/-1.01	1.05/-1.20	0.84/-1.06	1.10/-1.12	1.23/-1.21
b-tagging	8.85/-13.9	8.46/-11.41	7.72/-10.1	1.88/-2.45	0.92/-2.45
c-tagging	0.33/-0.33	1.93/-1.93	2.35/-2.35	7.05/-6.74	5.77/-5.51
mis-tagging	0.09/-0.09	1.67/-1.59	2.67/-2.65	11.9/-11.1	15.3/-14.1
W+jets shape	—	—	—	-7.26/0	—
Luminosity	1.18/-1.18	1.18/-1.18	1.18/-1.18	1.18/-1.18	1.18/-1.18
ISR/FSR	-1.39/1.39	-4.70/4.70	—	—	—
Theory modelling, s-ch.	-2.43/2.43	—	—	—	—
Theory modelling, /ttbar	—	-1.77/1.77	—	—	—
Parton showering, t-ch.	—	—	-2.87/2.87	—	—
Parton showering, Wt	—	—	-0.91/0.91	—	—
Normalization	—	11.0/-11.0	6.0/-6.0	66.0/-66.0	66.0/-66.0

Table 5.14: Relative symmetric (up/down) or asymmetric (up/0) variations due to the systematic uncertainties on the signal and background event yields in the 3 jets 3-tag sample, quoted in per cent.

Shape systematic	1J1B processes	2J2B processes	$3J2B_{exc}$ processes
Electron scale	W+jets, t-channel, Wt	W+jets	–
Jet scale	$t\bar{t}$, single top, W+jets, Z+jets, diboson	s-channel	$t\bar{t}$, t-channel, Wt
Jet resolution	$t\bar{t}$, single top	–	$t\bar{t}$
E_{T}^{miss} energy scale & res	t-channel, Wt, W+jets, Z+jets, diboson	$t\bar{t}$, single top	$t\bar{t}$, t-channel, Wt
E_{T}^{miss} pile-up	W+jets	s-channel, $t\bar{t}$	$t\bar{t}$
W+jets shape	—	—	W+jets

Table 5.15: Shape variations on the signal and background distributions due to instrumental and theoretical modeling uncertainties, included in the fit.

5.6 Results

By using the statistical framework illustrated in Section 4.6, we present in the following the expected and observed results of the s-channel cross-section measurement. The outcome of the simultaneous maximum likelihood fit to the $BDT_{t\bar{t}}$ output distribution in the 2J2B signal region, the $m_T(W)$ in the 1J1B sample and the $p_T(l, \nu, j1, j2)$ in the $3J2B_{exc}$ sample is summarized in Table 5.16. The parameters β (appearing in Eq. 4.16) represent, for each physics process, the ratio of the contributions preferred by data in the selected phase space, to the ones predicted by the Standard Model; the rescaled expectation values $\tilde{\nu}$ are also reported for the three jet bins.

Process	β	$\tilde{\nu} \cdot \beta$, $1J1B$	$\tilde{\nu} \cdot \beta$, $2J2B$	$\tilde{\nu} \cdot \beta$, $3J2B_{exc}$
s-channel	0.27 ± 0.49	94	19	27
$t\bar{t}$	0.98 ± 0.01	3943	812	15053
t-channel, Wt	1.00 ± 0.06	5547	163	1845
W+jets	1.01 ± 0.00	311397	415	5435
Z+jets, diboson	0.65 ± 0.07	7145	18	285
Multijet	1.00 (fixed)	12824	22	580

Table 5.16: Scale factors β extracted for the signal and background processes from the template fit of the $BDT_{t\bar{t}}$, $m_T(W)$ and $p_T(l, \nu, j1, j2)$ distributions; the corresponding errors account for the statistics and the normalization uncertainties. The rescaled expectation values $\tilde{\nu} \cdot \beta$ are also given.

For W+jets and $t\bar{t}$ the fitted β are close to unity and characterized by a very low uncertainty, which underlines that the control regions considered in the simultaneous fit actually improve the constraint on the two main background sources. Also the t-channel and Wt single top productions are found to be in agreement with the theoretical predictions, even if the fit uncertainty related to their scale factor is slightly higher. The β factor representing the combined production of Z+jets and diboson shows instead a large deviation from one even within the uncertainty band; it should be noticed, nonetheless, that this background is characterized by low statistics in the three samples, and a very large width of the gaussian constraint (Eq. 4.16). The most striking lack of sensitivity concerns the signal, whose scale factor is significantly lower than the SM prediction; considering the large fit uncertainty affecting it, such a result should be taken with a grain of salt. Given that the total expected uncertainty affecting the s-channel production measurement is of +153% -168%, we prefer to express the result in term of a limit on the cross section, rather than a measure for which the needed sensitivity has not been achieved. Before doing that, it is however instructive to investigate the relative contributions to the total uncertainty on the s-channel cross section, performing a systematic breakdown via the generation of separate ensembles of pseudoexperiments. As Table 5.17 illustrates, the sources of uncertainty having the highest impact on the s-channel cross section measurement are the jet energy scale (±89%), the b-tagging efficiency (±52%) and the missing

transverse momentum (±56% for the scale and resolution, ±44% for the pile-up); the contribution of the last two terms arises mainly from variations in the shapes, since the rates are almost unchanged with respect to the nominal sample. Also the effect of the data statistic (±50%) is considerable, while the one of MC statistic is mitigated by the use of the additional 1J1B and $3J2B_{exc}$ control samples.

Systematic	Uncertainty β_s [%]	
Data statistics	+50.8	-50.8
Simulation statistics	+19.0	-19.1
Luminosity	+12.5	-12.3
Theory & data-driven normalization	+28.8	-28.8
E_{T}^{miss} energy scale & res	+67.3	-65.8
E_{T}^{miss} pile-up	+38.2	-51.6
Lepton trigger & reconstruction	+21.9	-21.9
Electron energy resolution	+26.5	-17.7
Electron energy scale	+15.6	-13.6
Muon ID momentum resolution	+15.2	-15.2
Muon MS momentum resolution	+35.0	-41.0
Muon momentum scale	+8.1	-10.2
Jet energy resolution	+8.9	-8.9
Jet energy scale	+86.1	-92.3
Jet reconstruction	+20.4	-18.2
Jet vertex fraction	+7.7	-7.6
b-tagging	+49.4	-55.4
c-tagging	+35.2	-35.3
mis-tagging	+36.4	-36.4
ISR/FSR	+11.2	-11.4
Theory modelling, s-channel	+9.7	-9.9
Theory modelling, $t\bar{t}$	+18.5	-18.5
Parton showering, t-channel	+21.3	-21.3
Parton showering, Wt-channel	+7.8	-7.8
W+jets shape	+5.4	-3.9
Total systematic	+144.3	-160.2
Total (systematic+statistics)	+153.0	-168.1

Table 5.17: Breakdown of the relative contributions to the expected statistical and systematic uncertainties on the s-channel scale factor estimated for the signal events. The uncertainties are quoted in per cent.

The final $BDT_{t\bar{t}}$ classifier distribution with the background contributions subtracted is displayed in Figure 5.13, the signal and background Monte Carlo distributions being re-scaled to the likelihood fit results (Table 5.16). The data fluctuations are spreaded around zero not allowing to infer the presence of a visible s-channel signal, demonstrating qualitatively the lack of sensitivity of the analysis.

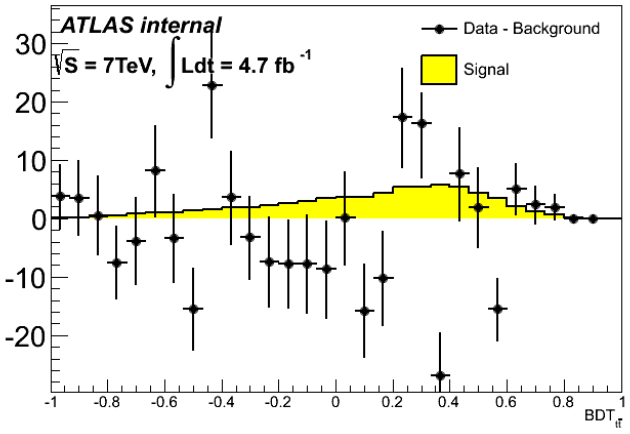

Figure 5.13: Signal distributions of the $BDT_{t\bar{t}}$ classifier after background subtraction for the signal events in the 2 jets 2-tag sample. The error bars only account for the statistical uncertainty.

5.6.1 Significance and limit

The cross section measurement presented above corresponds to an observed significance of 0.6 standard deviations, and an expected significance of 0.8 standard deviations, determined according to the procedure described in Section 4.6.2.
The slightly higher expected significance is due to an expected median value of the test statistic ($Q_{exp} = 0.4$) lower than its observation ($Q_{obs} = 1.8$) and therefore to a smaller probability that the signal contribution arises just from a background fluctuation (expected p-value equal to 0.2 compared to 0.3 for the observed p-value). Figure 5.14 shows the test statistic function obtained for the signal-plus-background and background-only ensembles tests, with the expected and observed Q values.
With the CLs method, the observed (expected) limit set at 95% C.L is found to be 4.7 (3.1) times the SM prediction, corresponding to $\sigma_{s-channel}$ <21.7 pb (14.3 pb).

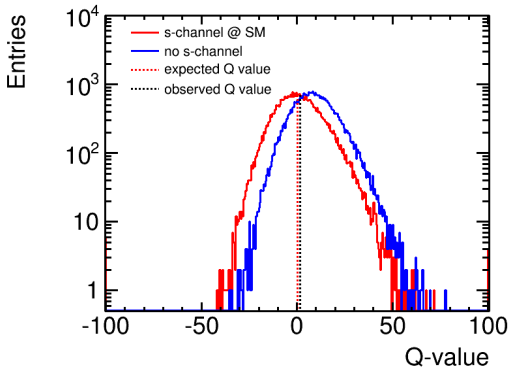

Figure 5.14: Test statistic distributions for the signal-plus-background (red histogram) and background-only (blue histogram) ensembles tests.

5.7 Conclusion

We presented in this chapter the challenging analysis of the single top s-channel production via proton-proton collisions taking place at a center of mass energy of 7 TeV. This process arises via quark-antiquark annihilation and is therefore not favoured at the LHC, where its approximate NNLO cross section is predicted to be very low, around 4.63 pb; as a result, the signal is almost drowned into the main sources of background, even after the event preselection.
The priority for this preliminary study, thus, consisted in achieving a reasonable s-channel discrimination owing to a multivariate technique based on the developement of two BDT classifiers trained against the main sources of background. The output distributions were used in a complementary way, one to implement a further event selection, and the other to perform a maximum likelihood fit to extract the signal contribution. As already stressed, the fit outcome was improved by the addition of two more variables defined in specific background-enriched control regions. The uncertainty affecting the cross-section measurement was estimated via the generation of pseudoexperiments accordingly to the rate and shape variations due to different systematic and statistical uncertainties. Unfortunately, the strong impact of the ones related to the jet energy scale, the b-tagging efficiency and the E_T^{miss} measurement, as well as the low statistics, jeopardized the sensitivity of the analysis, which does not reach the significance of 1 σ. It should be mentioned, however, that the measured upper limit of 21.7 pb (14.3 pb expected) on the s-channel cross section improves the previous ATLAS result. The conference note [151] reports the cut-based analysis performed with an integrated luminosity of 0.70 fb^{-1} and a reduced set of systematic uncertainties, which achieved a 95% C.L. limit of 26.5 pb (20.5 pb expected).
At the same time, some fragilities and intrinsic problems identified in this work have been considered under a pedagogical point of view to trace guidelines for the 8 TeV analysis that followed. First of all, we deduced the fundamental importance of an efficient b-tagger; the choice of the working point was dictated by the necessity of not degrading the data/MC agreement because of the b-tagging scale factors, but it was far to be the optimal solution to discriminate the signal. In a previous analysis version, in fact, a tighter b-tagging criterion resulted in a higher significance of the s-channel cross section measurement; however, the likelihood fit tried to compensate the data/MC discrepancy by assigning unrealistic scale factors to very precisly known background sources. This choice implied poor signal purity, which imposed an additional event selection realized in terms of a boosted decision trees to reduce the the W+jets contamination; such procedure granted high separation performance, but had the shortcoming of complicating the analysis strategy. Another problem we spotted concerned the size of the MC simulation samples. The low statistics affected the BDT training by limiting the options on the classifier parameters; a more "agressive" configuration could have been selected if no overtraing was present. In conclusion, despite the limited sensitivity of the 7 TeV s-channel analysis, many interesting lessons have been learned and allowed to approach the 8 TeV analysis with a deeper understanding of the signal phenomenology, and an improved knowledge of the multivariate techniques which have been proven to play a crucial role.

Chapter 6

s-channel cross section analysis at 8 TeV

After having detailed the s-channel analysis performed with proton-proton collisions at a center of mass energy of 7 TeV, we describe in this chapter how the same cross section measurement is extracted using the full dataset collected by the ATLAS detector at 8 TeV. The analysis at higher energy is made more difficult by the fact that the signal cross section increases with $\sqrt{s}$ more slowly than the background ones. Nonetheless, the higher cumulated statistics reduces in a significant way the impact of the uncertainty on the measurement.
A simpler strategy than the one specified in the previous chapter has been preferred, even if based on the same multivariate approach: a unique boosted decision trees classifier is implemented to discriminate the s-channel events from the top quark pair and W+jets productions. Such backgrounds are checked in specific control regions; the signal significance and cross section upper limit, however, are extracted via a template likelihood fit of the BDT output only, without including any additional variable defined in background-enriched samples. The next paragraphs follow the same structure than Chapter 5, giving an overview of the simulation samples employed to interpret the data, a description of the event selection and the multivariate technique, to conclude with the results achieved via the statistical analysis.

6.1 Dataset

6.1.1 Data sample

The analysis reported here is based on the LHC proton-proton collisions data collected by the ATLAS detector in 2012, at a center of mass energy of 8 TeV; the corresponding integrated luminosity is of 20.3 fb^{-1}.

6.1.2 Monte Carlo samples

The Monte Carlo simulation codes used to model the kinematic distributions of the signal and background processes at $\sqrt{s}$=8 TeV have been already introduced in Sec-

tion 4.4. We will therefore present here only two schematic tables collecting the list of samples used to simulate the electroweak and strong production of top quarks (Table 6.1), and the several sources of background (Table 6.2).

Sample	Generator	σ [pb]	N_{events}
s-channel (l+jets)	POWHEG+PYTHIA6	1.8	1 199 895
Wt (DR)	POWHEG+PYTHIA6	22.3	999 692
t-channel (l+jets, t)	POWHEG+PYTHIA6	18.4	2 994 591
t-channel (l+jets, $\bar{t}$)	POWHEG+PYTHIA6	9.9	1 999 888
$t\bar{t}$ (no full-had.)	POWHEG+PYTHIA6	137.3	14 996 424
$t\bar{t}$ (no full-had.)	POWHEG+HERWIG	137.3	29 960 959
$t\bar{t}$ (no full-had.)	MC@NLO+HERWIG	137.3	14 997 103
$t\bar{t} \rightarrow l\nu l\nu$ + 0 parton	ALPGEN+HERWIG	8.3	799 897
$t\bar{t} \rightarrow l\nu l\nu$ + 1 partons	ALPGEN+HERWIG	8.8	808 897
$t\bar{t} \rightarrow l\nu l\nu$ + 2 partons	ALPGEN+HERWIG	5.7	529 996
$t\bar{t} \rightarrow l\nu l\nu$ + 3 partons	ALPGEN+HERWIG	3.8	359 997
$t\bar{t} \rightarrow l\nu qq$ + 0 parton	ALPGEN+HERWIG	34.5	3 359 080
$t\bar{t} \rightarrow l\nu qq$ + 1 partons	ALPGEN+HERWIG	36.5	3 398 787
$t\bar{t} \rightarrow l\nu qq$ + 2 partons	ALPGEN+HERWIG	23.5	2 209 980
$t\bar{t} \rightarrow l\nu qq$ + 3 partons	ALPGEN+HERWIG	15.7	1 459 791
Wt (DS)	POWHEG+PYTHIA6	22.3	999 995
Wt	MC@NLO+HERWIG	22.3	1 999 194
t-channel (l+jets)	aMC@NLO+HERWIG	28.3	999 896
s-channel (e+jets)	MC@NLO+HERWIG	0.6	199 997
s-channel (μ+jets)	MC@NLO+HERWIG	0.6	200 000
s-channel (τ+jets)	MC@NLO+HERWIG	0.6	199 999
$t\bar{t}$ (no full-had., more PS)	ACERMC+PYTHIA6	137.3	14 985 986
$t\bar{t}$ (no full-had., less PS)	ACERMC+PYTHIA6	137.3	14 988 492

Table 6.1: Monte Carlo samples used to simulate the baseline top and top pair productions, and to estimate the systematic uncertainy related to their theory modelling. The associated cross sections (which include the W decay branching ratio of 0.108 per lepton flavour) are also shown. l indicates e, μ or τ.

Sample	Generator	σ [pb]	N_{events}
$Z \rightarrow ee + 0$ parton	ALPGEN+PYTHIA6	848.4	6 298 988
$Z \rightarrow ee + 1$ parton	ALPGEN+PYTHIA6	207.3	8 169 476
$Z \rightarrow ee + 2$ partons	ALPGEN+PYTHIA6	69.5	3 175 991
$Z \rightarrow ee + 3$ partons	ALPGEN+PYTHIA6	18.4	894 995
$Z \rightarrow ee + 4$ partons	ALPGEN+PYTHIA6	4.7	398 597
$Z \rightarrow ee + 5$ partons	ALPGEN+PYTHIA6	1.5	229 700
$Z \rightarrow \mu\mu + 0$ parton	ALPGEN+PYTHIA6	848.6	6 298 796
$Z \rightarrow \mu\mu + 1$ parton	ALPGEN+PYTHIA6	206.7	8 188 384
$Z \rightarrow \mu\mu + 2$ partons	ALPGEN+PYTHIA6	69.5	3 175 488
$Z \rightarrow \mu\mu + 3$ partons	ALPGEN+PYTHIA6	18.5	894 799
$Z \rightarrow \mu\mu + 4$ partons	ALPGEN+PYTHIA6	4.7	388 200
$Z \rightarrow \mu\mu + 5$ partons	ALPGEN+PYTHIA6	1.5	229 200
$Z \rightarrow \tau\tau + 0$ parton	ALPGEN+PYTHIA6	848.3	19 352 765
$Z \rightarrow \tau\tau + 1$ parton	ALPGEN+PYTHIA6	207.4	10 669 582
$Z \rightarrow \tau\tau + 2$ partons	ALPGEN+PYTHIA6	69.5	3 710 893
$Z \rightarrow \tau\tau + 3$ partons	ALPGEN+PYTHIA6	18.5	1 091 995
$Z \rightarrow \tau\tau + 4$ partons	ALPGEN+PYTHIA6	4.7	398 798
$Z \rightarrow \tau\tau + 5$ partons	ALPGEN+PYTHIA6	1.5	229 799
$W \rightarrow e\nu + 0$ parton	ALPGEN+PYTHIA6	9 208.2	29 434 220
$W \rightarrow e\nu + 1$ parton	ALPGEN+PYTHIA6	2 031.1	48 155 904
$W \rightarrow e\nu + 2$ partons	ALPGEN+PYTHIA6	614.3	17 554 347
$W \rightarrow e\nu + 3$ partons	ALPGEN+PYTHIA6	167.3	4 985 287
$W \rightarrow e\nu + 4$ partons	ALPGEN+PYTHIA6	42.8	2 548 292
$W \rightarrow e\nu + 5$ partons	ALPGEN+PYTHIA6	13.6	799 192
$W \rightarrow \mu\nu + 0$ parton	ALPGEN+PYTHIA6	9 208.0	31 965 655
$W \rightarrow \mu\nu + 1$ parton	ALPGEN+PYTHIA6	2 031.4	43 677 615
$W \rightarrow \mu\nu + 2$ partons	ALPGEN+PYTHIA6	614.4	17 611 454
$W \rightarrow \mu\nu + 3$ partons	ALPGEN+PYTHIA6	166.8	4 956 077
$W \rightarrow \mu\nu + 4$ partons	ALPGEN+PYTHIA6	42.7	2 546 595
$W \rightarrow \mu\nu + 5$ partons	ALPGEN+PYTHIA6	13.6	788 898
$W \rightarrow \tau\nu + 0$ parton	ALPGEN+PYTHIA6	9 208.0	31 902 157
$W \rightarrow \tau\nu + 1$ parton	ALPGEN+PYTHIA6	2 030.6	48 255 178
$W \rightarrow \tau\nu + 2$ partons	ALPGEN+PYTHIA6	614.4	17 581 943
$W \rightarrow \tau\nu + 3$ partons	ALPGEN+PYTHIA6	167. 2	4 977 982
$W \rightarrow \tau\nu + 4$ partons	ALPGEN+PYTHIA6	42.8	2 548 295
$W \rightarrow \tau\nu + 5$ partons	ALPGEN+PYTHIA6	13.6	789 096
$W \rightarrow l\nu + b\bar{b} + 0$ parton	ALPGEN+PYTHIA6	63.1	1 599 997
$W \rightarrow l\nu + b\bar{b} + 1$ parton	ALPGEN+PYTHIA6	51.3	1 398 396
$W \rightarrow l\nu + b\bar{b} + 2$ partons	ALPGEN+PYTHIA6	27.3	699 398
$W \rightarrow l\nu + b\bar{b} + 3$ partons	ALPGEN+PYTHIA6	12.7	398 397
$W \rightarrow l\nu + c\bar{c} + 0$ parton	ALPGEN+PYTHIA6	170.2	4 299 592
$W \rightarrow l\nu + c\bar{c} + 1$ parton	ALPGEN+PYTHIA6	150.3	3 987 891
$W \rightarrow l\nu + c\bar{c} + 2$ partons	ALPGEN+PYTHIA6	81.4	2 394 394
$W \rightarrow l\nu + c\bar{c} + 3$ partons	ALPGEN+PYTHIA6	32.3	985 295
$W \rightarrow l\nu + c + 0$ parton	ALPGEN+PYTHIA6	1228.2	22 769 047
$W \rightarrow l\nu + c + 1$ parton	ALPGEN+PYTHIA6	406.9	8 198 769
$W \rightarrow l\nu + c + 2$ partons	ALPGEN+PYTHIA6	106.2	2 090 290
$W \rightarrow l\nu + c + 3$ partons	ALPGEN+PYTHIA6	31.3	499 498
$W \rightarrow l\nu + c + 4$ partons	ALPGEN+PYTHIA6	6.6	199 499
WW	HERWIG	20.9	2 499 890
ZZ	HERWIG	1.5	245 000
WZ	HERWIG	7.0	999 998

Table 6.2: Monte Carlo samples used for the simulation of W+jets, Z+jets and diboson productions, with the associated cross sections. l indicates e, μ or τ.

6.2 Selection of lepton+jets events

By renouncing to the use of a second BDT classifier to improve the signal discrimination, the event selection is made tighter, as we will show in the following. First of all, we will remind some requirements established at the object reconstruction level, and introduce some further qualification criteria; afterwards, we will present more cuts aimed at selecting signal- and background-enriched final states.

6.2.1 Object definition

Electron candidates should be identified through a calorimeter cluster with $\eta_{cl} < 2.47$, excluding the barrel-endcap transition region ($1.37 < |\eta_{cl}| < 1.52$) where the instrumentation is limited. The transverse momentum threshold is raised to 30 GeV because some modelling issues are spotted in the low p_T range, and the expected signal over background ratio is improved within this new configuration. To reduce further the multijet background, the jet overlap removal, the EM calorimeter isolation of $\Delta R = 0.2$ and the track isolation of $\Delta R = 0.3$ at the working point of 90% efficiency are implemented, as for the 7 TeV study. Electrons, moreover, are demanded to have a longitudinal impact parameter from the primary vertex z_0 smaller than 2 mm and satisfy the tight++ selection.
Muon candidates, identified by combining track segments found in the inner detector and in the muon spectrometer, have to fulfill the tight requirements previously defined, including the variable isolation threshold. In order to have a common lepton selection, which is necessary when merging the two final states, muons should have a p_T larger than 30 GeV.
For **jets**, the same 7 TeV procedure of cleaning from the noisy calorimeter cells is applied; the suppression of in-time pileup is instead achieved in a slighly different way, by requiring $JVF > 0.5$ only for central jets with $p_T < 50$ GeV. Different p_T thresholds of 30 and 25 GeV are chosen to select signal- or background-enriched samples, respectively; the same approach is extended to the identification of jets originating from b-quarks, which is realized with the MV1 algorithm with tight or loose operating points. In order to select s-channel events, the b-tagging efficiency, estimated in data by using a combinatorial likelihood approach applied to dileptonic $t\bar{t}$ events, is 70%; the threshold applied on the tagger distribution is much tighter than the one chosen for the 7 TeV analysis, and corresponds in fact to a light jets rejection factor of 135. Fig. 6.1 illustrates the b-tagging efficiency scale factors as a function of the jet p_T, obtained by combining the four dileptonic $t\bar{t}$ decay channels. The control regions that will be defined hereafter are instead characterized by a looser b-tagging efficiency of 80%, which allows to obtain high statistics sets.
For leptonic single top events, it is assumed that the **missing transverse momentum**, reconstructed as explained in Section 3.4, corresponds to the neutrino transverse momentum. $p_z(\nu)$ is instead calculated with Eq. 5.1, which exploits the W-boson pole mass constraint. In case of negative discriminant, a more refined procedure than for the 7 TeV analysis has been implemented: the longitudinal momentum is still the solution obtained with Δ=0, but E_T^{miss} is modified (while preserving its azimuthal

angle) in such a way that it solves the quadratic equation corresponding actually to the configuration with a negative discriminant. The neutrino four-momentum described above is then combined with the lepton four-momentum in order to reconstruct the W-boson. The latter is finally associated to the b-jet which gives the W-b invariant mass closest to 172.5 GeV, to reconstruct the top quark candidate.

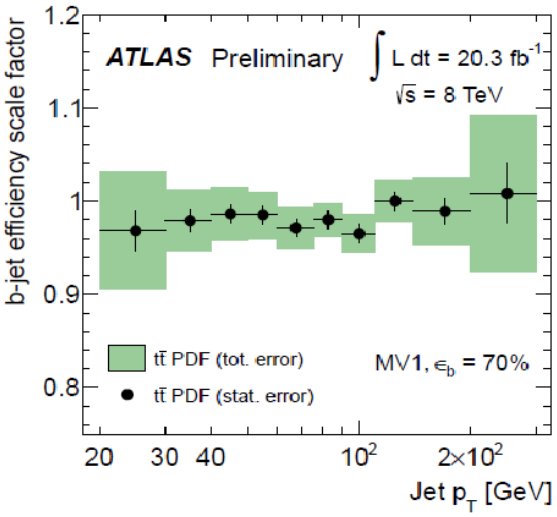

Figure 6.1: Data-to-simulation scale factors for the MV1 tagging algorithm at 70% efficiency. Both statistical only (black lines) and total errors (green shaded region) are shown.

6.2.2 Event selection

Once that the event quality requirements specified in Chapter 5 are satisfied, three different selection chains are developed in order to discriminate the single top s-channel production and define specific background-enriched control regions where the modelling can be easily checked. We insist on the fact that these additional samples, obtained by varying some criteria of the signal selection, will not be introduced in the fit to constrain $t\bar{t}$ and W+jets contributions, but just employed to verify that the simulation is reliable.

- The **Signal-enriched sample** is defined in a two step procedure. First of all, we preselect the final states outlined by one isolated electron or muon with $p_T > 30$ GeV, two b-jets identified with MV1 at 70% efficiency and with $p_T > 30$ GeV, $E_T^{miss} > 35$ GeV and $m_T(W) > 30$ GeV. Then, additional tight cuts are applied to better isolate s-channel events: the jet used to reconstruct the top candidate whose mass is the closest to the 172.5 GeV is asked to have $p_T > 50$ GeV and $m_T(W)$ is required to be greater than 50 GeV. Among the studied combinations of selection cuts, this is found to be the best compromise between the gain in signal discrimination (s-channel purity increases from 2.8% to 3.1%) and the loss in final statistics (62% of the preselected events are retained).

- The **W+jets-enriched sample** is constituted by the events with one isolated lepton with $p_T > 30$ GeV, two b-jets identified with MV1 at 80% efficiency and with $p_T > 25$ GeV, $E_T^{miss} > 35$ GeV and $m_T(W) > 30$ GeV. In order to define a control region orthogonal to the signal selection, b-tagged jets with $p_T > 30$ GeV fulfilling the MV1 identification criterion corresponding to the 70% efficiency are excluded. The expected W+jets purity reaches in this sample 57%, while the $t\bar{t}$ and s-channel contaminations are of 25% and 0.9% respectively.

- The **$t\bar{t}$-enriched sample** is selected by considering final states composed by one isolated lepton with $p_T > 30$ GeV, four jets with $p_T > 25$ GeV, among which two shoud be b-tagged using MV1 at 80% efficiency, $E_T^{miss} > 35$ GeV and $m_T(W) > 30$ GeV. The large $t\bar{t}$ purity of 91% overwhelms the tiny contributions from W+jets and s-channel, respectively of 4% and 0.2%.

6.3 Background data-driven estimates & modelling

For the 8 TeV analysis, the **multijet** background has been modelled with the same data-driven technique both for electron and muon final states. The matrix method, illustrated in Section 4.2.1, allows to estimate the number of fake lepton passing the signal selection (with an uncertainty of 50%), and to constitute the multijet template using real data involving loose lepton selection criteria.

The **W+jets** sample, on the other hand, is modelled via MC simulation, and normalized according to the output of the maximum likelihood fit of the multivariate discriminant distribution used for the s-channel production measurement. As it will be explained later, the scale factor associated to the W+jets, where all the flavour compositions are considered together, is found to be 1.12 ± 0.15 in the signal region. The fit output error depends on the statistics and the uncertainties with which the theorical cross section of all the background sources are known; the latters define in fact the width of the gaussian models described in Eq 4.16.

Two additional data-driven normalizations are realized in the $t\bar{t}$ and W+jets control regions (where the scale factors obtained in the likelihood fit can not be used) and applied only in the plots to compare the predicted kinematic distributions with the observed ones. The slight data/MC event yields disagreement in the W+jets-enriched sample is mainly due to the imprecise modeling of W+jets events, while in the $t\bar{t}$-enriched sample to the bias introduced by the consecutive application of the b-tagging efficiency scale factors. Similarly to what explained in Section 4.2.2, Eq 4.5 allows to determine an overall W+jets normalization for the W+jets control region and, with the suitable changes, an overall $t\bar{t}$ normalization for the $t\bar{t}$ control region. The SF_{W+jets} is found to be 0.97 in the electron channel and 1.11 in the muon channel; it is not surprising that the weighted average of the two values does not match the one obtained for the lepton sample after the signal selection, for which the flavour composition is different. The $SF_{t\bar{t}}$, instead, corresponds to 1.01 in the electron channel

and to 1.04 in the muon channel. The control distributions shown in Appendix D with these scale factors applied attest a rather good data/MC agreement in the shapes.

6.4 Event yields and control plots

Having established the data driven techniques to estimate the W+jets and multijet contributions, and checked the modelling of some crucial distributions in specific control regions where the largest sources of background after the preselection phase are dominant, we can begin to study the "signal sample". First of all, we report in Table 6.3 the event yields obtained before and after the selection cuts ($m_T(W) > 50$ GeV and $p_{T\ top\ jet} > 50$ GeV [1]); the contribution from top pair production increases from 62% to 67%, while the one from W+jets decreases from 16% to 12%, becoming smaller than the single top production, stable at 15%.

Process	Pre-selection	Selection
s-channel	674±6	457±5
t-channel	3067±22	1852±17
Wt	685±23	412±17
$t\bar{t}$	15252±67	10206±54
W+light jets	468±66	189±43
Wbb	2468±16	1272±14
Wcc	533±29	300±18
Wc	861±27	413±19
Z+jets	25±8	4±2
diboson	268±8	104±5
Multijet	944±472	279±139
Total expectation	24958 ±273	15433±124
Data	25900±161	16031±127
S/B [%]	2.8	3.1

Table 6.3: Event yields for the electron and muon channels in the signal region. The expectations are derived using theoretical cross sections with the exception of the multijet and W+jets samples, for which they are extracted with the data-driven techniques detailed in the text. The uncertainty parametrises the limited size of the MC samples and the error associated to the data-driven multijet normalization.

Then, we investigate the modelling of the main kinematic distributions, which is found to be good as Figure 6.2 illustrates. In the plots, each simulation process has been rescaled to the correction factors yield by the maximum likelihood fit that will be described in Section 6.7; the electron and muon channels are merged.

[1] $p_{T\ top\ jet}$ represents the transverse momentum of the jet used to reconstruct the top quark; the invariant mass of this jet and the W-boson is the one which is more close to the top quark pole mass.

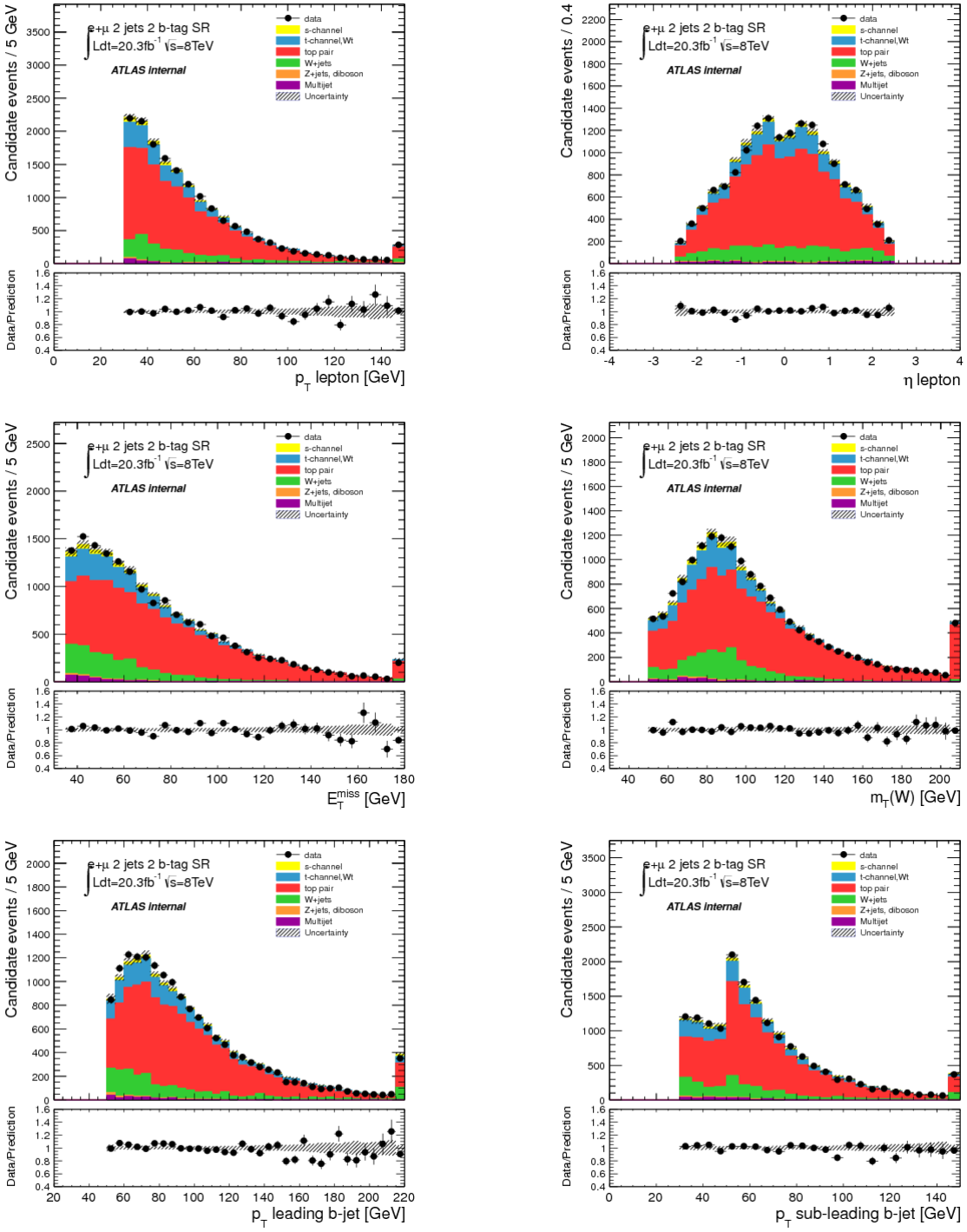

Figure 6.2: Main kinematic distributions for the signal-enriched sample: lepton p_T and η, transverse missing energy E_T^{miss}, W boson transverse mass $m_T(W)$, leading and subleading jet p_T . The sharp structure observed at 50 GeV in the distribution of the transverse momentum of the sub-leading jet is due to the cut applied on $p_{T\ top\ jet}$ in order to select signal events. The simulated distributions are normalized with the scale factors given by a likelihood fit to the data. The uncertainty band corresponds to the errors due to the MC samples statistics together with the 50% uncertainty on the multijet normalization.

6.5 Multivariate analysis

The experience gained with boosted decision trees at 7 TeV and the successful signal discrimination they have proven to achieve, suggest to adopt the same approach also at 8 TeV. The first point that needs to be assessed is whether the backgrounds should be included in the training phase or not; we already stressed that the main contributions arise from top pair, single top and W+jets production, the relative importance of the latters being reversed after the selection procedure. By testing several combinations of those processes, it was found that the presence of t-channel and Wt events degrades the performance of the BDT, and thus the total expected uncertainty on the s-channel cross section; this can probably be explained by the strong similarity of the topology of these processes and of the signal, that entails less harsh cuts on the input distributions. The second crucial question regards the usage of the preselection or the selection samples to train the classifier; both configurations have been checked, and the first was found to optimize the expected s-channel cross section uncertainty. This solution, suboptimal because the machine learning technique does not exploit the additional discrimination realized by the cuts on $m_T(W)$ and $p_{T\ top\ jet}$, has the avantage of allowing more statistics in the training procedure, which appears to be determinant. Highly populated templates allow in fact to set up a powerful and agressive BDT configuration without jeopardizing its stability due to overtraining.
In conclusion, the baseline s-channel POWHEG+PYTHIA, $t\bar{t}$ POWHEG+PYTHIA and W+heavy flavour ALPGEN+PYTHIA templates are used to train and test the BDT classifier. To obtain two statistically independent sets, the background samples are split into two subgroups of equal size, while for the signal, which suffers of low statistics, 80% of the events are used for the training and the 20% remaining are considered for testing.

The kinematic and angular distributions chosen to train the classifier are those giving a significant discrimination between the signal and the background event topologies; they are listed in Table 6.4, where for each one the definition and the corresponding separation power (S) is given. The S threshold, above which the input variables are selected, is adjusted in order to get the best expected total uncertainty on the cross section measurement. The good modelling of the input variables after the signal preselection is also verified by checking the agreement between data and expected distributions in Appendix E.

Variable	S	Definition
$\lvert\Delta\Phi(t2, j1)\rvert$	0.17	$\lvert\Delta\Phi\rvert$ between the leading jet and the top quark ($Top\_j2\nu l$ [1])
$\lvert\Delta\Phi(t1, j2)\rvert$	0.16	$\lvert\Delta\Phi\rvert$ between the subleading jet and the top quark ($Top\_j1\nu l$ [1])
$p_T(l) + E_T^{miss}$	0.15	Sum of lepton p_T and missing transverse energy
E_{T}^{miss}	0.11	Missing transverse energy
$m_{\mathrm{T}}(W)$	0.10	Transverse mass of the W-boson
$p_{\mathrm{T}}(l)$	0.09	Transverse momentum of the lepton
$\lvert\Delta\eta(l, j1)\rvert$	0.07	$\lvert\Delta\eta\rvert$ between the lepton and the leading jet
H_{T}	0.07	Scalar sum of jets p_T, lepton p_T and missing transverse energy
$\lvert\Delta\eta(t2, j1)\rvert$	0.07	$\lvert\Delta\eta\rvert$ between the leading jet and the top quark
$\lvert\Delta\Phi(j1, j2)\rvert$	0.07	$\lvert\Delta\Phi\rvert$ between the jets
$\lvert\Delta\Phi(l, E_{\mathrm{T}}^{miss})\rvert$	0.06	$\lvert\Delta\Phi\rvert$ between the lepton and the missing transverse energy
$\lvert\Delta\eta(l, j2)\rvert$	0.05	$\lvert\Delta\eta\rvert$ between the lepton and the subleading jet
$\lvert\Delta\eta(\nu, j_{no\ top})\rvert$	0.05	$\lvert\Delta\eta\rvert$ between the neutrino and the jet not used to reconstruct the top
$p_{\mathrm{T}}(j1, j2)$	0.05	p_T of the system composed by the two jets
W *helicity*	0.05	W helicity from the top quark (reconstructed via the leading jet) decay[2]
$\cos\theta(E_{\mathrm{T}}^{miss}, j2)$	0.05	Cosine of the angle between E_T^{miss} and the subleading jet
$m(l, j2)$	0.05	Mass of the system composed by the lepton and the subleading jet
$\cos\theta(Top\_j2\nu l)$	0.05	Top (reconstructed via the subleading jet) spin correlation in helicity basis[3]
$\cos\theta(Top\_j1\nu l)$	0.05	Top (reconstructed via the leading jet) spin correlation in helicity basis[3]

Table 6.4: Input variables for the BDT classifier.

[1] $Top\_j2\nu l$ ($Top\_j1\nu l$) represents the top quark reconstructed with the subleading (leading) jet.
[2] Cosine of the angle between the direction of the lepton in the W-boson reference frame, and the W-boson in the top quark reference frame.
[3] Cosine of the angle between the direction of the lepton in the top quark reference frame, and the top in the center of mass reference frame.

The BDT algorithm is optimized by a configuration (see Table 6.5) of 350 trees with a maximum allowed depth of 3, and a minimum percentage of 18 training events required in a leaf node; this stopping condition gives better output than the pruning. The number of cuts, representing the variable range granularity, is set to 35.
Finally, the classification performance is increased via the Gradient Boosting algorithm witih a shrinkage parameter of 0.6.

Table 6.5: Parameters of the BDT classifier

nTrees	350
MaxDepth	3
MinNodeSize	18
nCuts	35
BoostType	Gradient Boosting
Shrinkage	0.6

The classifier parameters are tuned in order to have a good compatibility between the training and testing samples, ensuring a stable response without overtraining, as Fig. 6.3(a) demonstrates for both the signal and background normalized BDT output. The overall discrimination performance is, on the other hand, assessed via the curve representing the background rejection versus the signal efficiency, displayed in Figure 6.3(b).

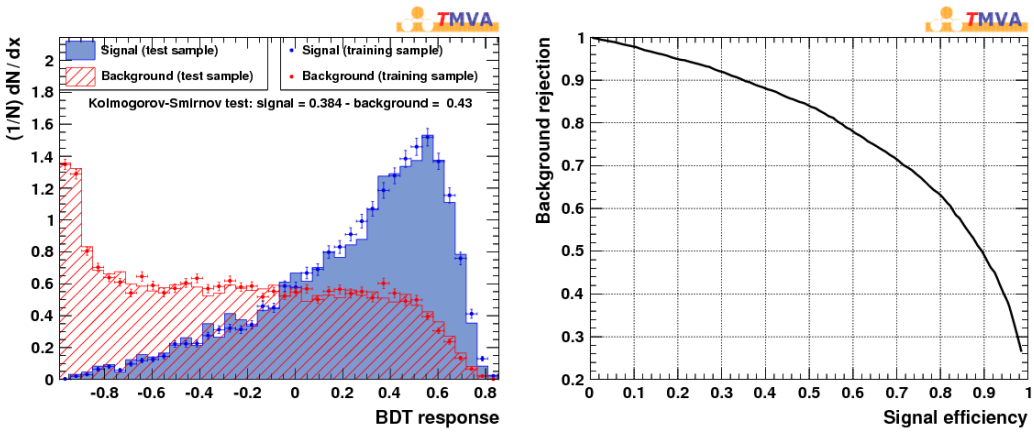

(a) (b)

Figure 6.3: (a) Classifier outputs for training and test signal (blue) and background (red) samples. The error bars on the points represent the statistical uncertainty of the Monte Carlo training samples. (b) Background rejection as a function of the signal efficiency for the BDT algorithm.

When the classification algorithm is applied to the data and all the Monte Carlo events fulfilling the signal selection, the distribution presented in Figure 6.4 [2] is obtained; it is important to stress that a rather good data/simulation agreement is present over the full range and that the corresponding separation power is 30%, much larger than the one of the best input variable (17%). Figure 6.5, showing the BDT distributions normalized to one for the signal (peaked on the right) and the largest background processes, emphasizes further the discrimination achieved with this multivariate technique. The classifier output in the signal region will be fitted to data using the maximum likelihood approach described in Section 4.6 to extract the s-channel cross section; the uncertainty on the measurement will be assessed via a frequentist technique based on the generation of pseudoexperiments with varied samples of simulated events.

[2]The binning of the distribution has also been optimized by minimizing the expected s-channel cross section uncertainty.

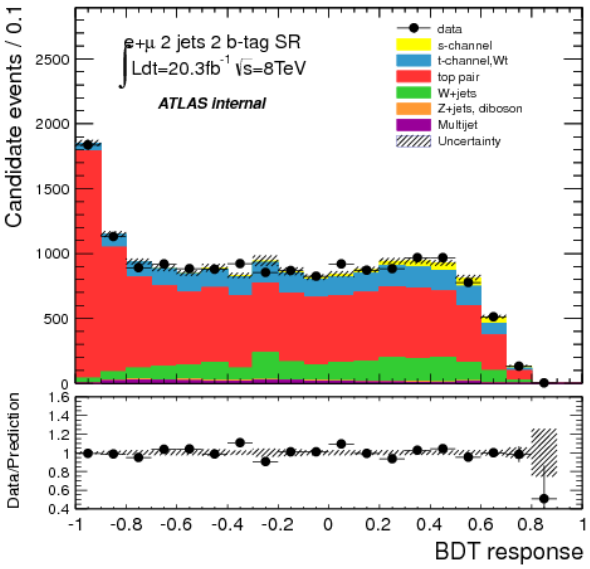

Figure 6.4: Output distribution of the BDT classifier for the signal and background events compared with the data in the signal region. The simulated distributions are normalized with the scale factors given by the likelihood fit. The uncertainty band corresponds to the errors due to the Monte Carlo sample statistics added in quadrature with the data-driven normalization uncertainty on the multijet contribution.

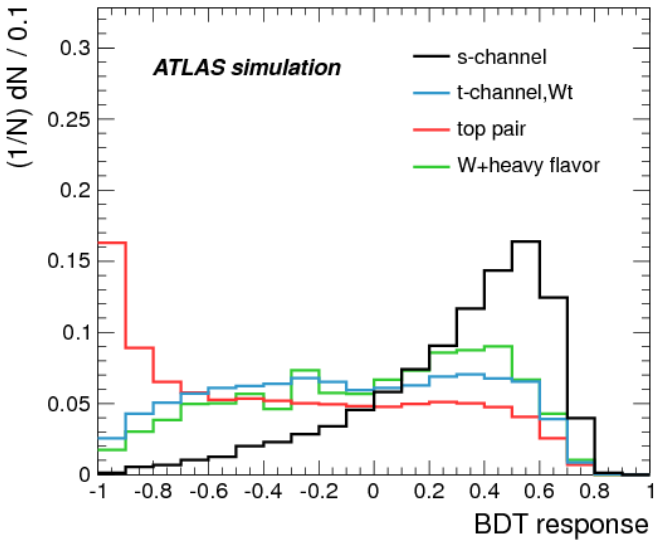

Figure 6.5: Expected signal and background template BDT distributions normalized to unity. The W+light jets, Z+jets, diboson and multijet curves are not drawn in view of the very low statistics of the corresponding Monte Carlo samples and/or their marginal contributions in the signal regions.

6.6 Systematic and statistical uncertainties

We illustrated in Section 4.5 the systematic uncertainties related to the detection and reconstruction of the physical objects in ATLAS, as well as the ones connected to the theoretical modelling and the normalization of the various processes. Such uncertainties, together with the statistical error on the size of the MC samples and the collected dataset, are introduced in the statistical interpretation of the results since they alter the acceptance of each process (Eq. 4.18) and, as well, vary bin-by-bin the nominal classifier distribution (Eq. 4.19).

6.6.1 Rate uncertainty

The relative uncertainties on the predicted signal and background rates are listed in Table 6.6; they refer to the signal region (defined after the event selection), where the boosted decision trees output will be fitted. Some channels have been grouped with the goal of mantaining a significantly high statistics for the samples used in the fit and in the generation of pseudoexperiments; the multijet background, moreover, is not tabulated because modeled via a loose data sample.

6.6.2 Shape uncertainty

The choice of the systematic uncertainties for which also the induced shape variation of the classifier distribution should be taken into account, is extremely delicate as affects deeply the result. For this reason, such analysis is realized on the basis of more refined criteria than what done at 7 TeV, and is further validated via a series of checks.

- First of all, we perform a Kolmogorov-Smirnov test by comparing, for each signal and background process and each systematic component, the Monte Carlo nominal distribution with the $\pm 1\sigma$ systematically varied distributions (Table 6.7). The shape differences leading to a positive and negative KS test value lower than 0.6 are retained as relevant sources of systematic shape uncertainties.

- Secondly, we proceed with the analysis of all the uncertainties characterized by a positive or a negative variation attending a KS test between 0.6 and 0.8. For this subset, our choice is based on a comparison between the expected impact on the s-channel cross section measurement of such shape uncertainty, and of the statistical fluctuations affecting the MC samples.

Once that the baseline criteria have been settled, we examine their reliability and stability when the setting of the BDT output is varied, that is for a different choice of binning or when smoothing one particular physics process.

Table 6.8 reports the Kolmogorov-Smirnov tests performed on distinct classifier configurations, for all the systematic uncertainties having KS values lower than 0.8 with the nominal setting of 20 bins[3]. A two-by-two bin grouping is applied in order to reduce the statistical variations without degrading the distribution. It is realized for each process in a different BDT output range, where the shapes are either almost flat or slightly evoluting over two successive bins: for the s-channel in the region (-1, -0.2), for the t-channel+Wt and W+jets in (-0.8, 0.6), and for $t\bar{t}$ in (-0.6, 0.5).
Also the merging of the last two full bins, which exhibit a large statistical errors, has been investigated, as well as the smoothing over the full variable range.
As expected, the Kolmogorov-Smirnov test shows an overall stability when performed on different distribution settings, and a poor sensitivity to fluctuations. Moreover, the sets of systematic uncertainties characterized by $KS < 0.6$ and by $0.6 < KS < 0.8$ are composed by the same elements for the nominal and the varied BDT configurations. The only anomaly spotted regards the Wt POWHEG DS generator uncertainy; the improvement in the KS value after rebenning and smoothing suggests that the statistical fluctuations may be important for this channel, which needs thus a further analysis (see Table 6.9).

With the aim of setting a strategy for the sources of shape variations associated to intermediate KS values, we realized a second batch of studies. The idea is to compare the uncertainty on the s-channel cross section derived from a particular systematic source and physics process, and the one arising from the statistics of the simulation sample for the same physics process. It is nevertheless instructive to investigate as well the role of the rebinning [4] and smoothing of the classifier distribution on such choice. As Table 6.9 illustrates, the E_T^{miss} resolution for the t-channel+Wt production influences the s-channel measurement less than the Monte Carlo statistics. The E_T^{miss} resolution and ISR/FSR for $t\bar{t}$, as well as the theory modelling (even the POWHEG DS generator) for Wt channel, show a reduced impact when considering different BDT settings, which is below the statistical threshold or of the same order of magnitude. The shape variations for all these systematic uncertainties, therefore, will be dropped. On the contrary, the E_T^{miss} scale for t-channel+Wt, the jet energy resolution and the generator scale for the s-channel, entail an uncertainty on the signal cross section which is larger than the one related to the statistics of the corresponding MC simulations. Such sources of uncertainty will be, therefore, added to the list of systematic shapes to be integrated in the statistical analysis.

In conclusion, the ultimate list collecting the sources of shape uncertainty considered in the analysis is documented in Table 6.10. Figures 6.6 and 6.7 ilustrate instead their effect on the classifier output in the signal region. The $\pm 1\sigma$ E_T^{miss} resolution distributions exhibit the same variation trend with respect to the nominal shape leading to a completely asymmetric contribution to the s-channel cross section uncertainty.

[3]For the systematic uncertainties having a KS value of 1 within the nominal BDT setting, the result is unchanged in any varied configurations.

[4]The merging of the two last filled bins is not reported since it does not entail significant changes.

Rate systematic [%]	s-channel	$t\bar{t}$	t-channel,W+jets	W+jets	Z,diboson
E_T^{miss} resolution	0.58/0.42	0.43/0.38	0.94/0.84	1.40/2.12	1.43/3.07
E_T^{miss} scale	1.03/-0.84	0.38/-0.17	0.82/-0.64	1.37/-1.89	2.70/-2.63
Lepton trigger	3.15/0.61	3.11/0.62	3.19/0.70	2.95/0.34	2.67/0.10
Lepton reconstruction	1.94/-1.94	1.87/-1.87	1.92/-1.92	1.64/-1.64	1.85/-1.85
Electron resolution	0.09/0.01	-0.02/-0.02	0.06/0.12	-0.78/-0.59	0.60/0.86
Electron scale	-1.02/0.79	-0.63/0.61	-0.91/0.92	-1.71/1.08	-2.20/1.44
Muon ID resolution	0.01/0.05	0.04/0.09	0.16/0.15	-0.37/-0.46	1.71/1.67
Muon MS resolution	0.06/-0.07	-0.01/0.08	-0.07/0.07	0.04/-0.45	-1.67/1.61
Muon scale	0.11/0.05	0.10/-0.00	0.01/-0.10	0.03/-0.33	0.86/1.71
Jet reconstruction	0.22/-0.22	0.15/-0.15	0.02/-0.02	-0.31/0.31	0.12/-0.12
Jet resolution	-2.15/2.15	-0.39/0.39	-0.84/0.84	0.70/-0.70	0.60/-0.60
Jet scale	0.63/-0.02	-5.02/5.18	2.15/-0.78	3.15/-2.37	12.59/-13.49
Jet vertex fraction	1.26/-2.30	2.87/-3.13	1.99/-2.01	-0.36/-2.35	-0.57/-2.28
b-tagging	6.44/-6.24	5.92/-5.75	5.82/-5.66	3.41/-3.32	5.60/-5.42
c,τ-tagging	0.06/-0.06	1.09/-1.09	1.84/-1.84	6.69/-6.29	3.00/-2.80
mis-tagging	0.07/-0.07	0.20/-0.20	0.84/-0.84	7.06/-6.50	2.26/-2.10
Luminosity	2.18/-2.18	2.18/-2.18	2.18/-2.18	2.18/-2.18	2.18/-2.18
PDF	2.67/-2.67	4.94/-4.94	2.72/-2.72	2.71/-2.71	3.29/-3.29
ISR/FSR	—	-6.93/6.93	—	—	—
Generator scale	3.47/-4.19	—	—	—	—
Theory modelling (McAtNlo+ Herwig)	-1.35/1.35	6.69/-6.69	-1.29/1.29	—	—
Theory modelling (McAtNlo+ Herwig)	—	—	3.19/-3.19	—	—
Generator (Powheg DS)	—	—	-0.03/0.03	—	—
Normalization	—	6.0/-6.0	5.0/-5.0	60.0/-60.0	60.0/-60.0

Table 6.6: Relative variations (up/down), due to the various instrumental and theoretical modeling sources of systematic uncertainty, on the signal and background event yields in the signal region. They are quoted in per cent.

Shape systematic	s-channel	$t\bar{t}$	t-channel,Wt	W+jets	Z,diboson
E_T^{miss} resolution	0.26/0.32	0.77/0.67	0.67/0.98	0.81/0.98	0.97/0.78
E_T^{miss} scale	0.02/0.09	0.11/0.18	0.84/0.32	0.97/1.00	1.00/0.99
Lepton trigger	1.00/1.00	1.00/1.00	1.00/1.00	1.00/1.00	1.00/1.00
Lepton reconstruction	1.00/1.00	1.00/1.00	1.00/1.00	1.00/1.00	1.00/1.00
Electron resolution	1.00/1.00	1.00/1.00	1.00/1.00	1.00/1.00	1.00/1.00
Electron scale	1.00/1.00	1.00/1.00	1.00/1.00	1.00/1.00	1.00/1.00
Muon ID resolution	1.00/1.00	1.00/1.00	1.00/1.00	1.00/1.00	1.00/1.00
Muon MS resolution	1.00/1.00	1.00/1.00	1.00/1.00	1.00/1.00	1.00/1.00
Muon scale	1.00/1.00	1.00/1.00	1.00/1.00	1.00/1.00	1.00/1.00
Jet reconstruction	1.00/1.00	1.00/1.00	1.00/1.00	1.00/1.00	1.00/1.00
Jet resolution	0.73/0.75	1.00/1.00	1.00/1.00	0.82/0.82	0.86/0.84
Jet scale	0.40/0.98	0.00/0.01	0.23/0.37	0.95/0.49	1.00/1.00
Jet vertex fraction	1.00/1.00	1.00/1.00	1.00/1.00	1.00/1.00	1.00/1.00
b-tagging	1.00/1.00	1.00/1.00	1.00/1.00	1.00/1.00	1.00/1.00
c,τ-tagging	1.00/1.00	1.00/1.00	1.00/1.00	1.00/1.00	1.00/1.00
mis-tagging	1.00/1.00	1.00/1.00	1.00/1.00	1.00/1.00	1.00/1.00
PDF	1.00/1.00	1.00/1.00	1.00/1.00	1.00/1.00	1.00/1.00
ISR/FSR	—	0.58/0.68	—	—	—
Generator scale	0.94/0.55	—	—	—	—
Theory modelling (McAtNlo+ Herwig)	0.04/0.05	0.09/0.06	0.66/0.67	—	—
Theory modelling (aMcAtNlo+ Herwig)	—	—	0.92/0.92	—	—
Generator (Powheg DS)	—	—	0.43/0.43	—	—

Table 6.7: Kolmogorov-Smirnov tests on the systematic shape variations of the signal and background classifier distributions in the signal region.

Shape systematic	Nominal (20 bins)	smoothing (applied once)	rebinning (low BDT range)	rebinning (last bins)
s-channel E_{T}^{miss} resolution	0.26/0.32	0.27/0.29	0.41/0.40	0.29/0.34
t-channel,Wt E_{T}^{miss} resolution	0.67/0.98	0.59/0.97	0.75/1.00	0.67/0.97
$t\bar{t}$ E_{T}^{miss} resolution	0.77/0.67	0.74/0.82	0.93/0.78	0.78/0.67
s-channel E_{T}^{miss} scale	0.02/0.09	0.02/0.13	0.05/0.17	0.02/0.10
t-channel,Wt E_{T}^{miss} scale	0.84/0.32	0.73/0.16	0.81/0.37	0.85/0.33
$t\bar{t}$ E_{T}^{miss} scale	0.11/0.18	0.15/0.26	0.16/0.22	0.12/0.20
s-channel jet energy resolution	0.73/0.75	0.76/0.79	0.98/0.98	0.70/0.73
s-channel jet energy scale	0.40/0.97	0.47/0.99	0.43/0.96	0.43/0.99
t-channel,Wt jet energy scale	0.23/0.37	0.21/0.26	0.41/0.42	0.23/0.35
W+jets jet energy scale	0.95/0.49	1.00/0.93	1.00/1.00	0.94/0.48
$t\bar{t}$ jet energy scale	0.00/0.01	0.00/0.04	0.00/0.01	0.00/0.01
W+jets shape	0.17/0.13	0.26/0.21	0.14/0.10	0.58/0.67
$t\bar{t}$ ISR/FSR	0.58/0.68	0.66/0.75	0.43/0.53	0.48/0.58
s-channel generator scale	0.94/0.55	0.98/0.53	0.92-1.00	0.54-0.58
s-channel modelling	0.04/0.05	0.08/0.09	0.08/0.08	0.04/0.04
Wt modelling	0.66/0.67	0.88/0.89	0.74-0.79	0.76-0.80
$t\bar{t}$ modelling	0.09/0.06	0.09/0.06	0.13/0.09	0.08/0.06
Wt generator (Powheg DS)	0.43/0.43	0.63/0.63	0.69/0.70	0.43/0.44

Table 6.8: Kolmogorov-Smirnov tests on the systematic shape variations for the nominal BDT distribution (20 bins) and after smoothing or rebinning.

Shape systematic	Nominal (no shape)	Nominal (20 bins)	smoothing (once)	rebinning (low range)	statistics MC sample
$t\bar{t}$ E_{T}^{miss} res.	+0.3/-0.0	+0.0/-12.4	+0.0/-11.3	+0.0/-12.0	±12.3
t-channel,Wt E_{T}^{miss} res.	+0.3/-0.0	+0.0/-4.7	+0.0/-4.3	+0.0/-4.8	±6.3
t-channel,Wt E_{T}^{miss} sc.	±1.0	±8.3	±11.9	±9.3	±6.3
s-channel jet energy res.	±1.9	±5.1	±4.4	±4.8	±1.6
s-channel jet energy sc.	±2.6	±0.8	±0.9	±1.9	±1.6
$t\bar{t}$ ISR/FSR	±2.7	±12.1	±6.9	±7.1	±12.3
s-channel generator sc.	±3.8	+5.2/-5.8	+4.9/-5.9	+5.4/-6.5	±1.6
Wt modelling	±0.0	±8.4	±4.2	±6.3	±6.3
Wt (POWHEG DS)	±0.0	±10.6	±8.6	±7.5	±6.3

Table 6.9: Estimated uncertainties arising from: the systematic rate variations (first column), the systematic rate+shape variations obtained with the standard BDT distributions of 20 bins (second column), the systematic rate+shape variations obtained after smoothing (third column) and rebinning in a particular range defined in Sec. 6.6.2 for each process (fourth column), the statistical fluctuations of the MC samples (fifth column). They are quoted in per cent.

Shape systematic	Processes
E_{T}^{miss} resolution	s-channel
E_{T}^{miss} scale	s-channel, $t\bar{t}$, t-channel, Wt
Jet energy resolution	s-channel
Jet energy scale	$t\bar{t}$, t-channel, Wt
Generator scale	s-channel
Theory modelling	s-channel, $t\bar{t}$, W+jets

Table 6.10: Systematic shape variations on the signal and background classifier distributions included in the statistical analysis.

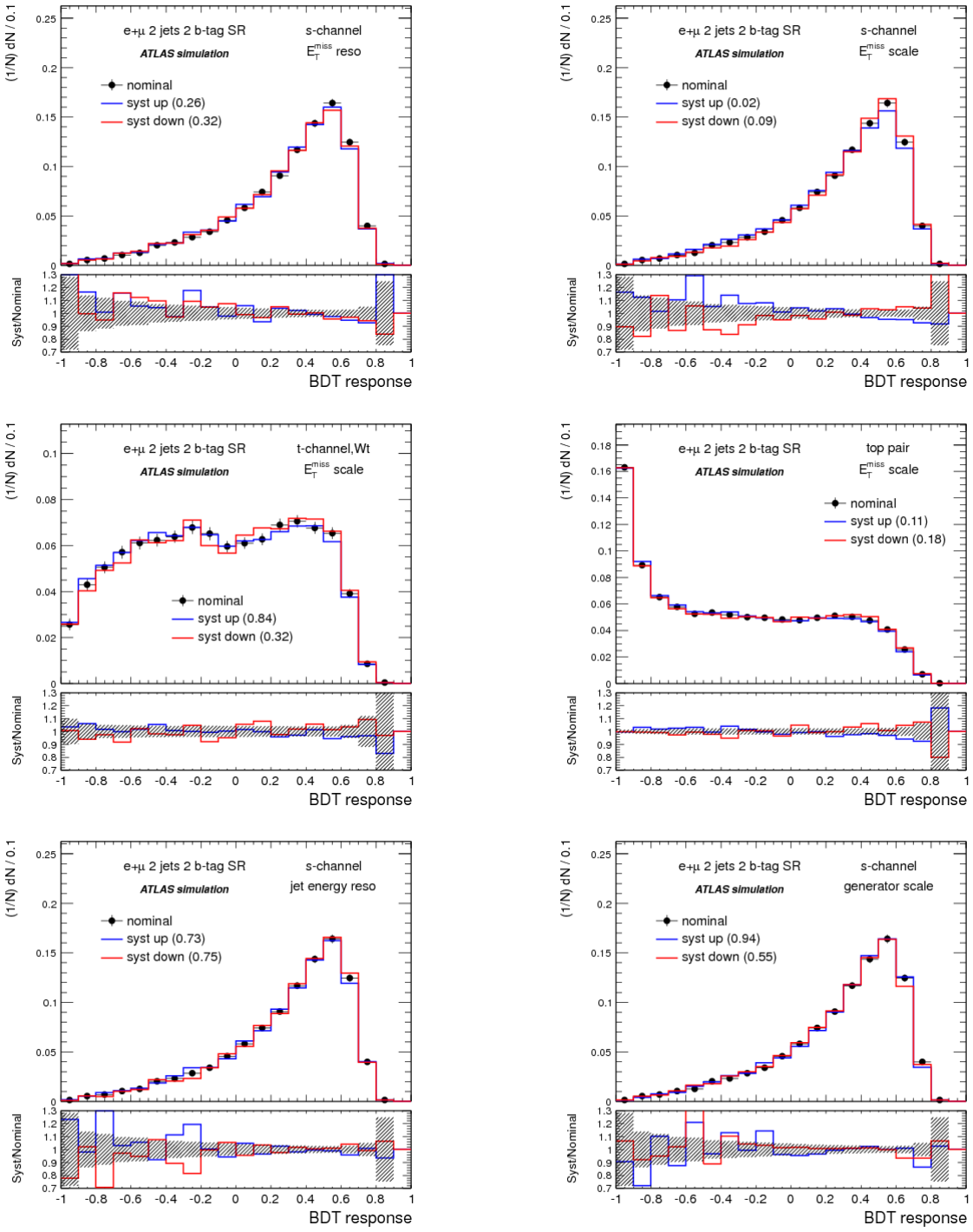

Figure 6.6: Comparison of the nominal and systematically varied normalized distributions of the BDT classifier: E_T^{miss} resolution and scale uncertainties for the s-channel, E_T^{miss} scale uncertainty for t-channel+Wt production and $t\bar{t}$, jet energy resolution and generator scale uncertainties for the s-channel. The error bars (upper plots) and shaded area (bottom plots) represent the statistical uncertainty on the MC samples.

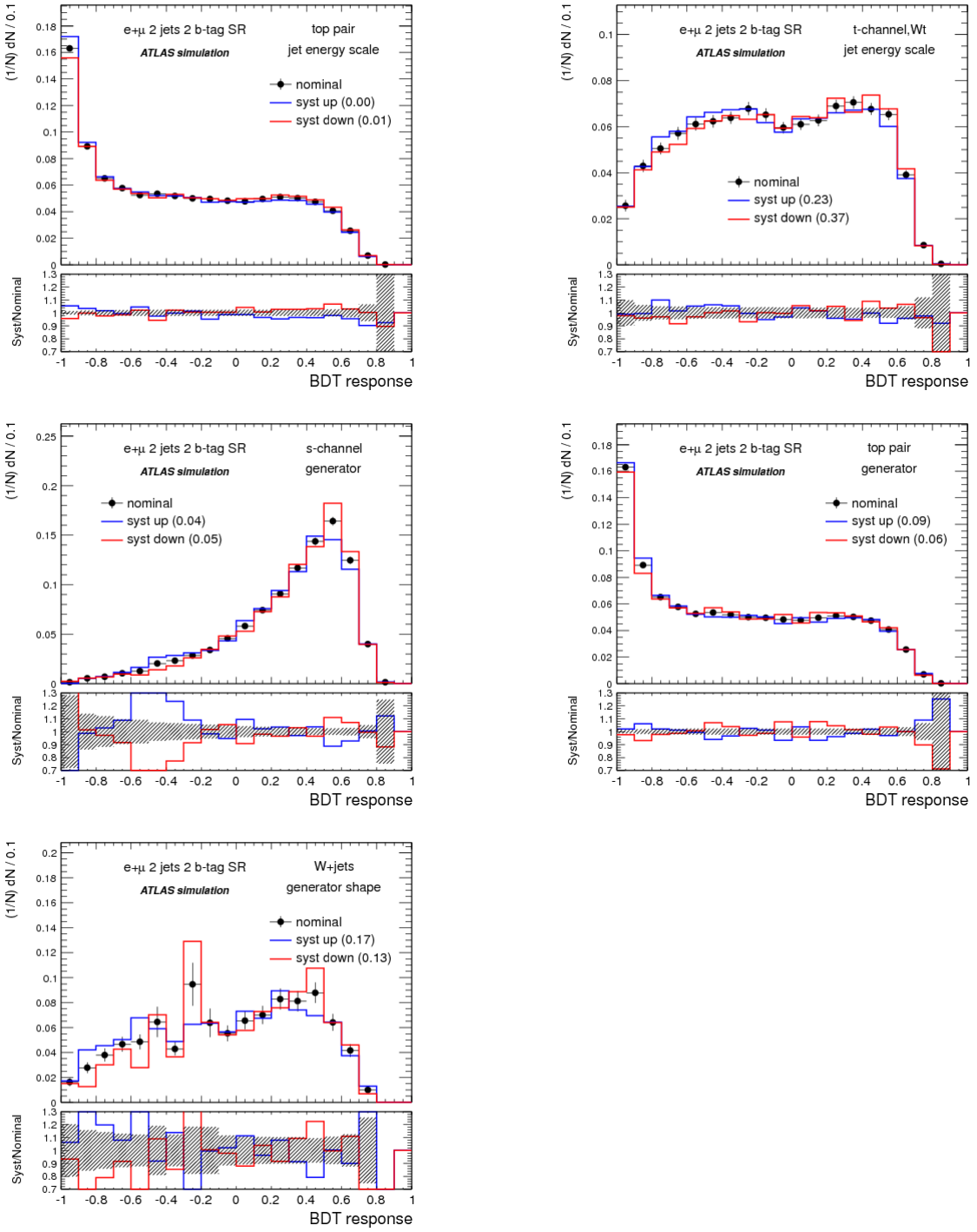

Figure 6.7: Comparison of the nominal and systematically varied normalized distributions of the BDT classifier: jet energy scale uncertainty for top pair, t-channel+Wt productions, theory modelling for $t\bar{t}$, s-channel, W+jets. The error bars (upper plots) and shaded area (bottom plots) represent the statistical uncertainty on the MC samples.

6.7 Results

The result of the likelihood fit to data of the BDT output distribution in the signal region (Figure 6.4) is provided in Table 6.11; we report the β scale factors extracted for the signal and background contributions, and the rescaled expectation values which are used as input of the pseudoexperiments when estimating the observed uncertainty.

Process	β	$\tilde{\nu} \cdot \beta$
s-channel	0.89±0.32	406
$t\bar{t}$	1.05±0.02	10753
t-channel, Wt	1.02±0.05	2317
W+jets	1.12±0.15	2180
Z+jets, diboson	1.07±0.59	115
Multijet	1.00 (fixed)	279

Table 6.11: Scale factors β extracted for the signal and background processes from the template fit of the BDT distribution in the signal region; the corresponding errors account for the statistics and the normalization uncertainties. The rescaled expectation values $\tilde{\nu} \cdot \beta$ are also given.

The fitted scale factors for $t\bar{t}$, t-channel and Wt, Z+jets and diboson, are found to be respectively 1.05, 1.02, and 1.07, in overall agreement with the Standard Model prediction. For the W+jet background, the β value of 1.12 represents the data-driven correction to be applied to renormalize the MC sample.
The s-channel production is finally measured [5] by rescaling the approximate NNLO cross section of 5.61 pb by β_s; the corresponding uncertainty is derived by generating pseudoexperiments which involve, simultaneously, all the systematic and statistical variations. The cross section is found to be in agreement with the theoretical expectation:

$$\sigma_s = 5.0 \pm 2.3(stat) \pm 3.6(syst) \text{ pb} = 5.0 \pm 4.3 \text{ pb} \quad .$$

With the observed breakdown in Table 6.12, moreover, we can assess the relative contributions to the total uncertainty of ± 87%. The sources of uncertainty having the highest impact on the measurement are the data (±35%) and simulation statistics (±29%), the missing transverse momentum scale (±55%), and the jet energy scale (±39%). Other significant contributions are due to the data-driven multijet normalization (±12%) and the modeling of the signal process (±11% from the generator and scale variations). It is important to mention that the observed uncertainties are significantly higher than the expected ones (± 76%) due to the fitted scale factor $\beta_s = 0.89$ associated to the signal contribution in the data.

[5] We assume here the existence of the s-channel, as its cross section has been measured with a significance of 6.3 standard deviations [40].

Systematic	Uncertainty β_s [%]	
Data statistics	+34.7	-34.7
Simulation statistics	+29.4	-29.4
Luminosity	+5	-5
Theory normalization	+2.7	-2.7
W+jets normalization	+6.1	-6.1
Multijet normalization	+11.8	-11.8
E_{T}^{miss} resolution	+0.0	-2.9
E_{T}^{miss} scale	+54.4	-54.6
Lepton trigger	+1.5	-0.0
Lepton reconstruction	+1.3	-1.3
Electron energy resolution	+0.0	-0.0
Electron energy scale	+0.8	-0.8
Muon ID momentum resolution	+0.0	-0.1
Muon MS momentum resolution	+0.1	-0.1
Muon momentum scale	+0.1	-0.0
Jet energy resolution	+5.1	-5.1
Jet energy scale	+39.3	-39.2
Jet reconstruction	+0.1	-0.1
Jet vertex fraction	+0.0	-0.8
b-tagging factor	+4.1	-4.1
c, τ-tagging factor	+0.2	-0.2
mis-tagging factor	+0.6	-0.6
PDF	+0.7	-0.7
W+jets shape	+8.0	-8.0
$t\bar{t}$ ISR/FSR	+3.1	-3.1
s-channel generator scale	+5.2	-5.8
$t\bar{t}$ generator McAtNlo	+5.9	-5.9
s-channel generator McAtNlo	+9.8	-9.8
t-channel generator	+0.0	-0.0
Wt generator McAtNlo	+0.0	-0.0
Wt generator Powheg DS	+0.0	-0.0
Total systematic	+72.6	-73.1
Total (systematic+statistics)	+86.9	-87.2

Table 6.12: Breakdown of the relative contributions to the observed statistical and systematic uncertainties on the s-channel scale factor estimated for the signal events. The uncertainties are quoted in per cent.

The final BDT classifier distribution with the background contributions subtracted is displayed in Figure 6.8, the Monte Carlo processes being rescaled to the likelihood fit results (Table 6.11). Since the data fluctuations are still important, it is difficult to determine whether the distribution is compatible with the background-only hypothesis or with an s-channel contribution.

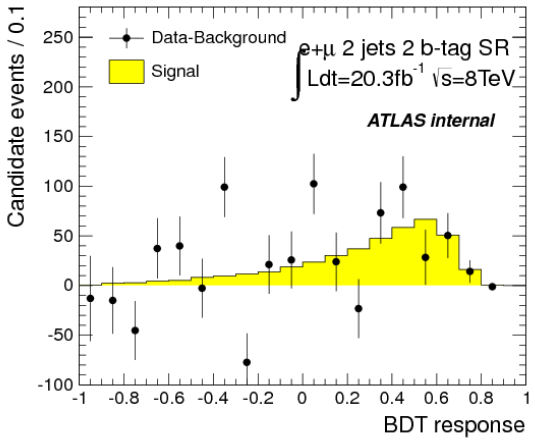

Figure 6.8: Signal distributions of the BDT classifier after background subtraction for the signal events. The error bars represent the statistical uncertainty of the data before background subtraction.

6.7.1 Significance and limit

The cross section results presented in the previous section correspond to an expected significance of 1.4 standard deviations and to an observed significance of 1.3 standard deviations. The slightly lower observed significance is due to an observed value of the test statistic ($Q_{obs} = -7.8$) greater than its expectation ($Q_{exp} = -9.2$) and therefore to a larger background-only probability (observed p-value equal to 0.10 compared to 0.08 for the expected p-value). Figure 6.9 shows the the test statistic distribution obtained for the signal-plus-background and background-only ensemble tests, with the expected and observed Q-values; the dependence of Q_{exp} on the scale factor fitted for the signal (β_s) is instead discussed in Appendix F.
The expected and observed upper limits on the s-channel production cross section set at the 95% confidence level are 1.4 and 2.6 times the Standard Model prediction, respectively. The measured upper limit is therefore 14.6 pb whereas the upper limit on the expected cross section is evaluated at 7.9 pb.
The difference found between the two values is related to the combination of the differences between the expected and observed background-only probabilities (p-values 0.08 and 0.10, respectively) with the differences between the expected and observed signal-plus-background probabilities (p-values of 0.10 and 0.47, respectively) obtained from the Standard Model predictions of the signal and background processes.

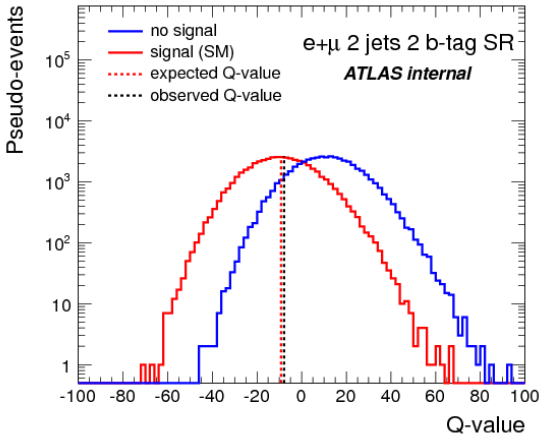

Figure 6.9: Expected test statistic distribution for the signal-plus-background (red histogram) and background-only (blue histogram) ensemble tests.

6.8 Conclusion

We reported in this chapter the single top s-channel cross section measurement at $\sqrt{s} = 8$ TeV, with 20.3 fb^{-1} of data collected with the ATLAS detector. In order to isolate signal events from the main sources of backgrounds, which have very similar event topology and kinematics which make them difficult to disentagle, an event selection and a multivariate approach have been undertaken. The implementation of a boosted decision trees classifier gives a highly discriminant distribution which is fitted to the data to extract the s-channel contribution. A frequentist statistical analysis allows moreover to infer the uncertainty related to the cross-section, for which an upper limit of 14.6 pb (7.9 pb expected) is set. The precision achieved with this measurement is undoubtly better than the one of the 7 TeV analysis, mainly due to the higher integrated luminosity which reduces the statistical and systematic uncertainties; the total observed uncertainty and the significance improves moreover the results published by CMS in [152]. The result presented here is not, however, comparable with the one provided at Tevatron in 2014, featuring a significance of 6.3 standard deviations.

Conclusion

This thesis, aimed at observing the top quark electroweak production in the s-channel, profitted from the singular opportunity of performing two analyses based on different proton-proton collision datasets collected by the ATLAS detector. Such an approach turned out to have an important pedagogical character, as allowed first to identify the critical issues for the cross section extraction using a limited integrated luminosity, and then to perform a more complete and refined study on a larger data sample.

For the analysis of the 7 TeV dataset (4.7 fb^{-1}), two boosted decision trees classifiers were trained to isolate the s-channel from the dominant background contributions; one was employed to implement a tight event selection, and the second was fitted, simultaneously with two distributions defined in specific control regions, to extract the signal cross section. Several technical limitations connected to the choice of the b-tagging algorithm working point and to the low statistics of some Monte Carlo samples, as well as the significant impact of the systematic uncertainties, lead to a limited sensitivity. An observed upper limit of 21.5 pb was set on the s-channel cross section, improving in any case the previous ATLAS result reported in [151].
The analysis of the 8 TeV dataset (20.3 fb^{-1}) was conceived in a two steps procedure, with the goal of simplifying the previous strategy, keeping its robustness. With a preliminary set of simple selection criteria, we retained the regions of phase space that single top events tend to populate; then, we exploited the acquired experience on boosted decision trees to set up a discriminant distribution. With a log likelihood fit procedure coupled to a frequentist statistical analysis, we derived a limit on the s-channel cross section of 14.6 pb, with a significance of 1.3 standard deviations. Such results, reported in a paper which will be submitted for publication to Physics Letter B, improve the sensitivity achieved by CMS in [152]; however, they are far from being competitive with the combined s-channel cross section measurement provided at TeVatron in 2014, which corresponds to a significance of 6.3 σ. This last measurement, of course, refers to a different center of mass energy and initial state, and it is notorious that LHC proton-proton collisions do not favour this single top production mechanism which proceeds from quark-antiquark annihilation.

The increase of the center of mass energy up to 14 TeV during the coming LHC run II will not favour the search for the single top s-channel, which will be on the contrary drowned into the main sources of background whose rate increases steeply with $\sqrt{s}$. At the same time, the boosted topology characteristic of high energy collisions would

probably introduce some additional difficulties in discriminating signal-enriched final states. We envisage, however, some prospects of further improvements relying on the contribution from another multivariate technique, the matrix element method, and a more extensive and refined use of the b-tagging. The matrix element method (MEM) has been developed by the DØ collaboration to measure the top quark mass [153], and represents a vital part of the TeVatron analyses; it could be implemented in the s-channel 8 TeV analysis by adding the leading order MEM discriminants to the list of boosted decision trees input variables, or by combining the output distributions. At the same time, the correlations between b-jets kinematics and b-tagging algorithms output could be exploited, together with the frequent b-jets semileptonic decays; also the weights associated to such objects may be directly injected in the boosted decision trees as input variables. If on one hand such approach would qualitatively improve the signal discrimination, on the other one should also work with the goal of reducing the impact of the statistical and systematical uncertainties. Some progress on the transverse missing energy and jet energy scales has been supplied in a recent reprocessing of the 8 TeV dataset; moreover, the production of larger samples of W+jets simulated events would reduce the issues related to the fluctuations in the BDT output distribution, and to the high statistical error. Another possibility to be invastigated is the effect of profiling the most important sources of uncertainty, that would help in constraining in situ some of the systematic errors.

Appendices

Appendix A

s-channel 7 TeV analysis: validation of the W+jets and s-channel additional samples

Since in the 2 jets bin the W+jets 2-tag sample suffers of loose statistics, some checks have been made to warrant the usage of the shapes extracted from the 1-inclusive-tag sample. The following plots (Figs. A.1 and A.2) represent some normalized distributions reproducing jets kinematics, which we consider meaningful, for each W+jets flavour type in the 2-tag sample (in blue) and in the 1-inclusive-tag sample (in red). A part for the big statistical fluctuations, no important difference in the shapes is spotted, justifying the usage of the 1-inclusive-tag sample to model the W+jets events in the BDT classifier training; this background is conveniently normalized as described in Section. 5.3.1
For completeness we point out that the underlying assumption is not verified for all the physics processes; if for exemple we investigate the same distributions for signal events, different trends are shown for 2-tag and 1-inclusive-tag samples. As Fig. A.3 higlights, these are mainly evident for the jets momentum.

In the 2 jets bin also the nominal MC sample describing the s-channel single top production is characterized by low statistics; in order to improve the performance of the BDT classifiers, which are very sensitive to this kind of issues, another generator has been introduced to model the signal in the training phase. As Fig. A.4 illustrates, the description of the kinematics realized by POWHEG and MC@NLO is almost equivalent.

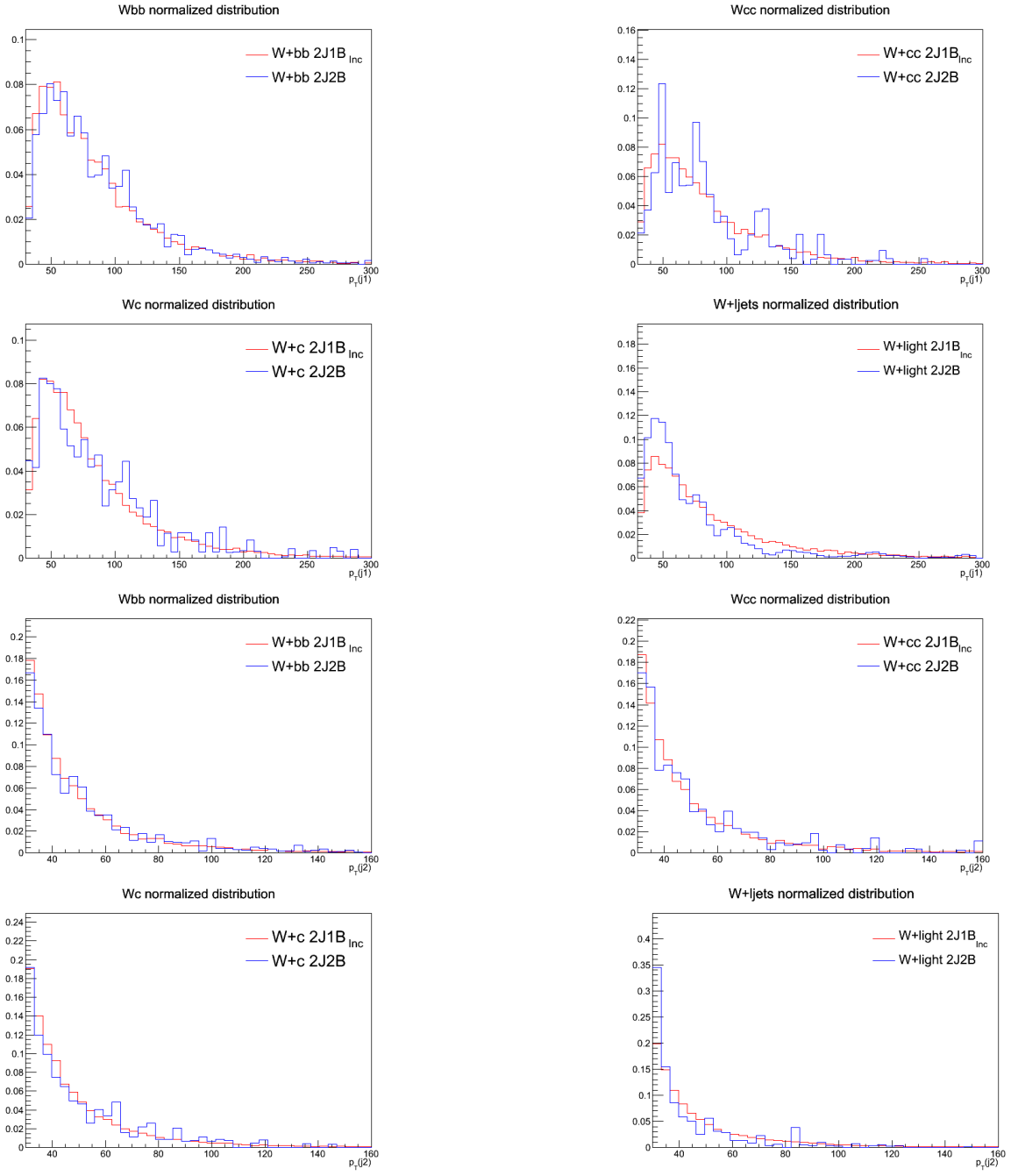

Figure A.1: Leading and subleading jet p_T normalized distributions for electron and muon channels combined. $Wb\bar{b}$+jets, $Wc\bar{c}$+jets, Wc+jets and W+light jets events are shown for the 2J2B sample (in blue) and the $2J1B_{inc}$ sample (in red).

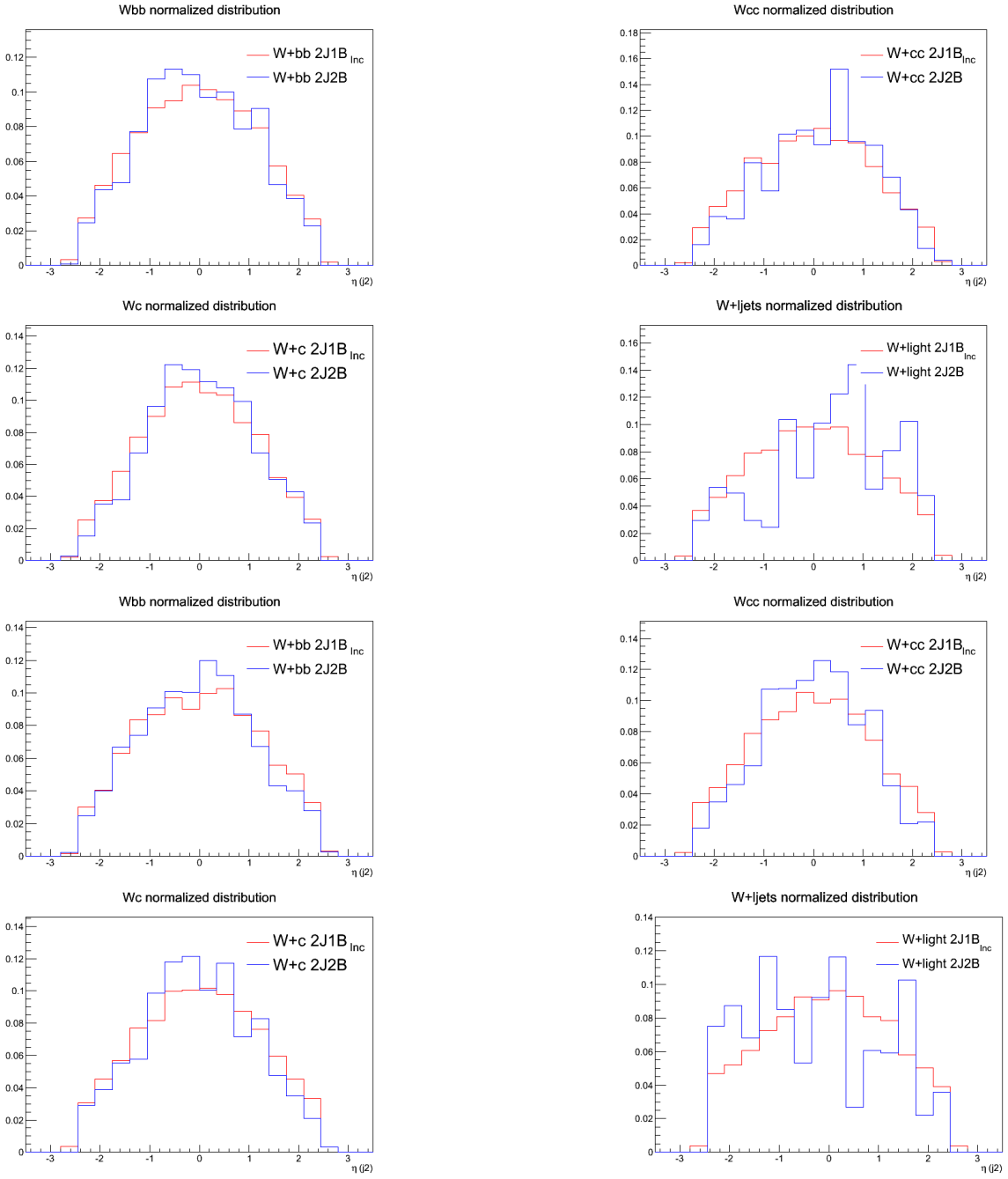

Figure A.2: Pseudorapidity normalized distributions of leading and subleading jet, for electron and muon channels combined. $Wb\bar{b}$+jets, $Wc\bar{c}$+jets, Wc+jets and W+light jets events are shown for the 2J2B sample (in blue) and the $2J1B_{inc}$ sample (in red).

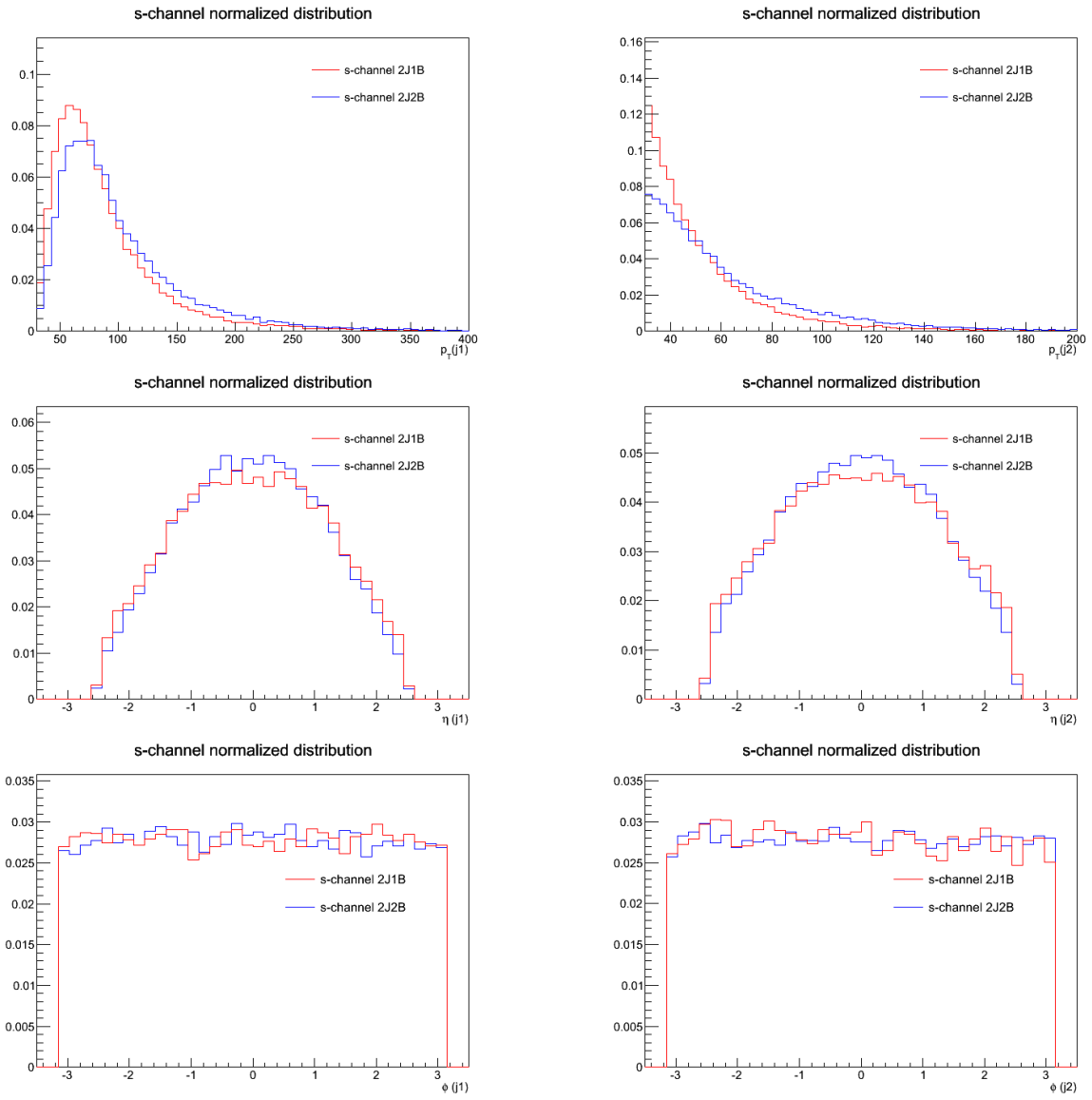

Figure A.3: Normalized distributions for leading jet p_T, η, ϕ and subleading jet p_T, η, ϕ for electron and muon channels combined. Single top s-channel events are are shown for the 2J2B sample (in blue) and the $2J1B_{inc}$ sample (in red).

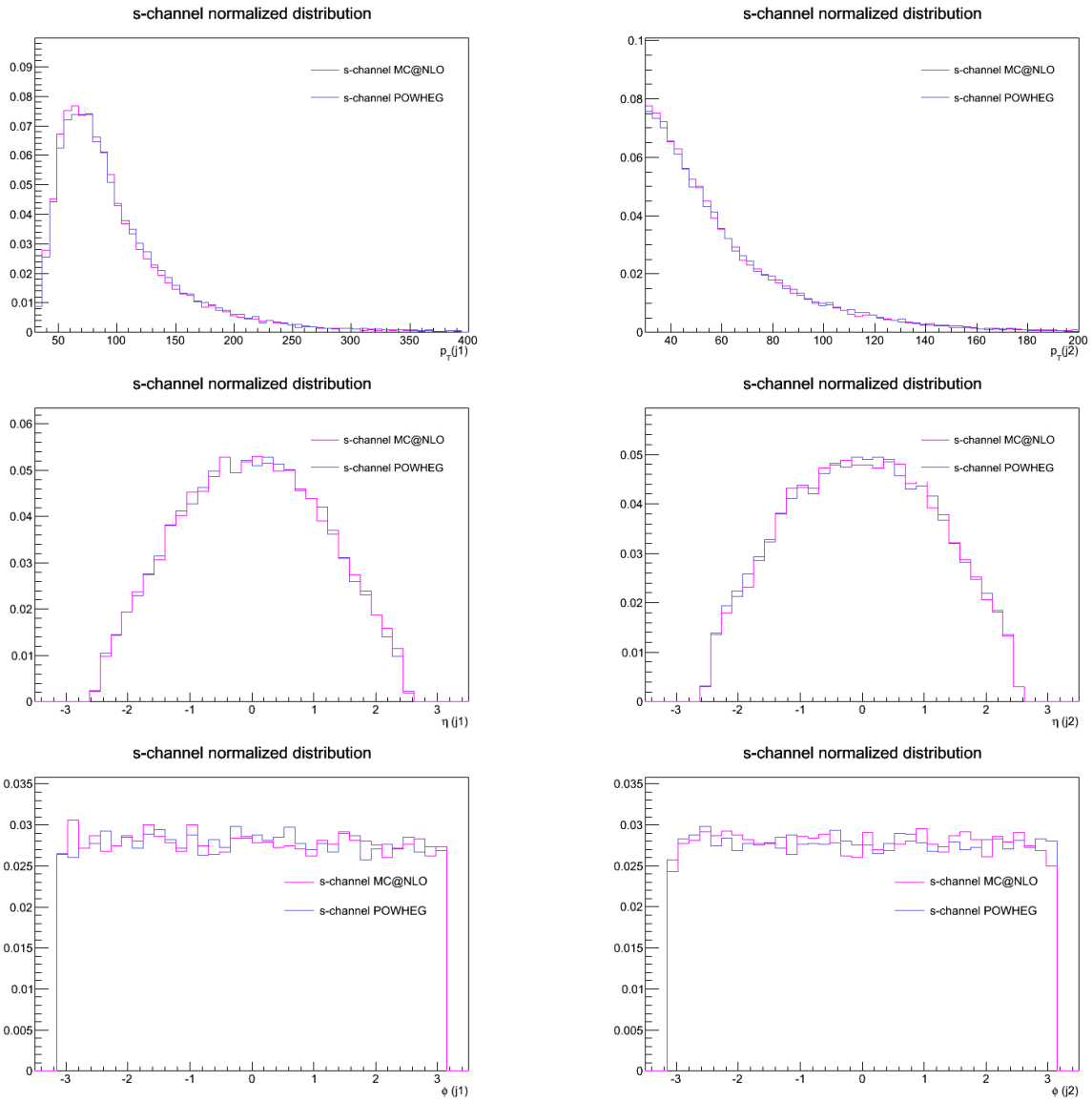

Figure A.4: Normalized distributions for leading jet p_T, η, ϕ and subleading jet p_T, η, ϕ for electron and muon channels combined. Single top s-channel events are are shown for the MC@NLO (in violet) and POWHEG generators (in magenta).

Appendix B

s-channel 7 TeV analysis: control plots in signal and background enriched regions

In order to investigate the modeling for the three "tag" samples used in the s-channel 7 TeV analysis, the most important kinematic distributions for the lepton and the jets are shown: the transverse momentum distribution for the lepton and the two jets, the transverse missing energy accounting for the escaping neutrino and the mass of the top quark reconstructed with the leading jet. In the upper plots, the shadowed bands correspond to the total statistical uncertainty in the expected Monte Carlo distributions added to a 50% uncertainty on the multijet normalization, derived from the data-driven procedures; the errors bars are instead associated to the observation. In the lower graphes, which represent the ratio between the data and the predicted yields, the convention is the same.

Figures B.1 and B.2, illustrating 1 jet 1-tag events separately for the electron and muon channels, attest a very good data/MC agreement in the shapes.

The main 2 jets 2-tag kinematics variables shown in Figs. B.3 and B.4 exhibit a rather good agreement between expectations and data, considering the reduced statistics with respect to the previous plots. Only the momentum of the leading jet does not show a satisfying modeling, and will not therefore be used as input variable for the Boosted Decision Trees.

Figures B.5 and B.6, representing the main kinematic distributions for the 3 jets 2-tag sample, present a reasonable data/MC agreement in the shapes considering the low statistics.

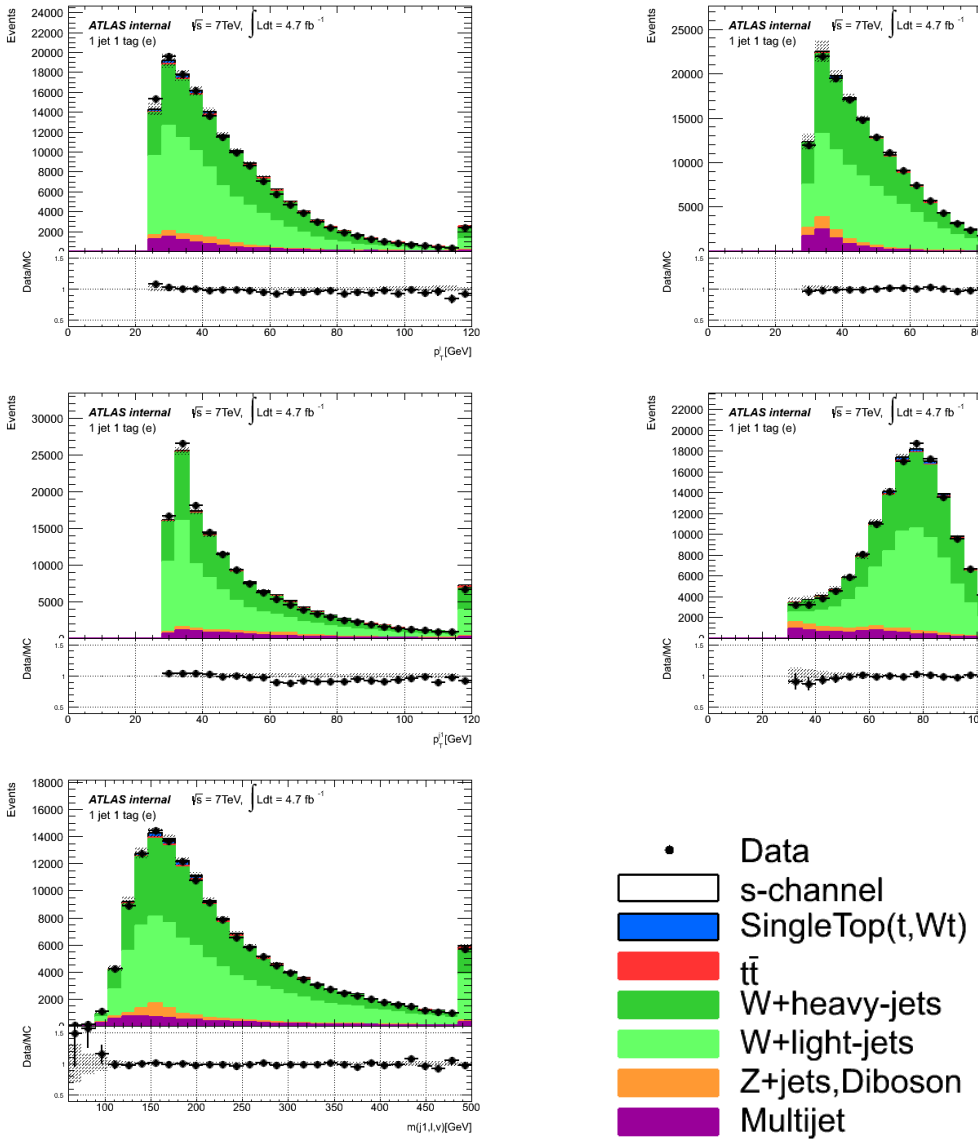

Figure B.1: Main kinematic distributions for the 1-tag W+jets-enriched sample in the **electron channel**: lepton p_T , transverse missing energy E_T^{miss}, jet p_T , W boson transverse mass $m_T(W)$, reconstructed mass of the top quark $m(j_1, l, \nu)$. W+jets events are normalized according to the data driven scale-factors, and multijet events are modelled via the jet-electron method.

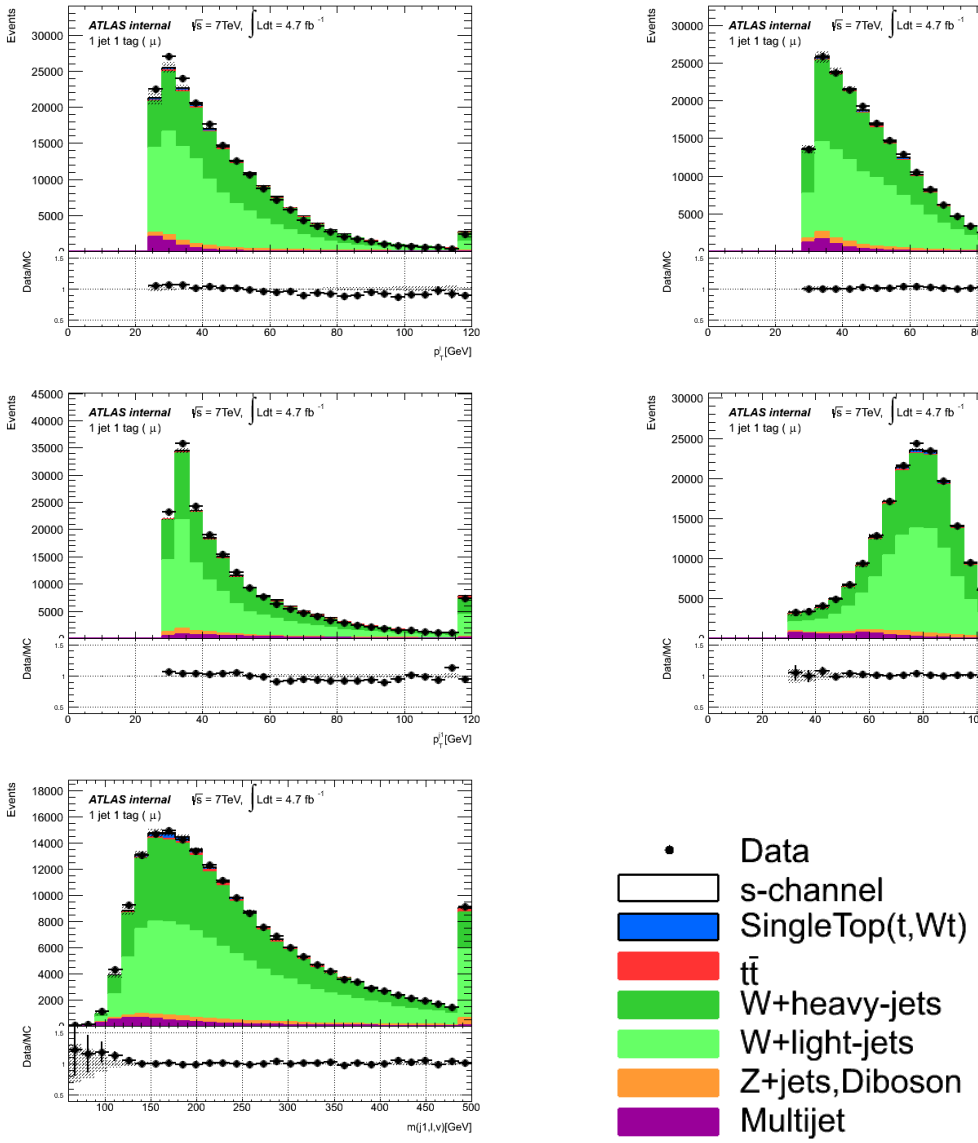

Figure B.2: Main kinematic distributions for the 1-tag W+jets-enriched sample in the **muon channel**: lepton p_T , transverse missing energy E_T^{miss}, jet p_T , W boson transverse mass $m_T(W)$, reconstructed mass of the top quark $m(j_1, l, \nu)$. W+jets events are normalized according to the data driven scale-factors, and multijet events via the matrix method technique.

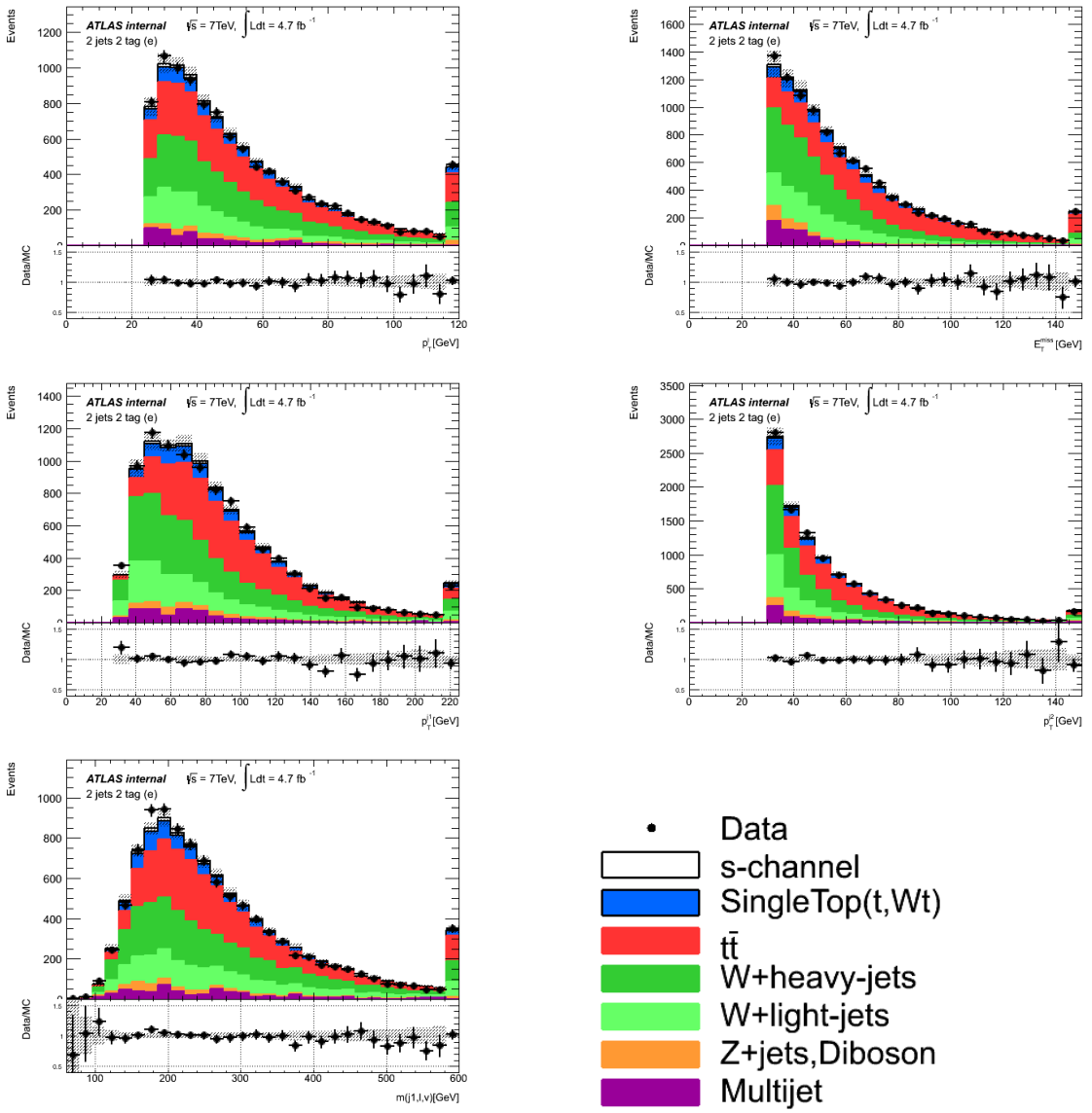

Figure B.3: Main kinematic distributions for the 2-tag signal-enriched sample in the **electron channel**: lepton p_T , transverse missing energy E_T^{miss}, leading jet p_T , second jet p_T , reconstructed mass of the top quark $m(j_1, l, \nu)$. W+jets events are normalized according to the data driven scale-factors, and multijet events via the jet-electron model.

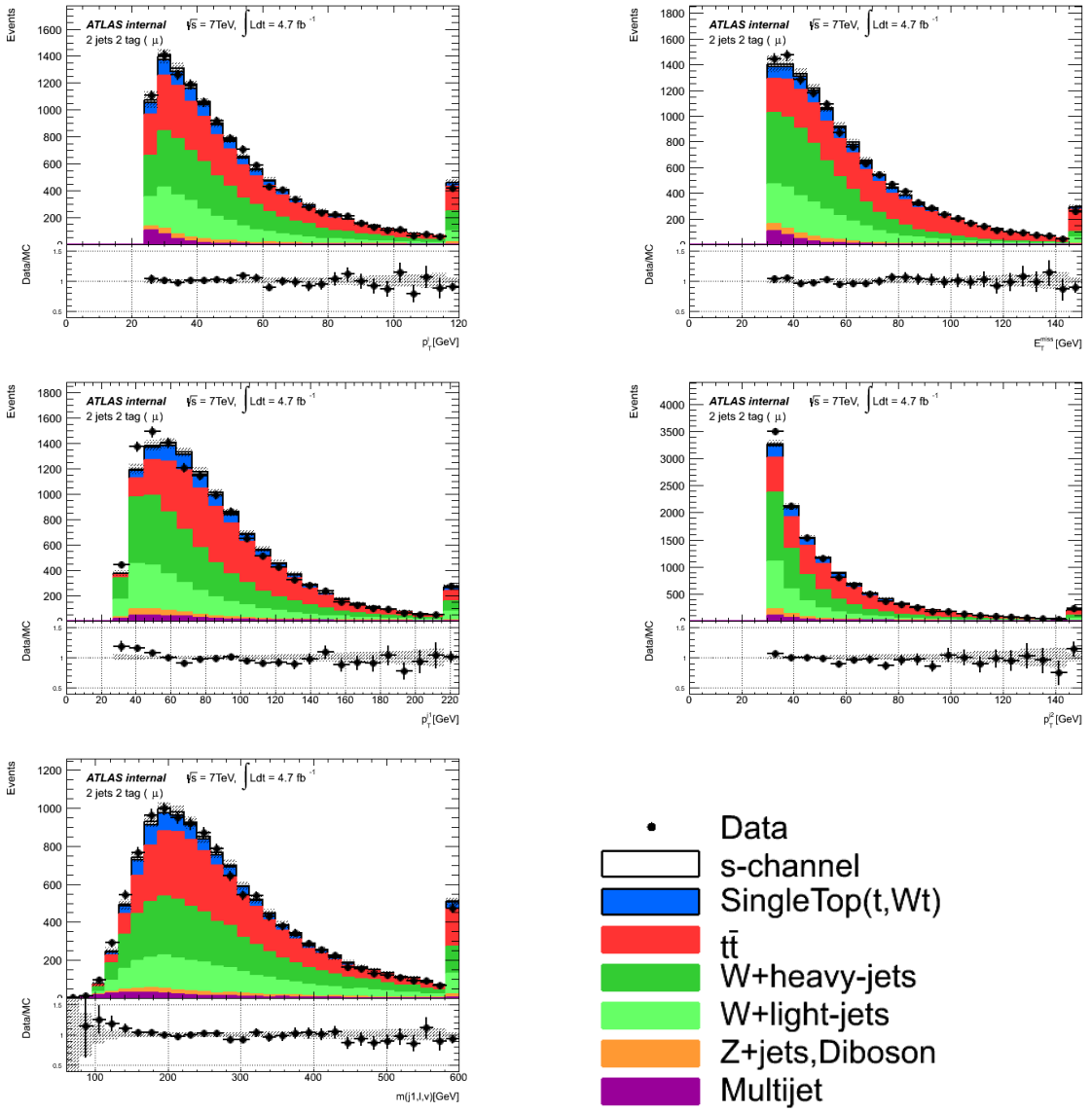

Figure B.4: Main kinematic distributions for the 2-tag signal-enriched sample in the **muon channel**: lepton p_T , transverse missing energy E_T^{miss}, leading jet p_T , second jet p_T , reconstructed mass of the top quark $m(j_1, l, \nu)$. W+jets events are normalized according to the data driven scale-factors, and multijet events via the matrix method technique.

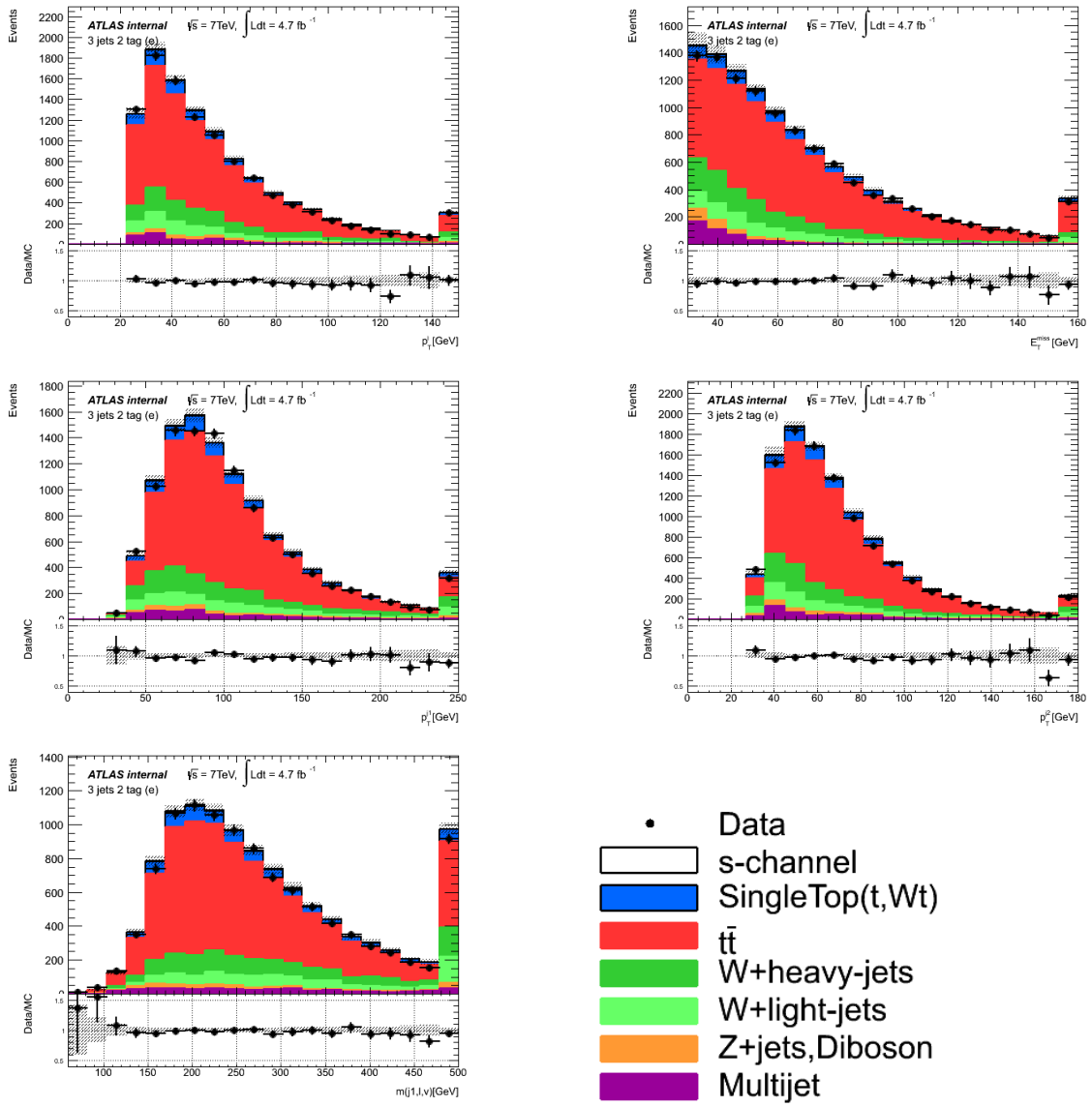

Figure B.5: Main kinematic distributions for the 2-tag $t\bar{t}$ -enriched sample in the **electron channel**: lepton p_T , transverse missing energy E_T^{miss}, leading jet p_T , second jet p_T , reconstructed mass of the top quark $m(j_1, l, \nu)$. W+jets events are normalized according to the data driven scale-factors, and multijet events via the jet-electron model.

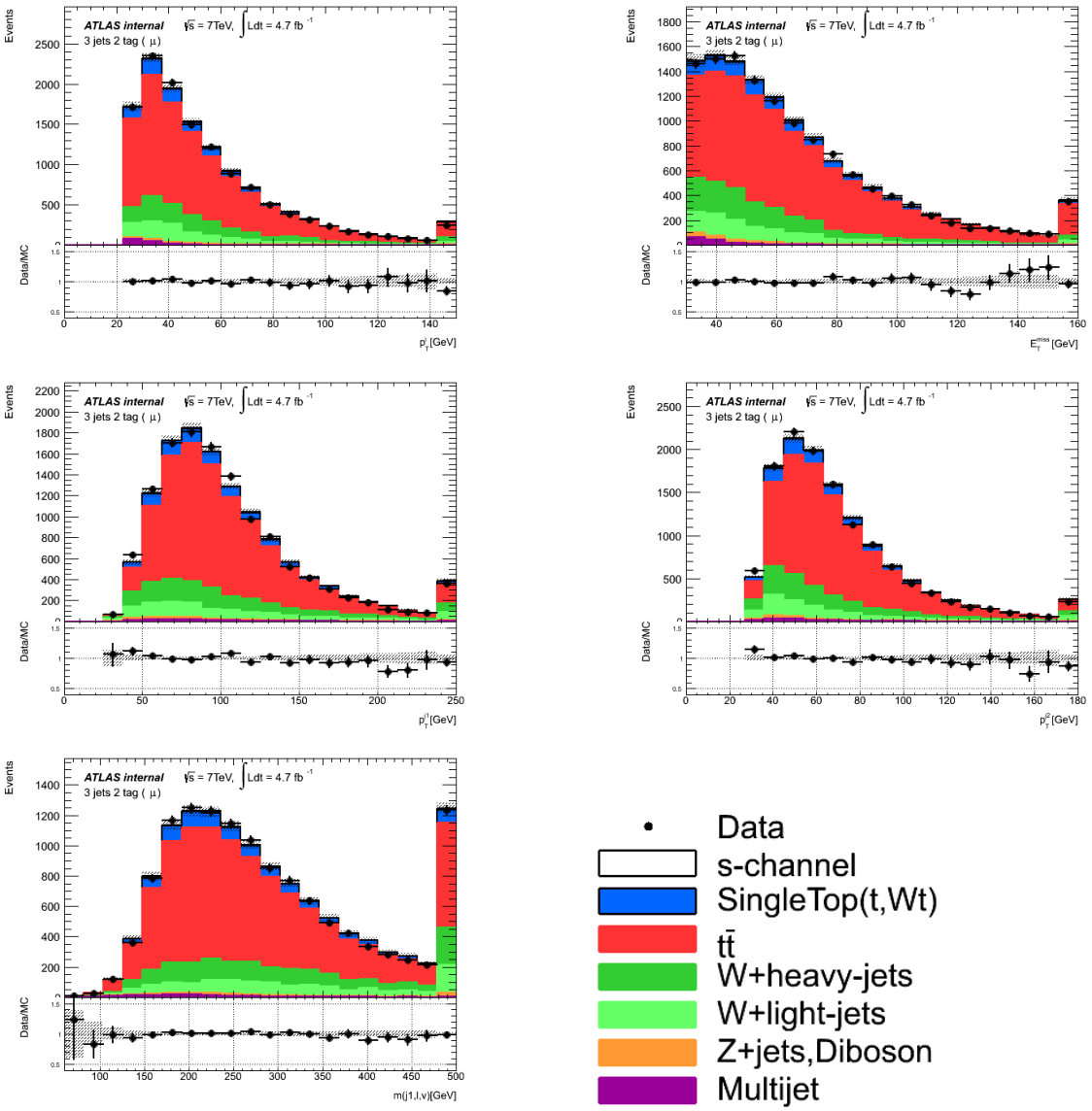

Figure B.6: Main kinematic distributions for the 2-tag $t\bar{t}$ -enriched sample in the **muon channel**: lepton p_T , transverse missing energy E_T^{miss}, leading jet p_T , second jet p_T , reconstructed mass of the top quark $m(j_1, l, \nu)$. W+jets events are normalized according to the data driven scale-factors, and multijet events via the matrix method technique.

Appendix C

s-channel 7 TeV analysis: BDT input variables in the signal region

The following control plots show the distributions of all the variables used as input of the BDT optimized against $t\bar{t}$ events (Figs. C.1, C.2, C.3, C.4) and W+jets events (Figs. C.5, C.6, C.7); the Monte Carlo and data samples belong to the 2 jets 2-tag signal region ($BDT_{W+jets} > 0.40$) and are presented for electron and muon channel combined. The distribution, with all the Monte Carlo channels (except the signal) rescaled to the fit results, show a reasonable data/MC agreement. In the upper plots, the shadowed bands correspond to the total statistical uncertainty in the expected Monte Carlo distributions added to a 50% uncertainty on the multijet normalization, derived from the data-driven procedures; the errors bars are instead associated to the observation. In the lower graphes, which represent the ratio between the data and the predicted yields, the convention is the same.

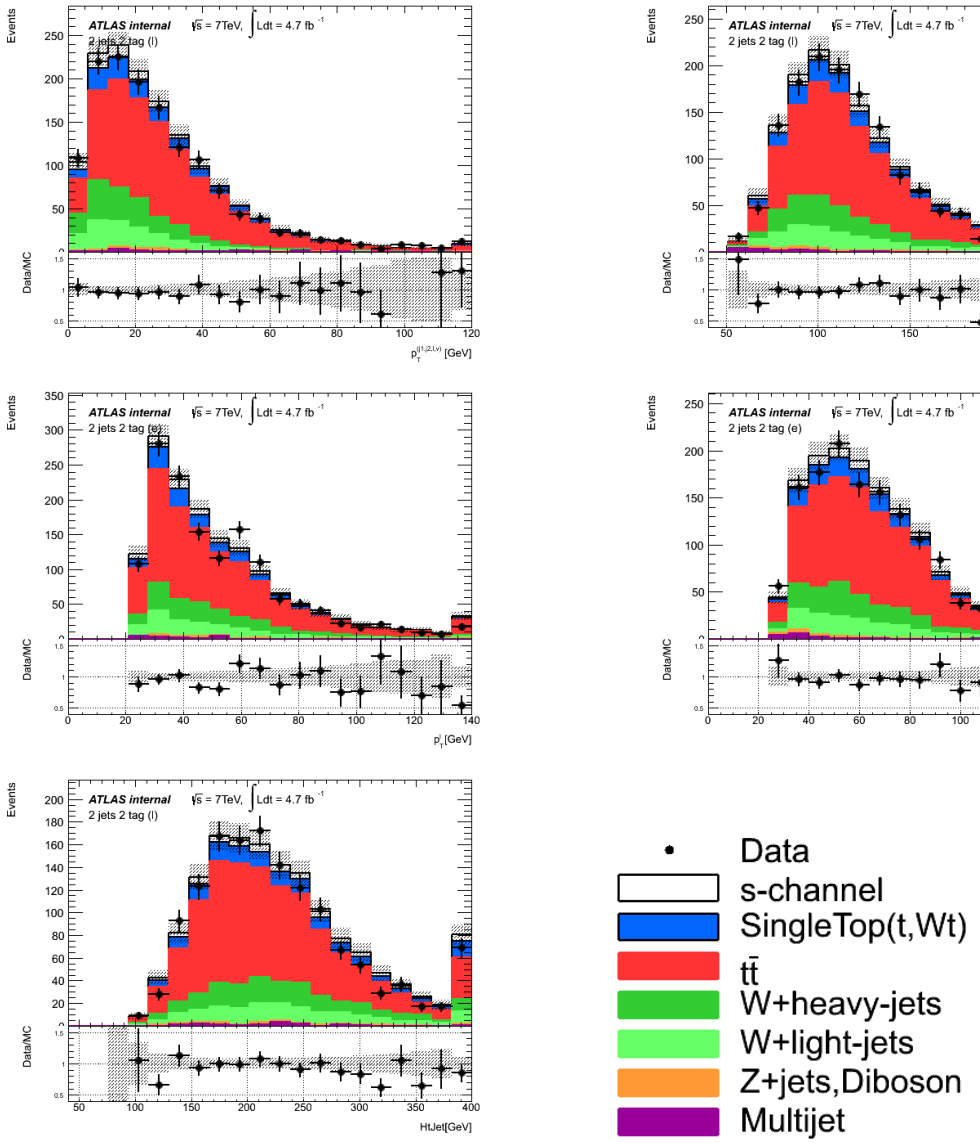

Figure C.1: Distributions of the discriminating variables used as input of the BDT against $t\bar{t}$ for 2 jets 2-tag events with $BDT_{W+jets} > 0.40$ in the lepton channel: transverse momentum of the final particles, sum of the transverse momentum of the lepton and the transverse missing energy, lepton p_T, E_T^{miss}, scalar sum of the jets p_T.

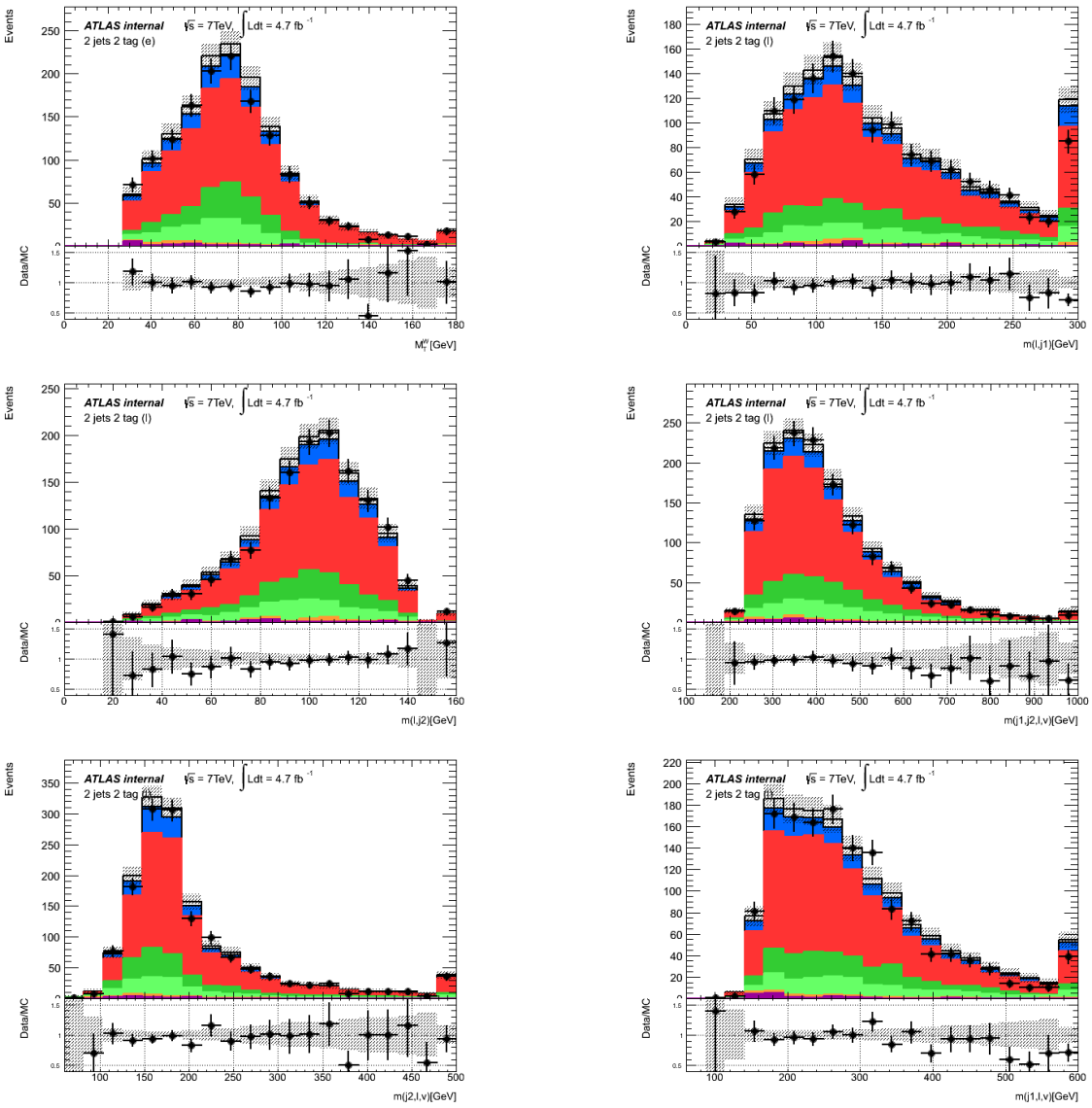

Figure C.2: Distributions of the discriminating variables used as input of the BDT against $t\bar{t}$ for 2 jets 2-tag events with $BDT_{W+jets} > 0.40$ in the lepton channel: transverse mass of the W boson, mass of the system composed by the lepton and the leading jet, mass of the system composed by the lepton and the subleading jet, mass of the system composed by all the final state particles, mass of the top-quark reconstructed with the subleading jet, mass of the top-quark reconstructed with the leading jet.

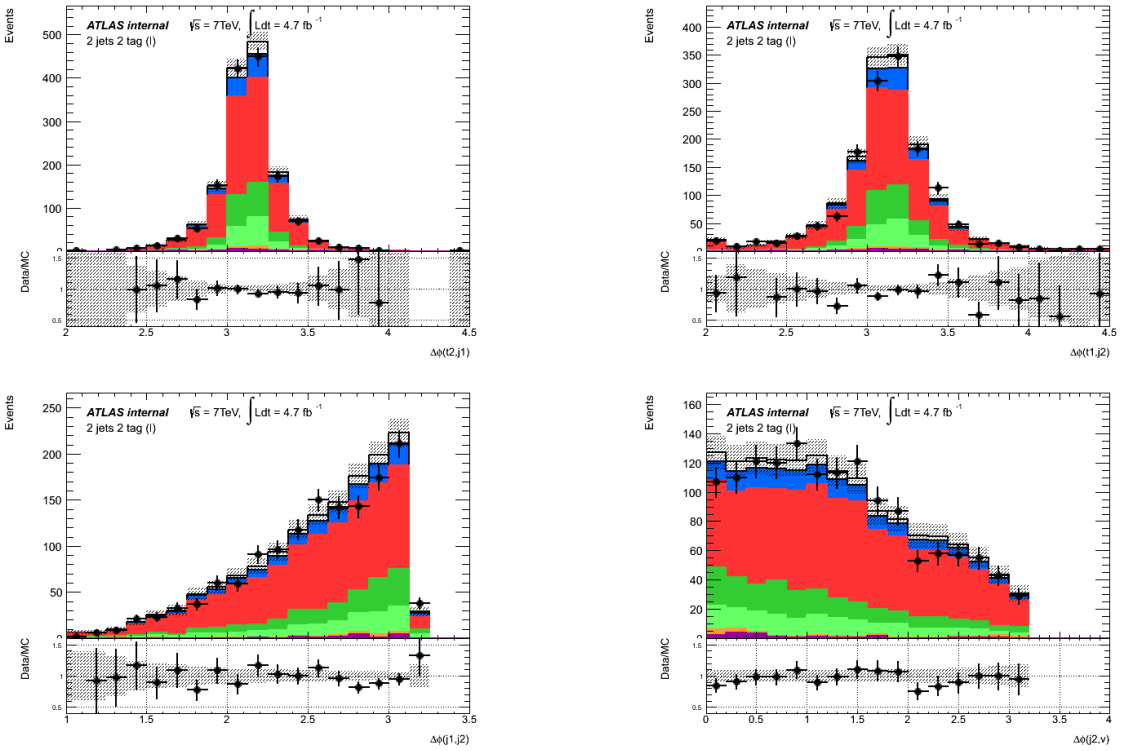

Figure C.3: Distributions of the discriminating variables used as input of the BDT against $t\bar{t}$ for 2 jets 2-tag events with $BDT_{W+jets} > 0.40$ in the lepton channel: $\Delta\Phi$ between the leading jet and the top quark, $\Delta\Phi$ between the sub-leading jet and the top quark, $\Delta\phi$ between the 2 jets, $\Delta\phi$ between the subleading jet and the neutrino.

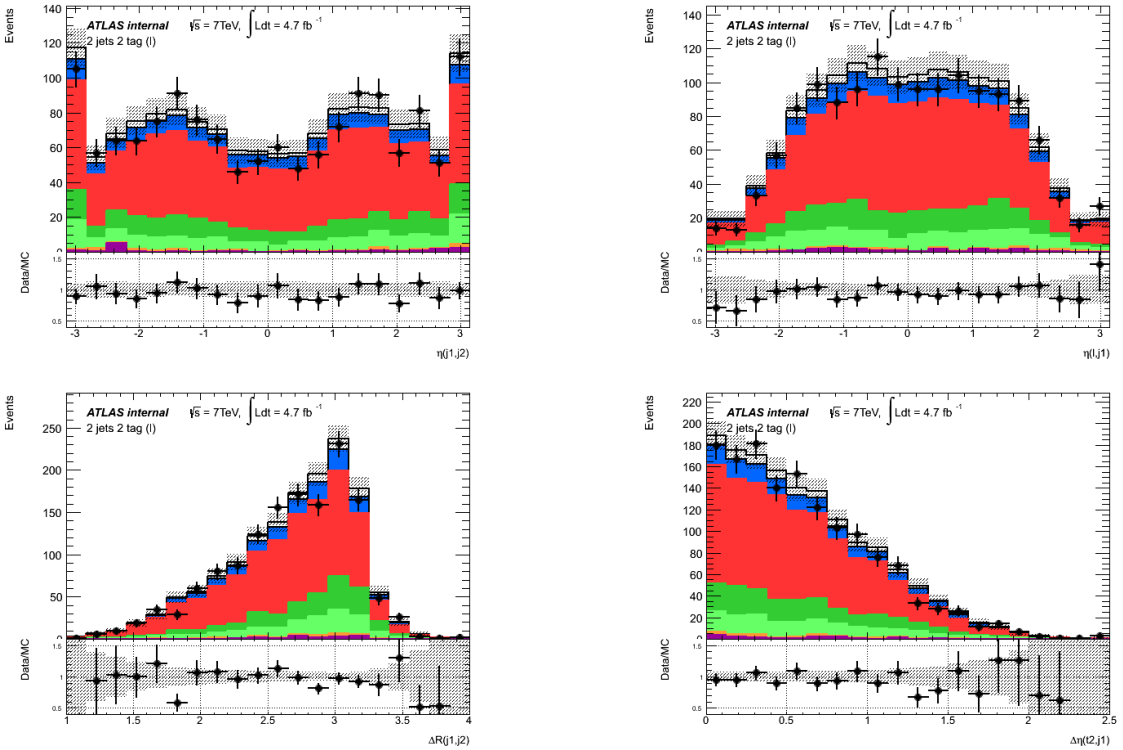

Figure C.4: Distributions of the discriminating variables used as input of the BDT against $t\bar{t}$ for 2 jets 2-tag events with $BDT_{W+jets} > 0.40$ in the lepton channel: pseudorapidity of the system composed by the two jets, pseudorapidity of the system composed by the lepton and the leading jet, ΔR between the 2 jets, $\Delta\eta$ between the top-quark reconstructed with the subleading jet and the leading jet.

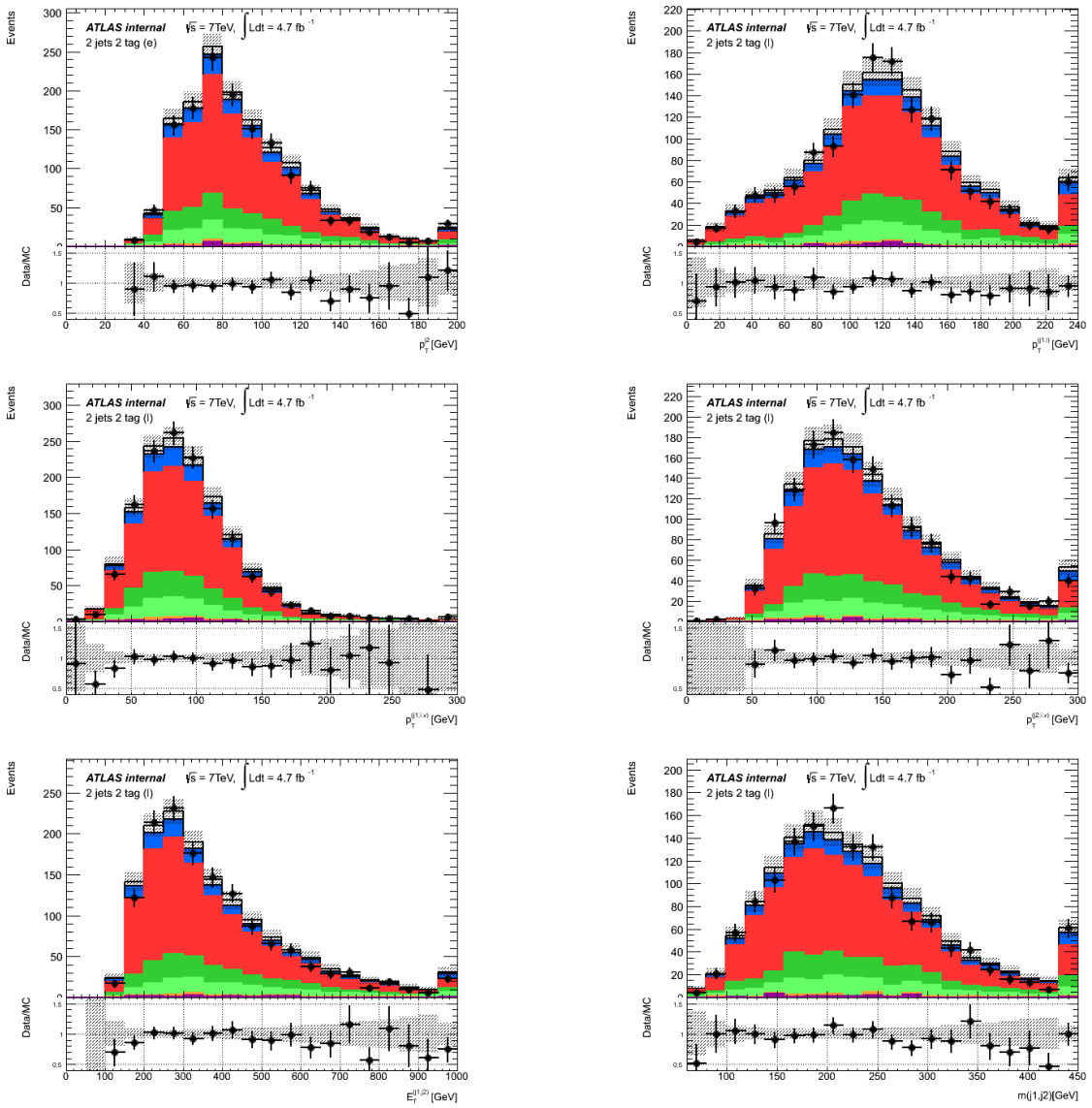

Figure C.5: Distributions of the most discriminating variables against W+jets for 2 jets 2-tag events with $BDT_{W+jets} > 0.40$ in the lepton channel: subleading jet p_T, p_T of the system composed by the lepton and the leading jet, transverse momentum of the top quark reconstructed with the leading jet and with the subleading jet, transverse energy of the system composed by the two jets, invariant mass of the leading and subleading jets.

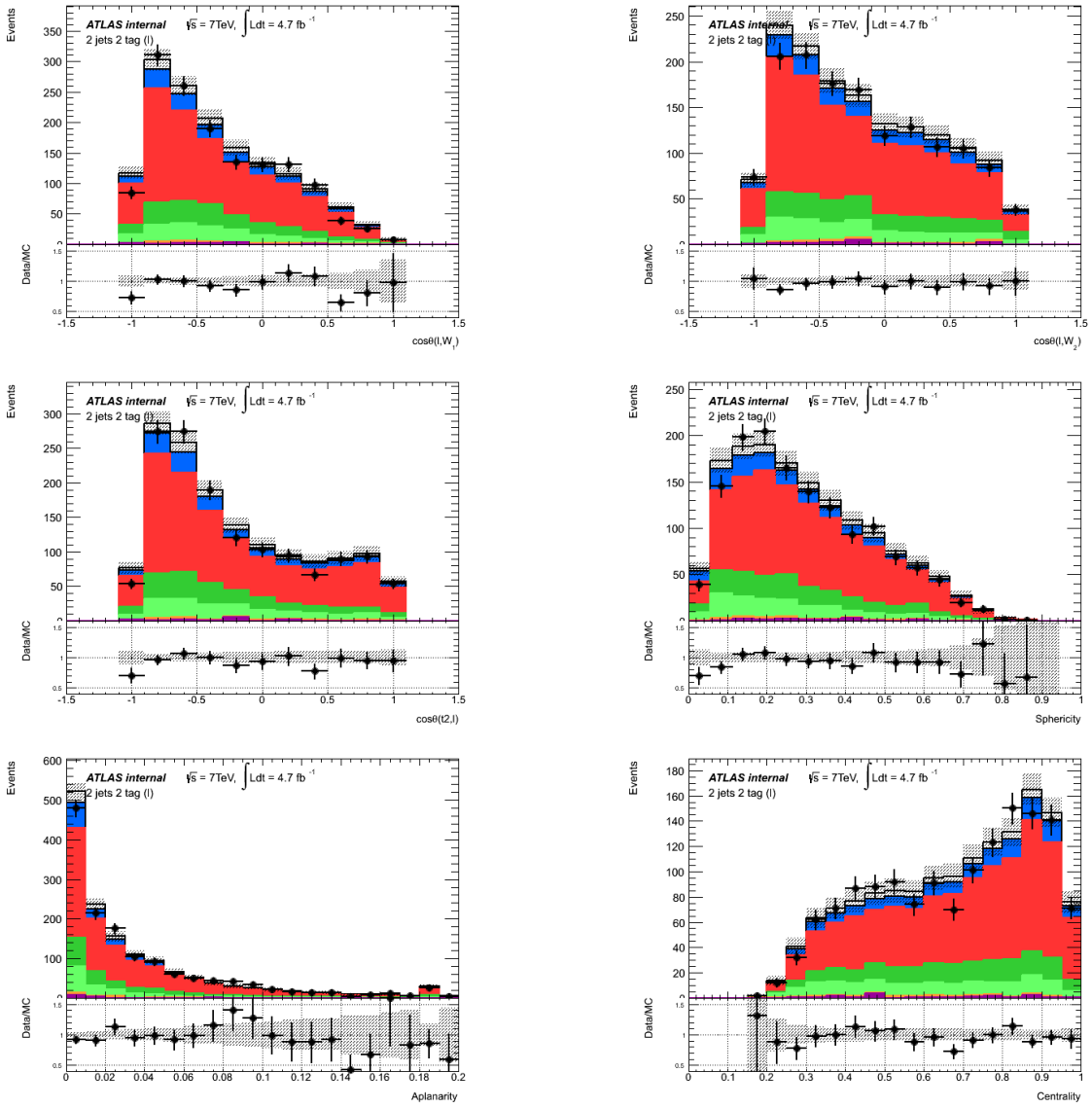

Figure C.6: Distributions of the discriminating variables used as input of the BDT against W+jets for 2 jets 2-tag events with $BDT_{W+jets} > 0.40$ in the lepton channel: cosine of the W helicity angle with the top quark being reconstructed through the leading and the subleading jet, top quark spin correlation in helicity basis, sphericity, aplanarity and centrality.

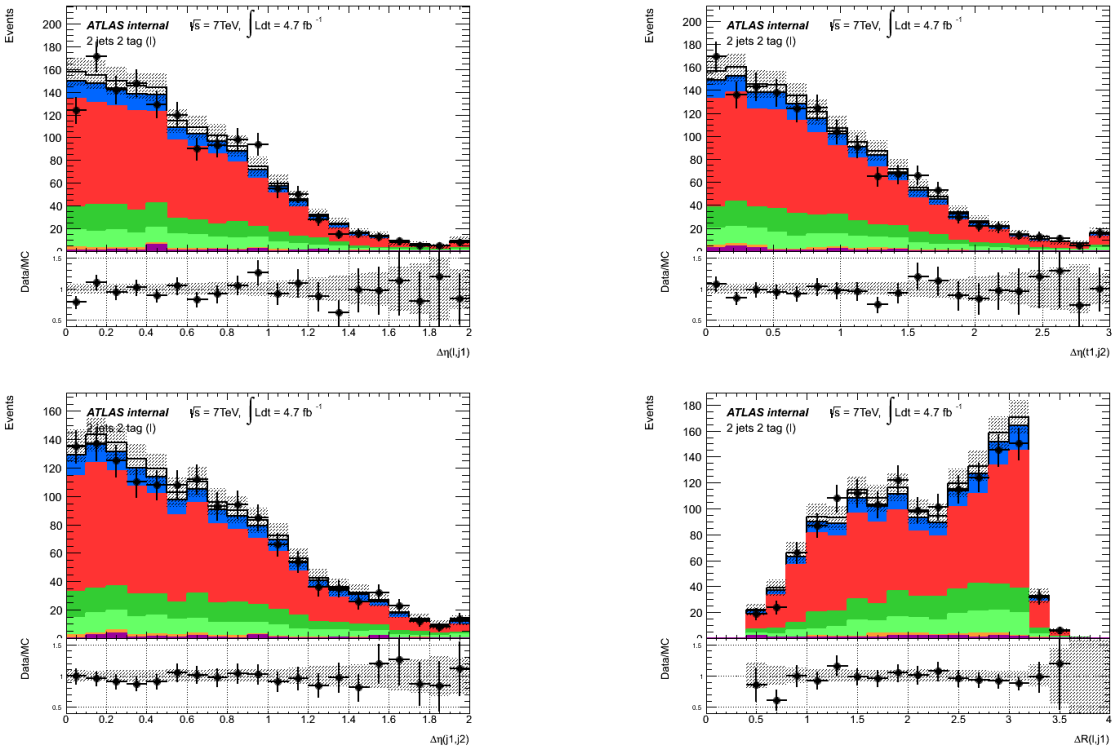

Figure C.7: Distributions of the discriminating variables used as input of the BDT against W+jets for 2 jets 2-tag events with $BDT_{W+jets} > 0.40$ in the lepton channel: $\Delta\eta$ between lepton and leading jet, $\Delta\eta$ between the top quark reconstructed with the leading jet and the subleading jet, $\Delta\eta$ between the two jets, ΔR between lepton and leading jet.

Appendix D

s-channel 8 TeV analysis: control plots in the background enriched regions

In order to investigate the modelling in the background-enriched samples used in the s-channel 8 TeV analysis, the most important kinematic distributions for the lepton and the jets are shown: the transverse momentum and the psudorapidity distribution for the lepton, the transverse missing energy accounting for the escaping neutrino and the transverse mass of the W-boson, as well as the transverse momenta of the two b-tag jets. In the upper plots, the shadowed bands correspond to the total statistical uncertainty in the expected Monte Carlo distributions added to a 50% uncertainty on the multijet normalization, derived via the matrix method; the errors bars are instead associated to the observation. In the lower graphs, which represent the ratio between the data and the predicted yields, the convention is the same.

Figures D.1 and D.2 are obtained in the W+jets control region defined with a released b-tagging and an event vetoing in order to make it orthogonal to the preselected signal region. In the plots, that are characterized by an overall good agreement between the observed and expected distribution shapes, W+jets production is renormalized according to the global scale factors extracted separately for the electron and muon channels (Section 6.3).

Figures D.3 and D.4 dispay the same variables in the $t\bar{t}$ control region, where two b-tagged jets and two non b-tagged jets are required. Again, the scale factors described in Section 6.3 are computed separately for the electron and muon channels in order to compare the shape of the variables without any hindrance due to the normalization that may arise after a double b-tagging. The good modelling of the $t\bar{t}$ background is evident from these plots, as expected.

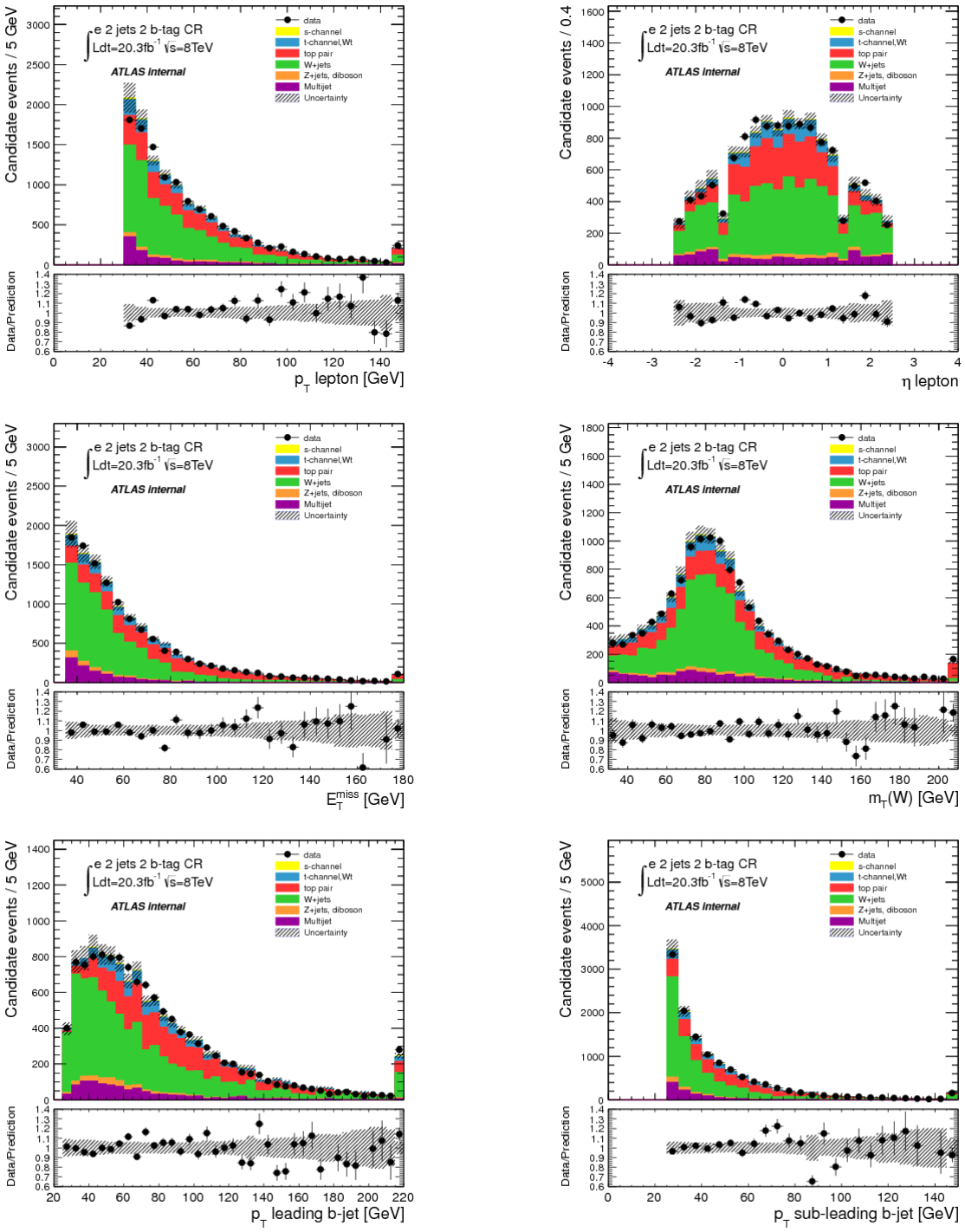

Figure D.1: Main kinematic distributions for the W+jets-enriched sample in the **electron channel**: lepton p_T, lepton η, transverse missing energy E_T^{miss}, W boson transverse mass $m_T(W)$, leading and subleading jet p_T. W+jets events are normalized according to the data driven overall scale-factors determined in this specific control region, and multijet events are modelled via the matrix method.

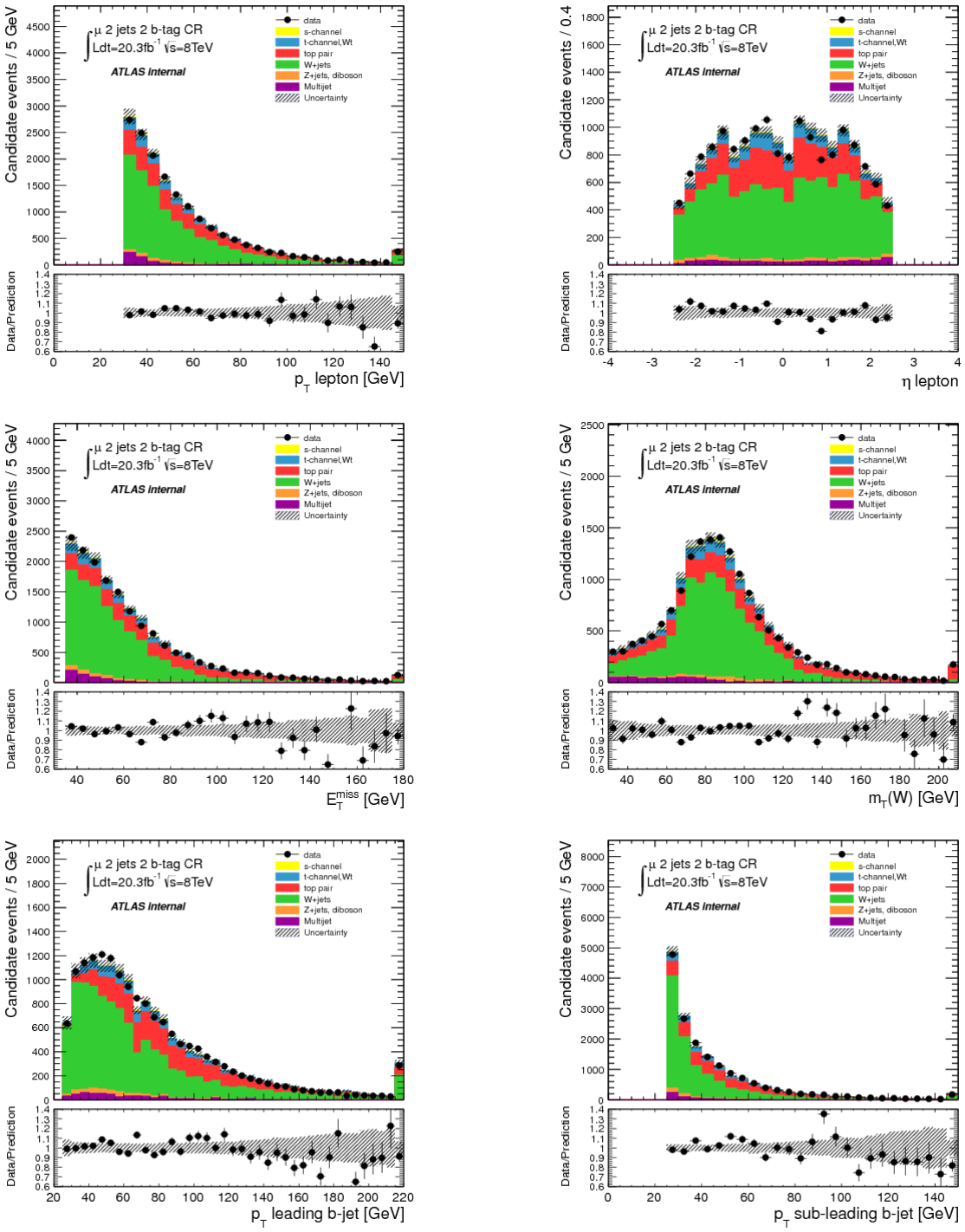

Figure D.2: Main kinematic distributions for the W+jets-enriched sample in the **muon channel**: lepton p_T, lepton η, transverse missing energy E_T^{miss}, W boson transverse mass $m_T(W)$, leading and subleading jet p_T. W+jets events are normalized according to the data driven overall scale-factors determined in this specific control region, and multijet events are modelled via the matrix method.

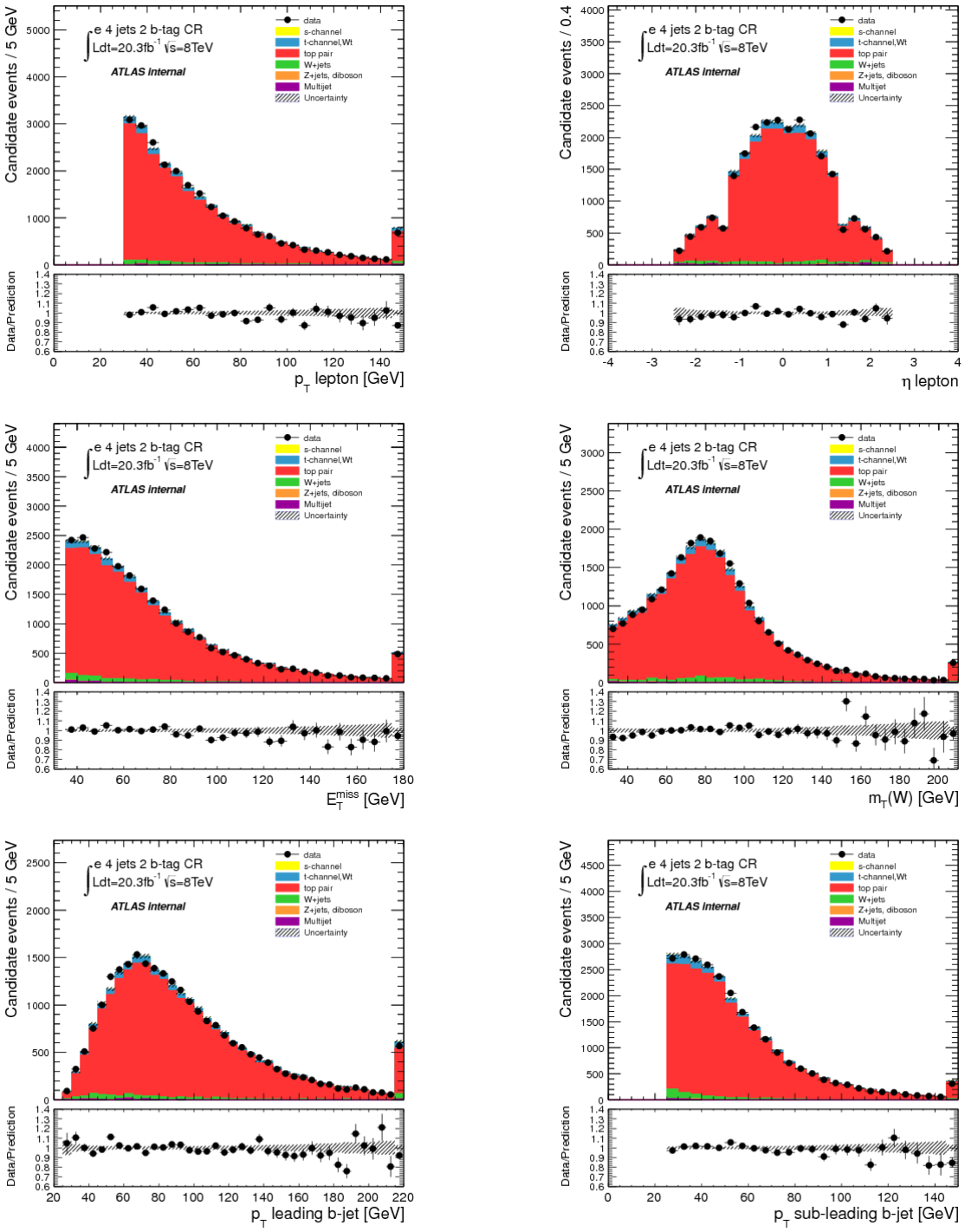

Figure D.3: Main kinematic distributions for the $t\bar{t}$ -enriched sample in the **electron channel**: lepton p_T, lepton η, transverse missing energy E_T^{miss}, W boson transverse mass $m_T(W)$, leading and subleading jet p_T. Top pair production is normalized according to the data driven overall scale-factors determined in this specific control region, and multijet events are modelled via the matrix method.

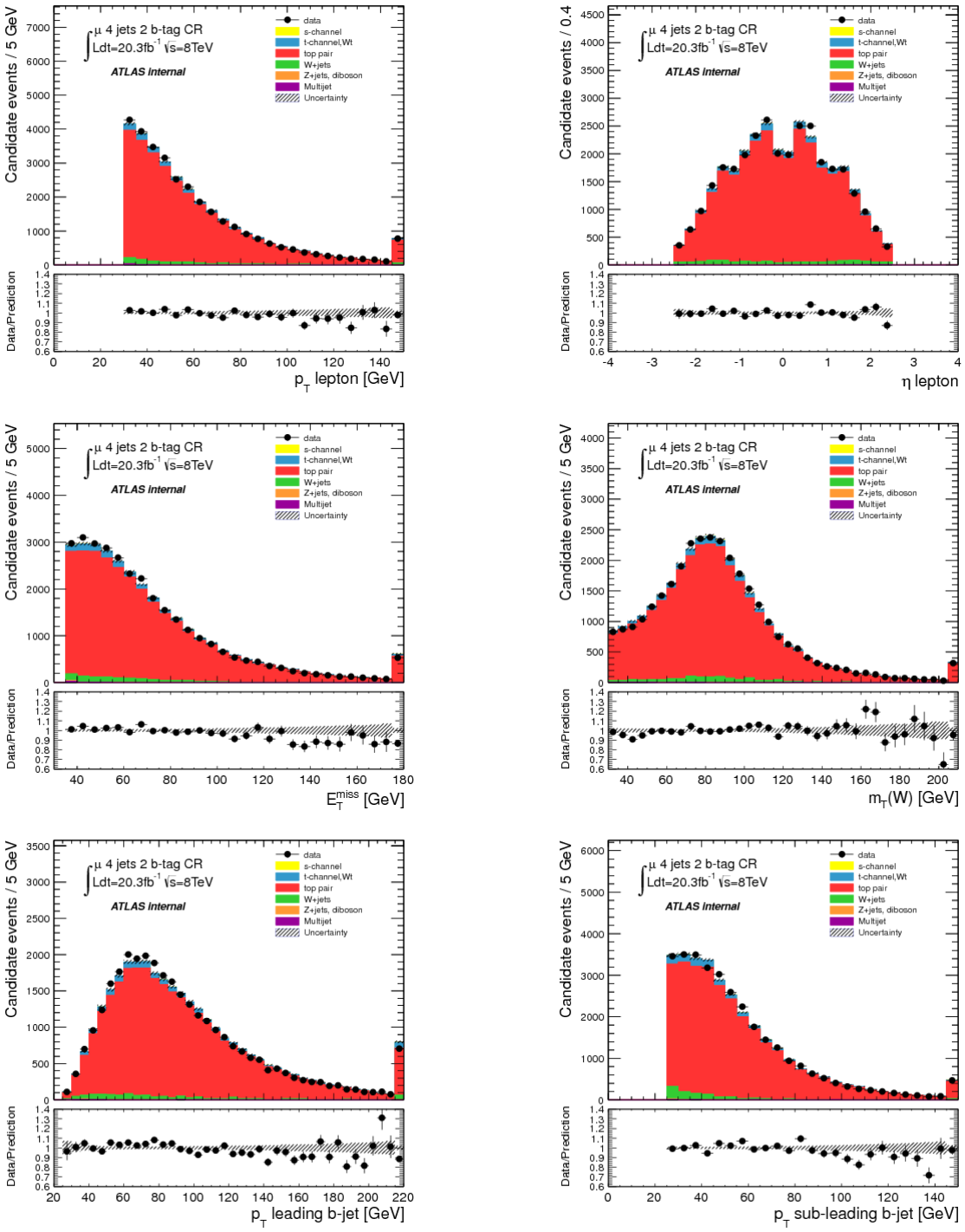

Figure D.4: Main kinematic distributions for the $t\bar{t}$ -enriched sample in the **muon channel**: lepton p_T, lepton η, transverse missing energy E_T^{miss}, W boson transverse mass $m_T(W)$, leading and subleading jet p_T. Top pair production is normalized according to the data driven overall scale-factors determined in this specific control region, and multijet events are modelled via the matrix method.

Appendix E

s-channel 8 TeV analysis: BDT input variables in the signal region

The following control plots show all the variables used as input of the BDT optimized against $t\bar{t}$ and W+heavy flavour jets productions. To legitimize both the training and validation procedures, the data/simulation agreement has been checked after the event preselection, but also after the selection; in both cases the distributions exhibit a good modelling, but for brevity we report here only the first kind of plots.
In the upper plots, the shadowed bands correspond to the total statistical uncertainty in the expected Monte Carlo distributions added to a 50% uncertainty on the multijet normalization, derived from the data-driven procedures; the errors bars are instead associated to the observation. In the lower graphes, which represent the ratio between the data and the predicted yields, the convention is the same. All the simulated distributions are renormalized with the scale factors given by the likelihood fit to the data.

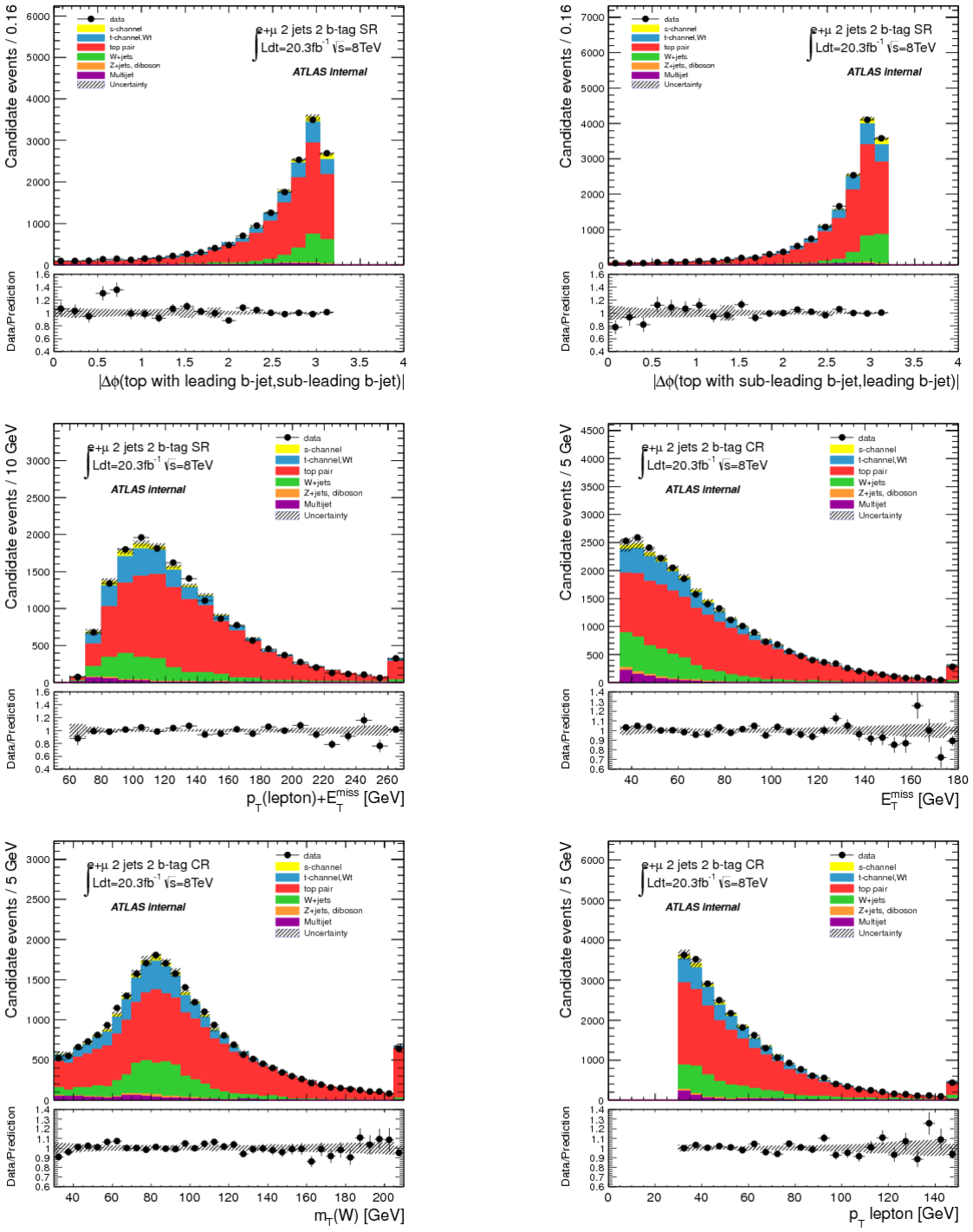

Figure E.1: Discriminating variable distributions in the preselected signal region: $\Delta\phi$ between the subleading jet and the top quark, $\Delta\phi$ between the leading jet and the top quark, sum of the lepton p_T and E_T^{miss}, transverse missing energy, transverse mass of the W-boson and lepton p_T.

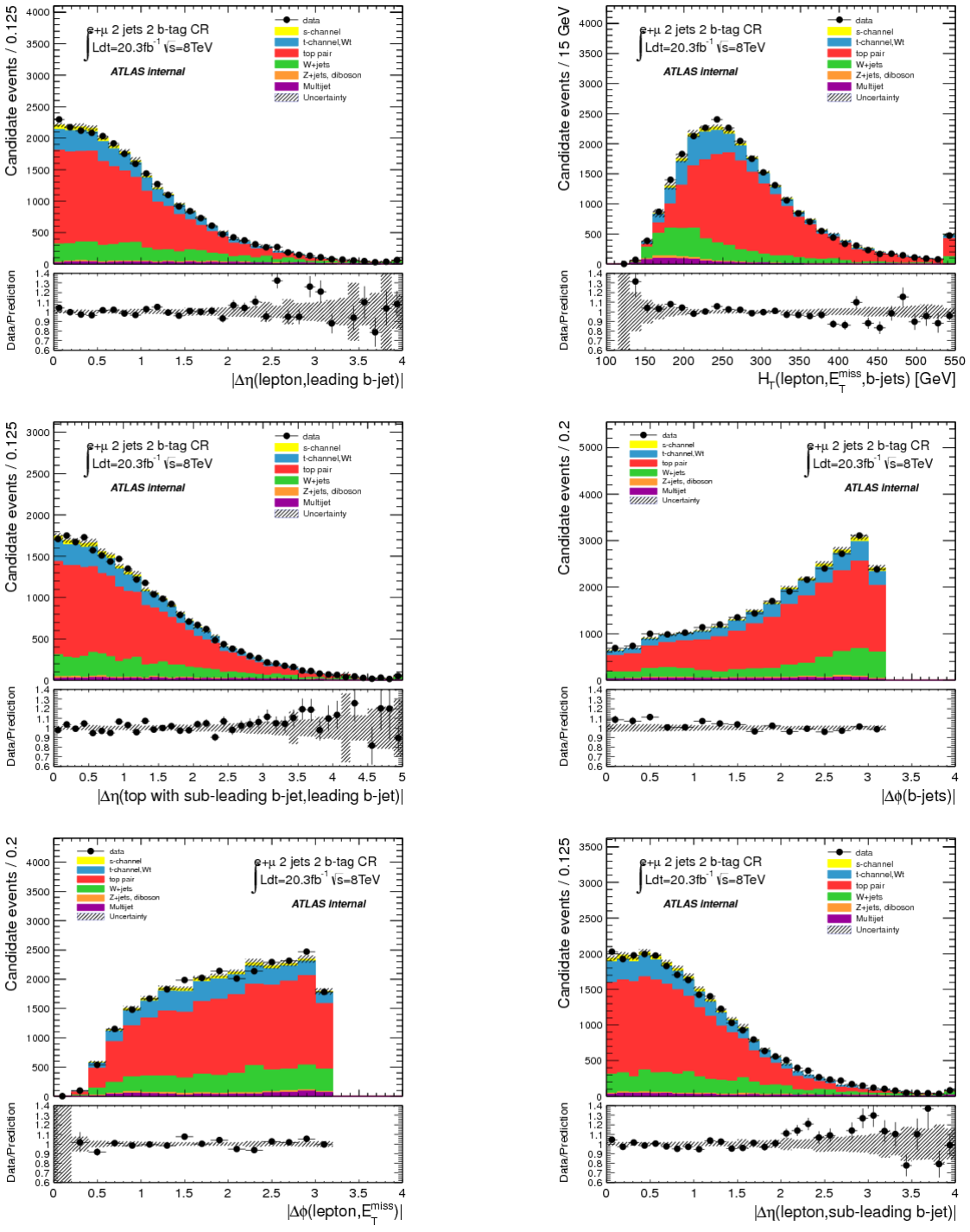

Figure E.2: Discriminating variable distributions in the preselected signal region: $|\Delta\eta|$ between the lepton and the leading jet, H_T, $|\Delta\eta|$ between the leading jet and the top quark, $|\Delta\phi|$ between the jets, $|\Delta\phi|$ between lepton and E_T^{miss} and $|\Delta\eta|$ between the lepton and the subleading jet.

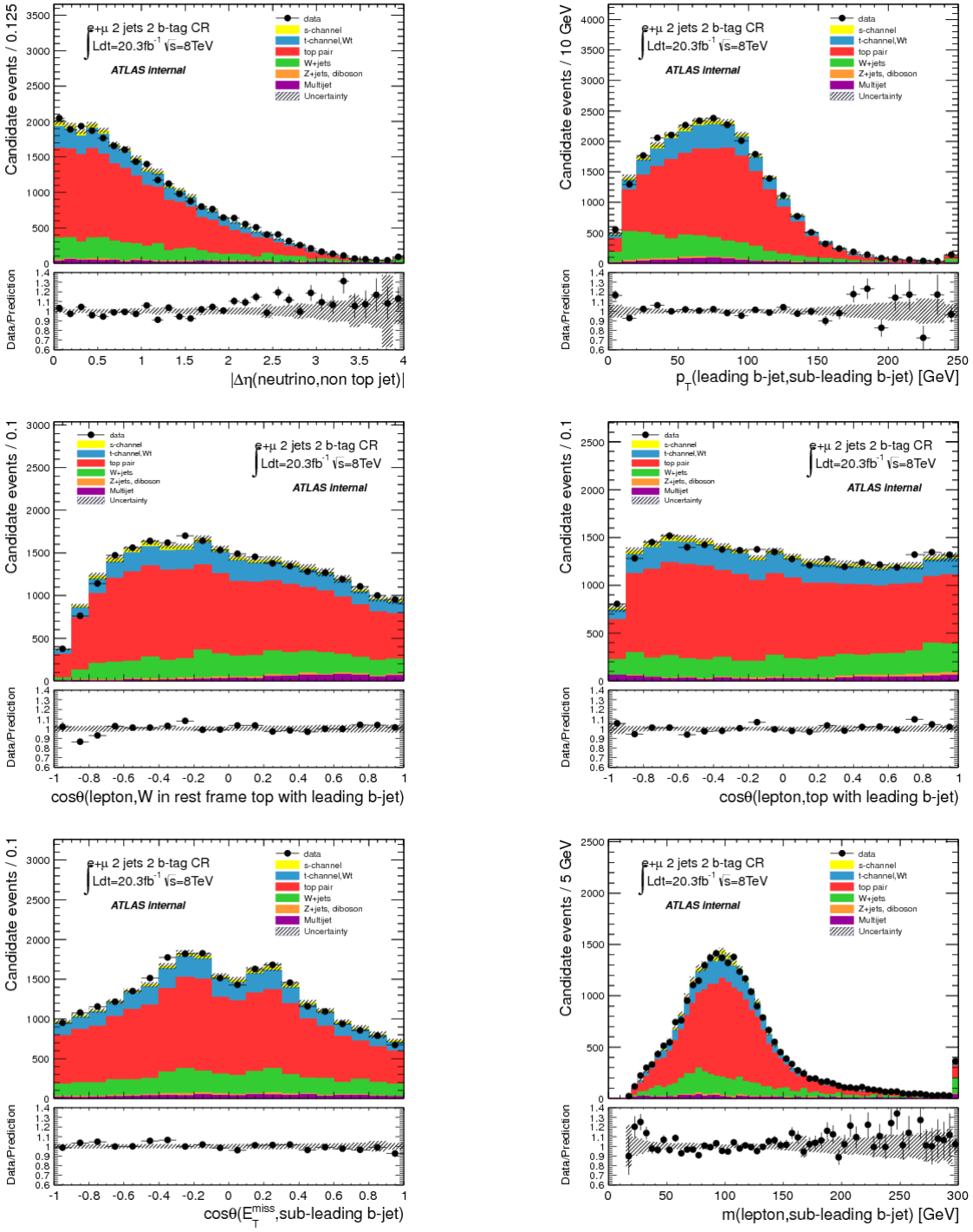

Figure E.3: Discriminating variable distributions in the preselected signal region: $|\Delta\eta|$ between the neutrino and the jet not used to reconstruct the top, p_T of the system composed by the two jets, cosine of the angle between the lepton in the W-boson rest frame and the W-boson in the top (reconstructed with the leading jet) rest frame, cosine of the angle between the lepton in the top rest frame and the top (reconstructed with the leading jet) in the center-of-mass frame, cosine of the angle between E_T^{miss} and the subleading jet and mass of the system composed by the lepton and the subleading jet.

Appendix F

s-channel 8 TeV analysis: validation

Likelihood fit

The linearity of the response of the likelihood fit of the classifier distribution is tested through the generation of pseudoexperiments in which the input signal Monte Carlo acceptance is rescaled by a factor ranging from 0.2 to 1.8 times the Standard Model expectation. An ensemble test of 50k pseudoexperiments is created for each rescaling configuration, considering only the variations corresponding to the statistics of the data and simulation samples since the goal of this test is to check the linearity of the measured cross section value independently of its systematic uncertainties (the procedure used to estimate the systematic uncertainties has no impact on the central measurement which is taken from the likelihood fit to the data). The linearity graph obtained for the signal events is displayed in Figure F.1, where the output scale factor is given by the mean value of the fitted β_s distribution. It shows that the likelihood fit response satisfies the closure test and is perfectly linear without any bias: the slope is very close to one and the shift very close to zero.

Systematic uncertainties

The total uncertainty on the cross section measurement is evaluated through the generation of pseudoexperiments implementing all sources of statistical and systematic variations. The positive and negative uncertainties are extracted from the output distribution of the fitted signal scale factor (β_s) by combining quadratically its standard deviation with the difference between its mean value and the nominal value ($\beta_s = 1$) as explained in Section 4.6. Asymmetric systematic input contributions can therefore lead to an asymmetric cross-section uncertainty due to a notable difference between the mean and nominal β_s values.
Figure F.2 shows the linearity test on the mean values of the output β_s distributions generated from ensemble tests including all the sources of rate and shape systematic variations used in the s-channel analysis. A small difference is spotted between the

mean value of the output β_s distribution and the input signal re-scaling factor, and increases with the latter. When adding quadratically this difference to the standard deviation of the distribution, a negligible cross section uncertainty bias is finally obtained: for the Standard Model expectation ($\beta_s = 1$), the difference of 7% found leads indeed to an up/down uncertainty bias of 0.3% when it is combined with the distribution width (76%).

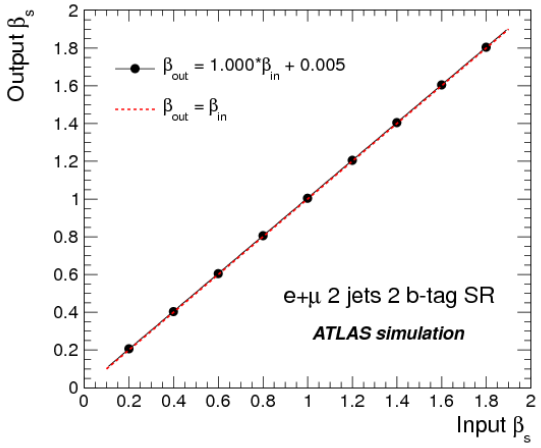

Figure F.1: Linearity test on the s-channel scale factor β_s extracted from the likelihood fit of pseudo-data distributions. The solid black line represents the linear fit of the response and the red dashed line corresponds to the closure test.

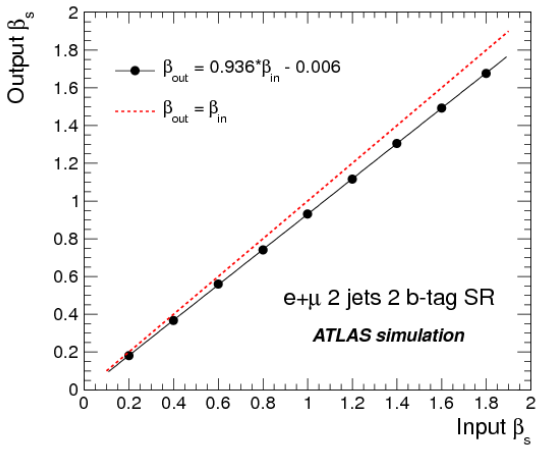

Figure F.2: Linearity test on the *mean value* of the s-channel scale factor β_s extracted from ensemble tests including all the statistical and systematic variations.

Signal distributions for the systematic uncertainties

To visualize the expected impact of a given source of systematic uncertainty on the measurement, one can build the corresponding positive and negative variations for the signal BDT response. A pseudo-data distribution is first generated by adding the signal and backgrounds, using the systematically varied $\pm 1\sigma$ rates and shapes; when the shape variation of a given process is not included in the uncertainty estimate, the nominal template distribution is renormalized by using the varied rate. The up and down BDT outputs for signal are then obtained by subtracting to the pseudo-data distribution the nominal background templates rescaled by the β factors. The positive and negative BDT outputs are finally compared to the ones of the non rescaled nominal signal in order to illustrate the overall normalization correction β_s needed to match the distributions.
Figures F.3 and F.4 show the signal BDT output corresponding to the main sources of shape uncertainties ($t\bar{t}$ E_T^{miss} scale and $t\bar{t}$ jet energy scale variations), compared to the distributions associated to the rate only variations; the fluctuations are much more evident for the first set. The signal scale factors β_s given by the likelihood fit to the generated up and down pseudo-data distributions are also quoted in the plots, showing the strong effect of the shape variations associated to a single process when combining the signal and background templates to create pseudo-data.

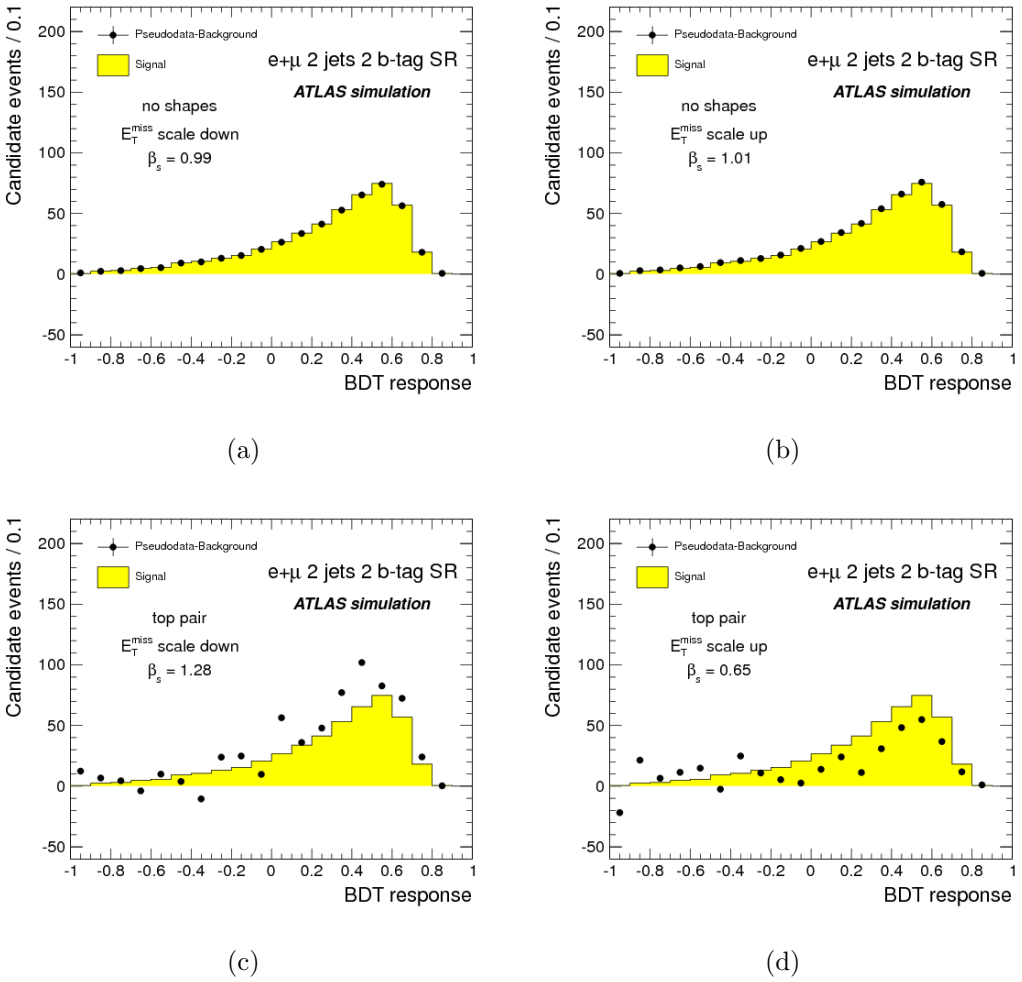

Figure F.3: Expected signal distributions of the BDT classifier after background subtraction to the pseudo-data including the E_T^{miss} scale $\pm 1\sigma$ variations (a) down uncertainty with rates only, (b) up uncertainty with rates only, (c) down uncertainty with $t\bar{t}$ shape and (d) up uncertainty with $t\bar{t}$ shape. The statistical errors of the Monte Carlo signal sample are smaller than the size of the points.

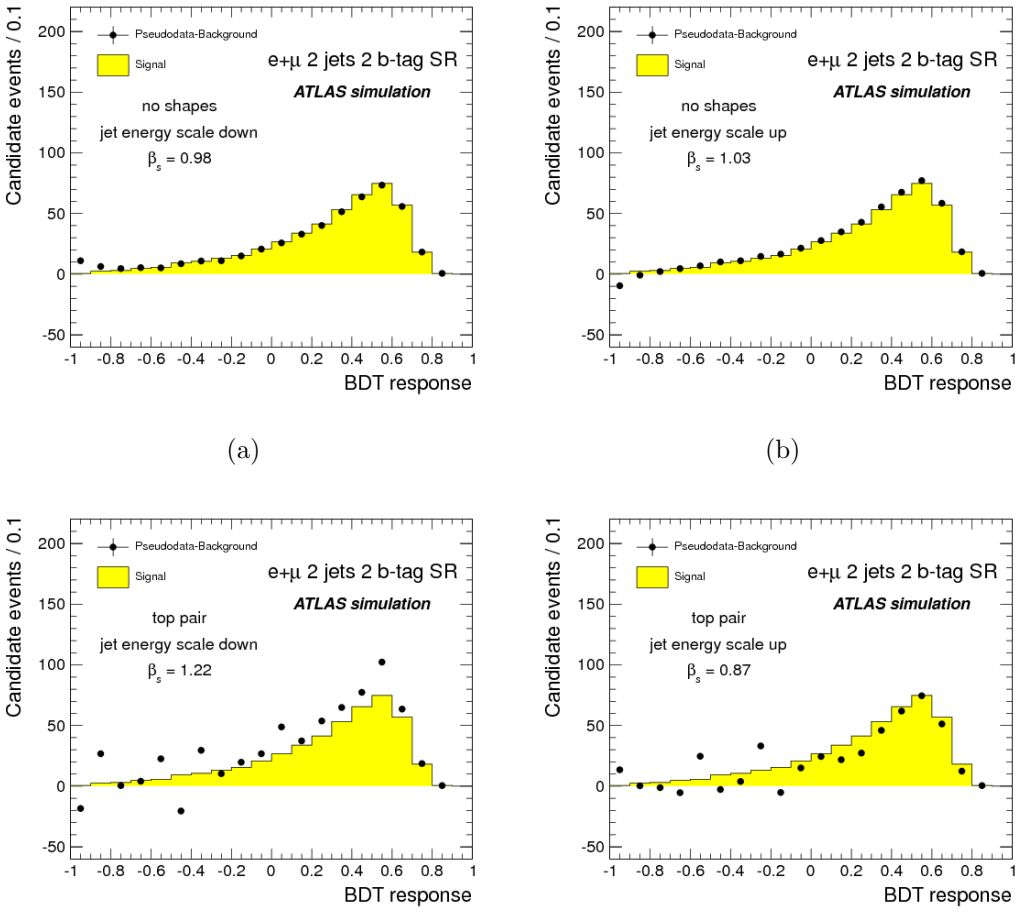

Figure F.4: Expected signal distributions of the BDT classifier after background subtraction to the pseudo-data including the jet energy scale $\pm 1\sigma$ variations (a) down uncertainty with rates only, (b) up uncertainty with down with rates only. (c) down uncertainty with $t\bar{t}$ shape and (d) up uncertainty with $t\bar{t}$ shape. The statistical errors of the Monte Carlo signal sample are smaller than the size of the points.

Scale factor distributions

Figure F.5 presents the expected distribution of the signal scale factor β_s obtained from an ensemble test of 50k pseudoexperiments in which all sources of uncertainties are simultaneously varied. The nominal and mean values are displayed, as well as the derived up and down total expected uncertainties.

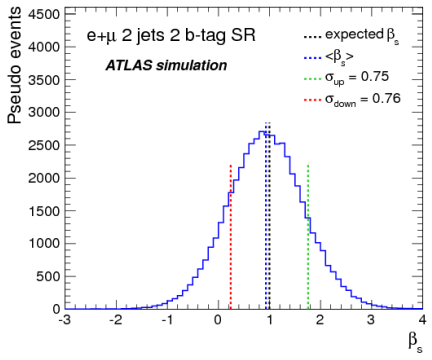

Figure F.5: Expected distribution of the s-channel scale factor β_s. The up and down uncertainties are determined with respect to the generated expected β_s (1): $\sigma_{up} = \sigma$ and $\sigma_{down} = \sqrt{\sigma^2 + \Delta^2}$ with $\Delta =< \beta_s > -1$.

The expected correlation between the Q-value and the signal scale factor β_s is displayed in Figure F.6, where the observed β_s and Q-values used in the cross section measurement are also plotted. One can see that the (β_s, Q-value) point associated with the data is inside the envelop given by the pseudoexperiments and very close to the most populated region; it corresponds to one of the most probable expected outcomes of the measurement. The expected Q-value defined as the median of the projection on the y-axis is also shown.

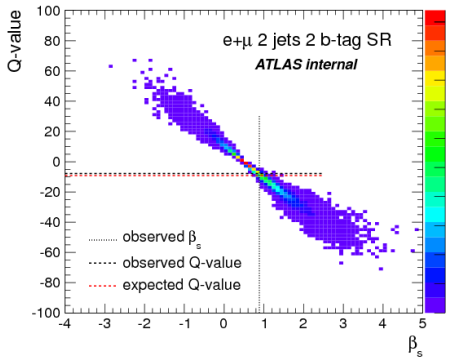

Figure F.6: Expected Q-value as a function of the s-channel scale factor β_s. The observed β_s and Q-value derived from the likelihood fit to the data are drawn, as well as the expected Q-value defined as the median of the projection on the y-axis.

Bibliography

[1] The CDF and D0 Collaborations. Combination of the top-quark mass measurements from the Tevatron collider. Phys. Rev. D 86, 2012.

[2] The ATLAS and CMS Collaborations. Top-quark mass measurements at the LHC. arXiv:1205.2175, 2012.

[3] Observation of top quark production in $p-\bar{p}$ collisions with the collider detector at fermilab. Phys. Rev. Lett. 74:2626–2631, 1995.

[4] The D0 Collaboration. Observation of the quark top. Phys. Rev. Lett. 74:2632-2637, 1995.

[5] C. N. Yang, R. L. Mills. Conservation of isotopic spin and isotopic gauge invariance. Phys. Rev. 96:191195, 1954.

[6] S. L. Glashow. Partial symmetries of weak interactions. Nucl. Phys. 22:579-588, 1961.

[7] A. Salam. Weak and electromagnetic interactions. Proceedings of the 8th Nobel Symposium on Elementary Particle Theory, Relativistic Groups and Analyticity :367-377, 1968.

[8] S. Weinberg. A model of leptons. Phys. Rev. Lett. 19 1264-1266, 1967.

[9] Ne'eman Y. Derivation of strong interactions from a gauge invanance. Nuclear Phys. 26:222-229, 1961.

[10] M Gell-Mann. A schematic model of baryons and mesons. Phys. Lett. 8 214, 1964.

[11] H Fritzsch, M Gell-Mann and H Leutwyler. Advantages of the color gluon octet picture. Phys. Lett. 47B, 1973.

[12] F. Englert, R. Brout. Broken symmetry and the mass of gauge vector mesons. Phys. Rev. Lett., 13:321-232, 1964.

[13] P. W. Higgs. Broken symmetries and the masses of gauge bosons. Phys. Rev. Lett. 13:508-509, 1964.

[14] The ATLAS Collaboration. Observation of a new particle in the search for the Standard Model Higgs boson with the ATLAS detector at the LHC. Phys. Lett. B 716:1-29, 2012.

[15] The CMS Collaboration. Observation of a new boson at a mass of 125 GeV with the CMS experiment at the LHC. Phys. Lett. B 716:30, 2012.

[16] J. Beringer et al. (Particle Data Group). The review of particle physics. Phys. Rev. D86, 010001, 2012.

[17] J. Charles, et al. CP violation and the CKM matrix: Assessing the impact of the asymmetric b factories. Eur. Phys. JC41:1-131, 2005.

[18] Quadt A. Top Quark Physics at Hadron Colliders. Advances in the physics of particles and nuclei, Journal 28, Springer, 2007.

[19] Hai H.L. et al. New parton distributions for collider physics. Phys. Rev. D 82, 074024, 2010.

[20] Reya E. Schuck C. Gluck M. Jimenez-Delgado P. On the role of heavy flavor parton distribution at hadron colliders. Phys. Lett. B 664:103-138, 2008.

[21] Ball R. D et al. Impact of heavy quark masses on parton distribution functions and LHC phenomenology. Nucl. Phys. B 849:296-263, 2011.

[22] H1 and ZEUS Collaborations. Combined measurement and QCD analysis of the inclusive $e^{+-}p$ scattering cross section at HERA. JHEP 1001 109, 2010.

[23] A.D. Martin, W.J. Stirling, R.S. Thorne, and G. Watt. Parton distributions for the LHC. Eur.Phys.J.C63:89-285, 2009.

[24] Cacciari M. Czakon M. Mangano M. Mitov A. Nason P. Top-pair production at hadron colliders with next-to-next-to-leading logarithmic soft-gluon resummation . Phys. Lett. B 710:612-622, 2012.

[25] Alexander Mitov Michal Czakon, Paul Fiedler. The total top quark pair production cross-section at hadron colliders through $O(\alpha_S^4)$. Phys. Rev. Lett. 110 252004, 2013.

[26] Nikolaos Kidonakis. Next-to-next-to-leading-order collinear and soft gluon corrections for t-channel single top quark production. Phys. Rev. D 83, 091503(R), 2011.

[27] Nikolaos Kidonakis. Two-loop soft anomalous dimensions for single top quark associated production with a W^- or H^-. Phys. Rev. D 82, 054018, 2010.

[28] Nikolaos Kidonakis. Next-to-next-to-leading logarithm resummation for s-channel single top quark production. Phys. Rev. D 81, 054028, 2010.

[29] Valentina Zaccolo. The Relevance of a Precise Determination of Vtb from Single-Top Production at LHC, Tesi di Laurea, Universita' degli studi di Trieste. AA 2010-2011.

[30] CDF Collaboration. Observation of Electroweak Single Top-Quark Production. Phys. Rev. Lett. 103, 092002, 2009.

[31] D0 Collaboration. Observation of Single Top-Quark Production. Phys. Rev. Lett. 103, 092001, 2009.

[32] The ATLAS Collaboration. Measurement of the t-channel single top-quark production cross section in pp collisions at with the ATLAS detector. Phys. Lett. B 717, 45:330–350, 2012.

[33] The CMS Collaboration. Measurement of the t-channel single top quark production cross section in pp collisions at $\sqrt{s} = 7$ TeV. Phys. Rev. Lett. 107 9:091802, 2011.

[34] The ATLAS Collaboration. Evidence for the associated production of a W boson and a top quark in ATLAS at $\sqrt{s} = 7$ TeV. Phys. Lett. B 716:142–159, 2012.

[35] The CMS Collaboration. Evidence for associated production of a single top quark and W boson in pp collisions at $\sqrt{s}$=7 TeV. Phys. Rev. Lett. 110 2:022003, 2013.

[36] Measurement of t-Channel Single Top-Quark Production in pp Collisions at $\sqrt{s} = 8$ TeV with the ATLAS detector. Technical Report ATLAS-CONF-2012-132, CERN, Geneva, 2012.

[37] The CMS Collaboration. Measurement of the single-top t-channel cross section in pp collisions at centre-of-mass energy of 8 TeV. Technical Report CMS-PAS-TOP-12-011, CERN, Geneva, 2012.

[38] The ATLAS Collaboration. Measurement of the cross-section for associated production of a top quark and a W boson at $\sqrt{s} = 8$ TeV with the ATLAS detector. Technical Report ATLAS-CONF-2013-100, CERN, Geneva, 2013.

[39] The CMS Collaboration. Observation of the associated production of a single top quark and a W boson in pp collisions at $\sqrt{s} = 8$TeV. Technical Report arXiv:1401.2942. CMS-TOP-12-040. CERN-PH-EP-2013-237, CERN, Geneva, 2014. Comments: Submitted to Phys. Rev. Lett.

[40] The CDF and D0 collaborations. Observation of s-channel production of single top quarks at the Tevatron. Phys. Rev. Lett. 112: 231803, 2014.

[41] The D0 Collaboration. Precision Measurement of the Ratio $\mathcal{B}(t \to Wb)/\mathcal{B}(t \to Wq)$ and extraction of $|V_{tb}|$. Phys.Rev.Lett. 107, 121802, 2011.

[42] Lacker h. et al. Model-independent extraction of $|V_{tq}|$ matrix elements from top-quark measurements at hadron colliders. Eur. Phys. J. C (72): 2048, 2012.

[43] CDF Collaboration. First observation of electroweak single top quark production. Phys. Rev. Lett. 103 9:092002, Aug 2009.

[44] T. M. P. Tait. Signals for the electroweak symmetry breaking associated with the top quark. Ph.D. Thesis, MSUHEP-90622, arXiv:hep-ph/9907462v1, 1999.

[45] Tim M. P. Tait and C.-P. Yuan. Single top quark production as a window to physics beyond the Standard Model. Phys. Rev. D 63 1:014018, 2000.

[46] C.P. Yuan Ehab Malkawi, Tim Tait. A model of strong flavor dynamics for the top quark. Phys. Lett. B 385:304-310, 1996.

[47] Gabriela Barenboim, José Bernabéu, Joaquim Prades, and Martti Raidal. Constraints on the R mass and C violation in left-right models. Phys. Rev. D 55 7:4213–4221, 1997.

[48] Gustavo Burdman, Bogdan A. Dobrescu, and Eduardo Pontón. Resonances from two universal extra dimensions. Phys. Rev. D 74 7:075008, 2006.

[49] Majid Hashemi. Single top events as a source of light charged higgs in the fully hadronic final state at LHC. Journal of High Energy Physics 05 112, 2013.

[50] Stefano Moretti Renato Guedes and Rui Santos. Charged Higgs boson production in single top mode at the LHC. J. Phys.: Conf. Ser. 447 012057, 2013.

[51] S. L. Glashow, J. Iliopoulos, L. Maiani. Weak interactions with lepton-hadron symmetry. Phys. Rev. D 2: 12851292, 1970.

[52] Alwall J.; Frederix R.; Gerard J.-M.; Giammanco A.; Herquet M.; Kalinin S.; Kou E.; Lemaitre V.; Maltoni F. Is V_{tb}=1? European Physical Journal C - Particles and Fields, Vol. 49 Issue 3, p791, 2006.

[53] The D0 collaboration. Evidence for s-channel single top quark production in $p\bar{p}$ collisions at $\sqrt{s} = 1.96$ TeV. Phys. Lett. B 726, 656, 2013.

[54] Jun Gao; Chong Sheng Li; Li Lin Yang; Hao Zhang. Search for anomalous top quark production at the early LHC. Phys. Rev. Lett. 107, 092002, 2011.

[55] C E Hill, C Andresen, J A Chamings, V Coco, D Kchler, A M Lombardi, E Sargsya, and R Scrivens. Characterisation and Performance of The CERN ECR4 Ion Source. AIP Conf. Proc. 749:161–164, 2004.

[56] Oliver Sim Brning, Paul Collier, P Lebrun, Stephen Myers, Ranko Ostojic, John Poole, and Paul Proudlock. *LHC Design Report*. CERN, Geneva, 2004.

[57] The ATLAS Collaboration. ATLAS DETECTOR AND PHYSICS PERFORMANCE, Technical Design Report, CERN/LHCC 99-14. 1999.

[58] The CMS Collaboration. CMS Physics TDR, CERN-LHCC-2006-001. 2006.

[59] The ALICE Collaboration. ALICE Technical Proposal for A Large Ion Collider Experimentat the CERN LHC, CERN/LHCC/9571. 1995.

[60] The LHCb collaboration. LHCf experiment : Technical Design Report, CERN-LHCC-2006-004. 2006.

[61] The TOTEM Collaboration. TOTEM Technical Design Report, CERN-LHCC-2004-002. 2004.

[62] The LHCf collaboration. LHCf experiment : Technical Design Report, CERN-LHCC-2006-004. 2006.

[63] The MoEDAL collaboration. MoEDAL Technical Design Report, CERN-LHC-2009-006. 2009.

[64] The ATLAS collaboration. Improved luminosity determination in *pp* collisions at $\sqrt{s} = 7$ TeV using the ATLAS detector. Eur. Phys. J. C73 2518, 2013.

[65] The ATLAS Collaboration. *ATLAS detector and physics performance, Technical Design Report, 1.* CERN, Geneva, 1999.

[66] The ATLAS Collaboration. *ATLAS detector and physics performance, Technical Design Report, 2.* CERN, Geneva, 1999.

[67] The ATLAS Collaboration. ATLAS magnet system. Technical Report CERN-LHCC-97-18, 1997.

[68] The ATLAS Collaboration. ATLAS inner detector. Technical Report CERN-LHCC-97-016, 1997.

[69] F Hugging. The ATLAS Pixel Detector. EEE Transactions on Nuclear Science 53, 3:1732–1736, 2006.

[70] Abdesselam et al. The integration and engineering of the ATLAS SemiConductor Tracker Barrel. Volume of Instrumentation 3 10:10006, 2008.

[71] V.A Mitsou. The ATLAS Tranistion Radiation Tracker. Astroparticle, Particle and Space Physics, Detectors and Medical Physics Applications, World Scientific, Volume of Instrumentation:497–501, 2004.

[72] A Vogel. ATLAS Transition Radiation Tracker (TRT): straw Tube Gaseous Detectors at High Rates. Nucl. Instrum. Meth. A 732:277–280, 2013.

[73] The ATLAS Collaboration. *ATLAS liquid-argon calorimeter: Technical Design Report.* CERN, Geneva, 1996.

[74] J. Colas et al. Position resolution and particle identification with the ATLAS EM calorimeter. Nucl. Instrum. Meth. A 550 96, 2005.

[75] The ATLAS collaboration. Readiness of the ATLAS Liquid Argon Calorimeter for LHC Collisions. Eur. Phys. J. C 70:723–753, 2010.

[76] The ATLAS collaboration. Electron performance measurements with the atlas detector using the 2010 lhc proton-proton collision data. Eur. Phys. J. C72 1909, 2012.

[77] The ATLAS Collaboration. *ATLAS tile calorimeter: Technical Design Report*. CERN, Geneva, 1996.

[78] P. Adragna, V. Cavasinni, D. Costanzo, T. Del Prete, A. Dotti, et al. The ATLAS hadronic tile calorimeter: from construction toward physics. IEEE Trans. Nucl. Sci. 53:1275–1281, 2006.

[79] Barillari T. The ATLAS liquid argon hadronic end-cap calorimeter: construction and selected beam test results. arXiv:physics/0407026, 2004.

[80] Krieger P. Performances of the ATLAS liquid argon forward calorimeter in beam tests. WSPC-Como proceedings, 2007.

[81] The ATLAS Collaboration. *ATLAS Muon Spectrometer: Technical Design Report*. CERN, Geneva, 1996.

[82] Aloisio A. et al. The Muon Spectrometer Barrel Level-1 Trigger of the ATLAS Experiment at LHC. IEE Trans. Nucl. Sci. 53, 2004.

[83] Peter Jenni, Marzio Nessi, Markus Nordberg, and Kenway Smith. *ATLAS high-level trigger, data-acquisition and controls: Technical Design Report*. Technical Design Report ATLAS. CERN, Geneva, 2003.

[84] Gabaldon C. Performance of the ATLAS Trigger System. Journal of Instrumentation 7 C01092, 2012.

[85] Beck H.-P. Bee C.P. Boissat C. Caprini M. Duval P.-Y. et al. The ATLAS event filter. Journal of Instrumentation, 2012.

[86] Y Nakahama. Designing the ATLAS trigger menu for high luminosities. Technical Report ATL-DAQ-PROC-2012-037, CERN, Geneva, Jun 2012.

[87] The ATLAS Collaboration. Performance of the ATLAS Electron and Photon Trigger in p-p Collisions at $\sqrt{s} = 7$ TeV in 2011. Technical Report ATLAS-CONF-2012-048, CERN, Geneva, 2012.

[88] The ATLAS collaboration. Electron performance measurements with the ATLAS detector using the 2010 LHC proton-proton collision data, Eur. Phys. J. C72 1909. 2012.

[89] The ATLAS Collaboration. Improved electron reconstruction in ATLAS using the Gaussian Sum Filter-based model for bremsstrahlung. Technical Report ATLAS-CONF-2012-047, ATLAS-COM-CONF-2012-068, 2012.

[90] The ATLAS Collaboration. Expected electron performance in the ATLAS experiment. Technical Report ATL-PHYS-PUB-2011-006, CERN, Geneva, 2011.

[91] Electron efficiency measurements with the ATLAS detector using the 2012 LHC proton-proton collision data. Technical Report ATLAS-CONF-2014-032, CERN, Geneva, Jun 2014.

[92] https://twiki.cern.ch/twiki/bin/view/AtlasPublic/EgammaTriggerPublicResults, 2013.

[93] The ATLAS Collaboration. Preliminary results on the muon reconstruction efficiency, momentum resolution, and momentum scale in ATLAS 2012 pp collision data. Technical Report ATLAS-CONF-2013-088, CERN, Geneva, 2013.

[94] The ATLAS Collaboration. Identification of muon candidates in pp collisions at $\sqrt{s}$=900 GeV with the ATLAS detector. Technical Report ATLAS-CONF-2010-015, CERN, Geneva, 2010.

[95] P. Hart R. Duda. Use of the Hough Transformation to Detect Lines and Curves in Pictures. Comm. ACM, Vol. 15, 1972.

[96] The ATLAS Collaboration. A measurement of the muon reconstruction efficiency in 2010 ATLAS data using J/ψ decays. Technical Report ATLAS-CONF-2012-125, CERN, Geneva, 2012.

[97] The ATLAS Collaboration. Muon reconstruction efficiency in reprocessed 2010 LHC proton-proton collision data recorded with the ATLAS detector. Technical Report ATLAS-CONF-2011-063, CERN, Geneva, 2011.

[98] https://twiki.cern.ch/twiki/bin/view/AtlasPublic/MuonPerformancePublicPlots, 2011.

[99] https://twiki.cern.ch/twiki/bin/view/AtlasPublic/MuonTriggerPublicResults, 2013.

[100] The ATLAS Collaboration. Jet energy scale and its systematic uncertainty in proton-proton collisions at $\sqrt{s}$= 7 TeV with ATLAS 2011 data. Technical Report ATLAS-CONF-2013-004, CERN, Geneva, 2013.

[101] The ATLAS Collaboration. Calorimeter clustering algorithms: description and performance. Technical Report ATLAS-LARG-PUB-002, CERN, Geneva, 2008.

[102] Matteo Cacciari, Gavin P. Salam, Gregory Soyez. The anti-kt jet clustering algorithm, JHEP 0804:063,2008, arXiv:0802.1189 [hep-ph]. 2008.

[103] The ATLAS Collaboration. Selection of jets produced in proton-proton collisions with the ATLAS detector using 2011 data. Technical Report ATLAS-CONF-2012-020, CERN, Geneva, 2012.

[104] The ATLAS Collaboration. Jet energy scale and its systematic uncertainty in proton-proton collisions at $\sqrt{s}$=7 TeV with ATLAS 2011 data. Technical Report ATLAS-CONF-2013-004, CERN, Geneva, 2013.

[105] Jet energy scale and its systematic uncertainty in proton-proton collisions at sqrt(s)=7 TeV in ATLAS 2010 data. Technical Report ATLAS-CONF-2011-032, CERN, Geneva, Mar 2011.

[106] The ATLAS Collaboration. Jet energy resolution in proton-proton collisions at $\sqrt{s}$ = 7 TeV recoreded in 2010 with the ATLAS detector. The European Physical Journal C, 73:2306, 2013.

[107] https://twiki.cern.ch/twiki/bin/view/AtlasPublic/JetEtmissApproved2013Jer2011, 2013.

[108] The ATLAS Collaboration. Pile-up subtraction and suppression for jets in ATLAS. Technical Report ATLAS-CONF-2013-083, CERN, Geneva, 2013.

[109] Commissioning of the ATLAS high-performance b-tagging algorithms in the 7 TeV collision data. Technical Report ATLAS-CONF-2011-102, CERN, Geneva, Jul 2011.

[110] Measurement of the b-tag Efficiency in a Sample of Jets Containing Muons with 5 fb^{-1} of Data from the ATLAS Detector. Technical Report ATLAS-CONF-2012-043, CERN, Geneva, Mar 2012.

[111] The ATLAS Collaboration. Performance of Missing Transverse Momentum Reconstruction in ATLAS with 2011 Proton-Proton Collisions at $\sqrt{s}$ = 7 TeV. Technical Report ATLAS-CONF-2012-101, CERN, Geneva, 2012.

[112] The ATLAS Collaboration. Performance of Missing Transverse Momentum Reconstruction in ATLAS studied in Proton-Proton Collisions recorded in 2012 at 8 TeV. Technical Report ATLAS-CONF-2013-082, CERN, Geneva, 2013.

[113] Hoecker A., Speckmayer P., Stelzer J., Therhaag J., von Toerne E., and Voss H. TMVA: Toolkit for Multivariate Data Analysis. PoS ACAT:040, 2007.

[114] Lombardo V. Diboson production cross section at LHC. arXiv:1305.3773, 2013.

[115] Nisius R. QCD results from the LHC. Nucl. Phys. Proc. Suppl.:216–227, 2012.

[116] B Acharya, S Adomeit, M Aoki, B Alvarez, F Balli, S Bilski, K Becker, D Benjamin, C Bernard, K Black, S Calvet, R Camacho, G Cortiana, G Compostella, C Doglioni, F Derue, K F Loureiro, N Ghodbane, D Hirschbuehl, V Kaushik, K Kendziorra, O M Kind, A Krasznahorkay, T Kuhl, H C Lee, A Lister, L Mijovic, J D Morris, R Moles Valls, O Nackenhorst, M zur Nedden, M Owen, U Pinamonti, M Rudolph, G Salamanna, U de Sanctis, J Schwindling, J Searcy, L Serkin, E Shabalina, K Shaw, J Sjoelin, R Soualah, D B Ta, T Theveneaux-Pelzer, M Vreeswijk, and H Zhu. Object selection and calibration, background

estimations and MC samples for the Winter 2012 Top Quark analyses with 2011 data. Technical Report ATL-COM-PHYS-2012-224, CERN, Geneva, 2012.

[117] B Acharya, S Adomeit, M Aoki, B Alvarez, F Balli, S Bilski, K Becker, D Benjamin, C Bernard, K Black, S Calvet, R Camacho, G Cortiana, G Compostella, C Doglioni, F Derue, K F Loureiro, N Ghodbane, D Hirschbuehl, V Kaushik, K Kendziorra, O M Kind, A Krasznahorkay, T Kuhl, H C Lee, A Lister, L Mijovic, J D Morris, R Moles Valls, O Nackenhorst, M zur Nedden, M Owen, U Pinamonti, M Rudolph, G Salamanna, U de Sanctis, J Schwindling, J Searcy, L Serkin, E Shabalina, K Shaw, J Sjoelin, R Soualah, D B Ta, T Theveneaux-Pelzer, M Vreeswijk, and H Zhu. Object selection and calibration, background estimations and MC samples for the Winter 2012 Top Quark analyses with 2011 data. Technical Report ATL-COM-PHYS-2012-224, CERN, Geneva, Feb 2012.

[118] B Acharya, J Adelman, S Adomeit, M Aoki, B Alvarez, F Balli, W Bell, K Becker, K Behr, D Benjamin, E Bergeaas Kuutmann, C Bernard, K Black, S Calvet, R Camacho, Y Coadou, G Cortiana, N Cooper-Smith, T Cornelissen, M Cristinziani, V Dao, U De Sanctis, C Doglioni, F Derue, K Finelli, KJ Grahn, J Groth-Jensen, S Head, A Henrichs, D Hirschbuehl, V Kaushik, OM Kind, H Khandanyan, A Krasznahorkay, T Kuhl, E Le Menedeu, HC Lee, A Lister, KF Loureiro, L Miljovic, JD Morris, R Moles Valls, O Nackenhorst, D Pelikan, M Owen, M Pinamonti, K Rao, K Rosbach, M Rudolph, G Salamanna, J Schwindling, J Searcy, E Shabalina, K Shaw, J Sjolin, R Soualah, S Stamm, DB Ta, T Theveneaux-Pelzer, E Thompson, K Uchida, L Valery, M Vreeswijk, C Wasicki, IJ Watson, K Yau, J Zhong, H Zhu, and M zur Nedden. Object selection and calibration, background estimations and MC samples for the Winter 2013 Top Quark analyses with 2012 data. Technical Report ATL-COM-PHYS-2013-088, CERN, Geneva, 2013.

[119] K Becker, T Cornelissen, F Derue, A Henrichs, D Hirschbhl, X Lei, O Nackenhorst, F O'Grady, D Pelikan, M Pinamonti, S Pires, J Sjlin, and P Tepel. Estimation of Fake Lepton Background for Top Analyses Using the $\sqrt{s} = 8$ TeV Dataset. Technical Report ATL-COM-PHYS-2013-1100, CERN, Geneva, 2013.

[120] The D0 collaboration. Evidence for production of single top quarks. Phys. Rev. D 78: 012005, 2013.

[121] Coadou Y. Multivariate analysis. ESIPAP - Physics of particle and astroparticle detectors, 2014.

[122] Ji Zhu Hai-Jun Yang, Byron P. Roe. Studies of Boosted Decision Trees for MiniBooNE Particle Identification. Nucl. Instrum. Meth. A 555: 370-385, 2005.

[123] Coadou Y. Boosted Decision Trees and Applications. EPJ Web of Conferences-Proceedings SOS 2012 IN2P3 School of Statistics, 2012.

[124] Friedman G.H. Greedy Function Approximation: A Gradient Boosting Machine. The Annals of Statistics 29 5: 1189-1232, 2008.

[125] GEANT4 collaboration. GEANT4: A simulation toolkit. Nucl. Inst. Meth. A 506:250, 2003.

[126] P. Nason. A new method for combining nlo qcd computations with parton shower simulations. JHEP 11:040, 2004.

[127] Hung-Liang Lai, Marco Guzzi, Joey Huston, Zhao Li, Pavel M. Nadolsky, et al. New Parton Distributions for Collider Physics. *Phys. Rev.*, D82:074024, 2010.

[128] T. Sjostrand, S. Mrenna and P. Skands. Pythia generator version 6.418. JHEP 05:026, 2006.

[129] P. Z. Skands. Tuning monte carlo generators: The perugia tunes. Phys. Rev. D82: 074018, 2010.

[130] B. Kersevan and R.W. Elzbieta. The Monte Carlo event generator AcerMC version 3.5 with interfaces to PYTHIA 6.4, HERWIG 6.5 and ARIADNE 4.1. arXiv:0405247 [hep-ph], 2008.

[131] B. Kersevan, I. Hinchliffe. A consistent prescription for the production involving massive quarks in hadron collisions. JHEP 0609:033, 2006.

[132] A. Sherstnev and R. Thorne. Parton distributions for lo generators. Eur. Phys. J. C 55:553, 2008.

[133] M.L. Mangano, M. Moretti, F. Piccinini, R. Pittau and A.D. Polosa. Alpgen, a generator for hard multiparton processes in hadronic collisions. JHEP 07:001, 2003.

[134] J. Pumplin et al. New generation of parton distributions with uncertainties from global qcd analysis. JHEP 07:012, 2002.

[135] G. Corcella et al. Herwig 6.5: an event generator for hadron emission reactions with interfering gluons (including supersymmetric processes). JHEP 01:010, 2001.

[136] M. Butterworth, J.R. Forshaw and M.H. Seymour. Multiparton interactions in photoproduction at hera. Z. Phys. C 72:637, 1996.

[137] https://twiki.cern.ch/twiki/bin/viewauth/AtlasProtected/HforTool, 2014.

[138] C. Anastasiou, L. J. Dixon, K. Melnikov, F. Petriello. High-precision qcd at hadron colliders: electroweak gauge boson rapidity distributions at nnlo. Phys. Rev. D69: 094008, 2004.

[139] The ATLAS Collaboration. New ATLAS event generator tunes to 2010 data. Technical Report ATL-PHYS-PUB-2011-008, CERN, Geneva, 2011.

[140] J. M. Campbell, R. K. Ellis, C. Williams. Vector boson pair production at the lhc. Journal of High Energy Physics 1107: 018, 2011.

[141] S. Frixione and B.R. Webber. Matching nlo qcd computations and parton shower simulations. JHEP 0206:029, 2002.

[142] The ATLAS Collaboration. Measurement of ttbar production with a veto on additional central jet activity in pp collisions at $\sqrt{s}$= 7 TeV using the ATLAS detector. Eur.Phys.J. C72: 2043, 2012.

[143] T. Gleisberg, et al. Event generation with SHERPA 1.1. Journal of High Energy Physics 0902: 007, 2009.

[144] M.Beneke P.Falgari S.Kleinb J.Picluma C.Schwinn. NNLL threshold resummation for the total top-pair production cross section . Phys. Lett. B 690: 483, 2010.

[145] S.D. Ellis, R. Kleiss and W.J. Stirling. Measurement of the standard model parameters from a study of z and w bosons. Phys. Lett. B 154:435, 1985.

[146] F.A. Berends, H. Kuijf, B. Tausk and W.T. Giele. On the Production of a W and Jets at Hadron Colliders. Nucl. Phys. B 357:32, 1991.

[147] Botje M., Butterworth J., Cooper-Sarkar A., de Roeck R., Feltesse J., Forte S., Glazov A., Huston J., McNulty R., Sjostrand T., Thorne R. The PDF4LHC Working Group Interim Recommendations. arXiv:1101.0538, 2011.

[148] T. Junk. Confidence level computation for combining searches with small statistics. Nucl. Instrum. Meth. in Phys. Res. A 434:435, 1999.

[149] A.L. Read. Presentation of search results: the CL_s technique. J. Phys G 28:2693, 2002.

[150] D.F.E. Richter-Was and L. Poggioli. ATLFAST2 2.0 a fast simulation package for ATLAS. Technical Report ATL-PHYS-98-131, 1998.

[151] ATLAS collaboration. Search for s-channel single top-quark production at $\sqrt{s}$=7tev using the atlas detector in 2011. Technical Report ATLAS-CONF-PHYS-2011-102, CERN, Geneva, 2011.

[152] Search for s-channel single top-quark production in pp collisions at sqrt(s) = 8 TeV. Technical Report CMS-PAS-TOP-13-009, CERN, Geneva, 2013.

[153] The D0 Collaboration. A precision measurement of the mass of the top quark. Nature 429, 638-642, 2004.